NOVA SCHOOL OF SCIENCE & TECHNOLOGY

DEPARTAMENT OF MECHANICAL AND INDUSTRIAL ENGINEERING

Welding of High Entropy Alloys

Jiajia Shen

Master in Marine and Ocean Engineering

DOCTORATE IN MECHANICAL ENGINEERING

NOVA University Lisbon
December, 2022

DEPARTAMENT OF MECHANICAL AND
INDUSTRIAL ENGINEERING

Welding of High Entropy Alloys

Jiajia Shen

Master in Marine and Ocean Engineering

Adviser: João Pedro de Sousa Oliveira,
Assistant Professor, NOVA School of Science and Technology

Composition of the Jury:

Chair: Telmo Jorge Gomes dos Santos
Full Professor, NOVA School of Science and Technology

Rapporteurs: António Manuel de Bastos Pereira
Associate Professor with Habilitation, Universidade de Aveiro
Ana Sofia Figueira Ramos,
Assistant Professor, Universidade de Aveiro

Adviser: João Pedro de Sousa Oliveira,
Assistant Professor, NOVA School of Science and Technology

Members: António Carlos Bárbara Grilo
Full Professor, NOVA School of Science and Technology
Telmo Jorge Gomes dos Santos
Full Professor, NOVA School of Science and Technology

DOCTORATE IN MECHANICAL ENGINEERING

NOVA University Lisbon
December, 2022

Welding of High Entropy Alloys

Acknowledgments

Opening the window, the breeze and the shadows of the trees are as calm as my mind at this moment, this peace comes from the exploration and experience of the three years of my Ph.D. studies, but also from the warmth and cares that I have felt during this period of my life.

I could not achieve this work alone. Therefore, I would like to express the following acknowledgment.

First, to my supervisor, Professor João Pedro Oliveira. During the 3 years of my Ph.D. study, he devoted a considerable effort, guiding me with endless patience and help. His rigorous and meticulous attitude, profound and broad intellectual vision have always inspired me to explore and improve myself. I can say that he is like a guiding light and strong backing on my way of scientific research, giving me the courage and confidence to explore the unknown, it is no exaggeration to say that he changed the trajectory of my career. So much touching and thankfulness, I can't express my gratitude in words, but I will always keep this gratefulness in my heart, and continue to carry on the path of academics with my passion to live up to his expectations.

Next, please allow me to express my gratitude to my family in Chinese.

爸爸，妈妈，奶奶,哥哥和嫂子，谢谢你们在我的背后一直做我最坚实的后盾，给了我足够的爱，支持和包容，让我有勇气和自由去追求自己的梦想，做自己真正热爱的事儿。你们不善于表达爱，却用行动把爱诠释成这个世界上最美妙的字符。谢谢你们给了我一个如此温暖的大家庭，我爱你们!

Special thanks to my country, China Scholarship Council (CSC No. 201808320394), for funding and supporting my study expenses during my Ph.D. abroad, allowing me to devote myself to my studies without any financial pressure.

Then to my friends and colleague, João Lopes, thank you for all your help with experiments and for the company that made my life in Portugal so much richer and more fulfilling! And, Tiago Rodrigues, Igor Felice, Frederico Videira, Samruddha, Isaque, and Rita Goncalves.

To Professor Priyanka (University of North Texas) and Ph.D. student Yeon (Pohang University of Science and Technology) for all the effort in my EBSD experiments. Thanks to DESY, a member of the Helmholtz Association HGF, for the provision of experimental facilities.

To my dear friends. To Xin Hu, we were separated by the Atlantic Ocean in terms of distance, but that didn't stop us from having a real friendship. Whenever I was stressed and anxious, you were always there for me, reassuring me and encouraging me to pick up my confidence and get back on the road. If without you, I don't think I would be in as positive and happy a mentality as I am now!

To Wei Zhang, although we haven't known each other for long, we always feel like old friends. I appreciate your personality and your attitude towards academic research and life. I can always learned a lot from talking with you, thank you very much!

To Hui Wang, we met at a math competition and became good friends. You were the first person to encourage me to apply for a scholarship to pursue a Ph.D. degree abroad, and the first person to give me the idea to do so, thank you for your suggestions and support in the very beginning.

To my roommates Spedia, as well as my Portuguese good friends Sonia, Everton, Mina, Monica, Saliha and Raul. Thank you all for coming along and bringing me a wonderful social life.

Resumo

As ligas de alta entropia são novos materiais de engenharia que possuem propriedades extraordinárias. Presentemente, estudos sobre a soldabilidade desta nova classe de materiais são ainda escassos. Por isso, o presente trabalho visa colmatar parte desta falta de informação focando na soldadura por arco eléctrico das ligas de alta entropia CoCrFeMnNi (sistema Co-Cr-Fe-Mn-Ni), liga eutéctica não-equiatómica $AlCoCrFeNi_{2.1}$ (sistema Al-Co-Cr-Fe-Ni) e ainda liga metaestável $Fe_{42}Mn_{28}Co_{10}Cr_{15}Si_5$ (sistema Fe-Mn-Co-Cr-Si).

Para a liga de CoCrFeMnNi, soldadura por Metal Inert Gas (MIG) utilizando dois materiais de adição distintos, aços inoxidáveis 308 e 410, foi realizada com sucesso. Caracterização multiescala, através da utilização de microscopia electrónica acoplada com análise das propriedades mecânicas e simulações termodinâmicas, é utilizada para avaliar o efeito do ciclo térmico ao longo da junta soldada. De um modo geral, esta liga possui excelente soldabilidade, com as juntas a apresentam boa resposta mecânica.

Soldadura da liga não-equiatómica $AlCoCrFeNi_{2.1}$ é reportada pela primeira vez utilizando soldadura Tungsten Inert Gas (TIG). Novamente, caracterização multiescala permite determinar o impacto do ciclo térmico ao longo das juntas soldadas. A fração volúmica da estrutura eutéctica, assim como os precipitados nanométricos, está directamente relacionada com a distância ao centro do cordão de soldadura. O material como soldado possui um boa combinação de resistência mecânica e ductilidade, evidenciando a boa soldabilidade do material.

Finalmente, soldadura TIG da liga metaestável $Fe_{42}Mn_{28}Co_{10}Cr_{15}Si_5$ foi igualmente realizada com sucesso. Microscopia electrónica, suportada por difração de raios-X com radiação de sincrotrão, são combinadas com simulações termodinâmicas para compreender como as fases existentes variam ao longo da junta soldada. De modo semelhante aos outros materiais estudados, a liga metaestável possui

igualmente boa soldabilidade, com as propriedades mecânicas observadas a permitirem considerar as juntas soldadas para aplicações estruturais.

Os resultados obtidos neste trabalho demonstram que processos de soldadura baseados no arco eléctrico são viáveis para estes novos materiais e que as propriedades resultantes permitem considerar as juntas soldadas para aplicações de índole estrutural.

Abstract

High entropy alloys are novel engineering materials which possess extraordinary properties. Current weldability studies regarding this novel class of materials are scarce. Hence, the present work addresses this shortcoming by focusing on the use of arc-based welding processes for joining of single phase equiatomic CoCrFeMnNi (Co-Cr-Fe-Mn-Ni system), a dual phase non-equiatomic eutectic $AlCoCrFeNi_{2.1}$ (Al-Co-Cr-Fe-Ni system) and a metastable $Fe_{42}Mn_{28}Co_{10}Cr_{15}Si_5$ (Fe-Mn-Co-Cr-Si system) high entropy alloys.

For the single phase CoCrFeMnNi, gas metal arc welding using 308 and 410 stainless steel fillers are used. Multiscale correlative microstructure characterization encompassing electron microscopy coupled with mechanical property analysis, alongside thermodynamic calculations, is used to address the effect of the weld thermal cycle across the joint. Overall, this material possesses excellent weldability, with the joints possessing good mechanical behavior.

The first successful welding of a non-equiatomic eutectic $AlCoCrFeNi_{2.1}$ is obtained using gas tungsten arc welding. Again, multiscale characterization enabled to determine the role of the weld thermal cycle across the welded joint. The volume fraction of the dual-phase structure, as well as those of the strengthening nanoscale precipitates was seen to be correlated to the distance to the heat source. The

as-welded material possessed a combination of good strength and ductility, showcasing the good weldability of this material.

Finally, gas tungsten arc welding of a metastable $Fe_{42}Mn_{28}Co_{10}Cr_{15}Si_5$ was also successfully performed. Electron microscopy, aided by high energy synchrotron X-ray diffraction, were combined with thermodynamic calculation to understand how the existing phases varied across the welded joint. Similarly, to the other welded joints, the metastable alloy was also seen to present good weldability, with the observed mechanical behavior of the joints enabling its use for structural applications in different industries.

The results obtained in this work show that arc-based welding processes are viable for welding of these novel materials and the resulting properties enable to consider the obtained joints for structural-oriented applications.

Keywords

Digital image correlation

Gas metal arc welding

Gas tungsten arc welding

High entropy alloys

Mechanical testing

Microstructure evolution

Synchrotron X-ray diffraction

Thermodynamic calculations

CONTENTS

LIST OF FIGURES

List of Tables

‘

List of Abbreviations

Abbreviation	Definition
BM	Base material
BCC	Body-centered Cubic
B2 BCC phase	Ordered body-centered cubic
CalPhaD	Calculation of Phase Diagrams
DIC	Digital image correlation
EBSD	Electron backscatter diffraction analysis
EDS	Energy dispersive X-ray spectroscopy
EDM	Electrical discharge machining
E-WIMV	Extended Williams-Imhof-Matthies-Vinel algorithm
FCC	Face-centered cubic
FZ	Fusion zone
FWHM	Full Width at Half Maximum
GTAW	Gas tungsten arc welding
GND	Geometrically Necessary Dislocation
GMAW	Gas metal arc welding
GSASII	General Structure Analysis System
HEAs	High entropy alloys
HCP	Hexagonal-close-packed
HEA	High entropy alloy
HAZ	Heat affected zone
HAZ1	HAZ near the BM
HAZ2	HAZ near the FZ
HAZ/FZ	HAZ and FZ near the boundary
IPF	Inverse Pole Figure
KAM	Kernel Average Misorientation
L	Liquid
LD	Longitudinal/Loading direction
MEPP	Maximum entropy production principle
M	Mushy zone
MRF	Microscopy Research Facility
MAUD	Material Analysis Using Diffraction
OM	Optical microscopy
ROM	Rule-of mixture

RD	Rolling direction
SEM	Scanning electron microscopy
S	Solid
SFE	Stacking fault energy
TRIP	Phase transformation induced plasticity
TD	Transverse direction
TWIP	Twinning induced plasticity
TEM	Transmission electron microscopy
TCHEA5.1	ThermoCalc high entropy alloy database 5.1
UNT	University of North Texas
WAAM	Wire Arc Additive Manufacturing

List of Symbols

Abbreviation	Definition
ΔS_{conf}	Mixing entropy of the system
R	Constant of the gas, R= 8.314J/(K.mol)
F	Degree of freedom
C	Number of components
P	Number of phases
E_k	Energy required to form the homogenous nucleus in the liquid phase
E_k'	Energy required to form a heterogeneous nucleus in the liquid phase
θ	Contact angle
G_L	Temperature gradient [^OC]
R	Solidification rate [$^OC\ S^{-1}$]
ΔT	Equilibrium freezing range
ε_{hkl}	Lattice strain for a given (hkl) plane
d_0	The reference d-spacing before loading
d_{hkl}	The d-spacing determined at different stress/strain level
σ_{vm}	Von Mises stresses
ε_{22}	Lattice strain in the TD
v	Poisson ratio
E	Orientation-dependent Young's modulus for a specific (h k l) plane
σ_{22}	Transverse stress
σ_{11}	Longitudinal stresses
λ	Wavelength
P	Dislocation density
ε_0	Lattice strain
B	Burger's vector
a	Lattice parameter

$\Delta\sigma_D$	Dislocation strengthening
M	Average Taylor factor
G	Shear modulus for both matrix phases
c_{11}, c_{12}, c_{44}	Single crystal elastic constants
ΔV	The transformation volume
$V_{\gamma\text{-f.c.c}}$	Volume of the γ-f.c.c. phase
$V_{\varepsilon\text{-h.c.p}}$	Volume of the ε-h.c.p. phase
$a_{\gamma\text{-f.c.c}}$	Lattice parameters for the γ-f.c.c. phase
$a_{\varepsilon\text{-h.c.p}}$	Lattice parameters for the ε-h.c.p. phase
$c_{\varepsilon\text{-h.c.p}}$	Lattice parameters for the ε-h.c.p. phase
$\sigma_{\gamma\text{-f.c.c.}}$	Phase stresses of the γ-f.c.c.
$\sigma_{\varepsilon\text{-h.c.p.}}$	Phase stresses of the ε-h.c.p.
$FWHM_{measured}$	Full width at half maximum measured from software
$FWHM_{microstrain + grain size}$	Peak broadening arising by the grain size and microstrain
$FWHM_{size}$	FWHM induced by grain size
$FWHM_{microstrain}$	FWHM induced by microstrain
$FWHM_{instrumental}$	FWHM induced by instrumental
D	Grain size
ε_{hkl}^{SF}	Lattice strain induced by staking faults
d_{hkl}^{0}	Stress-free lattice spacing
L_{sf}	Interspacing between stacking faults
P_{sf}	Stacking faults probability
d_{111}	(111) d-spacing
σ_{sf}	Stacking faults strengthening
K_{sf}	Strengthening coefficient
σ_{yield}	Yield strength
σ_a	Total strength contributed by various strengthening mechanisms other than stacking faults
$c_{\ \varepsilon\text{-h.c.p. phase}}$	Lattice constants of the ε-h.c.p. phase
$a_{\ \varepsilon\text{-h.c.p. phase}}$	Lattice constants of the ε-h.c.p. phase
$\sum 3$	Sigma 3
σ	Sigma
σ_{Calc}	Calculated stress
$\sigma_{\gamma\text{-f.c.c. DIS}}$	Strengthening contributions γ-f.c.c. phase
$\sigma_{\varepsilon\text{-h.c.p. DIS}}$	Strengthening contributions ε-h.c.p. phase
σ_{Macro}	Macroscopic stress
σ_{Extra}	The difference between the macroscopic stress imparted by the alloy

1.

INTRODUCTION

1.1 Motivation

Traditionally alloy design concepts are focused on using one principal element and then improving the desired properties with relatively minor alloying additions. However, in 2004, Cantor et al. [1] and Yeh et al. [2] independently proposed a new alloy design strategy that broke traditional alloys' design barriers, known as high entropy alloys (HEAs). Nowadays, HEAs are attracting significant interest owing to their attractive and unique properties, including strength, thermal stability, wear and oxidation resistance. Welding, as one of the most important metal processing methods for structural materials, is virtually used in any structural engineering application. Thus, coupling the development of new materials and determining their weldability is essential to either promote them as engineering solutions.

So far, research and development focusing on HEAs mainly concentrate on designing HEAs systems, their thermo-mechanical processing, characterization of the phase formation, evaluation of the mechanical properties, physical and chemical performances, and predictions on the potential applications of these alloys [3]. However, the application of joining techniques to HEAs is still relatively scarce. Hence a gap between the processing-microstructure-properties relationship exists.

In fusion-based welding techniques, although laser welding has significant technical advantages, such as high productivity and small heat source dimensions, the high initial capital investment required for this technology can be detrimental to its implementation in the industry. In contrast, based on arc-based technology, gas tungsten arc welding (GTAW) and gas metal arc welding (GMAW) are low-cost alternatives capable of achieving sound joints with good mechanical performance and appearance for multiple engineering alloys. However, the body of knowledge on the processability of the HEAs is missing the understanding of these materials' weldability. Moreover, filler materials are widely used during fusion-based welding processes to regulate and modify the welded joints composition aiming at producing desired microstructures and/or improve its mechanical performance.

In order to expand the range of industrial applications for HEAs, meeting the needs for dissimilar welded structures, dissimilar weldability (when two different base materials or the addition of filler wire is used) should also be assessed. The non-equilibrium solidification conditions found during fusion-based welding can promote the formation of metastable and/or detrimental phases, which can be mitigated by the adjustment of the process parameters and/or modification of the fusion zone (FZ) composition. The core difficulty during dissimilar welding is the need to control and/or adjust the chemical composition of the FZ so that its microstructure and mechanical properties are suitable for the targeted applications. Therefore, it is critical to have a systematic understanding on the evolution of the microstructure and mechanical properties of similar and dissimilar joints involving HEAs.

In conclusion, studying the weldability of HEAs is still a new topic, and the impact of different filler materials on the microstructure and mechanical properties is yet unknown. Thus, there is an urgent need for an in-depth study on its weldability.

1.2 Objectives

The main goal of this thesis is to study the weldability of different HEAs systems, providing new data for a more massive implementation of these advanced engineering alloys in different structural applications. Based on the development of HEAs, three representative HEAs were selected to be studied, namely the CoCrFeMnNi equiatomic HEA, the eutectic $AlCoCrFeNi_{2.1}$ HEA, and a metastable twinning induced plasticity / transformation induced plasticity (TWIP/TRIP) dual phase $Fe_{42}Mn_{28}Co_{10}Cr_{15}Si_5$ HEA, with the corresponding HEA systems being Co-Cr-Fe-Mn-Ni, Al-Co-Cr-Fe-Ni and Fe-Mn-Co-Cr-Si, respectively.

To achieve this goal, the microstructural evolution of the welded joints was investigated using light optical microscopy (OM), scanning electron microscopy (SEM) aided by electron backscatter diffraction analysis (EBSD), high energy synchrotron X-ray diffraction, and thermodynamic simulations. Additionally, uniaxial tensile testing coupled with digital image correlation (DIC) and microhardness mapping were used to evaluate the mechanical properties of the welded joints. As a result, the microstructural evolution and resulting mechanical properties were systematically evaluated, unveiling the correlation between processing, microstructure, and mechanical properties. Thus, improving the body of work on welded HEAs and expanding the application of HEAs as potential engineering structural materials.

The specific objectives were:

1. For the CoCrFeMnNi HEA, a single phase equiatomic HEA (Co-Cr-Fe-Mn-Ni system):

1) Study on the weldability of the CoCrFeMnNi HEA
    - Background: So far, researchers have focused on the weldability of CoCrFeMnNi HEAs with fusion-based welding processes, but they are mainly limited to similar welding combinations. To further expand its applications in nuclear and aerospace sectors,

joining of the CoCrFeMnNi HEA to other base materials or the addition of filler materials to adjust the composition and modify the material microstructure is required.

- Objectives: To evaluate the weldability of CoCrFeMnNi HEAs when using GMAW with 308 and 410 stainless steels as filler materials, correlating the microstructure evolution and resulting mechanical properties.

2. Eutectic $AlCoCrFeNi_{2.1}$ HEA, a dual phase non-equiatomic HEA (Al-Co-Cr-Fe-Ni system):

1) Study on the deformation behavior of an as-cast eutectic $AlCoCrFeNi_{2.1}$ HEA
    - Background: studies on the as-cast $AlCoCrFeNi_{2.1}$ eutectic HEA have been primarily focused on qualitatively exploring the mechanical properties of the alloy under different deformation conditions (e.g., low temperature vs. room vs. high temperature). A comprehensive quantitative study of the deformation mechanisms of the different phases in this alloy and their impact on the macroscopic mechanical response is yet lacking, thus hampering a complete understanding of microstructure/properties relationships.
    - Objectives: To perform in-situ high energy synchrotron X-ray diffraction to evaluate the micromechanical behavior and microstructure evolution of an as-cast $AlCoCrFeNi_{2.1}$ eutectic HEA during tensile deformation until failure.

2) Study on the weldability of eutectic $AlCoCrFeNi_{2.1}$ HEA
    - Background: Past studies that have addressed the weldability of the $AlCoCrFeNi_{2.1}$ eutectic HEA primarily concentrated on solid-state welding methods.
    - Objectives: To bridge the afore-mentioned gap in the literature, the as-cast $AlCoCrFeNi_{2.1}$ eutectic HEA was welded by gas tungsten arc welding.

3. Metastable TWIP/TRIP $Fe_{42}Mn_{28}Co_{10}Cr_{15}Si_5$ HEA, a dual phase non-equiatomic HEA (Fe-Mn-Co-Cr-Si system):

1) Study on the evolution of microstructure and deformation mechanisms in a metastable $Fe_{42}Mn_{28}Co_{10}Cr_{15}Si_5$ HEA
    - Background: Most studies on the mechanical behavior of metastable HEAs have primarily focused on advanced electron microscopy characterization, while only few studies use diffraction-based techniques to trace, in real time, the microstructure evolution and deformation mechanisms' activation during deformation. Specifically, for the optimized composition of $Fe_{42}Mn_{28}Co_{10}Cr_{15}Si_5$, there is still a gap in the microstructural evolution and assessment of the competing deformation mechanisms experienced by the alloy upon loading.
    - Objectives: To perform an in-situ high energy synchrotron X-ray diffraction to trace, in real time, the activation and changes in the deformation mechanisms of an-cast $Fe_{42}Mn_{28}Co_{10}Cr_{15}Si_5$ metastable HEA during tensile deformation.

2) Study the weldability of the metastable $Fe_{42}Mn_{28}Co_{10}Cr_{15}Si_5$ HEA
    - Background: Currently, there are only two reports on the weldability of metastable HEAs, both using the friction stir welding method. The weldability of metastable HEAs by fusion welding has not yet been reported.
    - Objectives: Evaluate the weldability of metastable $Fe_{42}Mn_{28}Co_{10}Cr_{15}Si_5$ HEA using gas tungsten arc welding.

The research tasks completed in this dissertation are listed in Figure 1-1 as below.

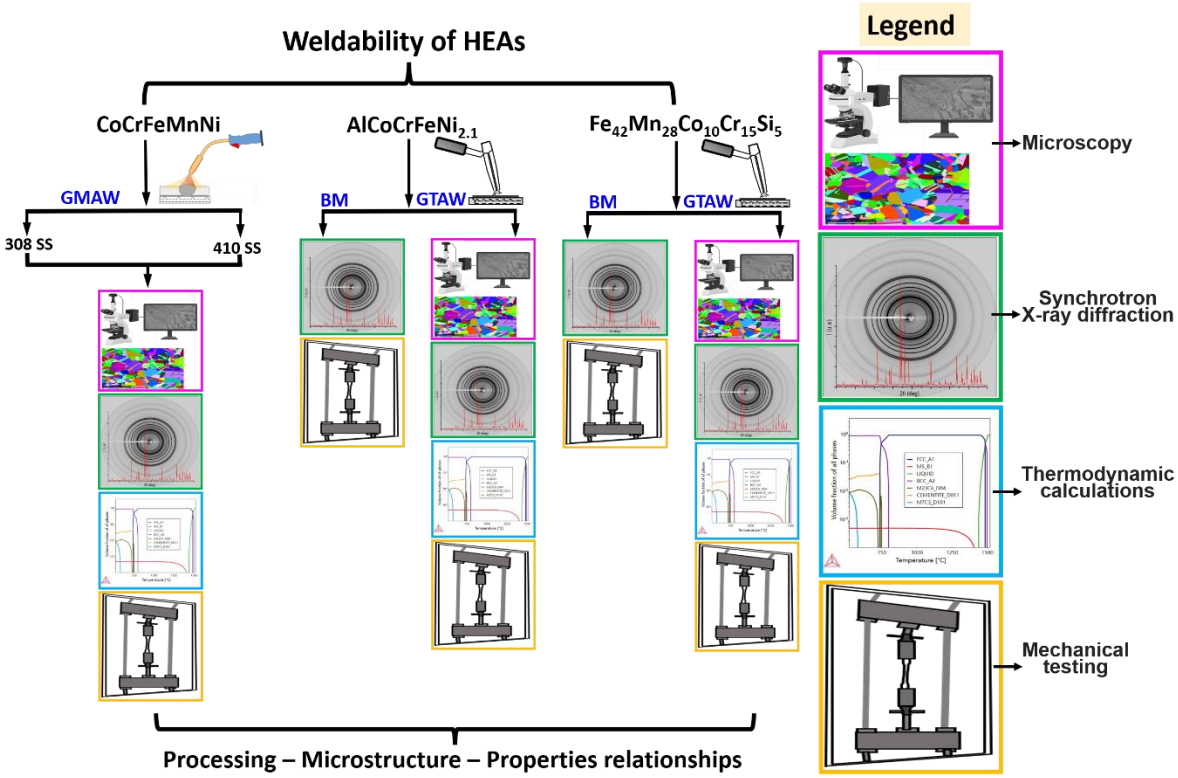

Figure 1-1. Technical route of the thesis.

1.3 Major Findings

A comprehensive analysis of the microstructure evolution and mechanical properties of GMAW CoCrFeMnNi joints obtained with different filler materials was performed. High energy synchrotron X-ray diffraction was used to determine the phase constituents within the joint, while thermodynamic simulations were employed to predict the effect of different dilution ratios on the solidification paths. It was found that a good agreement between experiments and simulations was obtained when considering carbon (C) as a fast diffuser in the Scheil-Gulliver calculations. The chemical composition gradient caused by the dilution of the filler material is closely related to the phase structure that is formed in the FZ. Local stress-strain curves for different regions of the joint were obtained using non-contact DIC, confirming the existence of preferential strain concentrations at the weld toe interface site where fracture is initiated. However, the joints can still be considered for structural application given their high strength and ductility (641 ± 7 MPa, 7.3 ± 0.2 %).

The micromechanical behavior of an as-cast $AlCoCrFeNi_{2.1}$ eutectic HEA during tensile deformation has been investigated by in-situ tensile testing at room temperature using high energy synchrotron X-ray diffraction. It was found that the stress is primarily transferred to the hard B2 BCC phase upon the onset

of plastic deformation. Moreover, plastic deformation of the hard B2 BCC phase is delayed until a macroscopic strain of 3.5% is achieved. It was revealed the possibility to tune the stress/strain response of eutectic HEAs by changing the volume fraction of the existing phases.

The suitability of using an arc-based welding process, in this case GTAW, to join a eutectic $AlCoCrFeNi_{2.1}$ HEA was assessed. It was found that GTAW was able to produce full penetration and defect-free welded joints, suggesting the potential of this fusion-based welding process to join these advanced engineering alloys. Good agreement between experimentally observed phases and thermodynamic predictions was obtained. The joint fracture occurred in the non-affected base material (BM), owing to the refined grain structure of the FZ compared to that of the as-cast BM. The GTAW $AlCoCrFeNi_{2.1}$ joint presented good strength/ductility balance, thus being suitable candidates for structural applications.

A comprehensive assessment of the microstructure/property's relationships of an as-cast metastable TWIP/TRIP dual phase $Fe_{42}Mn_{28}Co_{10}Cr_{15}Si_5$ HEA was probed by high energy in-situ synchrotron X-ray diffraction. It was found that stress partitioning and redistribution between the γ-f.c.c. and ε-h.c.p. phases were seen to be linked to the active deformation mechanisms of the alloy at a given loading step, which can be of great value for the scientific community who is devoted in evaluating the behavior of these extraordinary materials. The contributions of each deformation mechanical to the material strength were determined.

1.4 Document Organization

This thesis is structured in seven chapters and is organized as follows.

The present chapter details the motivation, objectives, and major findings of the presented doctoral dissertation.

Chapter 2 summarizes the definition of HEAs and the progress regarding weldability investigations of these materials. The first part of this chapter is dedicated to highlighting the advantages and application prospects of HEAs as potential engineering structural materials, followed by a brief description of key fusion-based welding processes. The remaining chapter details the characteristics of the three distinct regions in a fusion-based welded joint, with emphasis on the effects of the thermal cycle on the microstructure and mechanical properties of the HAZ, as well as the characteristics of the solidification of the melt pool. In addition, an overview of the current state of research on the weldability of HEAs mainly focused on Co-Cr-Fe-Mn-Ni, Al-Co-Cr-Fe-Ni, and Fe-Mn-Co-Cr-Si systems is presented.

Chapter 3 details the experimental procedures employed to characterize the microstructure and mechanical properties of the materials used in this study, including OM, SEM, EBSD, high energy

synchrotron x-ray diffraction, thermodynamic calculations, microhardness mapping measurements and non-contact DIC during tensile loading to failure.

Chapter 4 focuses on the effect of four different filler wires, 308 and 410 stainless steels, on the microstructure and mechanical properties of GMAW CoCrFeMnNi joints. A combination of extensive microstructure characterization, using OM, SEM coupled EBSD and high energy synchrotron X-ray diffraction, thermodynamic calculations, and mechanical characterization was used to comprehensively understand the microstructure evolution across the joint and correlate it with its mechanical performance.

Chapter 5 starts with the evaluation of the tensile deformation mechanisms of a cast $AlCoCrFeNi_{2.1}$ eutectic HEA probed by synchrotron X-ray diffraction. Then, a detailed analysis of the microstructure and mechanical properties of GTAW $AlCoCrFeNi_{2.1}$ joint is presented.

Chapter 6 explores the activation and changes in the deformation mechanisms of an as-cast metastable $Fe_{42}Mn_{28}Co_{10}Cr_{15}Si_5$ HEA during tensile deformation at room temperature using in-situ synchrotron X-ray diffraction. Then, the evaluation of microstructure and mechanical properties of a GTAW as-cast metastable $Fe_{42}Mn_{28}Co_{10}Cr_{15}Si_5$ HEA is performed combining multiscale material and mechanical characterization.

Chapter 7 summarizes the main conclusions of this work and highlights potential future research topics to be pursued.

1.5 Publications in international peer-reviewed indexed journals (ISI/Scopus)

The scientific output published, submitted, and under preparation in international indexed (ISI/Scopus) journals is listed below:

The published journal papers are presented below:

[1] **Jiajia Shen**, Priyanka Agrawal, Tiago A. Rodrigues, J.G.Lopes, N.Schell, Zhi Zeng, Rajiv S. Mishra, J.P.Oliveira, *Gas tungsten arc welding of as-cast $AlCoCrFeNi_{2.1}$ eutectic high entropy alloy,* Materials & Design, https://doi.org/10.1016/j.matdes.2022.111176.

[2] **Jiajia Shen**, Rita Goncalves, Yeon Taek Choi, J.G.Lopes, Jin Yang, N.Schell, Hyoung Seop Kim, J.P.Oliveira, *Microstructure and Mechanical Properties of Gas Metal Arc Welded CoCrFeMnNi Joints using a 410 Stainless Steel Filler Metal*, Materials Science & Engineering A, https://doi.org/10.1016/j.msea.2022.144025

[3] **Jiajia Shen**, Rita Goncalves, Yeon Taek Choi, J.G.Lopes, Jin Yang, N.Schell, Hyoung Seop Kim, J.P.Oliveira, *Microstructure and Mechanical Properties of Gas Metal Arc Welded CoCrFeMnNi joints using a 308 stainless steel filler metal*, Scripta Materialia, Volume 222, 2023, https://doi.org/10.1016/j.scriptamat.2022.115053

[4] **Jiajia Shen**, Alexander C. Martin, Carolin Fink, João P. Oliveira, *Microstructures in arc-welded multi-principal element alloys* $Al_{10}Co_{25}Cr_8Fe_{15}Ni_{36}Ti$ *and* $Al_{10.87}Co_{21.74}Cr_{21.74}Cu_{2.17}Fe_{21.74}Ni_{21.74}$*: comparison between experimental data and thermodynamic predictions*, Materials Today Communications, https://doi.org/10.1016/j.mtcomm.2022.104784

[5] **Jiajia Shen**, Priyanka Agrawal, Tiago A. Rodrigues, J.G.Lopes, N.Schell, Zhi Zeng, Rajiv S. Mishra, J.P.Oliveira, *Gas tungsten arc welding of as-cast* $Fe_{42}Mn_{28}Co_{10}Cr_{15}Si_5$ *metastable high entropy alloy,* Materials Science & Engineering A. https://doi.org/10.1016/j.msea.2023.144722

[6] **Jiajia Shen**, Zhi Zeng, Mohammadreza Nematollahi, Norbert Schell, Emad Maawad, RN Vasin, Keyvan Safaei, Behrang Poorganji, Mohammad Elahinia, João Pedro Oliveira, *In-situ synchrotron X-ray diffraction analysis of the elastic behaviour of martensite and H-phase in a NiTiHf high temperature shape memory alloy fabricated by laser powder bed fusion,* Additive Manufacturing Letters, Volume 1, 2021, 100003, ISSN 2772-3690, https://doi.org/10.1016/j.addlet.2021.100003.

[7] **Jiajia Shen**, J.G.Lopes, Zhi Zeng, Yeon Taek Choi, E.Maawad, N.Schell, Hyoung Seop Kim, Rajiv S. Mishra, J.P. Oliveira, *Deformation behavior and strengthening effects of an eutectic AlCoCrFeNi2.1 high entropy alloy probed by in-situ synchrotron X-ray diffraction,* Materials Science & Engineering A. https://doi.org/10.1016/j.msea.2023.144946.

[8] Wei Zhang, **Jiajia Shen**, J.P.Oliveira, Bart J. Kooi, Yutao Pei, *Crystallographic orientation-dependent deformation characteristics of addictive manufactured interstitial-strengthened high entropy alloys*, Scripta Materialia, Volume 222, 2023, https://doi.org/10.1016/j.scriptamat.2022.115049.

[9] Tiago A.Rodrigues, Francisco Werley Cipriano Farias, Kaiping Zhang, A.Shamsolhodaei, **Jiajia Shen**, N.Zhou, Norbert Schell, Jan Capek, E.Polatidis, Telmo G. Santos, J.P.Oliveira, *Wire and Arc Addictive Manufacturing of Stainless Steel 316L/Inconel 625 Functionally Graded Material: Developmet and Characterization*, Journal of Materials Research and Technology, https://doi.org/10.1016/j.jmrt.2022.08.169.

[10] JP Oliveira, A Shamsolhodaei, **Jiajia Shen**, JG Lopes, RM Gonçalves, Mariana de Brito Ferraz, Lourenço Piçarra, Z Zeng, N Schell, N Zhou, Hyoung Seop Kim, *Improving the ductility in laser welded joints of CoCrFeMnNi high entropy alloy to 316 stainless steel*, Materials & Design, Volume 219, 2022, 110717, ISSN 0264-1275, https://doi.org/10.1016/j.matdes.2022.110717.

[11] Tiago A. Rodrigues, N. Bairrão, Francisco Werley Cipriano Farias, A. Shamsolhodaei, **Jiajia Shen**, N. Zhou, Emad Maawad, Norbert Schell, Telmo G. Santos, J.P. Oliveira, *Steel-copper functionally graded material produced by twin-wire and arc additive manufacturing (T-WAAM)*, **Materials & Design**, Volume 213, 2022, 110270, ISSN 0264-1275, https://doi.org/10.1016/j.matdes.2021.110270.

[12] JP Oliveira, **Jiajia Shen**, Z Zeng, Jeong Min Park, Yeon Taek Choi, N Schell, E Maawad, N Zhou, Hyoung Seop Kim, *Dissimilar laser welding of a CoCrFeMnNi high entropy alloy to 316 stainless steel*, Scripta Materialia, Volume 206, 2022, 114219, ISSN 1359-6462, https://doi.org/10.1016/j.scriptamat.2021.114219.

[13] J.Charkhchian, A.Zarei-Hanzaki, A.Moshiri, H.R.Abedi, **Jiajia Shen**, J.P.Oliveira, Kanwal Chadha, Clodualdo Aranas Jr, *On the Short-Time Thermal Phase-Stability of As-cast AlCoCrFeNi$_{2.1}$ Eutectic High Entropy Alloy*, Journal of Materials Research and Technology, Volume 20, 2022, 551560, ISSN 2238-7854, https://doi.org/10.1016/j.jmrt.2022.07.058.

[14] Guilherme Gadelha de Sousa Figueiredo, Igor Jordão Marques, Lucas Oliveira Siqueira, **Jiajia Shen**, J.P.Oliveira, Tiago Felipe de Abreu Santos, A coupled computational fluid dynamics approach as a viable tool for thermal history assessment of UNS S32205 duplex stainless steels friction stir welded joints, Welding in the World, https://doi.org/10.1007/s40194-022-01416-z.

[15] Tiago A Rodrigues, JD Escobar, **Jiajia Shen**, Valdemar R Duarte, GG Ribamar, Julian A Avila, Emad Maawad, Norbert Schell, Telmo G Santos, JP Oliveira, *Effect of heat treatments on 316 stainless steel parts fabricated by wire and arc additive manufacturing: Microstructure and synchrotron X-ray diffraction analysis,* Additive Manufacturing , Volume 48, 2021, 102428, ISSN 2214-8604, https://doi.org/10.1016/j.addma.2021.102428.

[16] JP Oliveira, **Jiajia Shen**, JD Escobar, CAF Salvador, Norbert Schell, N Zhou, O Benafan, *Laser welding of H-phase strengthened Ni-rich NiTi-20Zr high temperature shape memory alloy, Material & Design, Volume 202, 2021,109533,ISSN 0264-1275,* https://doi.org/10.1016/j.matdes.2021.109533.

[17] Hamidreza Hekmatjou, Zhi Zeng, **Jiajia Shen**, João Pedro Oliveira, Homam Naffakh-Moosavy, *A comparative study of analytical rosenthal, finite element, and experimental approaches in laser welding of AA5456 alloy,* Metals, Volume 10, 2020, 436, ISSN 2075-4701, https://doi.org/10.3390/met10040436.

[18] Wenchao Ke, Zhi Zeng, J.P.Oliveira, Bei Peng, **Jiajia Shen**, Caiwang Tan, Xiaoguo Song, Wentao Yan, *Heat transfer and melt flow of keyhole, transition and conduction modes in laser beam oscillating welding*, International Journal of Heat and Mass Transfer, HMT-D-22-03705, https://doi.org/10.1016/j.ijheatmasstransfer.2022.123821.

[19] Igor O Felice, **Jiajia Shen**, André FC Barragan, Isaque AB Moura, Binqiang Li, Binbin Wang, Hesamodin Khodaverdi, Maryam Mohri, Norbert Schell, Elyas Ghafoori, Telmo G Santos, JP Oliveira,

Wire and arc additive manufacturing of Fe-based shape memory alloys: Microstructure, mechanical and functional behavior, Material & Design, https://doi.org/10.1016/j.matdes.2023.112004.

[20] JG Lopes, Priyanka Agrawal, **Jiajia Shen**, N Schell, Rajiv S Mishra, JP Oliveira, *Evolution of microstructure and mechanical properties in gas tungsten arc welded dual-phase Fe50Mn30Co10Cr10 high entropy alloy,* Materials Science and Engineering: A, https://doi.org/10.1016/j.msea.2023.145233.

[21] Hongbing Liu, Shanhui Lv, Yang Xuan, João Pedro Oliveira, Norbert Schell, **Jiajia Shen**, Jingyu Deng, Yuhua Wang, Jin Yang, *Effects of Heat Input on Weld Microstructure and Properties in Keyhole TIG Welding of Invar 36 Alloy*, Materials, https://doi.org/10.3390/ma16103692.

[22] Joao G Lopes, P Rocha, DA Santana, Jiajia Shen, E Maawad, N Schell, FG Coury, Joao P Oliveira, *Impact of arc‐based welding on the microstructure evolution and mechanical properties in newly developed Cr29. 7Co29. 7Ni35. 4Al4Ti1. 2 multi‐principal element alloy,* Advanced Engineering Materials, https://doi.org/10.1002/adem.202300109.

[23] Fissha Biruke Teshome, Bei Peng, JP Oliveira, Jiajia Shen, Sansan Ao, Haoyue Li, Long Chen, Caiwang Tan, Xiaoguo Song, Naixun Zhou, Zhi Zeng, *Role of Pd interlayer on NiTi to Ti6Al4V laser welded joints: Microstructural evolution and strengthening mechanisms*, Materials & Design, https://doi.org/10.1016/j.matdes.2023.111845.

[24] Guilherme Gadelha de Sousa Figueiredo, Igor Jordão Marques, Lucas Oliveira Siqueira, **Jiajia Shen**, Joao Pedro Oliveira, Tiago Felipe de Abreu Santos, *A coupled computational fluid dynamics approach as a viable tool for thermal history assessment of UNS S32205 duplex stainless steels friction stir welded joints,* Welding in the World.

[25] Javad Charkhchian, A Zarei-Hanzaki, A Moshiri, HR Abedi, **Jiajia Shen**, JP Oliveira, Kanwal Chadha, Clodualdo Aranas Jr, *On the short-time thermal phase-stability of as-cast AlCoCrFeNi2. 1 eutectic high entropy alloy,* https://doi.org/10.1016/j.jmrt.2022.07.058.

2.

LITERATURE REVIEW

2.1 Introduction

This chapter begins with the concept and properties associated to HEAs, followed by a detailed explanation of the typical regions that exist of a fusion-based welded joint, weld metal microstructure, the correlation between solidification mode, G/R ratio, and constitutional supercooling. An in-depth understanding of this theoretical knowledge is the basis for the work. Then, the current status of research on the weldability of Co-Cr-Fe-Mn-Ni, Al-Co-Cr-Fe-Ni and Fe-Mn-Co-Cr-Si HEAs systems based on fusion-based welding techniques is presented. This literature analysis of the current state of the art on the weldability of HEAs helps to understand current research gaps on the weldability of HEAs, which is the primary motivation and inspiration for conducting this work.

2.2 Basic concepts on high entropy alloys (HEAs)

2.2.1 Definition of HEAs

It is well known that the continuous revolution of metallic materials has dramatically contributed to the progress of human civilization. Tracing back to the past, melting of iron ores and using iron tools sent humankind to the stage of farming civilization. Then, addition of Cr provided stainless properties to steel, and the resulting stainless steel has become the epitome of modern society. Afterwards, Ni was added to austenitic stainless steel as a face-centered cubic (FCC) phase stabilizing element. Adding Al formed a more thermally stable Al_2O_3 oxide film than Cr_2O_3 and developed high-temperature stability of Fe-Cr-Al stainless steel and Fe-Cr-Ni-Al austenitic stainless steel. Moreover, Mo and W were added as solid solution strengthening elements. Nb, Ti, Ta, and V were added as carbide-forming elements to form MC nanometer-size carbides and to inhibit the precipitation of $Cr_{23}C_6$ at the grain boundaries. As a result, pursuing high-performance stainless steel requires adding more than a dozen alloying elements to regulate the distribution, shape, and size of the precipitated phases, in order to achieve improved alloy properties. Thus, in the history of the development of metallic materials (refer to Figure 2-1) there is a continuous trend toward diversification of composition and the pursuit of " increased entropy".

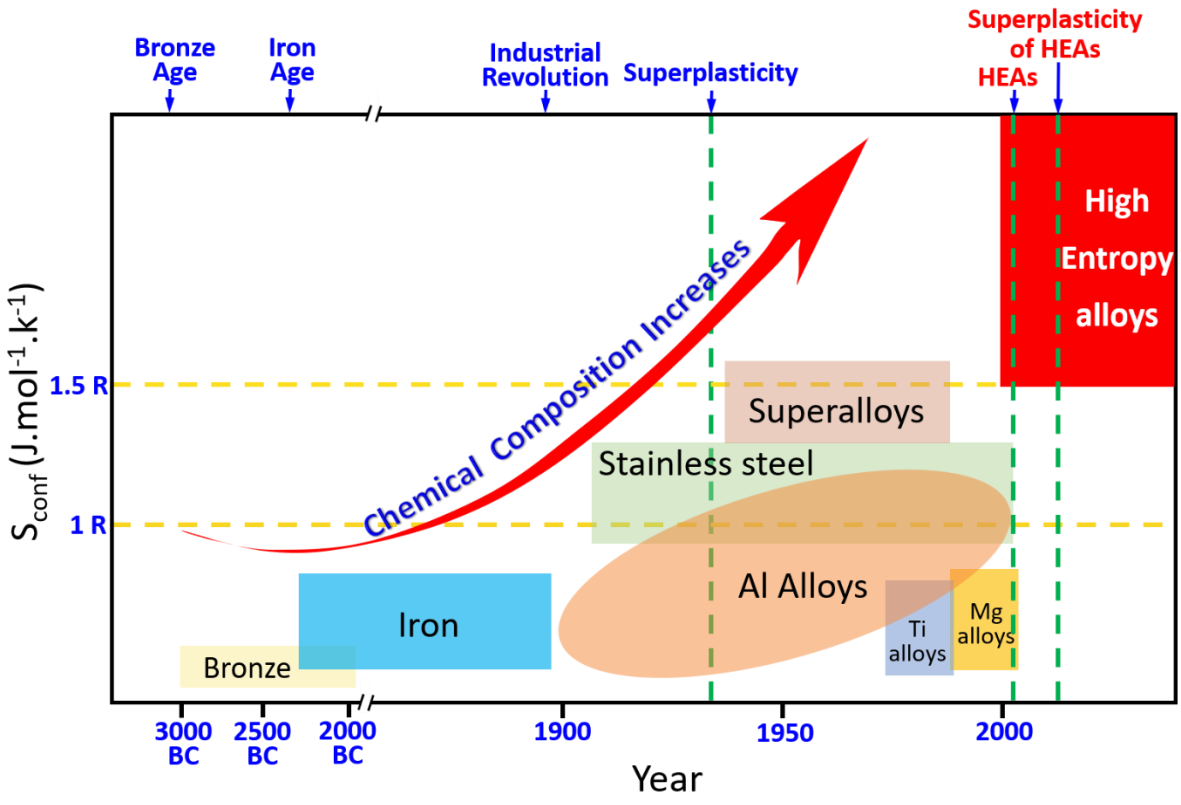

Figure 2-1. Trends in alloy development [4]

In recent years, HEAs have broken with the traditional design concept of a single element as the main component in an alloy, drawing the attention of researchers from the edge of the phase diagram to its central regions (refer to Figure 2-2), thus greatly expanding the scope of research into metallic materials.

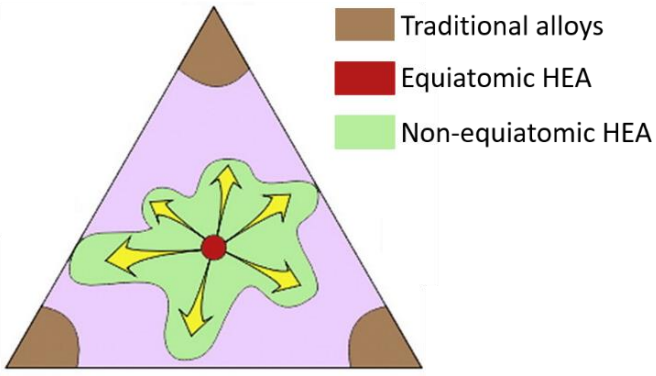

Figure 2-2. Position of the three alloys (traditional alloys, as well as equiatomic and non-equiatomic HEAs) in a ternary phase diagram [5].

Currently, the definition of HEAs exists in two main ways. One is based on the material chemical composition and was first defined as an alloy system containing at least five components with atomic percentages between 5 and 35% of each component [6]; the other is based on the entropy magnitude.

Entropy is one of the parameters used in thermodynamics to characterize the conditions of the material and is a measure of the degree of chaos in a system [7]. The degree of chaos of a system is positively correlated with the mixing entropy of the system. The more chaotic a system is, the more mixing entropy there exists. HEAs, which are alloys with high entropy values, also known as "multi-principle HEAs", represent a new type of solid solution alloy.

According to Boltzmann's thermodynamic statistical formula, the mixing entropy ΔS_{conf} of the system can be expressed by Equation (2-1) [4] as follows.

$$\Delta S_{conf} = K \ln w \tag{2-1}$$

In Equation (2-1), k refers to the Boltzmann constant, and w represents the degree of chaos in thermodynamics.

For multi-principal alloys, when n elements are mixed in equal atomic ratios to form a solid solution, the mixing entropy Equation for can be expressed as:

$$\Delta S_{conf} = R \ln n \tag{2- 2}$$

In Equation (2-2), R is the constant of the gas, $R = 8.314\, J/(K.mol)$.

Therefore, based on the magnitude of the entropy value, alloys can be divided into three categories (refer to Figure 2-3): when $\Delta S_{conf} < 0.69R$, they are termed as low EA; when $0.69R < \Delta S_{conf} < 1.61R$, designates medium EA; Once the $\Delta S_{conf} > 1.61R$, they are regarded as HEA.

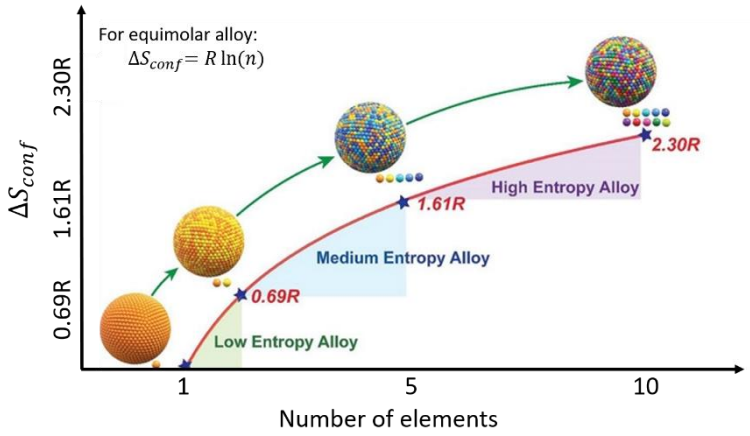

Figure 2-3. The mixing entropy of the equimolar alloys as function of the number of the components [8].

2.2.2 Core effects of HEAs

Novel design concepts and unconventional composition ratios have resulted in multi-principal HEAs that exhibit properties quite different from those of conventional alloys. Four significant effects for HEAs have been highlighted by researchers (Refer to Figure 2-4), including the thermodynamic high entropy effect, the structural lattice distortion effect, the kinetic sluggish diffusion effects, and the performance cocktail effect.

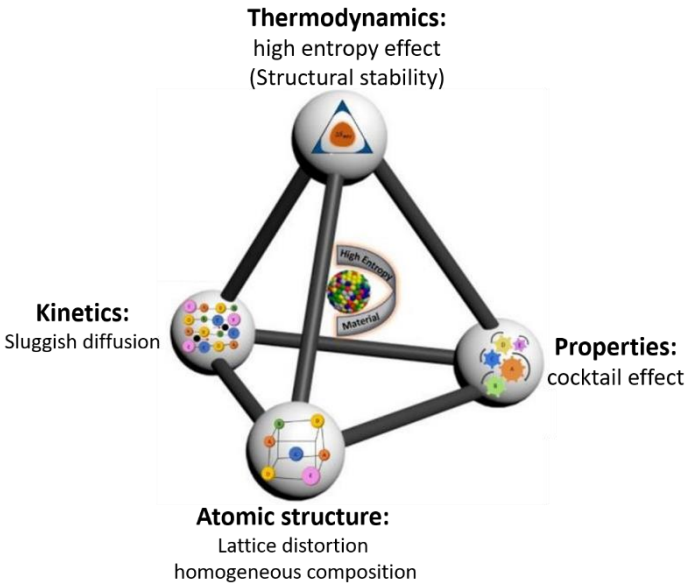

Figure 2-4. Schematic representation of the four core effects of HEAs.

2.2.2.1 The thermodynamic “high entropy effect”

Based on the classical Gibbs phase law which takes the form as below.

$$F = C - P + 1 \tag{2-3}$$

where, F is the degree of freedom; C and P represent the number of components and phases, respectively. Thus, the maximum number of equilibrium phases in an alloy system with the number of component elements C is P = C + 1. However, research on HEAs has found [5] that some HEAs systems are simply formed by solid solutions of FCC, body-centered cubic (BCC) or HCP (hexagonal-close packed) phases after solidification, with the number of phases being significantly less than the predicted maximum number of phases according to the Gibbs’ phase law. Without the formation of multiphase intermetallic compounds, this phenomenon was known as the high entropy effect.

The high entropy effect is a unique and essential characteristic of HEAs, and its importance is mainly reflected in two aspects: one is that higher mixing entropy affects the free energy of the alloy system, which in turn can affect the phase structure of the alloy during cooling. Another is that based on the maximum entropy production principle (MEPP) [9], high entropy tends to stabilize simple solid phases (FCC or BCC or HCP phases), i.e., solid solution phases, instead of intermetallic compound phases, are predominantly formed. The schematic diagram of high entropy effects as shown in Figure 2-5.

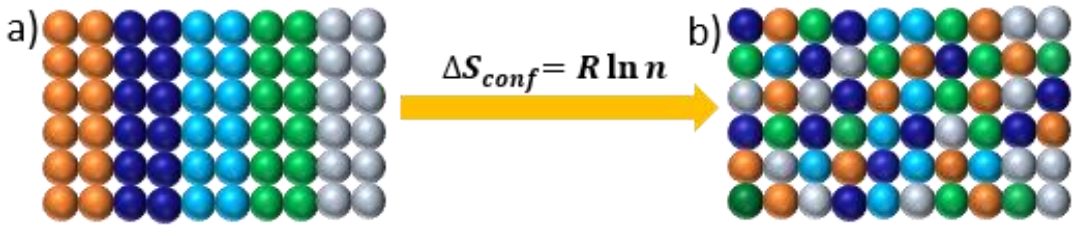

Figure 2-5. Schematic diagram of high entropy effect. (a) traditional alloys, as well as b) HEAs.

2.2.2.2 The structural "lattice distortion effects"

The microstructure of HEAs consists mainly of a solid solution phase composed by multiple principal elements. The atoms of each principal element are randomly distributed in the lattice of the solid solution phase, and the resulting solid solution lattice is severely distorted due to the different atomic sizes of the principal elements. The schematic diagram of lattice distortion effects is shown in Figure 2-6

The strain energy induced by this distortion will increase the internal free energy of the HEA, as well as affect the mechanical, electrical and chemical properties of the alloy. Specifically, it increases the potential for dislocation movement, strengthens the solid solution, and reduces the electrical and thermal conductivity of HEAs by causing the scattering of internal electrons.

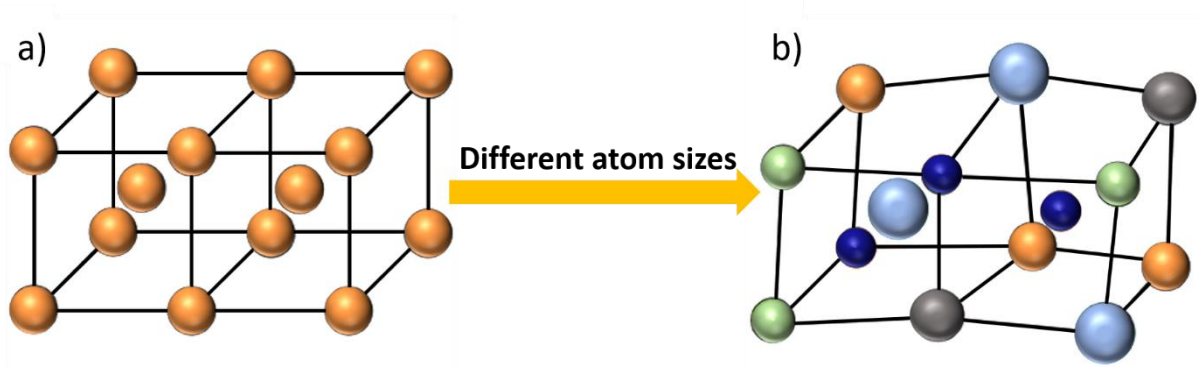

Figure 2-6. Schematic diagram of detailing the lattice distortion effect. (a) conventional alloys, as well as b) HEAs.

2.2.2.3 The kinetic "hysteresis diffusion effect"

In HEAs, the interaction between different elements and their lattice distortion can affect the synergistic diffusion between the principal components, reducing the effective diffusion rate of each atomic element and resulting in sluggish diffusion and phase transition kinetics. This phenomenon is known as the sluggish diffusion effect.

The existence of a slow diffusion effect makes the grain growth kinetics low, causing the alloy to form a nanocrystalline or even amorphous structure [10], which not only improves the hardness and soft magnetic properties of the alloy but also enhances some of the high temperature properties of the HEA, such as strength, high temperature stability and creep resistance.

2.2.2.4 The performance "cocktail effect"

In HEAs, the "cocktail effect" was first introduced by Ranganathan, who termed it "Multimetallic Cocktails" [11].

The cocktail effect suggests that regulating the constituent elements of an alloy and their content can achieve modulation of its properties. This concept is an extension of the design method for composites where materials are combined based on their individual properties to produce a material with a balance of these properties. In this case, HEAs can be considered a composite of elements chosen to create an alloy that possesses certain desired properties. For instance, by adding elements with very high melting points, such as W, Ta and Mo, the alloys are expected to exhibit excellent resistance to high temperature

softening. Adding lighter elements such as Al and Ti, should lead to a decrease in the alloy density. With the addition of Cr, W, Mo, and other elements can aid in obtaining high strength and hardness while decreasing the alloy ductility.

2.2.3 Applications of HEAs

The excellent properties of HEAs provide a wide range of applications. Potential applications include molds and tools, electronic components, engines, wear-resistant coatings, high-frequency AC materials, and materials of nuclear structural, optical transmissions, biomedical applications, thermal barriers and corrosion-resistant situations as in the oil & gas industry, for example.

Normally, materials required for aerospace applications need to have excellent high-temperature mechanical properties and high-temperature oxidation resistance. Due to the sluggish diffusion effect and high entropy effect of HEAs, these alloys can retain its high strength and phase at high temperatures, thus allowing them to be used in turbine blades for aerospace engines. HEAs can also be used as in applications required improved corrosion resistance as in the deep sea, taking advantage of their excellent corrosion resistance. Lightweight HEAs can be used as repair materials for ship coatings and naval equipment due to their low density and high strength. High-entropy alloys with high hardness, high wear resistance and low modulus of elasticity can be used in golf heads, which meet the requirement for long service life and enhance the quality of the product. Some of the potential applications of HEAs are shown in Figure 2-7

.

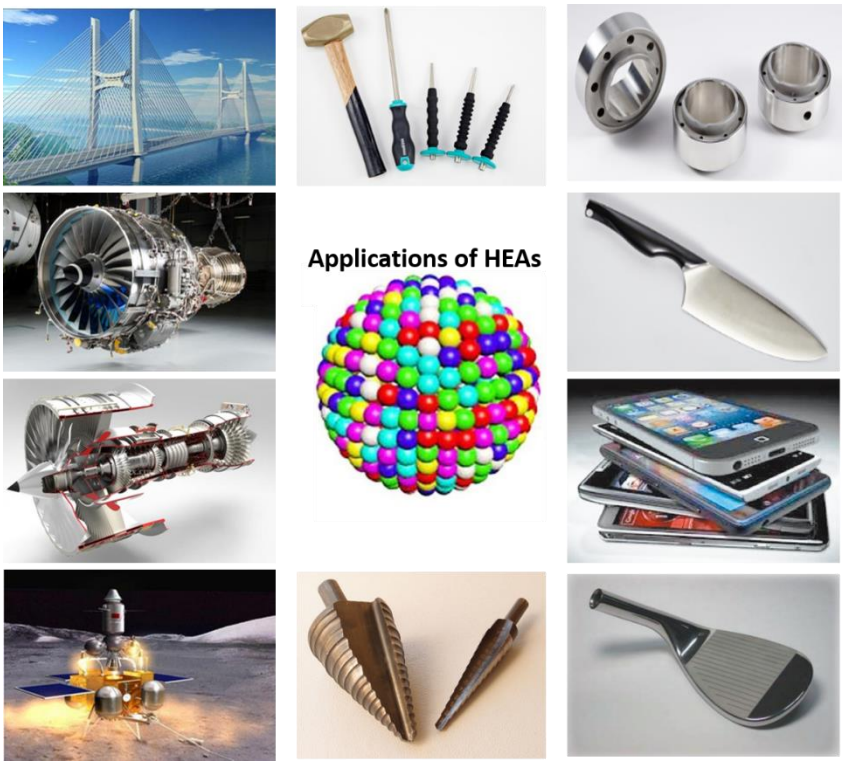

Figure 2-7. Potential application prospects of HEAs.

To ensure the feasibility of using HEAs in these potential fields, weldability studies are an urgent issue to be addressed, because almost all complex engineering structures cannot be formed without welding technologies.

Since the current work only involves the study of the weldability of CoCrFeMnNi, $AlCoCrFeNi_{2.1}$ and $Fe_{42}Mn_{28}Co_{10}Cr_{15}Si_5$ HEAs using GTAW and GMAW techniques, focus on the progress of weldability studies on HEAs using these fusion-based welding techniques is detailed next.

2.3 Current progress on weldability of HEAs

2.3.1 Fusion-based welding techniques

2.3.1.1 Gas tungsten arc welding (GTAW)

GTAW is a process in which the BM is heated by creating an electric arc between a non-consumable tungsten electrode and the metal, thereby melting and joining two workpieces [12], as shown in Figure 2-8. The welding torch holding the tungsten electrode is connected to a protective gas cylinder and to one of the terminals of the power source. The tungsten electrode is usually in contact with a water-cooled copper tube, called a contact tube, which is connected from the terminal to the welding cable.

This allows the welding current from the power source to enter the electrode as well as cooling of the electrode to prevent overheating.

GTAW is suitable for joining thin sections as it has a relatively limited heat input (in the case with low weld speed), and it is usually used to weld butt joints of thin sheets. Since GTAW conventionally uses inert shielding gas, it can be used to weld reactive metals, such as titanium and zirconium alloys. However, the deposition rate of GTAW is lower compared to others arc-based processes such as GMAW. Excessive welding currents can cause melting of the tungsten electrode, resulting in tungsten inclusions in the weld metal. Such must be avoided due to the potential deleterious effect of these inclusions on the FZ microstructure and resulting mechanical properties.

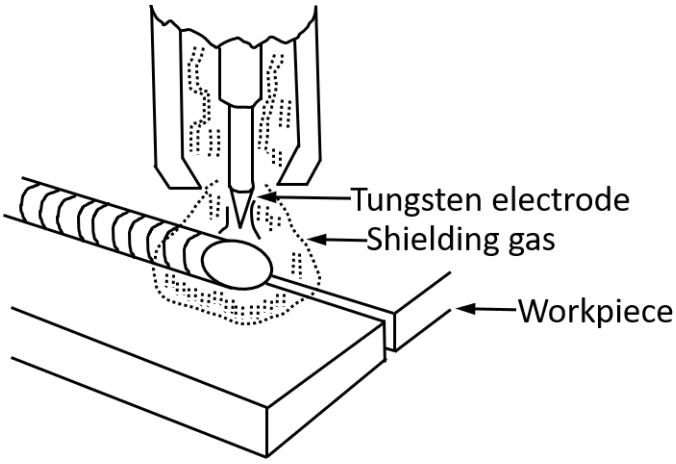

Figure 2-8. Schematic of the GTAW process.

2.3.1.2 Gas metal arc welding (GTAW)

GMAW is defined as an arc welding process using an arc between a continuous filler metal electrode and the weld pool, the process is used with shielding from an externally supplied gas and without the application of pressure [13], as schematically shown in Figure 2-9. Inert or active gases can be used as shielding gas to protect the FZ and HAZ from oxidation and incorporation of foreign particles by the melt pool.

One of the major advantages of GMAW it related to the significantly higher deposition rate over GTAW, allowing thicker workpieces to be welded at higher welding speeds. However, the joint appearance is often of poorer quality than in GTAW joints.

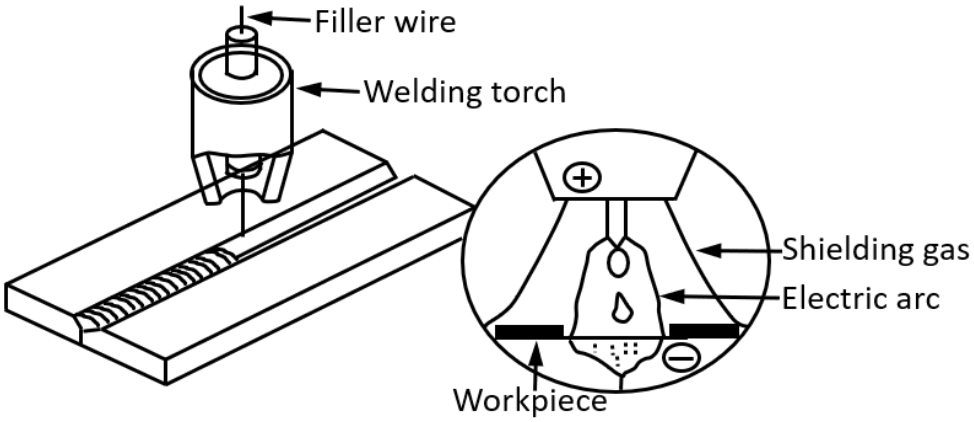

Figure 2-9. Traditional GMAW process.

2.3.2 Typical regions of fusion-based welded joints

Any fusion-based welded joint possesses three distinct regions: the FZ, the HAZ and the non-affected BM, as shown in Figure 2-10. Each of these regions is described in the following sub-sections.

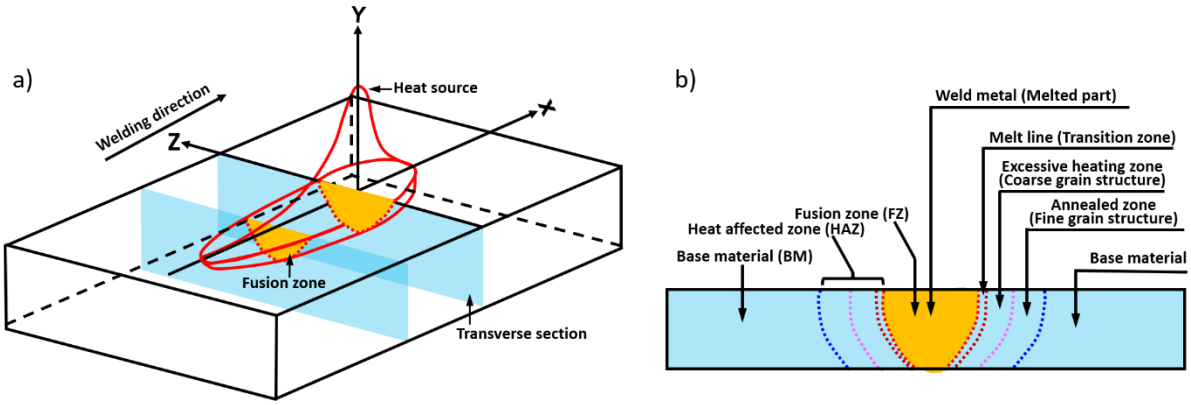

Figure 2-10. a) Schematic diagram of a fusion-based welded joint. b) Schematic diagram of typical regions that compose these welded joints.

2.3.2.1 Base material (BM)

The BM is the region furthest away from the centerline of the weld, unaffected by the weld thermal cycle, where the microstructure remains the same as prior to welding. Thus, any prior thermomechanical processing imposed to the starting material will be preserved after welding.

2.3.2.2 Heat affected zone (HAZ)

HAZ is the region where the metal has not been melted and has undergone solid state changes (recovery, grain growth, precipitation, phase dissolution and recrystallization, for example) in its

microstructure due to an exposure to relatively high temperatures during welding [14]. Specifically, the weld thermal cycle experienced at different distances from the heat source is different, thus the microstructural transformation that occurs at each point also differs, resulting in heterogeneous microstructures. This can translate into the formation of localized hardening, softening and/or brittleness depending on the local microstructure evolution.

Representative microstructure evolution of the HAZ of the steel, the most common example used to represent the effect of thermal cycles during fusion welding, is given in Figure 2-11. It should be mentioned here that the solid-state phase transformations that occur in the steels are different from those typically observed for HEAs. Thus, this schematic representation is only used to detail the potential different microstructures that can form in a steel HAZ, with some generalizations being possible to be made for HEAs.

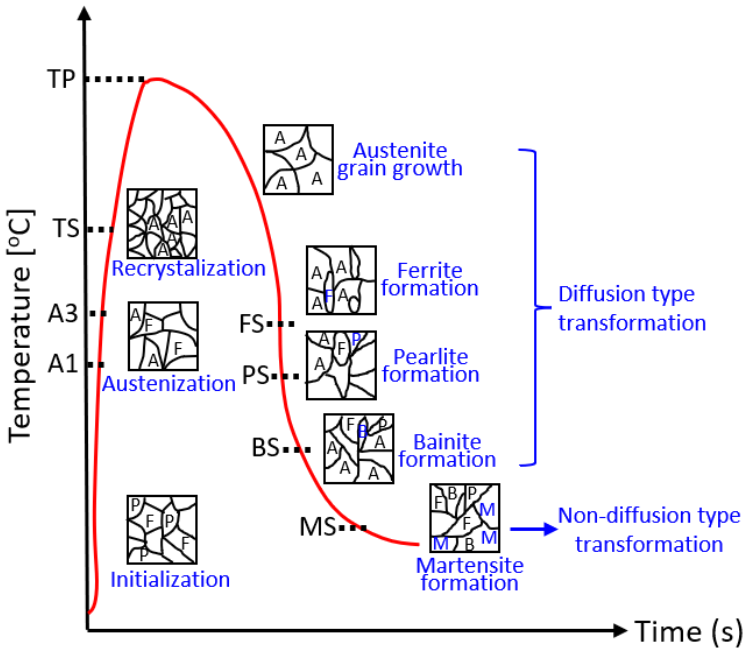

Figure 2-11. Evolution of solid-state phase on the temperature history in the HAZ [15].

For the microstructure evolution of the HAZ in heavy cold-rolled or deformed materials, from the HAZ near the BM (HAZ1) to the HAZ near the FZ (HAZ2), there are three distinct solid-state phenomena (depending on the distance to the heat source): recovery, recrystallization and grain growth. Recovery and recrystallization phenomena normally occur in the low temperature HAZ; predominance of grain growth usually occurs in the high temperature HAZ. The schematic diagram of microstructure evolution in the HAZ shown in Figure 2-12. It should be mentioned that during recovery no obvious changes in the microstructure of the material exist, except for a reduction in the dislocation density. While during recrystallization new grains are formed promote the existing of a refined grain structure. Grain growth

occurs after recrystallization and certain grains will grow and consume others, given raised to coarser grain structures.

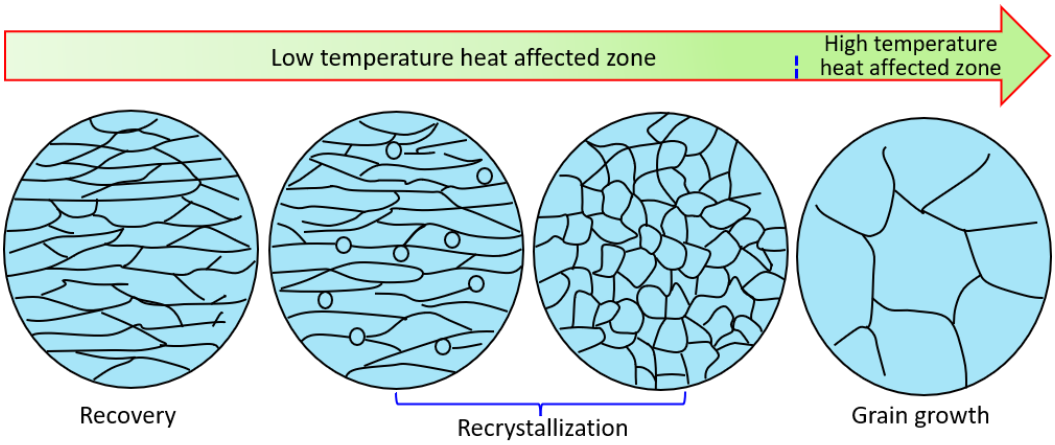

Figure 2-12. Schematic diagram of microstructure evolution in the HAZ.

In conclusion, the microstructural features of the HAZ not only depend on the weld thermal cycle experienced, but also on the composition and initial state of the BM.

2.3.2.3 Fusion zone (FZ)

During the welding process, part of the BM melts under the action of a high temperature heat source, and a complex and intense metallurgical reaction occurs, forming a molten pool (refer to Figure 2-13). From Figure 2-13, it can be seen that the melt pool behavior is dominated by complex patterns derived from the Marangoni flow, which depends on the local temperature, composition and density. Besides, the melt flow in the weld pool is also accompanied with heat transfer processes such as heat conduction, convection, and radiation, as schematically shown in Figure 2-13. Moreover, for GMAW, the poor mixing between the base and filler materials can also lead to the formation of compositionally complex patterns across the FZ. When the welding heat source is removed, the molten pool cools down rapidly, and as the temperature reaches the solidus temperature, the molten pool begins to solidify and crystallize, eventually forming the solidified weld metal.

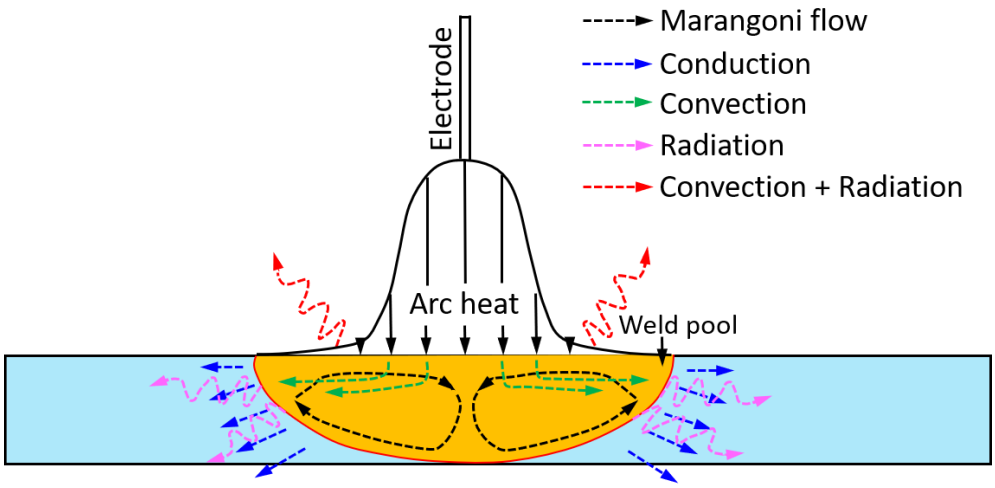

Figure 2-13. Schematic diagram of heat transfer and Marangoni flow in the weld pool [16].

2.3.2.3.1 Nucleation

From classic metallurgy, the thermodynamic and kinetic requirements for the nucleation of a crystal to form in a liquid is the reduction in its free energy due to overcooling, and the degree of free energy reduction, respectively. During welding both of these requirements are met.

There are two types of nucleation: heterogeneous and homogenous [14]. However, both types of nucleation are accompanied by energy consumption. For welding, heterogeneous nucleation dominates the solidification process in the weld pool. The following Equations can express the energy required to form a heterogeneous nucleus in the liquid phase.

$$E_k' = \frac{16\pi\sigma^3}{3\Delta F_v^2}\left(\frac{2-3\cos\theta+\cos^3\theta}{4}\right) \quad (2\text{-}4)$$

$$E_k = \frac{16\pi\sigma^3}{3\Delta F_v^2} \quad (2\text{-}5)$$

E_k refers to the energy required to form a homogenous nucleus in the liquid phase, θ means the surface tension coefficient between the new phase and the liquid phase, ΔF_v means the difference in the liquid and solid phases per unit volume, the substituting Equation (2-5) into (2-4), leads to Equation (2-6), as follows.

$$E_k' = E_k\left(\frac{2-3\cos\theta+\cos^3\theta}{4}\right) \quad (2\text{-}6)$$

In Equation (2-6), θ is the contact angle. When θ = 0°, E_k' will equal 0, which means that there are a large number of suspended particles and existing substrate in the liquid phase. Thus, the crystal can nucleate on the substrate without overcoming any energy barrier required for nucleation. When θ = 180°,

then E_k' will equal to E_k, indicating that only the homogenous nucleus will occur in the liquid phase. When $0^o < \theta < 180^o$, the liquid phase will exist in the substrate, which will induce the energy required to form a critical nucleus.

For fusion-based welding processes, the HAZ to FZ interface acts as a cold substrate, promoting the formation of fine equiaxed and columnar grains, with competitive and columnar growth towards the weld centerline occurring.

2.3.2.3.2 Grain growth

The temperature gradient G, growth rate R, chemical composition and the degree of undercooling, all are key parameters in determining the final grain morphology of a given alloy. Of these, the G/R ratio determines the morphology of the solidification structure, while G x R controls the size of the solidification structure. The effect of the relationship between G and R on the size and morphology of the final microstructure is shown in Figure 2-14. From Figure 2-14, it can be seen that the solidification modes of an alloy can either be planar, cellular, columnar dendritic and equiaxed dendritic. Regulating the relationship between G and R parameters enables to control the solidification microstructure and properties of the material.

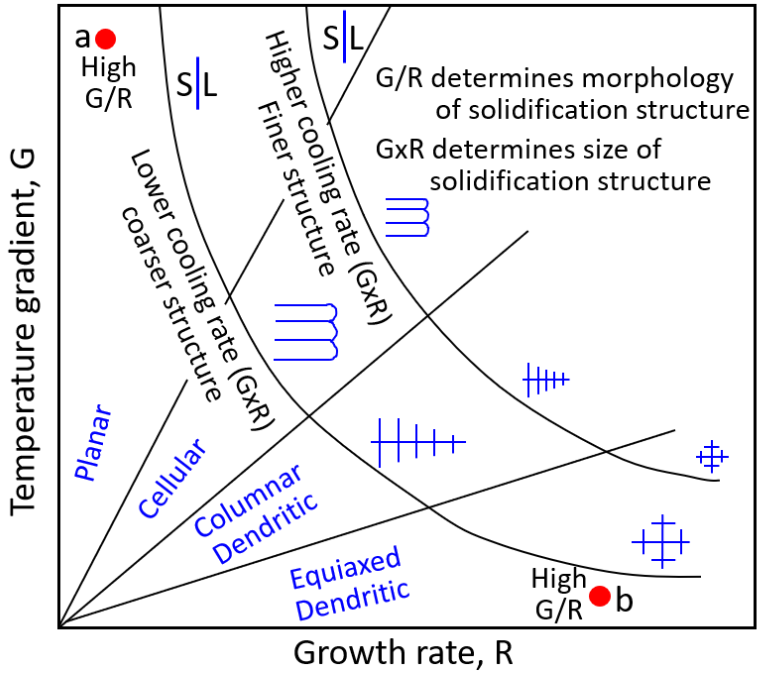

Figure 2-14. Effect of the temperature gradient, G, and growth rate, R, on the morphology and size of solidification structure [14].

The constitutional supercooling in the weld pool varies and contributes to different weld solidification modes. At the boundary of the HAZ and FZ (HAZ/FZ boundary), due to the large temperature gradient, as well as the small grain growth rate, the constitutional supercooling approaches 0, resulting in the

development of planar crystals. Approaching to the weld center line, the temperature gradient gradually becomes smaller, while the growth rate of the crystal increases, leading to the development of the solidification mode from a planar to a cellular crystal, then to cellular dendrites and eventually to an equiaxed morphology. This evolution is schematically detailed in Figure 2-15.

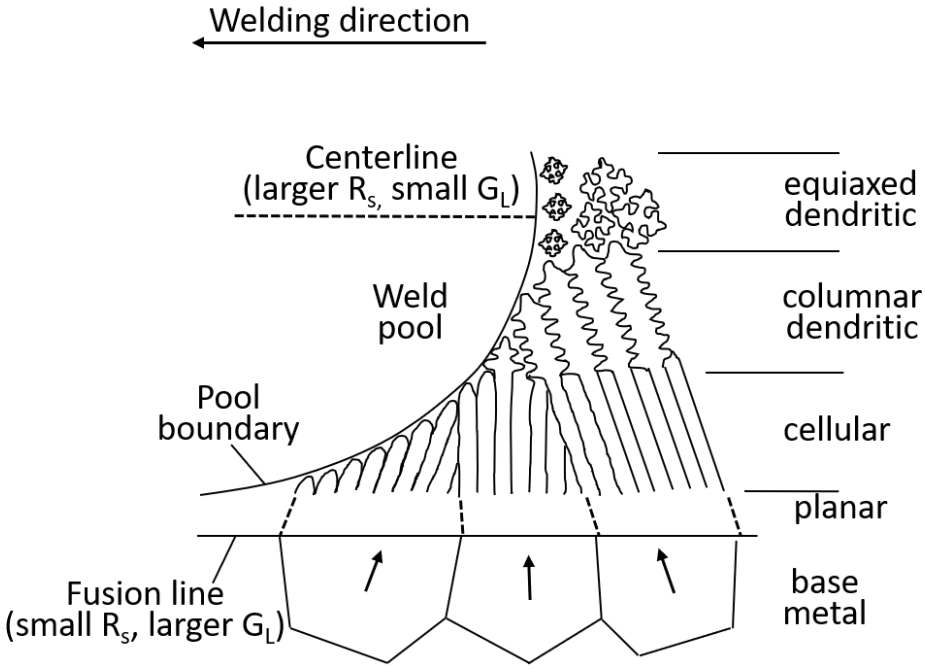

Figure 2-15. Schematic drawing of structural variation of weld microstructure across FZ (Rs is the growth rate, GL is the temperature gradient) [14].

Figure 2-16 presents the effect of constitutional supercooling on solidification mode. S refers to the solid, L to the liquid and M to the mushy zone (the region where dendrites and liquid phase coexist simultaneously). The shaded area under the liquidus temperature distribution in Figure 2-16 indicates the region where the actual liquid temperature is below the liquidus temperature, that is, the region of constitutional supercooling. This area lies within the solid-liquid region of the phase diagram, which depends on D_L and R. Here, D_L corresponds to the diffusion coefficient.

To ensure a stable planar S/L interface, the G/R ratio at the S/L interface must be less than $\Delta T/D_L$ (refer to Equation (2-7). Here, ΔT is the equilibrium freezing range, equal to T_L-T_S. When the G/R ratio is above $\Delta T/D_L$, the planar S/L interface will break down to a cellular, columnar dendritic or equiaxed dendritic.

$$\frac{G}{R} \geq \frac{\Delta T}{D_L} \tag{2-7}$$

Based on Equation (2-7), the higher the temperature gradient, G, and the lower the growth rate, R, the easier for a planar S/L interface to be stable. In the weld area, locations with high temperature gradients and low growth rates correspond to the vicinity of the fusion line (refer to Figure 2-15). From another

perspective, the higher the freezing range, ΔT, and the lower the diffusion coefficient, D_L, the more difficult it is for a planar S/L interface to be stable.

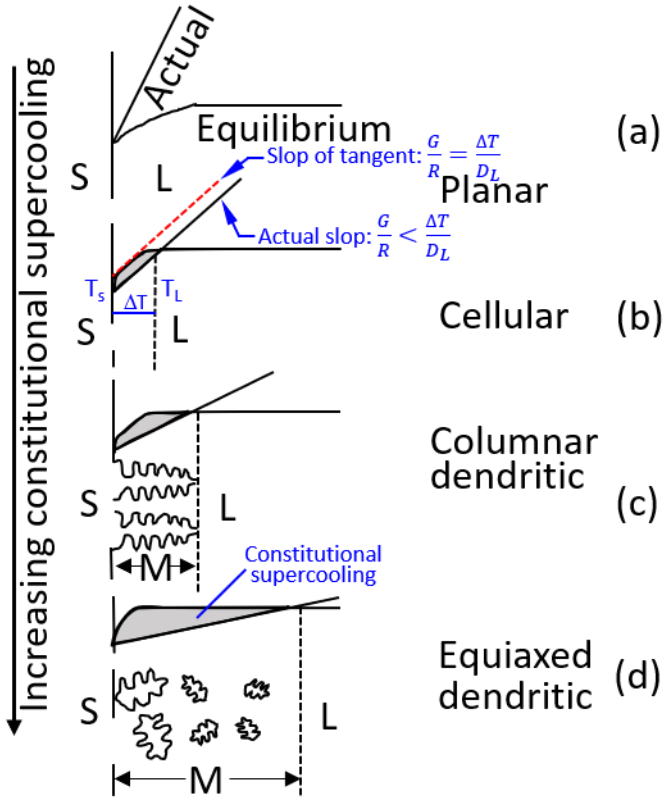

Figure 2-16. Effect of constitutional supercooling on solidification mode: (a) planar; (b) cellular; (c) columnar dendritic; (d) equiaxed dendritic (S: solid, L: liquid, M: mushy zone) [14].

It should be mentioned that for certain materials, and to improve the properties of the weld metal, different amounts of alloying elements (e.g., molybdenum, vanadium, titanium, and niobium) can be added to the weld material as non-spontaneous nucleation points in the melt pool, aiming to refine the microstructure or enabling new phases to be formed.

2.3.3 Weld thermal cycle

Under the welding heat source's effect, the temperature change of a certain region of the weld is dependent on that associated to the local weld thermal cycle [17]. The weld thermal cycle will reflect the thermal effect of the heat source across the welded joint. However, the distance from the heat source to a certain location within the joint varies, thus the peak temperature and cooling rate will also change accordingly. This will lead to distinct microstructure changes across the processed material. A schematic representation of different thermal cycles as function of distance to the heat source are schematically shown in Figure 2-17.

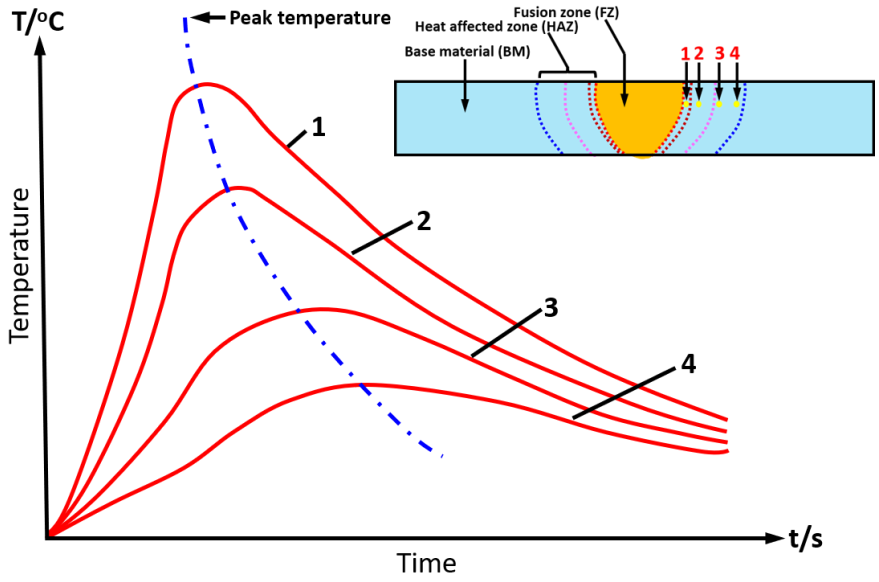

Figure 2-17. Schematic representation of different weld thermal cycle curves for different positions in the HAZ.

2.3.3.1 Parameters of the weld thermal cycle

In the weld thermal cycle, there are three important parameters, which are the peak temperature T_m, the dwell time above the phase transformation temperature, T_H, and the cooling rate. These parameters are detailed in Figure 2-18. Depending on the conditions experienced by the material, as well as previously thermomechanical condition of the BM, the microstructure changes can be significant. In fact, the weld thermal cycle experience within the HAZ can resemble relatively short heat treatments as it will be evidenced in this work. As for the FZ, the weld thermal will not be impacted by the previous thermomechanical processing, since upon melting there is a complete loss of all the microstructure features that existed prior to welding.

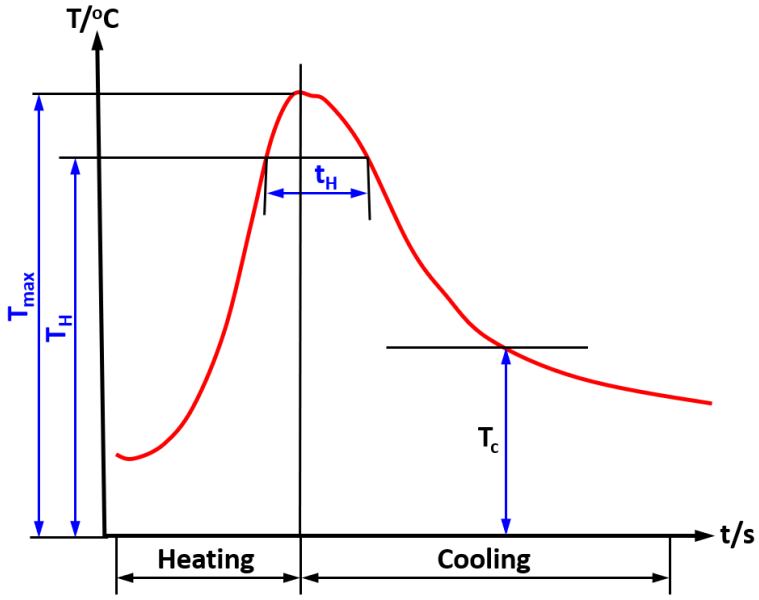

Figure 2-18. Weld thermal cycle curve with important parameters.

2.3.4 Fusion-based welding of HEAs

Fusion-based welding is a key joining method where part of the material is melted, enabling the fabrication of complex-shaped structures. Fusion-based welding technologies have significant potential value for future application-oriented research and technological developments linked to the discovery of new structural materials. Therefore, assessing the weldability of these new materials is critical.

2.3.4.1 Co-Cr-Fe-Mn-Ni HEA system

Currently, weldability studies focused on CoCrFeMnNi HEAs is expanding, mainly focusing on gas tungsten arc welding [18], laser beam welding [19–21], electron beam welding [22,23], and friction stir welding [24–26]. Recently, Lin et al. [27] joined the CoCrFeMnNi HEA by ultrasonic welding, obtaining a sound joint with no defects or detrimental phases. Overall, the CoCrFeMnNi alloy exhibits good weldability under different welding methods when similar joining is attempted. To expand the range of industrial applications for CoCrFeMnNi HEAs, meeting the needs for dissimilar welded structures, such as in those found in nuclear reactors and in high temperature components, researchers started to turn their attention to the dissimilar welding (when two different base materials or the addition of filler wire is attempted) involving the CoCrFeMnNi alloy [28–35]. The main challenge during dissimilar welding is the need to control and/or adjust the chemical composition of the FZ so that its microstructure and mechanical properties are suitable for the targeted applications. However, the mixing of two materials with different compositions, combined with the weld thermal cycle, can promote the formation of undesirable phases and/or intermetallic compounds. Therefore, it is critical to have a systematic understanding of the evolution of the microstructure and mechanical properties of dissimilar joints involving HEAs.

Regarding this topic, the existing literature details works on dissimilar welding of the CoCrFeMnNi HEA to both 316 stainless steel [28,33] and duplex stainless steel [35] using fusion-based methods, while dissimilar joining of CoCrFeMnNi to 304 stainless steel by friction stir welding was also accomplished [34]. Recently, Nam et al. [31] used 308L stainless steel and CoCrFeMnNi HEA as filler materials to weld an as-cast CoCrFeMnNi alloy, and the mechanical properties (yield strength, maximum tensile strength and elongation) obtained were slightly superior to those of the original BM. Afterwards, they used the same filler wire to weld as-rolled CoCrFeMnNi HEAs [29], but now a decrease in the tensile properties was observed. The same group then welded 304 stainless steel using the CoCrFeMnNi HEA as a filler material [32]. Moreover, a CuCrFeMnNi filler wire was used to join rolled CoCrFeMnNi [36], while a Cu-coated CoCrFeMnNi filler wire was seen to increase the mechanical performance of the joint [30]. The above studies all have reported obtaining sound dissimilar welded joints, however, research around this theme is still scarce, especially given the large number of filler materials that exist.

2.3.4.2 Al-Co-Cr-Fe-Ni HEA system

A literature review considering the past 18 years reveals that the two most widely studied HEAs are the single-phase FCC CoCrFeMnNi HEAs, also known as the Cantor alloy [37] and the single-phase BCC AlCoCrFeNiTi alloy [38]. However, it is now well accepted that focusing only on single-phase alloys usually hinders the development of both high strength and ductility. In order to overcome this strength-plasticity barrier, Lu et al. [39] developed the $AlCoCrFeNi_{2.1}$ eutectic HEA with a dual phase (ordered $L1_2$ FCC and B2 BCC phases), which provided both high strength and high ductility. Resulting from breaking the strength/ductility paradigm, it was hypothesized that the eutectic $AlCoCrFeNi_{2.1}$ alloy could replace some high temperature alloys [40] and other engineering alloys [41] used in low temperature environments.

Up to now, studies on $AlCoCrFeNi_{2.1}$ eutectic HEAs have mainly focused on their as-cast or heat treated states, studying their preparation process [42,43] and resulting properties [44,45]. The welding metallurgy and weldability of the $AlCoCrFeNi_{2.1}$ eutectic HEA has been studied scarcely, especially in the context of microstructure evolution and resulting mechanical properties in both the HAZ and FZ. Owing to the characteristics of fusion-based welding, namely the non-equilibrium solidification conditions, as well as the existence of fast heating and cooling cycles and high peak temperatures, can lead to the formation of unexpected phases or microstructural features.

Past studies that have addressed the weldability of the $AlCoCrFeNi_{2.1}$ eutectic HEA, primarily concentrated on solid-state welding methods such as rotary and friction stir welding [46,47] and diffusion joining [48,49]. Moreover, only one work has focused on fusion-based welding [50]. Zhang et al. [50] used laser beam welding for joining the $AlCoCrFeNi_{2.1}$ eutectic HEA, obtaining good mechanical properties. Although laser welding has significant technical advantages, such as high productivity and small heat source dimensions, the high initial capital investment required for this technology can be detrimental for its implementation in industry. In contrast, gas tungsten arc welding, which is based on

arc-based technology, is a low-cost alternative capable of achieving sound joints with good mechanical performance and appearance for multiple engineering alloys. Currently, the body of knowledge on the processability of the eutectic $AlCoCrFeNi_{2.1}$ alloy is missing the understanding of the material weldability using gas tungsten arc welding, which is a low-cost welding process for multiple industries including in the aerospace and oil & gas fields.

2.3.4.3 Fe-Mn-Co-Cr-Si HEA system

In order to further overcome the strength-ductility paradigm, TRIP [51,52], TWIP [53,54], or combined activation of TWIP and TRIP mechanisms have become new concepts in the design of non-equiatomic HEAs in the recent years [55]. Such HEAs containing TRIP and/or TWIP effects are generally referred to as metastable HEAs [56]. In addition, such metastable HEAs often introduce auxiliary strengthening mechanisms such as precipitation strengthening [57,58] and solid solution strengthening [59] which further increase the material strength.

Li et al. [60] focusing on the the Fe-Mn-Co-Cr system showed that the deformation mechanisms, such as dislocation slip, TWIP and TRIP were adjustable by varying the Mn content, and that the strain-induced phase transition from γ-f.c.c. to ε-h.c.p. could simultaneously improve the strength and plasticity of the alloy. From their work, resulted a $Fe_{50}Mn_{30}Co_{10}Cr_{10}$ metastable HEA with a good strength/ductility balance. Earlier work reported that the addition of Si promotes the reduction of the stacking fault energy (SFE) in this HEA system, which is effective in improving the metastability of the γ-f.c.c. matrix phase [61]. Thus, based on this metastable engineering approach, Nene et al. [62] used thermodynamic simulations to assess the effect of Si addition on the metastability of the matrix γ-f.c.c. phase, showing that the addition of 5 at. % Si leads to a maximum metastability of the γ-f.c.c. phase, which corresponded to a final nominal composition of $Fe_{42}Mn_{28}Co_{10}Cr_{15}Si_5$.

So far, studies on the weldability behavior of metastable HEAs have focused on friction stir welding [63–66], while no work has been performed focusing on fusion-based welding of metastable HEAs. Thus, studying on the weldability of metastable HEAs based on fusion welding techniques, establishing the relationship between the microstructural evolution of welded joints and their mechanical properties, filling this knowledge gap, is an urgent issue needs to be addressed.

2.4 Summary

In conclusion, as detailed from the existing body of knowledge on welding of HEAs, this is a research topic that is still in its infancy. Nonetheless, the already obtained successful welded joints based on these materials are promising for structural applications. Thus, weldability studies of HEAs are an urgent issue to be addressed to further expand the potential applicability of these novel engineering materials.

3.

EXPERIMENTAL METHODS

3.1 Introduction

The main objective of this thesis is to establish the correlation between the processing conditions, microstructure evolution and mechanical properties of different arc welded HEAs joints.

To achieve this goal, the microstructure of welded joints was evaluated by OM, SEM coupled with EDS and EBSD, high energy synchrotron X-ray diffraction and thermodynamic calculations. Meanwhile, the mechanical behavior of the welded joints, as well as the local mechanical response were investigated with microhardness mapping measurements and with non-contact DIC during tensile loading to failure.

Thus, this chapter provides a detailed description of the experimental procedures used throughout this work.

3.2 Materials

In this work, as-rolled CoCrFeMnNi equiatomic HEA, as-cast eutectic $AlCoCrFeNi_{2.1}$ HEA and as-cast metastable TWIP/TRIP $Fe_{42}Mn_{28}Co_{10}Cr_{15}Si_5$ HEA were selected as base materials to study their weldability using different welding processed. The chemical compositions of the starting BMs are detailed in Table 3-3.

Table 3-1 – Chemical composition of the base materials used in this work (at. % / wt. %).

Material	Elemental content (at. %)						
	Co	Cr	Fe	Mn	Ni	Al	Si
CoCrFeMnNi	20	20	20	20	20	-	-
$AlCoCrFeNi_{2.1}$	16.39	16.39	16.39	-	34.44	16.39	-
$Fe_{42}Mn_{28}Co_{10}Cr_{15}Si_5$	10	15	42	28	-	-	5.0
	Elemental content (wt. %)						
	Co	Cr	Fe	Mn	Ni	Al	Si
CoCrFeMnNi	21	18.53	19.9	19.6	21.01	-	-
$AlCoCrFeNi_{2.1}$	18.59	16.40	17.61	-	38.89	8.51	-
$Fe_{42}Mn_{28}Co_{10}Cr_{15}Si_5$	10.93	14.46	43.49	28.52	-	-	2.60

Besides, 308 stainless steel and 410 stainless steel (corresponding to ER308LSi and ER410-NiMo, respectively) were selected as filler materials for welding the CoCrFeMnNi HEA by GMAW. The filler

materials chemical compositions are detailed in Table 3-2. For the $AlCoCrFeNi_{2.1}$ and $Fe_{42}Mn_{28}Co_{10}Cr_{15}Si_5$ HEAs no filler materials were used since the weldability of these material is still relatively unknown. For these two alloys GTAW was used.

Table 3-2 – Chemical composition of the filler materials used in the welding of CoCrFeMnNi HEA in this work (at. % / wt. %).

	Elemental composition (at. %)								
	C	Mn	Si	Cr	Ni	Mo	Cu	Fe	Co
ER 410-NiMo	0. 3	0.47	1.87	17.25	2.82	0.38	-	77.18	-
ER308LSi	0.14	1.12	1.62	21.94	9.4	0.43	0.65	64.74	-
	Elemental composition (wt. %)								
	C	Mn	Si	Cr	Ni	Mo	Cu	Fe	Co
ER 410NiMo	0.05	0.6	0.6	13.5	4.5	0.5	-	80.25	-
ER308LSi	0.03	1.12	0.83	20.75	10	0.75	0.75	65.77	-

Before welding, the base materials surface oxidation was removed by mechanical polishing, and then ethanol and acetone were used to clean the resulting surface.

3.3 Welding experiments

3.3.1 Gas tungsten arc welding procedure for welding $AlCoCrFeNi_{2.1}$ and $Fe_{42}Mn_{28}Co_{10}Cr_{15}Si_5$ HEAs

To study the weldability of the as-cast $AlCoCrFeNi_{2.1}$ eutectic HEA and TWIP/TRIP $Fe_{42}Mn_{28}Co_{10}Cr_{15}Si_5$ metastable HEA, GTAW was used. It's worth mention here that the machine used for welding is resembling a welding robot, a laboratory-developed welding platform, rather than a hand welding machine. To minimize oxidation of the FZ and HAZ, 99.99% pure Ar was selected as the shielding gas. The gas was injected at both the face and root of the weld to protect both sides of the joint, as schematically detailed in Figure 3-1. Butt joining was performed using the welding parameters detailed in Table 3-3.

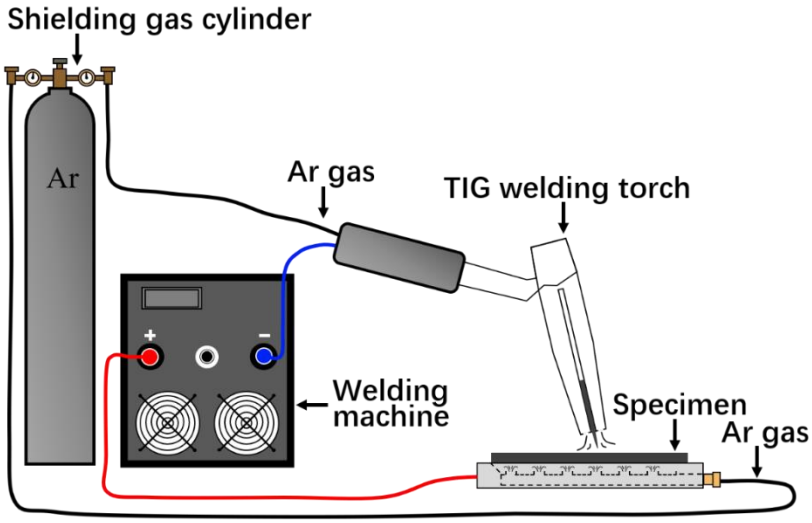

Figure 3-1. Schematic representation of the experimental setup used for gas tungsten arc welding.

Table 3-3 – GTAW parameters for the as-cast AlCoCrFeNi2.1 eutectic HEA and TWIP/TRIP $Fe_{42}Mn_{28}Co_{10}Cr_{15}Si_5$ metastable HEA.

Welded joints	Current [A]	Voltage [V]	Welding speed [mm/min]	Shielding gas	Gas flow rate [L/min]
$AlCoCrFeNi_{2.1}$	30	8	125	Argon	16
$Fe_{42}Mn_{28}Co_{10}Cr_{15}Si_5$	25	8	150	Argon	14

To further investigate the microstructure and mechanical properties of the as-cast $AlCoCrFeNi_{2.1}$ eutectic and $Fe_{42}Mn_{28}Co_{10}Cr_{15}Si_5$ metastable HEA after welding, electrical discharge machining (EDM) was used to prepare specimens, with dimensions shown in Figure 3-2.

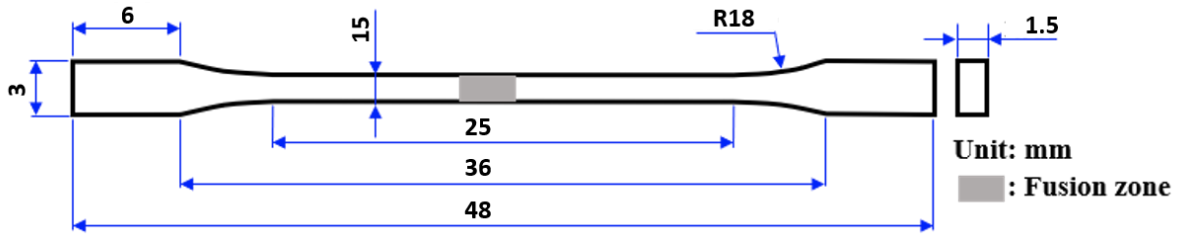

Figure 3-2. Geometry and dimensions of specimens used for uniaxial tensile testing.

3.3.2 Gas metal arc welding procedure for welding of CoCrFeMnNi HEAs

Previous work on autogenous welding of the CoCrFeMnNi material revealed good material weldability [67]. To evaluate if the addition of filler material had a positive effect on the mechanical response of the CoCrFeMnNi alloy joints, GMAW using various filler materials was performed. Here, the same as mentioned above, this welding platform resembling a welding robot, it is an independent welding platform developed by the laboratory. The process schematic is detailed in Figure 3-3. Two types of solid filler wires were selected and used for this study, all with 1 mm diameter.

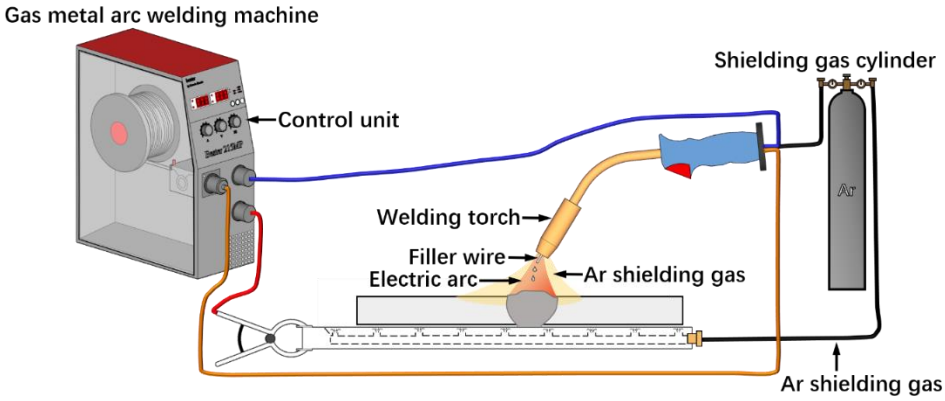

Figure 3-3. Schematic of the GMAW set-up used in this work.

To prevent oxidation of the fusion and heat affected zones the top and bottom surfaces of the specimens as shielding gas. The selected welding parameters are detailed in Table 3-4. These parameters ensured full penetration welds with no evident defects. It's worth to note that the stick-out distance used through all the final trials was 10 mm. This distance was chosen based on tests and visual inspection of the welding needs.

Table 3-4 – GMAW parameters used in this work.

Welded joints	Voltage V	Torch travel speed mm/min	Wire feed speed mm/min	Gas flow rate L/min
CoCrFeMnNi with ER410 NiMo filler wire	16.4	220	2000	16
CoCrFeMnNi with ER308LSi filler wire	18	185	2500	16

After welding, EDM was used to obtain samples for microstructure and mechanical characterization as detailed next, as shown in Figure 3-4. It should be mentioned here that the dog bone dimensions are

different for those prepared for both GMAW CoCrFeMnNi and GTAW $AlCoCrFeNi_{2.1}$ joint (refer to Figure 3-2 and Figure 3-4).

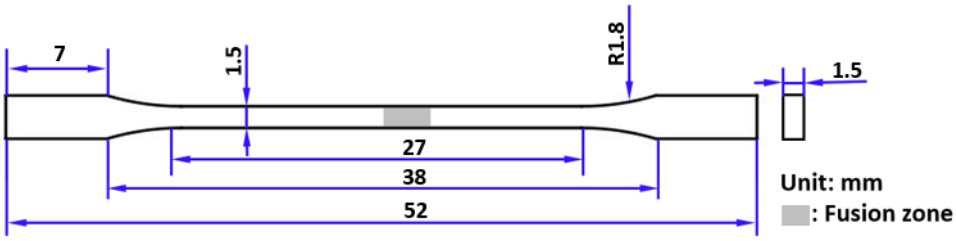

Figure 3-4. Geometry and dimensions of gas metal arc welded specimens used for uniaxial tensile testing.

3.4 Microstructure characterization

3.4.1 Optical and scanning electron microscopy

For microstructural characterization, all GMAW and GTAW welded specimens were first placed in epoxy resin, then ground with 400, 600, 1200, 2500 and 4000-grit SiC papers, and finally with a 3.0 µm diamond polishing paste until a mirror-like surface was obtained. To reveal the material microstructure, the polished specimens were immersed in different etching solutions at room temperature. The chemical composition of each etchant used to reveal the microstructure of the different processed materials is presented in Table 3-5.

Table 3-5 – Etchant composition used to reveal the microstructure of each alloy.

Material	Reagent	Composition		Immersion time
$AlCoCrFeNi_{2.1}$ BM	Aqua regia	Hydrochloric acid	75ml	15 s
		Nitric acid	25ml	
$AlCoCrFeNi_{2.1}$ GTAW joint	Vilella's	Ethanol	100ml	30-40 s
		Hydrochloric acid	5ml	
		Picric acid	1g	
$Fe_{42}Mn_{28}Co_{10}Cr_{15}Si_5$ BM	Kalling's-2	$CuCl_2$	5g	40-50 s
		HCl	5g	
		C_2H_5OH	100ml	
CoCrFeMnNi GMAW joint with ER410-NiMo /ER308LSi filler wire	Aqua regia	Hydrochloric acid	75ml	BM and HAZ: 90-110 s FZ: 190-220 s
		Nitric acid	25ml	
		HCl	5g	
		C_2H_5OH	100ml	

To observe the microstructure of the welded joints, a Leica DMI 5000M inverted OM was used for light optical microscopy. SEM and energy dispersive X-ray spectroscopy (EDS) were used for more detailed microstructural characterization using a FEI Quanta 200 environmental scanning electron microscope. In addition, EBSD was employed to study the crystallographic orientation and existing phases on a FEI

Nova Nano SEM 230 with EDAX Hikari Super EBSD. TSL OIM Analysis 7.2 software was used to analyze the raw EBSD data.

3.5 Synchrotron X-ray diffraction

The synchrotron X-ray experiments were performed at the P07 High Energy Materials Science beamline of PETRA III at DESY (Hamburg, Germany). LaB6 powder was used for the calibration of the instrument parameters, and to determine the sample-to-detector distance. A monochromatic X-ray beam with an energy of 87 keV, corresponding to a wavelength of 0.14235 Å, was used which allowed to perform diffraction experiments in transmission mode. These transmission mode experiments enabled the determination of bulk microstructure information during in-situ and ex-situ measurements.

A two-dimensional PerkinElmer fast detector was used to collect the Debbye-Scherrer rings. After the acquisition of the 2D images, post-processing of the raw data was performed using Fit2D [68], with HighScore Plus software being used for the phase identification [69], while Rietveld refinement was performed using Material Analysis Using Diffraction (MAUD) software [70].

3.5.1 In-situ tensile testing using synchrotron X-ray diffraction analysis for characterization of the eutectic $AlCoCrFeNi_{2.1}$ and metastable $Fe_{42}Mn_{28}Co_{10}Cr_{15}Si_5$ HEAs

To investigate the deformation behavior of the eutectic $AlCoCrFeNi_{2.1}$ and metastable $Fe_{42}Mn_{28}Co_{10}Cr_{15}Si_5$ HEAs when subjected to uniaxial tensile testing at room temperature, in-situ high-energy synchrotron X-ray was performed. The CoCrFeMnNi HEA was not analyzed since this material was already significantly studied in the literature [71–74].

3.5.1.1 X-ray diffraction methodology used for probing the tensile deformation mechanisms of an-cast eutectic $AlCoCrFeNi_{2.1}$ HEA

The experimental setup for the in-situ high-energy synchrotron X-ray diffraction is depicted in Figure 3-5. Dog-bone specimens were mounted on a laboratory scale Universal Testing Machine with a maximum load capacity of 20 kN. The beam size was of 200 × 200 µm. The material was loaded to predefined strains to analyze both the elastic and plastic behaviors of the eutectic alloy. Prior to the in-situ testing, LaB_6 was used to determine the peak broadening associated with the beamline and its optics, as well to determine the sample to detector distance (which was calculated to be 1226 mm).

To understand the orientation dependence on the microstructure evolution during tensile testing, the diffraction rings were caked into 24 parts, each corresponding to an azimuthal angle of 15º. According to the laboratorial reference (refer to Figure 3-5), the azimuthal angle ranges from 82.5 to 97.5 º was used to determine the microstructural evolution along the loading direction (LD), whereas the azimuthal

range between -7.5 and 7.5 º corresponded to the transverse direction (TD), i.e., perpendicular to the tensile loading axis. The caking procedure was performed using Fit2D software [68]. By integrating along specified azimuthal ranges, the two-dimensional Debye-Scherrer rings can be converted into a conventional one-dimensional intensity vs 2θ diffraction patterns.

The lattice strain and orientation-dependent elastic modulus for different (h k l) planes, as well as the dislocation density evolution and phase stress partitioning were calculated as further detailed below. A pseudo-Voigt function was used for single peak fitting to determine key peak parameters such as peak position, peak intensity and Full Width at Half Maximum (FWHM) using the General Structure Analysis System (GSASII) software [75]. In addition to this, MAUD [70] software was used to determine the volume fraction of existing phases via Rietveld refinement as well as for phase identification. From the Rietveld refinement, the lattice parameters of the existing phases within the as-cast eutectic $AlCoCrFeNi_{2.1}$ HEA were also determined.

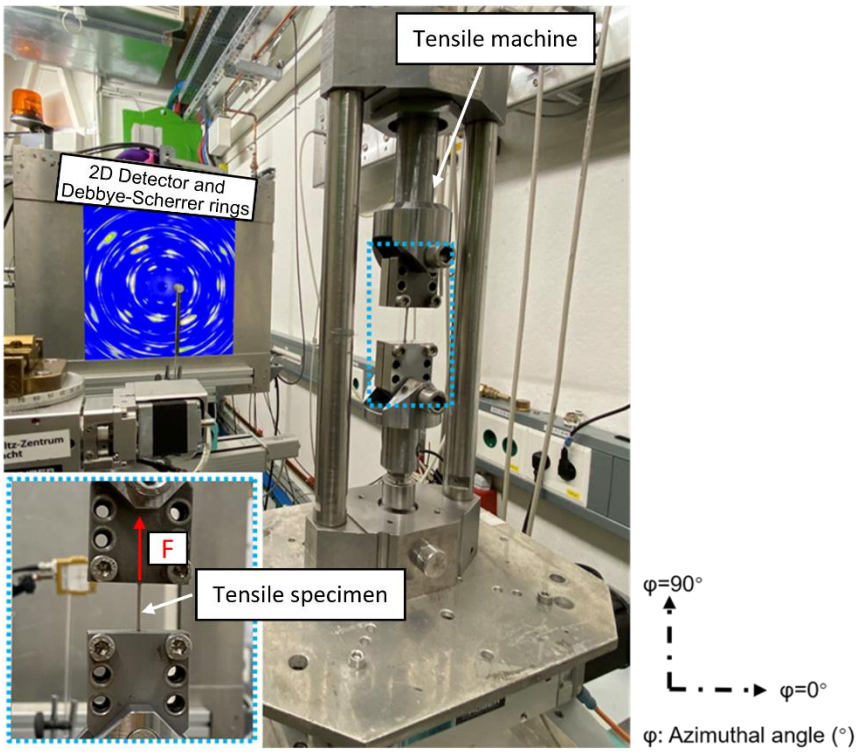

Figure 3-5. High-energy in-situ synchrotron XRD experimental set-up.

In the following sub-sections, the definition for the calculation of several microstructural features of interest are detailed.

3.5.1.1.1 Lattice strain calculation

To study the evolution of the lattice strain during tensile loading along the LD and TD, individual reflections of the existing phases are fitted and the d-spacing at each loading step was obtained. Then, the lattice strain for a given (h k l) plane, ε_{hkl}, can be calculated according to Equation (3-1) [76]:

$$\varepsilon_{hkl} = \frac{d_{hkl} - d_0}{d_{hkl}} (x10^6) \tag{3-1}$$

where (h k l) refers to a specific lattice plane, d0 is the reference d-spacing before loading, neglecting any initial internal stresses [76], and dhkl is the d-spacing determined at different stress/strain levels. The d0 and dhkl values can be obtained directly from the individual peak fitting procedure.

3.5.1.1.2 Phase stress calculation

To understand the mechanical behavior of the as-cast $AlCoCrFeNi_{2.1}$ eutectic HEA, the (3 1 1) FCC and (2 1 1) BCC B2 planes were chosen as the representative crystallographic planes to calculate the phase stress evolution. The (3 1 1) plane for an FCC structure and the (2 1 1) plane for a BCC structure are known to be the least affected by intergranular stresses (since grains with different orientations are subjected to different stress states), thus enabling the reliable calculation of the stress partitioning during tensile testing [77–79]. This has been demonstrated by numerical simulations as detailed in [80]. Based on the lattice strain evolution, the distribution of the applied load between both phases during deformation can be approximated. Thus, the Von Mises stress (σ_{vm}) is employed to quantify the phase stress partitioning during tensile deformation [78–80]. The Von-Mises stress is defined as,

$$\sigma_{vm} = \frac{1}{\sqrt{2}}[(\sigma_{11} - \sigma_{22})^2 + (\sigma_{22} - \sigma_{33})^2 + (\sigma_{33} - \sigma_{11})^2]^{1/2} \tag{3-2}$$

where,

$$\sigma_{11} = \frac{\mathrm{E}}{1+\upsilon}\varepsilon_{11} + \frac{\upsilon \mathrm{E}}{(1+\upsilon)(1-2\upsilon)}(\varepsilon_{11+}\varepsilon_{22} + \varepsilon_{33}) \tag{3-3}$$

$$\sigma_{22} = \sigma_{33} = \frac{\mathrm{E}}{1+\upsilon}\varepsilon_{22} + \frac{\upsilon \mathrm{E}}{(1+\upsilon)(1-2\upsilon)}(\varepsilon_{11+}\varepsilon_{22} + \varepsilon_{33}) \tag{3-4}$$

$$\upsilon = -\frac{\varepsilon_{transverse}}{\varepsilon_{longitudianl}} \tag{3-5}$$

Here, ε_{11} is the lattice strain along the LD (obtained from the azimuthal range from 82.5 to 97.5 º), ε_{22} is the lattice strain in the TD (obtained from the azimuthal range from -7.5 º to 7.5 º). ε_{33} is assumed equal to ε_{22} [78–81]; v is the Poisson ratio, which is known to vary within 0.35 and 0.39 for the as-cast $AlCoCrFeNi_{2.1}$ HEA studied in this work [82]; E is the orientation-dependent Young's modulus for a specific (h k l) plane, which can be obtained by fitting the evolution of the lattice strain during elastic deformation; σ_{11} is the principal stress in the LD, σ_{22} and σ_{33} are the principal stresses in the other two perpendicular directions. It is worth noting that, since the transverse stress (σ_{22}) is significantly smaller

than the σ_{11} longitudinal stresses (with the sample applying for the σ_{33} stress, due to the reduced thickness of the material [83]), it is assumed here that $\sigma_{22} = \sigma_{33} \approx 0$ [78–81,83,84].

3.5.1.1.3 Dislocation density evolution

To evaluate the dislocation density during the room temperature tensile testing, the modified Williamson-Hall method [85,86] was used. The FWHM for a given (h k l) plane obtained from the individual peak fitting routine is mainly composed by three components: instrumental broadening, grain size broadening and microstrain broadening, the latter resulting directly for the generation of defects such as dislocations and stacking fault [87]. After subtracting the instrumental peak broadening, the structural FWHM is mainly caused by grain size, $FWHM_{size}$, and microstrain, $FWHM_{microstrain}$ as shown in Equation (3-6).

$$FWHM = [(FWHM_{measured})^2 - (FWHM_{instrumental})^2]^{1/2} \quad (3\text{-}6)$$

$$FWHM = FWHM_{size} + FWHM_{microstrain} \quad (3\text{-}7)$$

where,

$$FWHM_{size} = \frac{K\lambda}{L\cos\theta} \quad (3\text{-}8)$$

$$FWHM_{microstrain} = 4\varepsilon\frac{\sin\theta}{\cos\theta} \quad (3\text{-}9)$$

The FWHM induced by grain size ($FWHM_{size}$) and microstrain ($FWHM_{microstrain}$) are detailed in Equation (3-8) and Equation (3-9), respectively. Here, λ is the wavelength (0.14235 Å), L is the average grain size, k is the Scherrer constant (≈ 0.9) [88], θ is half of the diffraction angle of the selected reflection.

Then, (3-10) is obtained by substituting Equation (3-8) and (3-9) into Equation (3-7) and the average lattice strain, ε_0, and the crystallite size, L, are respectively the slope and line intercept of the linear relationship obtained when plotting FWHM x cos (θ) against 4 x sin (θ) for each of the selected diffraction peaks at different stress/strain levels [88–91],

$$FWHM\ x\ cos\theta = \frac{\kappa\lambda}{L} + 4\varepsilon_0\sin\theta \quad (3\text{-}10)$$

The dislocation density evolution of the two major phases of the eutectic alloy (disordered FCC and ordered B2 BCC) can be derived from the modified Williamson-Hall method as described by Equation (3-11) [92],

$$\rho = \frac{\kappa{\varepsilon_0}^2}{b^2} \quad (3\text{-}11)$$

where ρ refers to the dislocation density, ε_0 corresponds to the lattice strain as defined above, b is the Burgers vector, considering the $\{111\}\langle 110\rangle$ slip systems of the FCC phase and $\{110\}\langle 111\rangle$ slip systems

of the B2 BCC phase [93]. The Burgers vector of the FCC phase and B2 BCC phase can be estimated by using $b_{FCC} = \sqrt{2}a/2$ and $b_{B2\,BCC} = \sqrt{3}a/2$, respectively, where *a* is the corresponding lattice parameter, k is a constant, with the values of k for the FCC and B2 BCC phases being 16.1 and 14.4, respectively [92].

After plastic deformation of the $AlCoCrFeNi_{2.1}$ alloy, dislocations are generated, move and accumulate inside the material. This leads to the hardening behavior of the material upon plastic deformation. Therefore, in order to further understand the strength contribution resulting from the generation of new dislocations in both FCC and B2 BCC phases, the Bailey-Hirsch model was used as detailed by Equation (3-12) [91],

$$\Delta\sigma_D = \mathrm{M}\alpha G b \rho^{1/2} \tag{3-12}$$

where $\Delta\sigma_D$ is the contribution due to the dislocations that are generated within each phase, M is the average Taylor factor, and takes the value of 3.06 for the FCC phase [94] and of 2.8 for the B2 BCC phase [95], α is a constant, and the value for the FCC and B2 BCC phase is the same, being equal to 0.23 [77], G is the shear modulus for both matrix phases, with the FCC matrix phase having 76.9 GPa [96] and the B2 BCC phase possessing 80 GPa [97], b is the length of Burgers vector [97], ρ is the dislocation density, which was calculated as detailed above. It should be mentioned that there are other strengthening mechanisms that can contribute to modify the mechanical response of this eutectic HEA. These include solid solution, grain boundaries, and precipitates [91]. However, in this work the only microstructural change that is occurring pertains to the dislocation density, while the other features were constant during deformation. For this reason, the mechanical behavior and strain-hardening behavior of the studied alloy has been primarily derived from the dislocation density evolution in both phases as it will be shown in the results and discussion section.

3.5.1.2 X-ray diffraction methods used for the tensile deformation mechanism analysis of cast eutectic $Fe_{42}Mn_{28}Co_{10}Cr_{15}Si_5$ HEA

In-situ high energy synchrotron X-ray diffraction also was used to investigate the deformation behavior of the metastable $Fe_{42}Mn_{28}Co_{10}Cr_{15}Si_5$ HEA during the loading process, including the TRIP and TWIP effects.

High energy X-rays with a beam size of 700 x 700 μm^2 penetrated the specimen and a Perkin Elmer 2D detector with a pixel size of 200 x 200 μm^2 is employed to collect the scattered intensity in the form of Debye-Scherrer rings at 12 different loading stresses. The setup used is the same as that previously shown in Figure 3-5.

Figure 3-5 shows the schematic overview of the experimental setup. Here, full integration along the azimuthal angle was performed to get an overall understanding of the microstructural changes induced

in the material upon tensile loading. To evaluate the orientation-dependent microstructural evolution of certain lattice planes of both phases, partial integration along the LD, and TD, was performed. The integration ranges were set from 85 to 95° for LD and from -5 to 5° for TD.

A single-peak fitting routine was performed on the 1D X-ray diffraction patterns using the structural analysis software GSAS II [75], to determine the diffraction peak positions of different lattice planes, their integrated intensity and FWHM. These microstructure features were then used to calculate the dislocation density, dislocation strengthening, stacking fault strengthening, and the evolution of the lattice strain during the tensile process, as it will be described in detail in the next sections.

In addition to this, Rietveld refinement using the MAUD software [70] was used for full spectrum fitting to determine the evolution of lattice parameters, phase volume fraction, and to support the phase identification of the acquired diffraction spectra.

Data processing of the synchrotron X-ray diffraction data applied for the $Fe_{42}Mn_{28}Co_{10}Cr_{15}Si_5$ HEA is similar to that used for the analysis of the tensile deformation evolution of the $AlCoCrFeNi_{2.1}$ eutectic HEAs. However, due to different microstructure features and deformation behavior that exist when comparing both samples some different approaches must be followed. The details are as follows.

3.5.1.2.1 Phase volume fraction and transformation volume calculations

The physics-based diffraction models used in MAUD software enable to successfully capture the effects of variations in crystallographic properties, phase fraction as well as material/phase texture, enabling quantitative analysis of the microstructural evolution of the material upon mechanical loading. For the Rietveld refinement procedure used in this work, a polynomial function of degree four was used to reproduce the pattern background [98], while the Cagliotti PV model was chosen for the instrumental broadening and the Popa model was selected for anisotropic broadening [99]. The extended Williams-Imhof-Matthies-Vinel algorithm (E-WIMV) [100] with a cell size of 5° in orientation was used as the texture model for considering the texture evolution under tensile loading, as described by Wenk et al. [101]. A triaxial elastic stress model with $\sigma_{11} \neq 0$ and $\sigma_{22} = \sigma_{33} \approx 0$ [102] was used and the c_{11}, c_{12} and c_{44} single crystal elastic constants for both γ-f.c.c. phase and ε-h.c.p. phase were obtained from [103], while the mechanical parameters based on the Young's modulus, E, [104] and Poisson's ratio, ν, can be derived by the Hill-averaged Voigt and Reuss bound as described by the following Equations.

$$E = \frac{9BG}{3B+G} \tag{3-13}$$

$$v = \frac{3B-2G}{2(3B+G)} \tag{3-14}$$

where,

$$G = \frac{\left\{\frac{5(c_{11}-c_{12})c_{44}}{4c_{44}+3(c_{11}-c_{12})}+\frac{c_{11}-c_{12}+3c_{44}}{5}\right\}}{2} \quad (3\text{-}15)$$

$$B = \frac{c_{11}+2c_{12}}{3} \quad (3\text{-}16)$$

here E is the Young's modulus, ν is the Poisson's ratio, c_{11}, c_{12} and c_{44} are the single crystal elastic constants.

The transformation volume, ΔV, is determined as follows [105,106],

$$\Delta V = \frac{2V_{\varepsilon-\text{h.c.p.}}-V_{\gamma-\text{f.c.c.}}}{V_{\gamma-\text{f.c.c.}}} \quad (3\text{-}17)$$

$$V_{\gamma-\text{f.c.c.}} = {a_{\gamma-\text{f.c.c.}}}^3 \quad (3\text{-}18)$$

$$V_{\varepsilon-\text{h.c.p.}} = \frac{\sqrt{3}}{2}{a_{\varepsilon-\text{h.c.p.}}}^2 x\ c_{\varepsilon-\text{h.c.p.}} \quad (3\text{-}19)$$

where $V_{\gamma\text{-f.c.c,}}$ and $V_{\varepsilon\text{-f.c.c,}}$ are the volume of the γ-f.c.c. and ε-h.c.p. phases, respectively, with $a_{\gamma\text{-f.c.c.}}$ and $a_{\varepsilon\text{-h.c.p.}}$ and $c_{\varepsilon\text{-h.c.p.}}$ being the lattice parameters for the γ-f.c.c. and ε-h.c.p. phases.

Taking Equation (3-18) and (3-19) into (3-17) gives the following simplified Equation.

$$\Delta V = \frac{(\sqrt{3}{a_{\varepsilon-\text{h.c.p.}}}^2 * c_{\varepsilon-\text{h.c.p.}})-({a_{\gamma-\text{f.c.c.}}}^3)}{{a_{\gamma-\text{f.c.c.}}}^3} \quad (3\text{-}20)$$

3.5.1.2.2 Phase stress partitioning calculation

An in-depth understanding of the deformation behavior of the constituent phases in the metastable $Fe_{42}Mn_{28}Co_{10}Cr_{15}Si_5$ HEA during macroscopic tensile deformation and a quantitative analysis of the stress/strain relationship between the soft γ-f.c.c. phase and the hard ε-h.c.p. phase is essential for gaining an insight into the deformation mechanisms of the material and for the design of new materials. Therefore, in order to investigate the micromechanical behavior of the currently studied alloy, the von Mises criterion was introduced to evaluate the stress distribution in both γ-f.c.c. and ε-h.c.p. phases [106].

The phase stress partitioning was calculated considering the (311) lattice plane of the γ-f.c.c. phase [77] and of the $(10\bar{1}2)$ lattice plane of the ε-h.c.p. phase [107] since these planes have a relatively low intergranular strain sensitivity, as demonstrated by crystal plasticity simulations. Thus, by focusing on these two specific lattice planes, it is possible to obtain a representative stress/strain behavior of the individual phases that compose the metastable HEA used in this work.

The von Mises stress, σ_{vm}, used to calculate the phase stresses is detailed as follows,

$$\sigma_{vm} = \frac{1}{\sqrt{2}}[(\sigma_{11} - \sigma_{22})^2 + (\sigma_{22} - \sigma_{33})^2 + (\sigma_{33} - \sigma_{11})^2]^{\frac{1}{2}} \quad (3\text{-}21)$$

Here, σ_{11} refers to the principal stress parallel to the LD and σ_{22} and σ_{33} correspond to the principal stresses perpendicular to the direction of loading (TD). $\sigma_{22} = \sigma_{33} \approx 0$ is assumed here for a square section specimen in this study. The value of σ_{11} can be obtained from lattice strain calculations [108] by the following Equations,

$$\sigma_{11} = \frac{E}{1+v}\varepsilon_{11} + \frac{vE}{(1+v)(1-2v)}(\varepsilon_{11} + \varepsilon_{22} + \varepsilon_{33}) \quad (3\text{-}22)$$

$$v = -\frac{\varepsilon_{transverse}}{\varepsilon_{longtigudinal}} \quad (3\text{-}23)$$

Here, ε_{11} is the lattice strain along the LD, ε_{22} and ε_{33} are the lattice strains perpendicular to the LD (assuming $\varepsilon_{22} = \varepsilon_{33}$ [107]). The azimuthal integration ranges corresponding to the LD and TD were from 85 to 95° and from -5 to 5°, respectively, as previously described. The specific calculation procedure for determination of the lattice strain has been described in subsection 3.5.1.2.6. E denotes the Young's modulus of the selected lattice planes, i.e., (311) for γ-f.c.c. and $(10\bar{1}2)$ for ε-h.c.p. calculated along LD, which can be determined by linearly fitting the evolution of the lattice strain in the elastic range. The ratio of the transverse lattice strain, ε_{22}, to the longitudinal lattice strain, ε_{11}, is the Poisson's ratio, ν, as shown in Equation (3-23).

$$v = -\frac{\varepsilon_{transverse}}{\varepsilon_{longtigudinal}} \quad (3\text{-}23)$$

Subsequently, the rule-of mixture (ROM) [109], for the mechanical properties of multiphase materials was used to further investigate the contribution from each constituent phase to the total tensile stress. The fraction-weighted average stress can be calculated by summing up the contribution stresses of both γ-f.c.c. and ε-h.c.p. phases [110].

$$\sigma = V_{\gamma-\text{f.c.c.}}\,\sigma_{\gamma-\text{f.c.c.}} + V_{\varepsilon-\text{h.c.p.}}\,\sigma_{\varepsilon-\text{h.c.p.}} \quad (3\text{-}24)$$

where $V_{\gamma-\text{f.c.c.}}$and $V_{\varepsilon-\text{h.c.p}}$ correspond to the phase volume fraction of the γ-f.c.c. and ε-h.c.p. phases (subsection 3.5.2.2.1 previously detailed this calculation procedure). $\sigma_{\gamma\text{-f.c.c.}}$ and $\sigma_{\varepsilon\text{-h.c.p.}}$ refer to the phase stresses of the γ-f.c.c. and ε-h.c.p. phases, which were obtained from the representative lattice planes, i.e., (311) for γ-f.c.c. and $(10\bar{1}2\}$ for ε-h.c.p., respectively.

3.5.1.2.3 Dislocation density calculations

Increase in dislocation density is a main source of strengthening in most engineering alloys [95], and its quantitative measurement is essential for understanding its contribution to overall strengthening and even for making qualitative judgements on the main deformation mechanisms of a material.

Conventional transmission electron microscopy (TEM) [111] and X-ray diffraction line profile analysis [111,112] are indirect methods for measuring the dislocation density. However, when the dislocation density is high enough (> 10^{14} m^{-2}), its determination by TEM is hard [113–115]. This difficulty can be overcome by using X-rays [116]. In addition, a modified Williamson-Hall model has been shown as a possible method to correlate the broadening of different diffraction peaks with dislocation density, and thus derive the dislocation density [117].

In this study, the dislocation density evolution of the metastable $Fe_{42}Mn_{28}Co_{10}Cr_{15}Si_5$ HEA during tensile deformation was calculated by combining the analysis of the FWHM obtained by X-ray line profile analysis with the modified Williamson-Hall model. The diffraction peaks used here were obtained by integrating along the full azimuthal angle, as well as along LD and TD. A pseudo-Voigt function in the GSAS software was used for the single-peak fitting, and the obtained FWHM is named $FWHM_{measured}$, and it consists of three main contributions. One is the instrumental-induced peak broadening [118] (specified as $FWHM_{instrumental}$) and its value can be obtained from the LaB_6 standard powder calibration. The other two components include the peak broadening due to the average microstrain, ε_0, which is caused by dislocations, and grain size-induced peak broadening. The peak broadening arising by these two contributions is termed $FWHM_{microstrain\ +\ grain\ size}$. Thus, the broadening of a diffraction peak caused by dislocations and grain size can be obtained from the following Equations [86,117],

$$FWHM_{microstrain+grain\ size} = [(FWHM_{measured})^2 - (FWHM_{instrumental})^2]^{\frac{1}{2}} \quad (3\text{-}25)$$

$$FWHM_{microstrain+\ grain\ size} = FWHM_{microstrain} + FWHM_{grain\ size} \quad (3\text{-}26)$$

Here, $FWHM_{grain\ size}$ can be estimated from the Scherrer formula, as shown below,

$$FWHM_{microstrain} = 4\ \varepsilon_0\ \frac{sin\theta}{cos\theta} \quad (3\text{-}27)$$

$$FWHM_{grain\ size} = \frac{k\ \lambda}{D\ cos\theta} \quad (3\text{-}28)$$

Here, ε_0 is the average microstrain [119], θ is half of the Bragg angle of a selected diffraction peak [120], D is the average grain size [117], k is a constant, assumed as 0.9 here [90,120], λ is the wavelength of the X-ray beam (0.14235Å) [121]. Taking Equation (3-27) and (3-28) into (3-26), Equation (3-22) will be simplified as follows,

$$FWHM_{microstrain+\ grain\ size}\ x\ cos\theta = 4sin\theta\ x\ \varepsilon_0 + \frac{k\lambda}{D} \quad (3\text{-}29)$$

To derive the average microstrain, ε_0, as well as the grain size, D, Equation (3-29) can be considered as a linear Equation of one variable as below,

$$y = kx + b \tag{3-30}$$

where y can be treated as $FWHM_{microstrain + grain\ size}$ x cos (θ), while x corresponds to 4 x sin (θ), K is the average microstrain ε_0 and b is (k x λ) / D. In this approach, the values of the $FWHM_{microstrain + grain\ size}$ x cos (θ) and 4 x sin (θ) were obtained from different diffraction peaks [86]. It is worth noting the definition of the parameter ε_0. Although it is usually referred to as "strain" or "lattice strain" in the literature [117], it does not simply mean the average strain scale (e.g., strain measured by an extensometer upon loading). Venkateswarlu et al. called it an inhomogeneous strain [122], but its definition remains vague, and some researchers avoid the definition of this parameter [86,123]. In the current work, we define it as the average microstrain experienced by each phase during macroscopic loading.

Based on the above calculated microstrain, ε_0, and grain size, D, the dislocation density, ρ, can be estimated by the modified Williamson-Hall method [124,125]. The specific equation is as follows,

$$\rho = \frac{2\sqrt{3}\,\varepsilon_0}{Db} \tag{3-31}$$

where b refers to the Burgers vector, and its magnitude depends on the dislocation slip syste. For the γ-f.c.c. phase structure, the magnitude of Burger's vector changes from $\frac{\sqrt{2}}{2}a_{f.c.c.}$ into $\frac{1}{\sqrt{6}}a_{f.c.c.}$ [77], due to the evolution of the [110]{111} perfect dislocation slip system into a $[11\bar{2}]\{111\}$ Schockley partial dislocation slip system [96]. $a_{f.c.c.}$ is the lattice parameter of the γ-f.c.c. phase. Similarly, for the ε-h.c.p. phase structure, the slip system transforms from a basal slip to a pyramidal slip as plastic deformation progresses [97]. Correspondingly, the magnitude of the Burgers vector for ε-h.c.p. changes from $\frac{\sqrt{6}}{3}$ to $\frac{\sqrt{16}}{3}$, depending on the slip system, with the former corresponding to the basal < a > slip plane, and the latter to the prismatic < c > and pyramidal < c + a > slip planes [97]. A more detailed description of the evolution of the slip mechanisms for both the γ-f.c.c. and ε-h.c.p. phases contained in the metastable $Fe_{42}Mn_{28}Co_{10}Cr_{15}Si_5$ HEA during tensile deformation has been provided in the discussion section.

3.5.1.2.4 Strengthening contributions calculations

To further investigate the strengthening contributions arising from the different deformation mechanisms experienced by the $Fe_{42}Mn_{28}Co_{10}Cr_{15}Si_5$ alloy during tensile deformation, the Bailey-Hirsch model [43,127,128]was applied to describe the dislocation strengthening effect, $\Delta\sigma_D$, in the material,

$$\Delta\sigma_D = M\alpha Gb\rho^{\frac{1}{2}} \tag{3-32}$$

where M is the Taylor factor, α is a proportionality factor [129], G is the sear modulus, b is the burgers vector, and ρ is the dislocation density [130].

In this work, the following parameters were used: i) for the ε-h.c.p. phase, M is 3.06 [124,131], the value of α is 1.16 [130,132] in the $< c + a >$ slip system, which is larger than that in the basal-basal interaction [129] while in the $< a >$ slip system is assumed as 0.2 [129] and G is 78 GPa [132]; ii) for the γ-f.c.c. phase, M is 3.06 [133], α is 0.36 [134] and G is 76 GPa [96]. The selection of the Burgers vectors, b, for the different deformation stages of both γ-f.c.c. and ε-h.c.p. phases, as well as the dislocation densities obtained by the Williamson-Hall model, have been described previously in section 2.4.1.2.2.

In addition to the dislocation density strengthening mechanism, the strain induced transformation from γ-f.c.c. to ε-h.c.p. is another primary deformation mechanism [135]. However, the transition from γ-f.c.c. to ε-h.c.p. requires the presence of large number of stacking faults in the γ-f.c.c. phase [53]. In other words, stacking faults are the core of the ε-h.c.p. phase formation. Specifically, the quantitative study of stacking fault strengthening, σ_{sf}, can be achieved by tracking the changes in the stacking faults interspacing, L_{sf}, which impedes dislocation movement during deformation, and the probability of forming stacking faults, P_{sf}.

Holden et al. [136] using neutron diffraction experiments, reported that the difference in the diffraction peaks in the (111) and (222) γ-f.c.c. lattice planes may not be caused by elastic strain but by structural factors in the stacking faults among the γ-f.c.c. phase. Jeong et al. [137] achieved a similar conclusion using synchrotron radiation. Since the (111) and (222) γ-f.c.c. lattice planes have equivalent crystallographic orientations, the occurrence of stacking faults can lead to differences in lattice strain in these reflections [138]. Based on these literature studies, the shifts of the diffraction peaks of the γ-f.c.c (111) and (222) lattice planes obtained by full azimuthal integration were chosen to be used in this study to evaluate the evolution of the stacking faults interspacing, L_{sf}, stacking fault probability, P_{sf}, and hence the stacking fault strengthening, σ_{sf}, contribution of the $Fe_{42}Mn_{28}Co_{10}Cr_{15}Si_5$ HEA.

The lattice strain, ε_{hkl} of the γ-f.c.c. (111) and (222) planes, which was obtained using the previously described peak fitting routine using the GSAS software, consists of the elastic lattice strain, ε_{hkl}^{e}, and the lattice strain induced by staking faults, ε_{hkl}^{sf} [139,140]. Since the (111) and (222) γ-f.c.c. planes are equivalent in terms crystallographic orientation, the elastic lattice strains of γ-f.c.c. (111) and (222) planes are equal ($\varepsilon_{222}^{e} = \varepsilon_{111}^{e}$). The detailed derivation is detailed as follows.

$$\varepsilon_{(hkl)} = \varepsilon^{e}_{(hkl)} + \varepsilon^{sf}_{(hkl)} = \frac{d_{hkl} - d^{0}_{hkl}}{d^{0}_{hkl}} \tag{3-33}$$

$$\varepsilon^{e}_{222} = \varepsilon^{e}_{111} \tag{3-34}$$

$$\varepsilon_{222} - \varepsilon_{111} = \left(\varepsilon^{e}_{222} + \varepsilon^{sf}_{222}\right) - \left(\varepsilon^{e}_{111} + \varepsilon^{sf}_{111}\right) = \varepsilon^{sf}_{222} - \varepsilon^{sf}_{111} = \frac{d_{222} - d^{0}_{222}}{d^{0}_{222}} - \frac{d_{111} - d^{0}_{111}}{d^{0}_{111}} \tag{3-35}$$

where d_{hkl} is the hkl-specific lattice spacing obtained at different loading steps, and d^{0}_{hkl} is the corresponding stress-free lattice spacing. The stacking faults and hkl-dependent lattice strain ε_{hkl} can be correlated with the experimentally measured lattice strain via the following Equation [139],

$$\varepsilon_{hkl} = -\frac{\sqrt{3}}{4\pi} \frac{\sum_b (\pm L_0)}{h_0^2 (u+b)} P_{sf} \tag{3-36}$$

In Equation (3-36), u, b, h and L_0 in $\frac{\sum_b (\pm L_0)}{h_0^2 (u+b)}$ are crystal structure-related parameters [141], with values of +1/4 and -1/8 being reported [139] for the (111) and (222) γ-f.c.c. orientations, respectively; u and b correspond to the non-broadened and broadened components due to the stacking faults, respectively [140,142]. This leads to the following simplified Equations for the lattice strain ε_{111}, ε_{222} and stacking faults probability, P_{sf} [140],

$$\varepsilon_{222} = -\frac{\sqrt{3}}{4\pi}\left(-\frac{1}{8}\right) P_{sf} = 0.0173 P_{sf} \tag{3-37}$$

$$\varepsilon_{111} = -\frac{\sqrt{3}}{4\pi}\left(\frac{1}{4}\right) P_{sf} = -0.0344 P_{sf} \tag{3-38}$$

$$\varepsilon_{222} - \varepsilon_{111} = 0.0173 P_{sf} - \left(-0.0344 P_{sf}\right) = 0.0517 P_{sf} \tag{3-39}$$

$$P_{sf} = \frac{\varepsilon_{222} - \varepsilon_{111}}{0.0517} = \frac{\frac{d_{222} - d^{0}_{222}}{d^{0}_{222}} - \frac{d_{111} - d^{0}_{111}}{d^{0}_{111}}}{0.0517} \tag{3-40}$$

Then, the interspacing between stacking faults, L_{sf}, can be obtained from d_{111} and P_{sf} [143], and is given by the following relation [128,143],

$$L_{sf} = \frac{d_{111}}{P_{sf}} \tag{3-41}$$

where d_{111} and P_{sf} refer to the (111) d-spacing (obtained from full azimuthal integration) and stacking faults probability, respectively.

Based on the results obtained from the above calculations, the stacking faults strengthening, σ_{sf}, can be obtained by the following Equation [143],

$$\sigma_{sf} = \frac{K_{sf}}{L_{sf}} \quad (3\text{-}42)$$

where L_{sf} is the interspacing between stacking faults, which can be obtained from Eq. 3-41, K_{sf} is the strengthening coefficient, and the following formula can be used to calculate this parameter,

$$\sigma_{yield} = \sigma_a + K_{sf}\frac{1}{L_{sf}} \quad (3\text{-}43)$$

K_{sf} is the slope of the linear fit between $1/L_{sf}$ (corresponding to the x-axis) and the yield strength, σ_{yield}, (corresponding to the y-axis) [128,143], which can be interpreted as the extra energy consumed by dislocations to cut through stacking faults when dislocations are impinged at them [128,143]. Additional details for determining K_{sf} can also found in [128]. σ_a is the total strength contributed by various strengthening mechanisms other than stacking faults [144]. The K_{sf} value calculated in this work is 2610 MPa.nm indicating for this material that the stacking faults act as a strong barrier against dislocation slip.

3.5.1.2.5 c/a ratio calculations

The c/a ratio is a key structural parameter of the h.c.p. phase that can be directly related to the lattice spacing [145], and is also closely related to the structural plane features that control the activation of the structural slip systems in this phase [105,145]. The ideal value of the c/a ratio is 1.633, although this value can be adjustable in magnitude [105]. On one hand, the c/a ratio depends on the alloy composition and the addition of ε-h.c.p. phase stabilizers (such as Co, Mn, Si) can increase the c/a ratio but the addition of γ-f.c.c. phase stabilizers (Cu, Al) can decrease it. On the other hand, thermomechanical processing and deformation is another way of changing the c/a ratio due to the dependence of the lattice parameters on the microstructure and stress state, but it is necessary to exclude the conventional ε-h.c.p. phase metals (e.g. Mg and Ti) as these materials have c/a ratios that depend on the alloy composition but remain almost constant during processing or deformation [105]. Bu et al. had determined the a and c lattice parameters in the ε-h.c.p. phase among different regions in a friction stir processed $Fe_{50}Mn_{30}Co_{10}Cr_{10}$ HEA by X-ray diffraction. The c/a ratio for BM and stir region were of 1.622 and 1.616, respectively [145]. This small change in this structural parameter allows to infer that different slip systems can be activated, for example the non-basal slip system, and thus affect the ductility of the ε-h.c.p. phase [146].

The Rietveld refinement methodology previous described was used to determine the c/a ratio change during tensile loading. The formula used to calculate the c/a ratio is as follows,

$$c/a_{ratio} = \frac{c_{\,\varepsilon-\text{h.c.p.phase}}}{a_{\,\varepsilon-\text{h.c.p.phase}}} \quad (3\text{-}44)$$

where $c_{\,\varepsilon\text{-h.c.p. phase}}$ and $a_{\,\varepsilon\text{-h.c.p. phase}}$ refer to the lattice constants of the ε-h.c.p. phase.

3.5.1.2.6 Lattice strain calculations

The response of different lattice planes to the applied load during deformation of a material is important for understanding the alloy micromechanical behavior. In this study, the lattice strain evolution of the γ-f.c.c. and ε-h.c.p. phases in the metastable $Fe_{42}Mn_{28}Co_{10}Cr_{15}Si_5$ HEA was calculated along the LD and TD. Specifically, the (111), (200) and (311) lattice planes of the γ-f.c.c. phase, and the $(10\bar{1}0)$, $(10\bar{1}1)$, $(10\bar{1}2)$ and $(10\bar{1}3)$ planes of the ε-h.c.p. phase have been chosen. Each diffraction peak was fitted individually using the GSAS software and the lattice strain, ε_{hkl}, for a selected (h k l) plane was calculated as,

$$\varepsilon_{hkl} = \frac{d_{hkl} - d^0_{hkl}}{d^0_{hkl}} \; x \; 10^{-6} \tag{3-45}$$

where d_{hkl} and d^0_{hkl} represent the interplanar spacings for a certain (h k l) plane under loading and in the stress-free condition, respectively.

3.5.2 Synchrotron X-ray diffraction for characterization of the welded joints

High energy synchrotron X-ray diffraction was used to probe the phase structure evolution throughout all the welded joints. A beam with a size of 200 x 200 μm^2, started to scan the welded joints in the BM, passing through the HAZ and FZ, until it reaches the BM on the opposite side of the weld. A schematic representation of the setup used is shown in Figure 3-6.

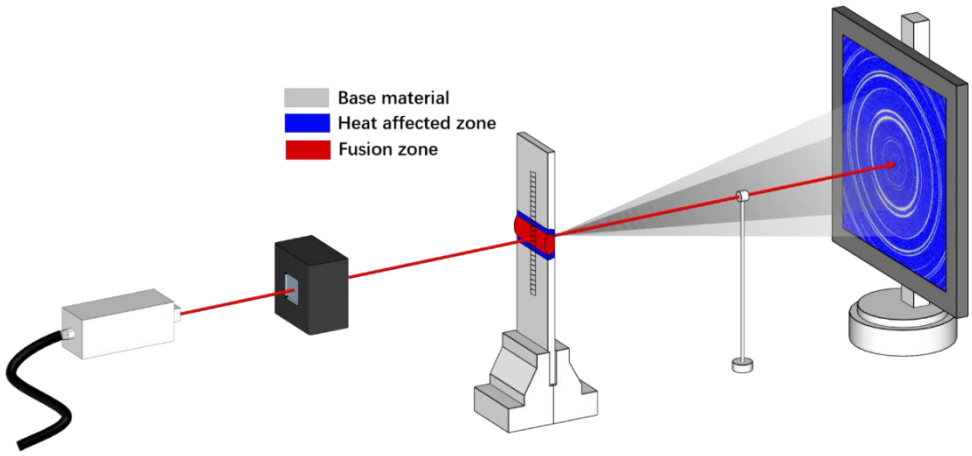

Figure 3-6. Synchrotron X-ray diffraction setup (not to scale).

3.6 Thermodynamic calculations

3.6.1 Thermodynamic calculations used for gas tungsten arc welded joints

Thermodynamic calculations based on the CalPhaD method were used to predict how the weld thermal cycle affected the phase evolution and elemental partitioning in the FZ. Owing to the non-equilibrium solidification conditions experienced by the FZ, the Scheil-Gulliver model was used in ThermoCalc with the TCHEA 5.1 HEA database. The experimental data was then compared with the predicted results for analyzing the reliability of the thermodynamic calculations, and for providing reference for further improvements on currently existing thermodynamic databases.

3.6.2 Thermodynamic calculations used for gas metal arc welded joints

To evaluate the effect of the filler wires on the potential compositional heterogeneity of the fusion-based welded joints (i.e., mixing ratio of BM and filler wire) Scheil-Gulliver calculations with 1 or 10% dilution steps (depending on the welded joint) were implemented. These calculations were also used to predict the number of phases and solidification temperature range. During non-equilibrium thermodynamic calculations using the Scheil-Guliver model, certain elements can be set as fast diffusers, as theycan greatly influence the solidification path experienced by the material. For steels and related alloys, carbon is usually set as fast diffuser [147]. Here, calculations were made with and without carbon selected as a fast diffuser to evaluate the impact on this element on the solidification microstructure. The TCHEA5.1 database of ThermoCalc was used for these calculations. Owing to the large number of potential compositions probed, a python-based routine was implemented in Thermocalc using the TCHEA 5.1 database.

3.7 Microhardness mapping and tensile testing

Microhardness mapping across all the welded joints was performed on a Mitutoyo HM-112 Hardness Testing Machine with a load of 300 N, duration of 10 s, and a distance of 200 μm between consecutive indentations. This allowed to obtained hardness maps that enable the visualization of the hardnening and softening effects induced by the microstructure changed within the welded joints.

Uniaxial tensile testing was performed along with DIC on a Shimadzu tensile machine equipped with a 50 kN load cell (refer to Figure 3-7). The dimensions of the dog-bone specimens are the same as those detailed in Figure 3-2 and Figure 3-4). Tensile tests were performed at room temperature, at a strain rate of 1×10^{-3} s^{-1}, with the loading direction being perpendicular to the welding direction. In order to evaluate the variability of tensile properties, three welded samples were tested. Before testing, the specimens were prepared for DIC by applying a random black speckle pattern over a previously painted matt white surface. Data analysis was performed using Vic-2D software. At least three specimens were used to assess the reproducibility of the tensile properties after welding. After tensile testing, a Hitachi SU3800 scanning electron microscope was used to observe the fracture morphology of the welded specimens.

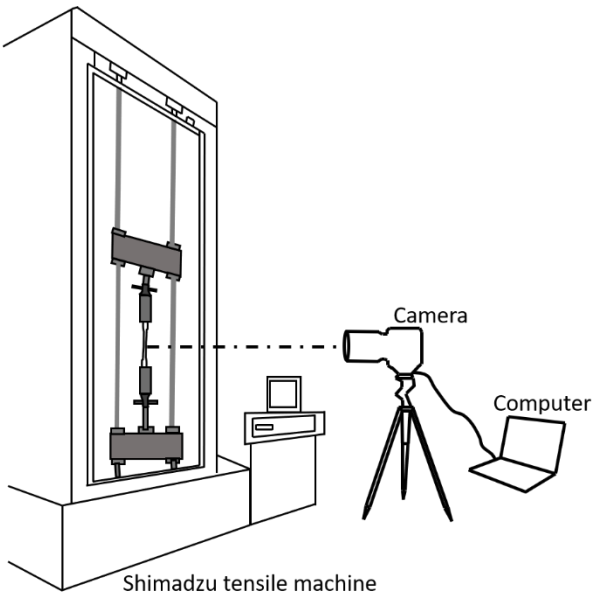

Figure 3-7. Schematic diagram of tensile test with DIC.

3.8 Summary

In this section the welding parameters and all characterization techniques, both for microstructure and mechanical assessment, were described in detail. GMAW was used to join the CoCrFeMnNi HEA using four different filler materials (308 and 410 stainless steels). GTAW was used to join the eutectic

$AlCoCrFeNi_{2.1}$ and metastable $Fe_{42}Mn_{28}Co_{10}Cr_{15}Si_5$ HEA in similar combinations. The welding parameters and subsequent microstructure (OM, SEM, as well as synchrotron X-ray diffraction) and mechanical characterization, coupled with thermodynamic calculations were described in this section. The multiscale correlative microstructure and properties characterization will enable to obtain a correlation between the welding process, microstructure, and mechanical properties as detailed in the next chapters.

In the next chapter the results and discussion pertaining to all the welded joints obtained is detailed. First focus is given to the role of different filler materials during GMAW of the CoCrFeMnNi HEA. Then, the effect of GTAW of the eutectic $AlCoCrFeNi_{2.1}$ and metastable $Fe_{42}Mn_{28}Co_{10}Cr_{15}Si_5$ HEAs is detailed, including the in-situ characterization performed on these two BM.

4.

MICROSTRUCTURE AND MECHANICAL PROPERTIES OF GAS METAL ARC WELDED CoCrFeMnNi JOINTS USING DIFFERENT FILLER MATERIALS

4.1 Introduction

Traditionally alloy design concepts are focused on using one principal element and then improving the desired properties with relatively minor alloying additions. Cantor et al. [148] and Yeh et al. [2] independently proposed a new alloy design strategy which broke the design barriers of traditional alloys. Nowadays, HEAs are attracting significant interest owing to their attractive and unique properties including strength, thermal stability, wear and oxidation resistance [149–154].

One of the most widely studied HEAs is the FCC single phase CoCrFeMnNi [148,155,156], being considered a potential structural material due to its remarkable mechanical properties over a wide range of temperatures [157].

Welding, as one of the most important metal processing methods for structural materials, is virtually used in any structural engineering application. Thus, coupling the development of new materials and determining their weldability is essential to promote them as engineering solutions.

So far, researchers focused on the weldability of CoCrFeMnNi HEAs with fusion-based welding processes, including laser beam welding [19–21], electron beam welding [18,22] and GTAW [158]. Although well performing joints have been obtained, they are mainly limited to similar welding combinations. Based on the state of art presented in chapter 2.3.4.1, as well as the current section, furthering expanding the applications prospects CoCrFeMnNi HEAs in nuclear and aerospace sectors, joining them to other BMs or the addition of filler materials to adjust the composition and modify the material microstructure is required.

The use of filler materials during fusion-based welding processes is widely used to regulate and modify the composition of the welded joints aiming at producing a desired microstructure and/or achieving an improvement in its mechanical performance. Welding of HEAs is still a new topic and the impact of different filler materials on the microstructure and mechanical properties is yet unknown.

Thus, this chapter the role of different filler materials (308 and 410 stainless steel) during GMAW of the CoCrFeMnNi HEA is assessed.

In order to achieve the goal of establishing a correlation between the weld thermal cycle, microstructure evolution and resulting mechanical properties and provide a wider basis for promoting the applications of GMAW of HEAs for industrial application. The microstructural evolution of welded joints was evaluated by OM, SEM aided by EBSD, high energy synchrotron X-ray diffraction and thermodynamic calculations. Meanwhile, the mechanical behavior of the welded joint, as well as the local mechanical response were investigated with microhardness mapping measurements and with non-contact DIC during tensile loading to failure. The role of the filler material in the solidification path experienced by the FZ was evaluated using Scheil-Gulliver calculations. Moreover, the Scheil-Gulliver model was also used considering dilution steps to investigate the effect of dilution of the filler materials on the solidification phases and solidification temperatures range.

A comprehensive analysis of the microstructure and mechanical properties for each of the welded joints obtained with different filler wires is first performed. Then, a summary and comparison of the microstructural characteristics and mechanical properties of the four different welded joints is provided in order to clarify the role of each filler wire and its suitability for different structural applications.

4.1 Starting material

In this work, an equiatomic CoCrFeMnNi HEA with a thickness of 3 mm was prepared by vacuum induced melting as described in [159]. Following cold rolling at room temperature, a thickness of 1.5 mm was obtained. Before welding, the as-rolled material was cut by machining into 60 x 60 mm squares for butt joining. The faying edges were polished and cleaned with acetone and alcohol to remove any contaminants that could be harmful to the welded joint.

4.2 Results and discussions

4.2.1 Gas metal arc welded CoCrFeMnNi joints using a 410 stainless steel filler metal

Microstructure evolution Figure 4-1 a) details a macroscopic overview of the cross-section of the gas metal arc welded joint. No welding defects are observed. Figure 4-1 b), c) and d) detail the light OM images of the BM, HAZ and FZ, respectively. The fusion boundaries, marked with white dashed lines in Figure 4-1, delimitate the FZ. As typically for welded joints obtained with filler material, there is the formation of a reinforcement on the face and root of the weld, as marked in Figure 4-1 a), owing to the extra material coming from the filler wire. The face reinforcement is formed upon the addition of the molten filler wire and protrudes slightly as the wire moves forward during welding. The root reinforcement on the bottom surface of the joint is more obvious due to the surface tension of the melted wire during solidification [160]. From Figure 4-1 b), c) and d), it can be broadly seen the evolution of the grain size and microstructure across the welded joint. The BM region (Figure 4-1 b)) has the smallest grain size due to the cold rolling imposed prior to welding. The grain size increases when entering in the HAZ (Figure 4-1 c)). Before reaching the HAZ/FZ boundary, within the partially melted zone, there is evidence of partial liquation of the existing grains (refer to Figure 4-1 d)). At the HAZ/FZ interface, a typical solidification structure composed by dendrites is observed. Within the center of the FZ (Figure 4-1 e)), coarse columnar grains grew owing to the highly directional solidification conditions experienced.

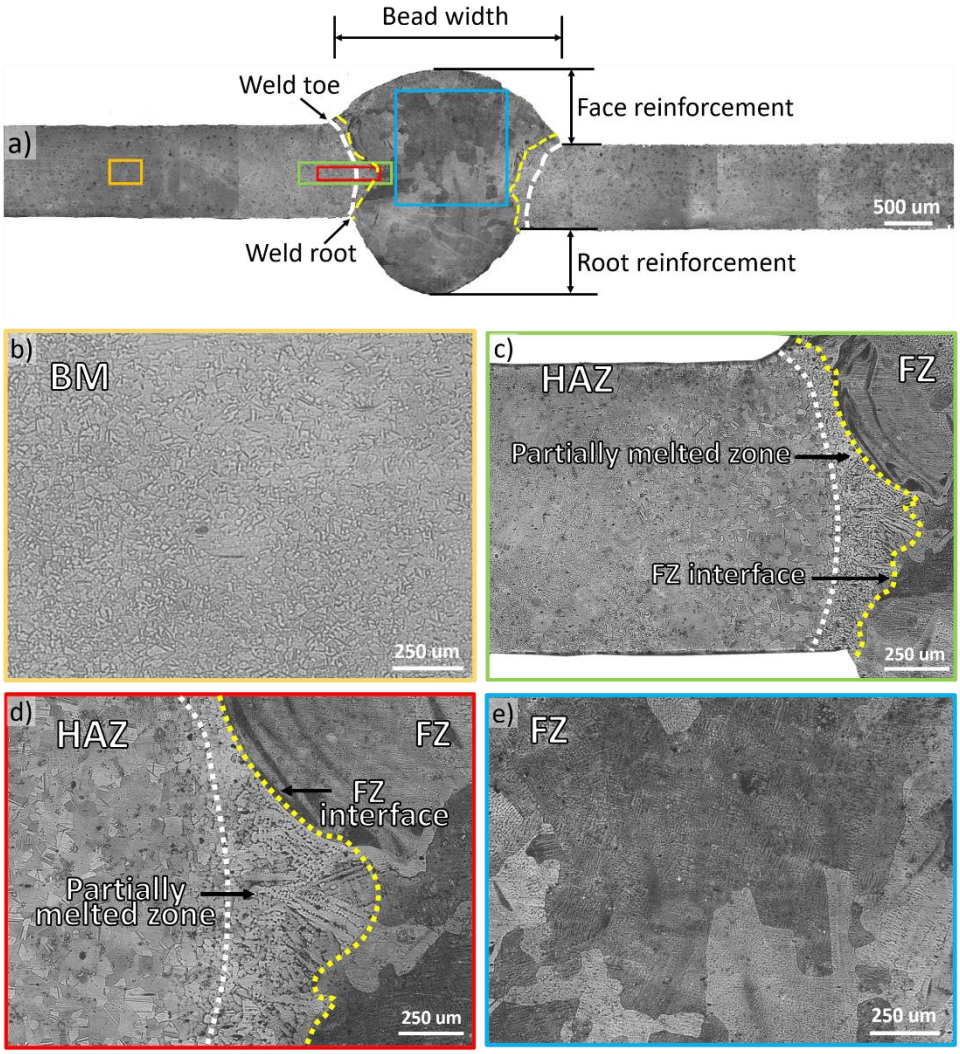

Figure 4-1: Light OM of the gas metal arc welded CoCrFeMnNi joint obtained with ERNiMo-410 filler wire: a) overview of the cross-section of the welded joint; b) BM; c) HAZ and HAZ/FZ boundary; d) magnified HAZ and HAZ/FZ interface; e) FZ.

To further evaluate the microstructure evolution, EBSD was used. The EBSD map of the welded joint is depicted in Figure 4-2. Due to the large size of the as-welded sample, the as-rolled CoCrFeMnNi BM is not included in the EBSD map shown in Figure 4-2. At this instance, focus is mainly given to the HAZ and FZ regions, since the as-rolled BM was already significantly studied in the literature [67,161]. In Figure 4-2, the white dashed lines represent the HAZ/FZ interface. Combined with the macroscopic overview of welded joint previously shown in Figure 4-1, it can be clearly seen that there are no macroscopic defects such as porosity or cracks, indicating that a reliable metallurgical mixing between the CoCrFeMnNi alloy and the ERNiMo-410 stainless steel occurred. This also confirms that the selected welding parameters enabled to obtain a full penetration and defect-free joint.

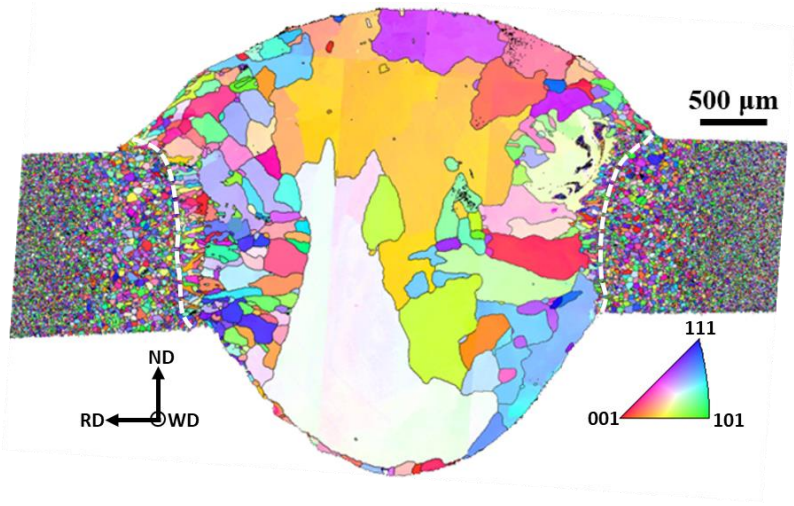

Figure 4-2. EBSD map of the gas metal arc welded CoCrFeMnNi HEA with ERNiMo-410 filler wire.

The grain size evolution across the joint reproduces the impact of the weld thermal cycle on the recrystallization and growth behaviors, as it will be shown when a more detailed analysis of each region of the joint is presented. For now, and only considering the EBSD map of Figure 4-2, it can be observed that the grain size increases towards the HAZ/FZ interface, which is due to the increased local peak temperature and permanence time at high temperatures. The higher the temperature and/or permanence time at critical temperatures, the easier is the growth of the previously recrystallized grains.

At the edge of the FZ, the grain structure is significantly refined due to the presence of the cold HAZ. However, moving away from the HAZ/FZ boundary towards the weld centerline, there is a reduction of the thermal gradient while the temperature experienced by the material is higher which enabled to the development of large columnar grains. It should also be mentioned that the evolution and growth of these grains is also dependent on competitive growth mechanisms experienced by the material, where grains more favorably oriented will have their growth facilitated. These microstructure observations of the HAZ and FZ regions are in good agreement with the light optical micrographs previously shown in Figure 4-1 c). For further visualization and analysis of the microstructural features in different regions of the welded joint, attention is now given to representative EBSD maps obtained in four distinct regions: BM, HAZ 1, HAZ2 and HAZ/FZ interface. Figure 4-3 a) and b) details the Inverse Pole Figure (IPF) and the Kernel Average Misorientation (KAM) maps for the as-rolled CoCrFeMnNi BM. As observed in Figure 4-3 a), the grains are elongated along the rolling direction (RD), forming a refined, pancake-like grain structure with a width of about 2 µm. This grain morphology is common in rolled CoCrFeMnNi HEAs [67]. In addition, considering the IPF map of Figure 4-3, it is evident that the rolled BM is primarily oriented along the (1 1 1) direction. This is due to the fact that the (1 1 1) plane is the main slip plane for FCC materials. When the material is plastically deformed, dislocations tend to pile up along the primary slip system, forming slip bands parallel to the (1 1 1) close-packed plane [162,163].

KAM maps detail the local misorientation of grains within the surrounding microstructure with point-to-point measurements. This can be used to evaluate the relationship between plastic deformation and microstructural misorientation. High KAM values correlate with high a dislocation density and/or with a region with high local strain. It can be seen from Figure 4-3 b) that the KAM values preferentially lie between 4 and 5° (red color) in most areas of the BM (61.4%), implying a high dislocation density, which is associated to the large plastic deformation imposed during cold rolling of the CoCrFeMnNi HEA.

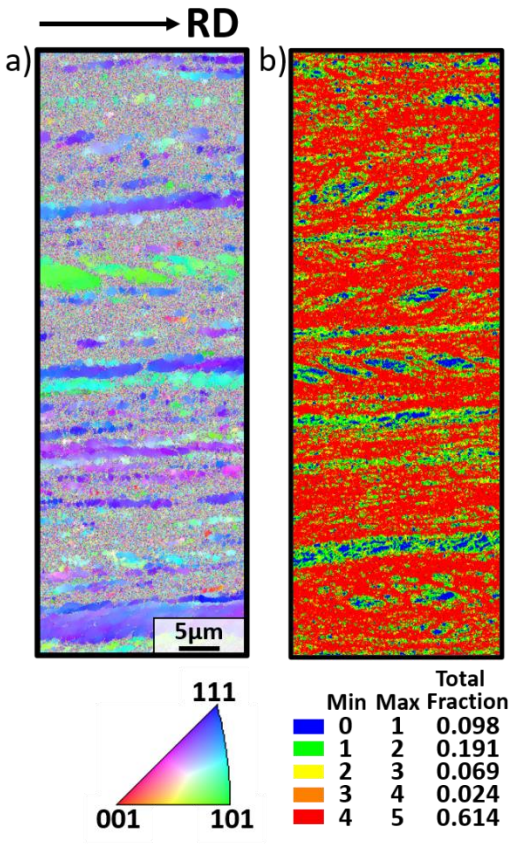

Figure 4-3. EBSD maps of the as-rolled CoCrFeMnNi BM: a) IPF map; b) KAM map.

When entering in the HAZ, microstructural changes induced by the weld thermal cycle start to be clearly noticed. Figure 4-4 a) details the IPF EBSD map obtained in the HAZ1 region, which corresponds to the low temperature HAZ region, i.e., further away from the weld centerline. The pancaked-shaped and highly deformed grains that previously existed are replaced by equiaxed ones, which is typical of recrystallized microstructures. The BM in the rolled condition possesses a large amount of stored strain energy due to the previously imposed plastic deformation. Owing to the relatively low temperature experienced by the HAZ1 region during welding, grains will experience recovery, recrystallisation and (eventually) minor grain growth. As a result, aside from evolving into an equiaxed morphology, there was also a minor increase of the grain size in this region, growing from ≈ 2.0 µm (in the BM) to ≈ 8.5 µm. It should be mentioned here that the main driving forces for recrystallisation and grain growth are

related to the process heat input, but also with the stored strain energy in the material. Comparing the distribution of the KAM values in the BM and HAZ1 regions, corresponding to Figure 4-3 b) and Figure 4-4 b), respectively, it can be found that the strain energy stored in the grains within the HAZ1 is significantly reduced compared to the BM. This can be attributed to the low temperature annealing-like treatment produced in this region during welding. This relatively low temperature cycle is usually associated with stress relaxation and can lead to grain growth, if higher temperatures and/or permanence times are imposed on the material [164]. In other words, the release of the previously stored strain energy contributes to the development of solid-state transformations triggered by the weld thermal cycle. These solid-state transformations include recovery, recrystallisation and minor grain growth, which then translates into reduced dislocation density. Figure 4-4 c) details the EBSD phase map in the HAZ1 region. This region consists primarily of FCC phase and a small amount (≈ 2.7%) of BCC phase. As it will be shown after, when combining both EDS and synchrotron X-ray diffraction data (Figure 4-8 and Figure 4-9, respectively), this BCC phase can be assigned to the presence of Cr-Mn-based oxides. The presence of a large number of annealing twins was detected in the HAZ1 region, with multiple ∑3 twin boundaries being observed, as identified by the red solid lines of Figure 4-4 d). The driving force for the formation of these ∑3 twins is the high strain energy (dislocation density) stored in the material and sufficiently high temperature. Generally, annealing twins are produced in recrystallized grains, and their density is proportional to the twin boundary fraction. From the ∑3 twin boundary map shown in Figure 4-4 d), the fraction of ∑3 twins are approximately ≈ 40.5%, uncovering that the weld thermal cycle, with a low peak welding temperature in the HAZ1 region, can induce the formation these ∑3 twins in the previously cold worked material.

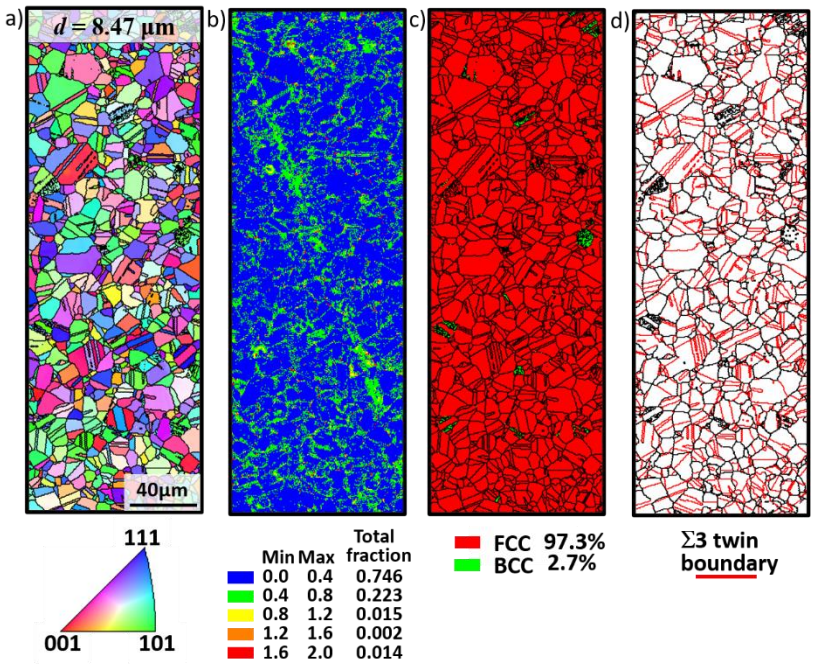

Figure 4-4. EBSD maps of the HAZ1 region: a) IPF map; b) KAM map; c) Phase diagram; d)∑3 twin boundaries map.

Attention is now given to the HAZ2 region Figure 4-5 details the EBSD maps at this location, which correspond to the high temperature HAZ region. Here, the grains become significantly coarser increasing from ≈ 8.5 µm, in the low temperature HAZ, to ≈ 32.5 µm (refer to Figure 4-4 a) and Figure 4-5 a), respectively). This significant increase indicates a dominance of a grain growth mechanism over recrystallization. Solid state phenomena such as those observed in this work, i.e., recovery, recrystallization and grain growth, are intimately related to the starting material condition and distance to the welding heat source. Specifically, regarding the HAZ1 and the HAZ2 regions, the former experienced a lower peak temperature than the latter, which would be similar to a short low-temperature annealing, in which recrystallization and minor grain growth occurred. However, for the HAZ2 region, there is evidence of significant grain growth, since higher peak temperatures are experienced at this location. This would resemble the effect of a short and high temperature heat treatment where grain growth is favored. The essence of grain growth is the migration of grain boundaries in the material, which promotes mutual engulfment and subsequent growth of preexisting grains. The main driving forces for this process originate from the difference in the energy stored in adjacent grains or in the decrease of the grain interfacial energy, i. e., as the grain growth behavior occurs, its stored energy per unit volume of grain boundary area decreases. Comparing the KAM maps of the low and high temperature HAZ regions, refer to Figure 4-4 b) and Figure 4-6 b), respectively, reveals a significant increase in the fraction of KAM values between 0 and 0.4 º for the high temperature HAZ (74.6 to 82.7%), with a decrease in the 0.4 to 0.8º range (22.3 to 16.4%). This change evidences the effect of high temperature in the promotion of a reduced dislocation density of the previously highly deformed BM.

Moreover, owing to the dependence of the consumption of stored energy with temperature, it is also clear that high temperatures and/or permanence times are conducive to a more significant reduction in the material stored energy. Despite the higher temperature experienced by the HAZ2 region, there was no change in the phase content, with the microstructure being dominated by the FCC phase (≈ 97.5%) with trace amounts of BCC Cr-Mn-based oxides (≈ 2.5%), as shown in Figure 4-5 c). The fraction of ∑3 twin boundaries decrease to ≈29.8% in the HAZ2 region (refer to Figure 4-5 d) and Figure 4-5 d)). This is again attributed to the high temperature experienced by this region of the welded joint. In fact, the reduction in the fraction of ∑3 boundaries is related to the grain growth process, where grains collide with each other, causing a reduction in the mobility of the grain boundaries. Besides, the rapid movement of adjacent grain boundaries or twins can easily consume preexisting twin boundaries during grain growth, resulting in the partial or full annihilation of the previously existing annealing twin boundaries, which ultimately leads to a reduction in the number of annealing twins as grain growth proceeds. Finally, when the grain growth process is finished, large grains will exist, while stable twins can be kept in the material microstructure. This assessment has been previously confirmed in [165,166], where it was shown that annealing twins can gradually disappear through migration of grain boundaries or twin boundaries during grain growth. It should be noted that, in this work, annealing twins were only observed in the HAZ of the welded joint.

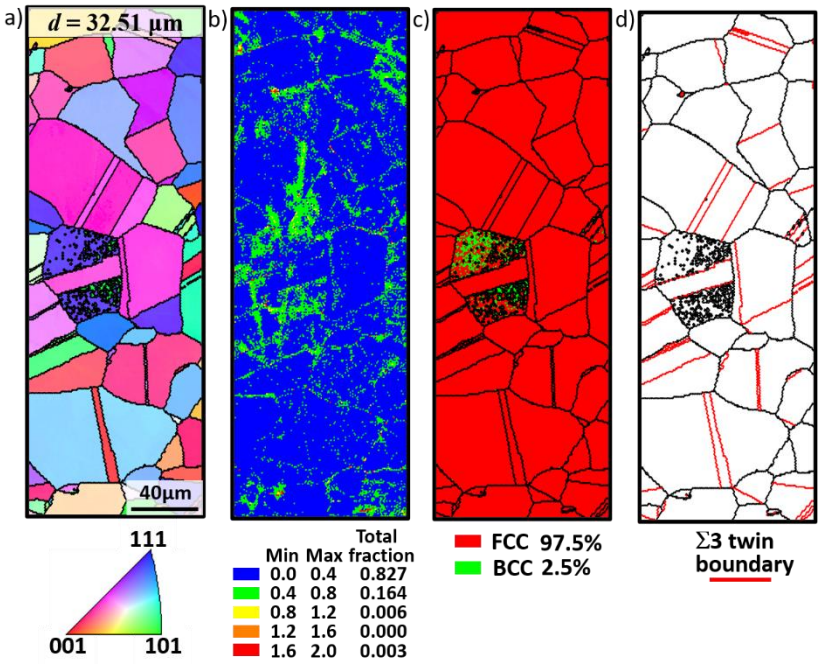

Figure 4-5. EBSD maps of the HAZ2 region: a) IPF map; b) KAM map; c) phase diagram map; d) ∑3 twin boundaries map.

Figure 4-6 details the EBSD data obtained at the HAZ/FZ interface which can be used to elucidate on the epitaxial growth phenomenon experienced in the FZ. When entering the FZ, small equiaxed and columnar grains nucleate from the cold substrate. Here, the temperature gradient is maximum, which

enables to obtain a refined grain structure compared to the bulk of the FZ. Moreover, at the FZ boundary, there is no evidence of preferred orientation (refer to Figure 4-6 a). While progressing away from the HAZ/FZ interface toward the weld centerline, there is a decrease on both the temperature gradient and cooling rate, and the tendency for a refined grain structure to be formed significantly decreases. In fact, columnar-like grains start to be predominant roughly 30 µm away from the FZ boundary. These coarser columnar grains will grow in the opposite direction to the heat flow extraction and nearly perpendicular to the FZ boundary. Grains that have their preferential growth direction aligned with the heat flow extraction will have their growth facilitated.

Quantification of the average KAM values shown in Figure 4-6 b) revealed that the peak of residual strain occurs on the boundary line of HAZ/FZ interface within the refined grain structure that exists at this location. This can be attributed to thermally induced strains derived from the large heat input of arc-based processes. In the presence of the cold substrate, the cooling rate is significantly more abrupt preventing the material to freely accommodate these thermal strains upon cooling and subsequent solidification. Towards the bulk of the FZ, the thermal conditions are not as severe, since the thermal gradient is reduced, which allows the material to more easily accommodate the thermal strains. Nonetheless, it should be mentioned that the KAM values obtained at this location are, in magnitude, lower than those in the BM, implying that despite the occurrence of thermal strains due to the weld thermal cycle, these are not as severe as those imposed by the cold rolling of the BM.

The EBSD phase map shown in Figure 4-6 c) details that the phase constituents near the HAZ/FZ interface are again the FCC phase (97.5%) and the BCC phase (2.5%). Thus, even though the peak temperatures are maximum at this location, while staying below the CoCrFeMnNi BM melting point, there was no significant influence on the existing phases and their volumetric fraction. Interestingly, the $\sum 3$ annealing twins observed in the HAZ region (refer to Figure 4-4 d) and Figure 4-5 d)) disappear when crossing the HAZ/FZ interface towards the FZ (refer to Figure 4-6 d)). This is related to the fact that upon melting any previous thermomechanical processing is lost. Thus, the effect of rolling followed by permanence times at relatively high temperatures is not preserved, with the resulting material microstructure resembling that of the material in the as-cast state.

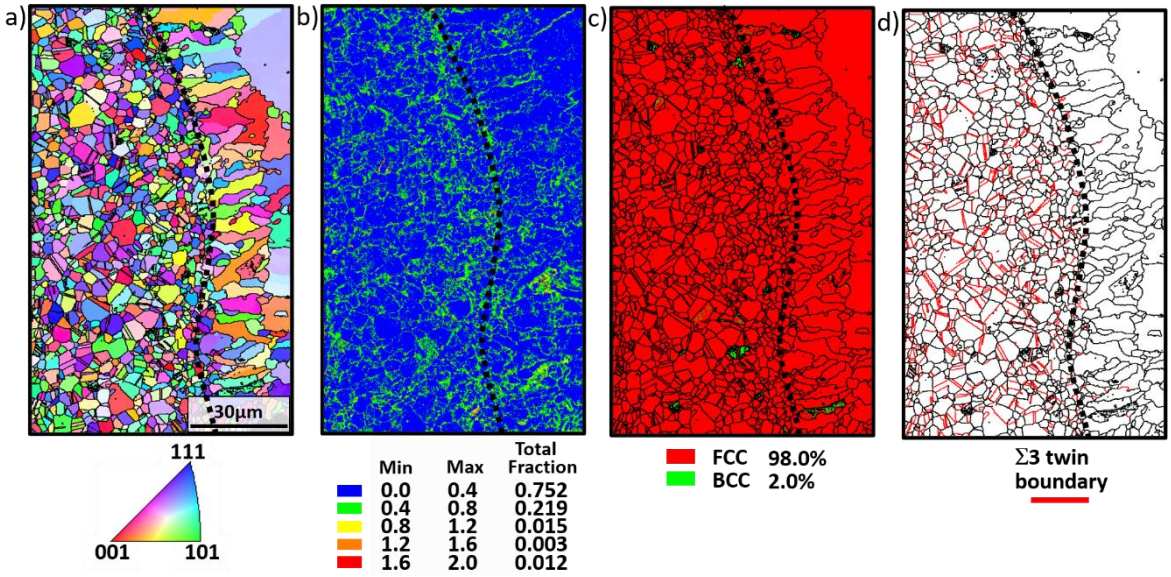

Figure 4-6. EBSD analysis of the HAZ/FZ interface: a) IPF map; b) KAM map; c) phase diagram map; d)∑3 twin boundaries map.

Within the center of the FZ, the previously fine equiaxed and columnar grains transform into coarse columnar grains that preferentially grew perpendicular to the fusion boundary (refer to Figure 4-2). Most grains at the edge of the FZ are oriented along the <0 0 1> and <1 0 1> preferred growth orientations, suggesting that grain growth in the <1 1 1> orientation is inhibited, this being attributed to the competitive grain growth mechanism occurring during solidification [167]. The evolution of the microstructure within the FZ is in line with the solidification theory of fusion welding [168], i.e., the larger cooling rate at the boundary of HAZ/ FZ, which is determined by the thermal gradient and growth rate product, promoted the formation of a small grain structure, which eventually turned into coarse columnar grains when the temperature gradient was reduced towards the weld centerline.

Although the FZ is again predominantly composed of FCC phase (≈ 96.0 %), a small amount of the previously reported BCC phase was also detected, as detailed in Figure 4-6 c). Although not detected by EBSD owing to the small volume fraction, it should be mentioned that σ phase was detected upon the use of synchrotron X-ray diffraction. The formation of σ phase within the FZ will be described together with the synchrotron X-ray diffraction data detailed in Figure 4-9 d).

No evidence of twins was observed in the bulk of the FZ (as depicted in Figure 4-2 and Figure 4-6 d)), due to the remelting and fast solidification experienced by the material, which would promote the development of a microstructure similar to that of casting processes [169]. Besides, it is worth mentioning that in the FZ, there is no driving force for annealing twins to be formed, since the thermal stresses resulting from the welding procedure are not conducive to the formation of these features.

Figure 4-7 a) to e) detail a large-scale EDS map performed across the FZ of the joint for the main elements (Co, Cr, Fe, Mn and Ni) that compose it. Figure 4-7 f) details the analyzed area, while the white dashed lines delimitate the HAZ/FZ interface, and the black dashed line corresponds to the local of the EDS line scan detailed in Figure 4-7 g). During fusion-based welding, elemental redistribution is a typical feature within the FZ. The molten pool behavior is dominated by complex patterns that derive from the Marangoni currents which depend, among other things, on the local temperature, composition and density. Moreover, the poor mixing between the base and filler materials can also lead to the formation of complex patterns across the FZ.

Overall, the EDS mapping results show a good mixture of different elements that compose both the CoCrFeMnNi BM and the ER-410 filler material, with a relatively uniform distribution of elements and no evidence of macrosegregation. The EDS line scan detailed in Figure 4-7 g), shows a significant Fe enrichment within the FZ compared to the BM. This was already expected owing to the fact that the ER-410 filler material is Fe-rich. The amount of Cr within the FZ is kept approximately the same compared to the BM, while the remaining elements evidence a decrease upon the dissolution of the filler material within the melt pool. The high temperatures experienced by the melt pool during welding can also aid in the preferential loss of certain elements. Mn loss can be favored due to its low melting and boiling points, as well as higher vapor pressure.

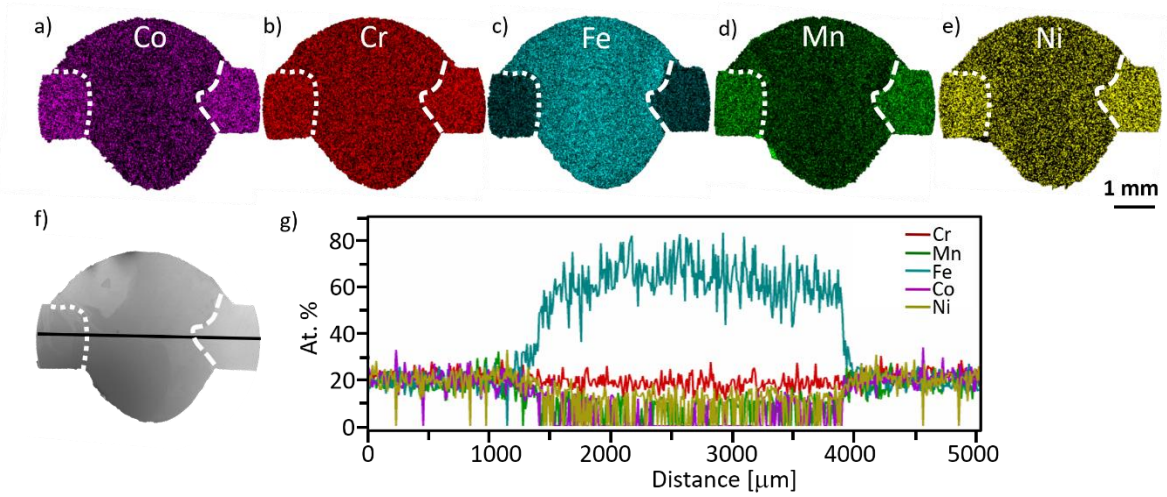

Figure 4-7. a) – e) EDS mapping of the welded joint; g) EDS line scanning across the weld along the black line of f).

As detailed when presenting the EBSD data, across the joint it was identified the presence of a secondary phase. To promote its identification EDS analysis was also performed. The morphology and composition maps obtained in representative regions of the BM, HAZ and FZ are detailed in Figure 4-8 a), b) and c), respectively. This data confirms the presence of Cr-Mn-rich oxides. In fact, the detection of such Cr-Mn-rich oxide particles in the CoCrFeMnNi HEA is common [170,171], which is mainly attributed to the potential contamination of the raw material, as well as oxidation occurring during the

casting procedure. Although both the top and bottom surfaces of the welded specimens were protected during the welding process using argon, this still did not avoid the formation of this phase in the FZ zone. This is common in arc-based processes, and is related to the high heat source dimensions and potential turbulent flow of the gas during the process. Previously, Kim et al. [172] investigated the high temperature oxidation behavior (between 900 and 1100 ^{o}C) of the CoCrFeMnNi HEA, and found that at high temperatures, Cr-Mn-based oxides are easily formed owing to the high affinity of these two elements with oxygen at those temperatures. The presence of such oxide particles detected in the FZ prove that at high temperatures, and even with the use of inert shielding gas, it is difficult to avoid the formation of such oxides in this HEA system. It should be mentioned that the presence of these oxide particles are not always detrimental to the mechanical properties of the material, as their volume fraction will play a role on the resulting mechanical performance [173].

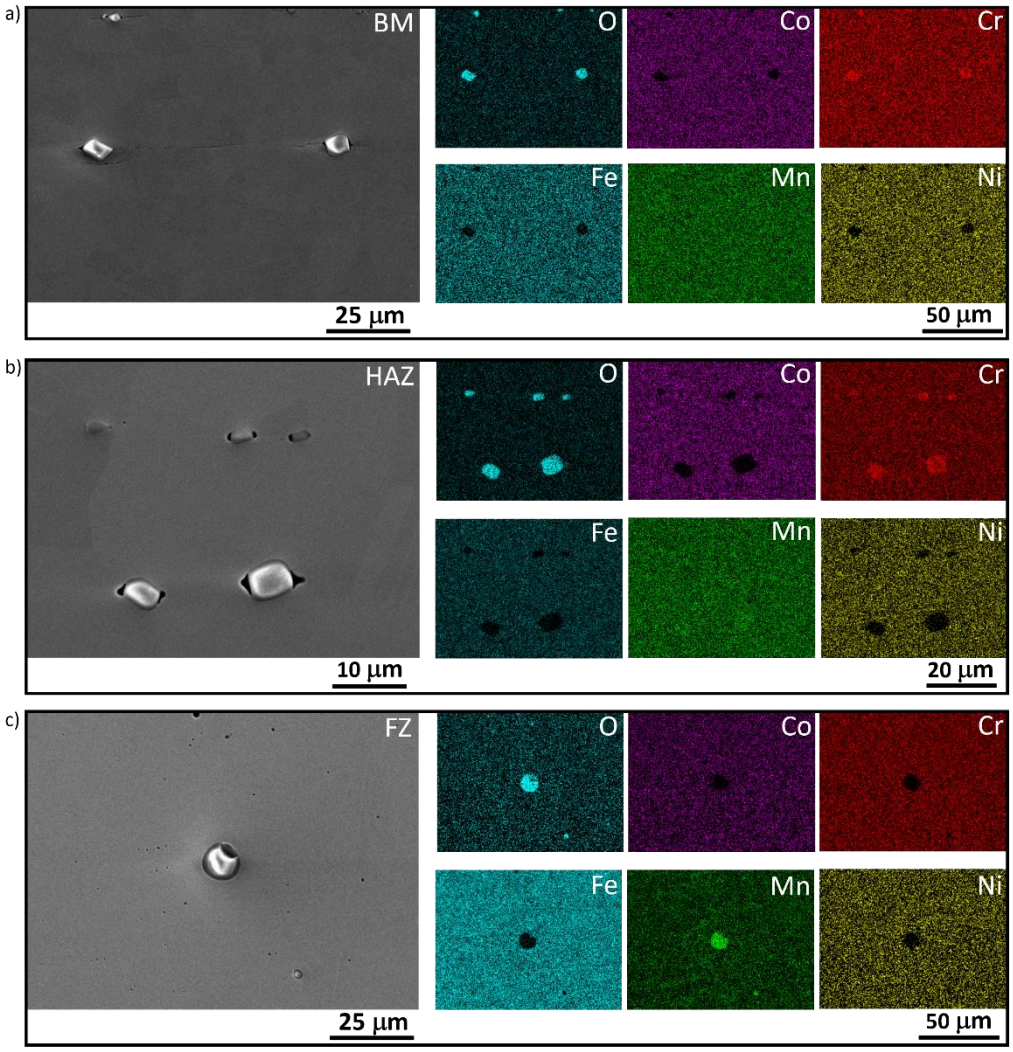

Figure 4-8. SEM images and corresponding EDS mapping of Cr-Mn-based oxides: a) BM; b) HAZ; c) FZ.

4.2.1.1 High energy synchrotron X-ray diffraction

Figure 4-9 a) depicts the superimposition of the X-ray diffraction patterns obtained at room temperature across the welded joint. To better understand the microstructural changes between the different regions, typical representative diffraction patterns for each region (BM, HAZ and FZ) are detailed in Figure 4-9 b) – d). The phase volume fractions, as obtained by Rietveld refinement, are depicted in Table 4-1. The effects of the weld thermal cycle on the existing phases and their volume fraction over welded joint are explored next in combination with the previous electron microscopy characterization data.

Overall, Figure 4-9 a) reveals minor microstructure variation among the BM and the HAZ regions, with evident changes occurring in the FZ. Considering the representative individual diffraction patterns depicted in Figure 4-9 b) - d) it is possible to observe the presence of Cr-Mn oxides in all three regions. Although the phase volume fraction of these Cr-Mn oxide particles increases slightly when determined using the diffraction data (1.3, 1.8 and 2.5 % in the BM, HAZ and FZ, respectively), it is expected that

these volume fractions do not have a detrimental effect on the mechanical performance of the welded joint [173]. Besides, the slightly higher volume fraction of these oxides in the FZ can be related to (minor) oxygen pick up during welding.

Besides the Cr-Mn oxide particles, only a disordered FCC phase was identified in the BM and HAZ regions, which is the typical microstructure of this material when it undergoes rolling or short to medium time heat treatments [174]. Interestingly, more phases formed in the FZ upon the addition and mixing of the ERNiMo-410 filler wire. In addition to the FCC matrix phase (≈ 96.3%) and the Cr-Mn oxides, it was identified the presence of another BCC phase (≈ 2.3%), as well as of σ phase (≈ 0.7%). The appearance of these two phases (BCC and σ) is the result of compositional differences caused by the dilution of the ER410-NiMo stainless steel filler wire with the BM, which translates into a different solidification behavior. Qin et al. [175] have studied the effect of the addition of Mo on the microstructure evolution of CoCrFeMnNi HEAs, and showed that the addition of this element can facilitate the formation of σ phase. Moreover, the addition of Cr, which exists in FZ coming from both the BM and filler wire, can aid in the formation of σ phase. Previous work by Zaddach et al., [176,177] have shown that when the Cr to Ni ratio increases, as it occurs in the bulk of the FZ zone, the formation of σ phase is enabled by the reduction of the material SFE. It is worth mentioning that the σ phase is not detected by EBSD due to its small volume fraction (≈ 0.7 %), showcasing the potential for high energy synchrotron X-ray diffraction to fine probe complex microstructures even for phases with residual volume fractions. The effect of the dilution rate of the ER410-NiMo martensitic stainless steel filler wire on the microstructure of the FZ will be discussed further in the thermodynamic calculations section.

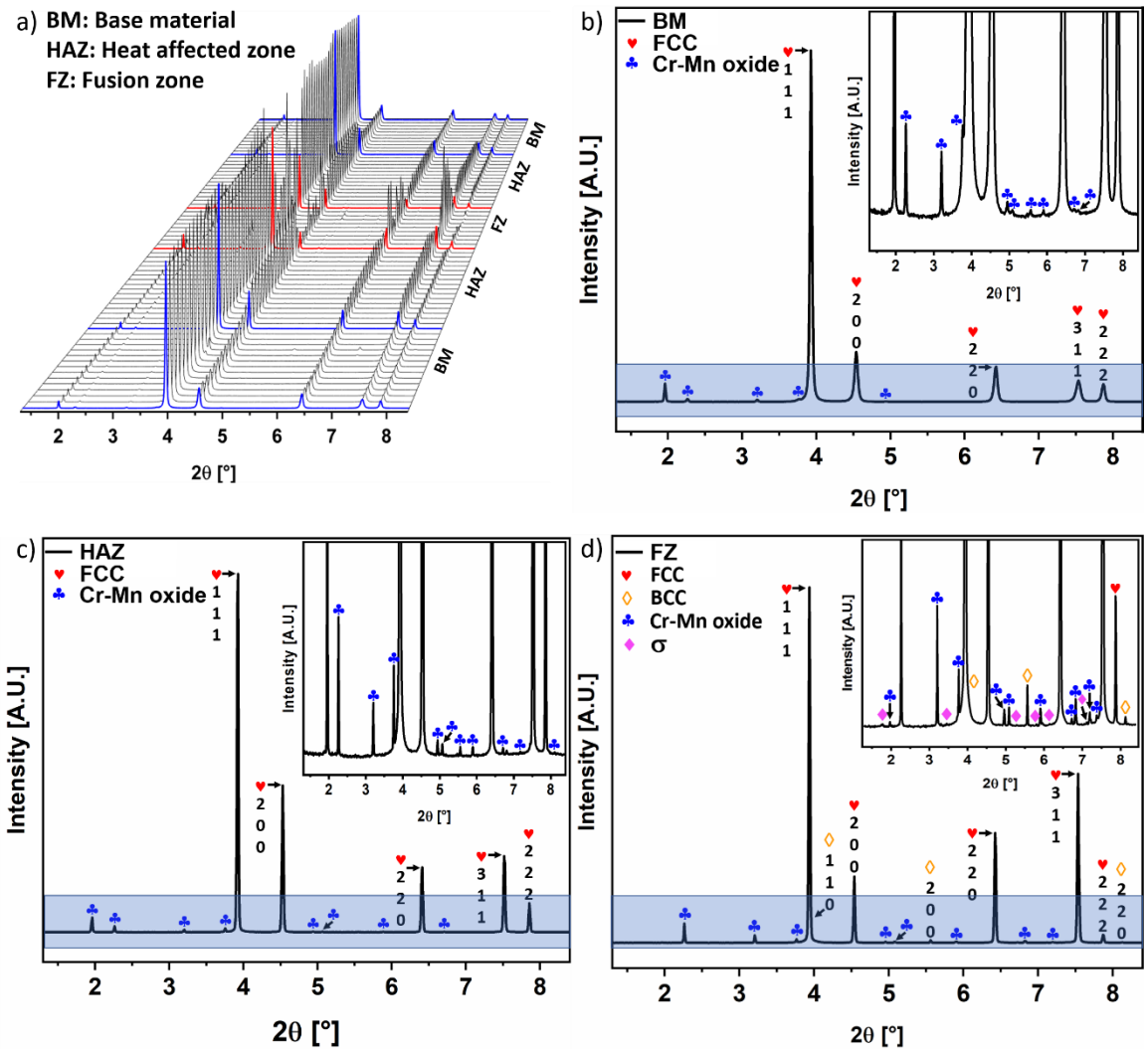

Figure 4-9. 3D plot and phase identification of existing phases within the welded joint using high energy synchrotron X-ray diffraction: a) superimposition of diffraction patterns across the welded joint; b), c) and d) are representative diffraction patterns from the BM, HAZ and FZ, respectively. The blue boxes highlight the inserts of a), b) and c) diffraction patterns.

Table 4-1 – Volume fraction evolution of the FCC, Cr-Mn oxide, BCC and σ phases across the welded joint as obtained by Rietveld refinement.

		Phase volume fraction [%]			
		Disordered FCC	Cr-Mn oxide	Disordered BCC	σ
Region	BM	~98.7%	~1.3%	-	-
	HAZ	~98.2%	~1.8%	-	-
	FZ	~94.5%	~2.5%	~2.3%	~0.7%

Since the FWHM of X-ray diffraction peaks is typically sensitive to both microstrain and grain size effects, the analysis of the FWHM of selected diffraction peaks along the welded joint can help to trace the effects of the weld thermal cycle on microstructural evolution [178]. Here, focus is given on the (2 2 0) and (3 1 1) diffraction peaks. The former was selected due to its relatively high intensity and lack of neighboring peaks that could interfere with the single peak fitting routine, while the latter was selected due to its insensitivity to intergranular stresses [80]. Moreover, taking advantage of the 2D diffraction images obtained during the synchrotron radiation diffraction measurements, it is possible to analyze the orientation dependence of certain microstructure features within the laboratorial reference frame. Thus, the raw data was integrated along the 0 and 90 º azimuthal angles, which correspond to the parallel and perpendicular directions of the welded joint, respectively, as previously indicated in Figure 3-7. Figure 4-10 details the variation of the FWHM along both directions and it can be observed that both have the same pattern, although the magnitude of the observed changes is distinct. The largest FWHM values are observed in the BM region, which confirms that the BM possesses high plastic strain arising from the rolling process. Moreover, it can be inferred that this region of the BM has a high dislocation density, since heavily deformed regions tend to show relatively broader diffraction profiles [179]. When entering in the HAZ, a significant reduction in FWHM is observed. Here, it is important to mention that the main factors contributing to a reduction of FWHM are coarse grain sizes, as well as decreased microstrain and dislocation density. Evidently, in the HAZ, recovery, recrystallisation and grain growth reduce the dislocation density and release the strain energy stored in the BM, which is predicted to induce a softening behavior at this location, except if strengthening phases are formed due to the weld thermal cycle. Interestingly, in the FZ, no diffraction peaks are observed in some regions, which is related to the large and highly oriented columnar grains which do not diffract for certain azimuthal orientations. This is referred to as a textural effect, which is a typical feature of the non-equilibrium solidification conditions experienced by FZ [67].

As it will be discussed later, the evolutionary trend of the FWHM and the hardness distribution (presented in Figure 4-10 and Figure 4-13) have almost the same profile. However, closer inspection reveals that the HAZ extension, as captured through the FWHM analysis, is slightly larger than that captured using microhardness mapping. This is related to the effect of the weld thermal cycle, which, in the low temperature HAZ, promotes the occurrence of recovery thus translating into less structural defects in the material, although without any appreciable change in the material microhardness [67]. Based on this and combining the distribution of hardness (Figure 4-13) and the evolution of the FWHM (Figure 4-10), the width of the HAZ is of ≈ 6mm (half of each side of the joint). Within the HAZ, the regions where recovery, recrystallization and significant grain growth occur have an extension of ≈ 1, ≈ 3.5 and ≈ 1.5 mm, respectively.

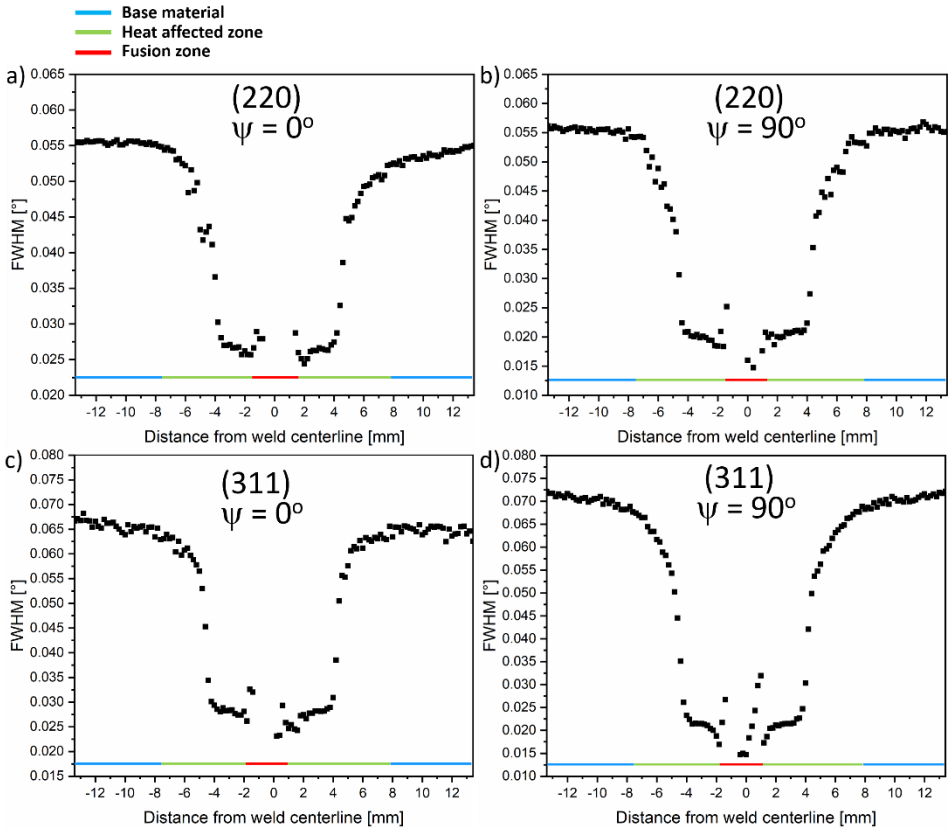

Figure 4-10. Evolution of the FWHM for the CoCrFeMnNi gas metal arc welded joints considering the (2 0 0) (Figure 4-10 a) and b)) and (3 1 1) (Figure 4-10 c) and d)) diffraction peaks integrated along the 0 and 90° azimuthal angles.

4.2.1.2 Thermodynamic calculations

To predict the effect of different dilution ratios (mixing ratio between the BM and filler material) on the solidification path experienced by the FZ, thermodynamic calculations were performed based on the Scheil-Gulliver model considering 10 % dilution steps. Here, 0 % dilution represents the FZ containing only ER410-NiMo stainless steel filler wire, while 100 % dilution corresponds to the FZ consisting only

of the CoCrFeMnNi HEA. As detailed in the experimental procedure, the role of C as a fast diffuser was also evaluated.

The potential solidification paths considering C as a fast diffuser are detailed in Figure 4-11 and it is clear that the solidification path is closely related to the dilution ratio of the ER410-NiMo filler wire. Nonetheless, regardless of the dilution considered, the FCC phase is always present. When the dilution ranges between 0 and 40%, i.e., when the ER410-NiMo stainless steel filler wire is predominant in the FZ, the phase structure formed by rapid solidification will include a BCC phase. When the dilution ratio varies between 40 and 60 %, σ phase formation is favored. Above these ratios, σ phase formation is inhibited.

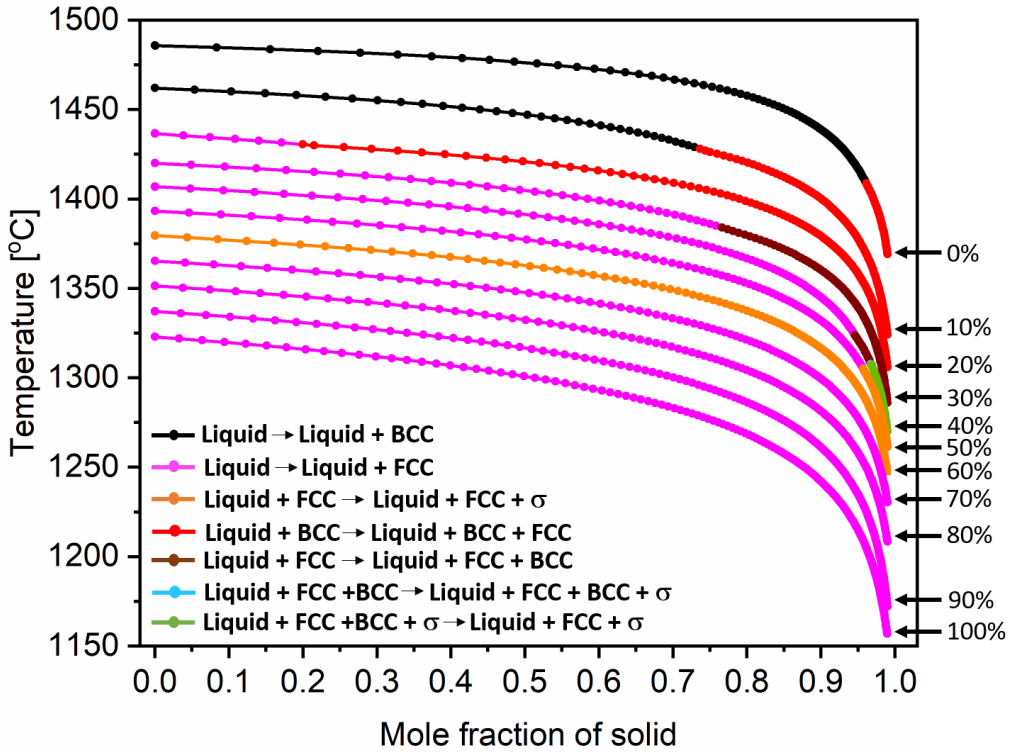

Figure 4-11. Scheil-Gulliver calculations for the CoCrFeMnNi HEA with ER410-NiMo filler wire welded joint considering different dilution conditions using C as a fast diffuser. 0% dilution rate corresponds to the ER410-NiMo martensitic stainless steel, while 100% dilution corresponds to the CoCrFeMnNi HEA.

As can be seen from Figure 4-12, the solidification path still varies with the variation of the dilution ratio. However, comparing withFigure 4-11, it can be noticed that the phases formed with and without C being selected as fast diffuser are different under the same dilution ratio. For example, for a 10 % dilution ratio, when C is selected as fast diffuser, the solidification path is Liquid → Liquid + BCC → Liquid + BCC + FCC (refer to Figure 4-11), but when C is not considered as a fast diffuser, the solidification path obtained is Liquid → Liquid + BCC → Liquid + BCC + FCC → Liquid + FCC + M_7C_3. Evidently, the dilution ratio of ERNiMo-410 filler wire and the diffusion rate of C are both influential factors for the phase

formation in the FZ. Nevertheless, when both conditions varied, the first phase to form (and that is kept during solidification) is the FCC. The BCC phase only appears for a dilution range between 0 and 40 %, suggesting that BCC phase was also independent of the C diffusion rate (refer to Figure 4-11 and Figure 4-12). Removing C as a fast diffuser, only enables the formation of the σ phase for 40 to 50 % dilution ratios, while only a single FCC phase is formed when the dilution ratio is above 50 %, which is slightly different from the results predicted when C was set as fast diffuser. The most significant difference is the predicted formation of M_7C_3 carbides for a wide dilution ratio range (0 to 50 %) when C was not selected a fast diffuser. When this element was imposed a fast diffuser no carbides where thermodynamically predicted. It is worth mention here that thermodynamic calculations predict that the σ phase that is formed in the FZ will be Fe-Cr- or Cr-Mn-rich. EDS mapping near one particle of this phase, detailed in Figure 4-13, shows an enrichment in both Cr and Mn, which further validates these thermodynamic calculations.

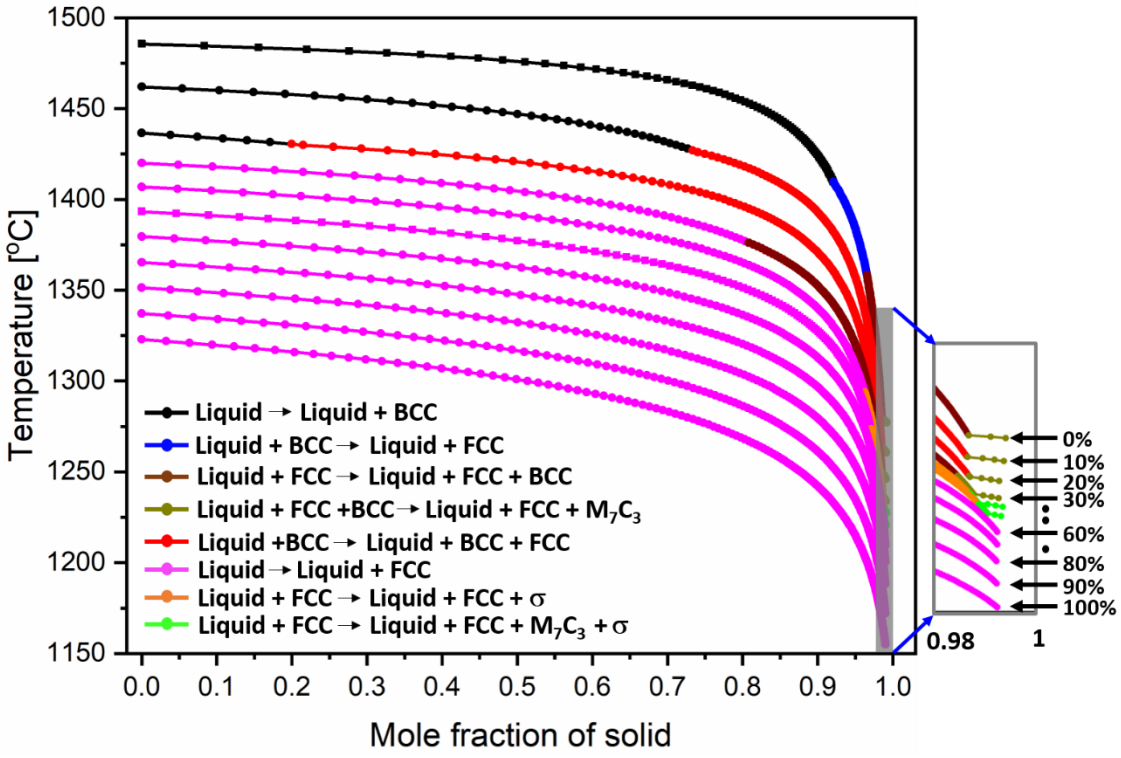

Figure 4-12. Scheil-Gulliver calculations for the CoCrFeMnNi HEA with ERNiMo-410 filler wire welded joint considering different dilution conditions without C as a fast diffuser. 0% dilution rate corresponds to the ERNiMo-410 martensitic stainless steel, while 100% dilution corresponds to the CoCrFeMnNi HEA. The grey box details a close-up view of the solidification paths for mole fraction values above 0.98.

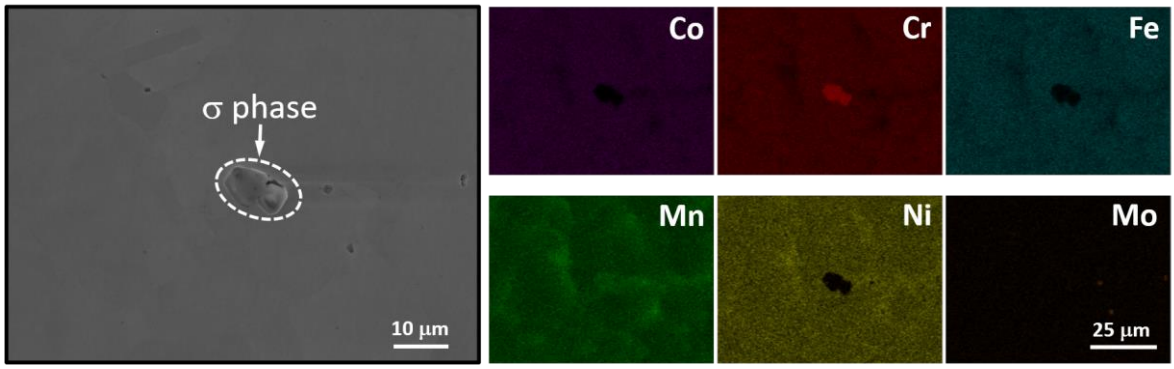

Figure 4-13. SEM images and corresponding EDS mapping near one particle of σ phase.

Importantly, coupling of the synchrotron X-ray diffraction data (shown in Figure 4-9 d)) enables to confirm that the most likely solidification path is that obtained when considering C as a fast diffuser. In fact, no evidence of M_7C_3 across the FZ was observed. Thus, the predicted phases using the Scheil-Gulliver model with C set as a fast diffuser are in good agreement with the high resolution diffraction data obtained.

4.2.1.3 Mechanical behavior

Microhardness mapping was performed on the welded joints to further investigate the relationship between the microstructure and local strength across the welded material. Figure 4-14 a) details the 2D microhardness map of the whole welded joint, identifying the three regions of the joint (BM, HAZ and FZ). The results show that the hardness values of the BM, HAZ and the FZ differ significantly, with a U-shaped distribution trend.

The BM has the highest hardness of about ≈ 400 HV0.5, which is due to the strain hardening imposed by cold rolling. Here, it is worth mentioning that the hardness of the BM used in this work is slightly higher than that reported in [161], which is related to the location from where the BM sheets were removed after rolling [180]. When entering the HAZ, the material starts to exhibit a softening behavior, and the hardness decays from ≈ 400 to ≈ 150 HV0.5. This reduction in hardness is attributed to the thermal cycle experienced by the HAZ, which promotes an annealing-like heat treatment promoting both grain recrystallization and growth. However, the extent of these two solid state transformations differs depending on distance to the heat source. Thus, closer to the BM, the prevalence of recrystallization with associated minor grain growth leads to a reduced decrease in the material hardness, within the 250 to 350 HV0.5 range, whereas closer to the FZ grain growth overturns recrystallization as the main solid state transformation leading to an abrupt decrease in hardness down to 150 HV0.5. However, the lowest hardness across the joint (≈ 125 HV0.5) occurs in the FZ. The average hardness across the FZ is similar to that of as-cast CoCrFeMnNi HEAs [155]. This suggests that the different composition induced by the mixing of the filler material within the FZ is not conducive to an evident solution strengthening. It should be stated that the large grain size of the FZ also aids in the development of low hardness at this location,

as known from the Hall-Petch effect. In addition, small fluctuations in microhardness were observed in the FZ, which may be related to complex composition changes induced by the chaotic fluid flow typical of fusion-based welding processes. Based on the above analysis, it can be concluded that the variation in the hardness distribution in the welded joints is closely related to the homogeneity of the microstructure, degree of recrystallization and grain size evolution, as well as dislocation density.

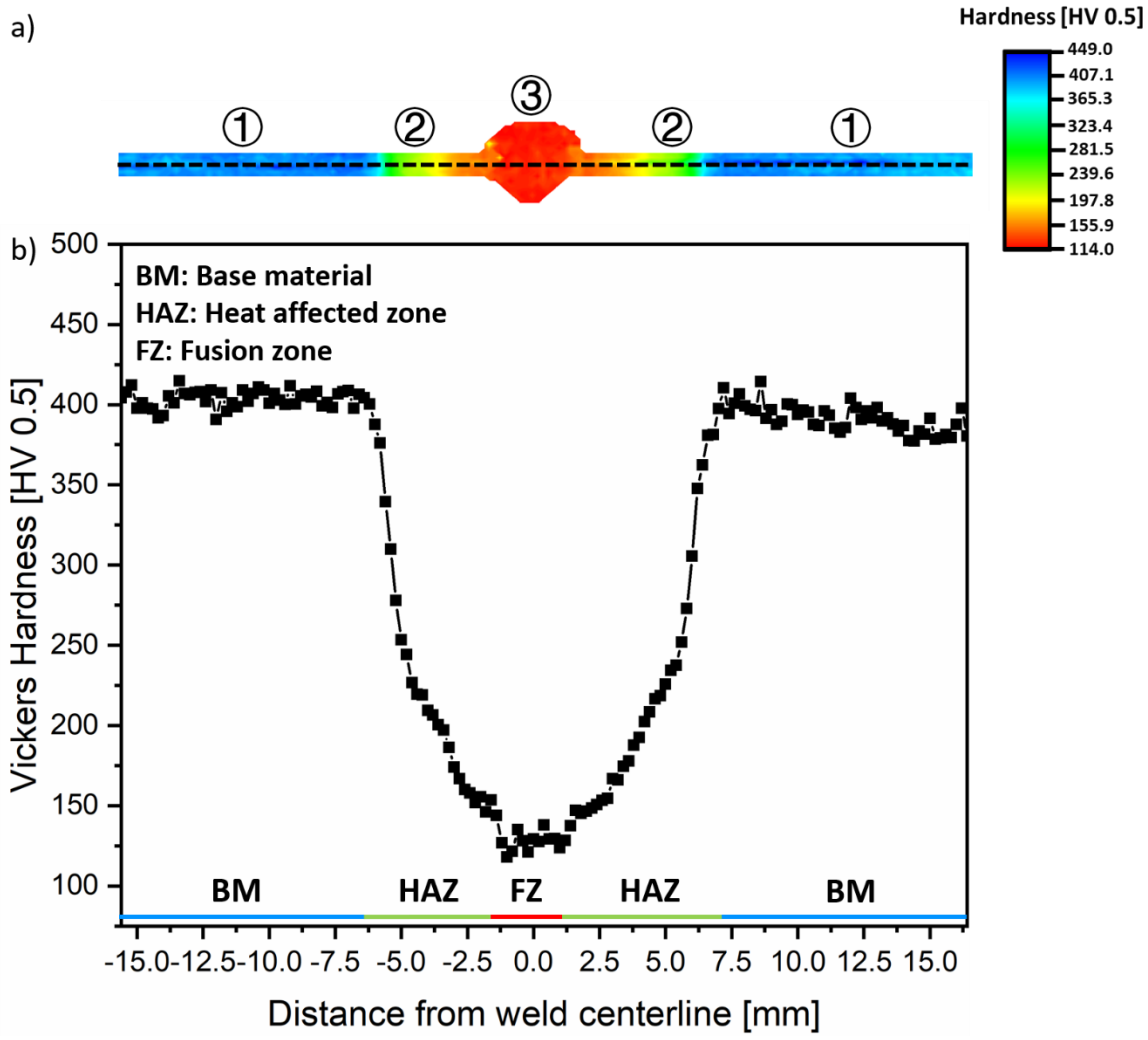

Figure 4-14. a) Microhardness map across the welded joint; b) microhardness profiles obtained at the middle of the joint (black dashed line across the hardness map of a)).

To evaluate the effect of the addition of the ER410-NiMo filler wire on the joint mechanical properties, the stress-strain curves of the gas metal arc welded joints obtained with the ER410-NiMo filler wire were benchmarked against gas tungsten arc welded joints obtained without addition of filler wire (with the latter welds being done by the present research team as detailed in [67]), as depicted in Figure 4-15. The solid line represents the engineering strain-stress curves. A summary of the mechanical properties (yield strength, ultimate tensile strength and ductility) is shown in Table 4-2. Comparing the tensile mechanical behavior of the two welded joints, it can be seen that the welded joint with the addition of

filler wire is clearly superior to the tungsten inert gas welded joint in terms of both yield strength (355 vs 284 MPa) and ultimate tensile strength (641 vs 519 MPa). This is mainly attributed to the excess weld metal introduced by the added filler wire (refer to Figure 4-2) [181], which increases the cross-sectional area of the FZ, resulting in a location where the stress per unit area under the same tensile external load is significantly lower than that imparted in the BM and HAZ. Thus, the presence of weld face/root reinforcement promotes an overall increase in both the yield and tensile strength of the gas metal arc welded welded joint compared to the filler-free welded material. Although, the face and root reinforcements can aid in increasing the stress imparted by the material, it can also promote stress concentrations, especially at the weld toe. This can make crack initiation and propagation at those locations easier thus accelerating joint fracture. This can be the reason for the reduced fracture strain of the joint. Nonetheless, the gas metal arc welded joint still exhibits a relative higher fracture strain with potential to be considered for structural applications. It should be mentioned here that, due to the scarcity of samples, no comparative study of the mechanical properties of the joints after removal of the face/root reinforcement was carried out. Therefore, studies in this direction were not included in this work. However, in the future, further studies will be carried out on this. Also, the Young modulus shown from the tensile strain-stress curve is not accurate because of the aging problem of the tensile machine used, thus the young modulus for both BM and as-welded joints will not discussed here.

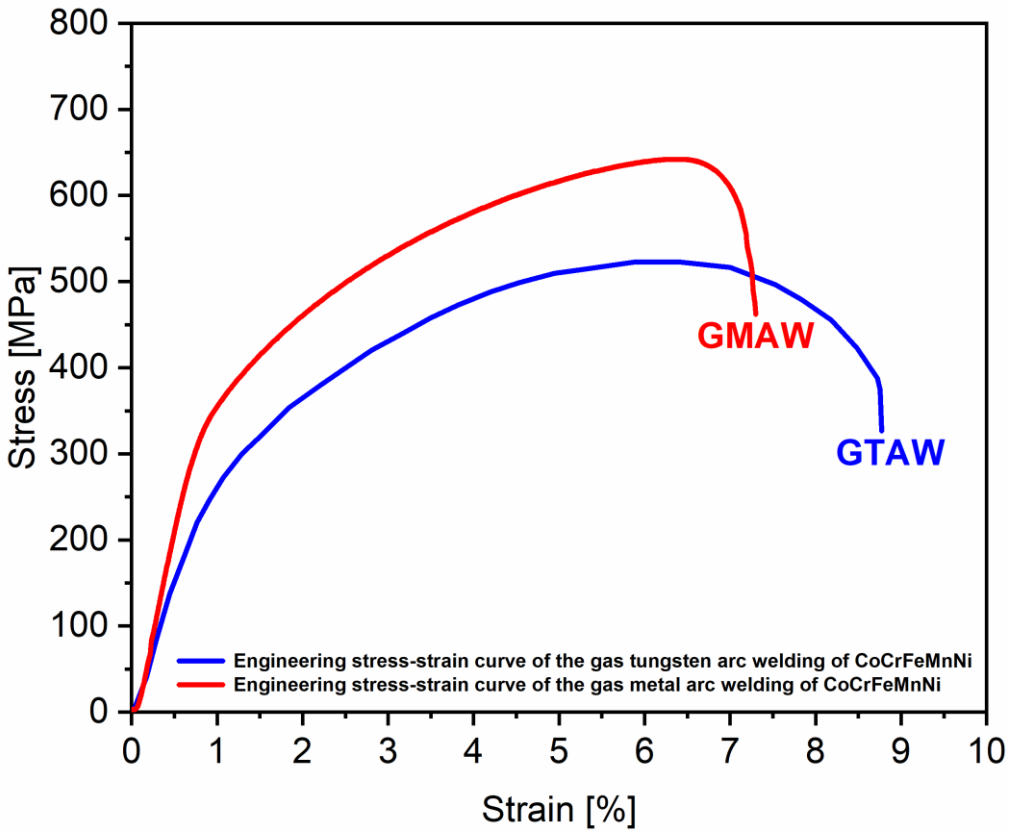

Figure 4-15. Representative stress-strain curves of a gas tungsten arc welded CoCrFeMnNi (obtained from [67]) and gas metal arc welded CoCrFeMnNi with ER410-NiMo filler material.

Table 4-2 – Summary of tensile properties of BM, gas tungsten arc welded CoCrFeMnNi (obtained from [67]) and gas metal arc welded CoCrFeMnNi with ER410-NiMo filler material.

Sample	Yield strength [MPa]	Ultimate tensile strength [MPa]	Elongation [%]
BM (from [67])	587 ± 7	943 ± 6	9.5 ± 0.2
Gas tungsten arc welded joint with no filler wire (from [67])	284 ± 4	519 ± 3	8.4 ± 0.4
Gas metal arc welded joint with ER410-NiMo filler wire	355 ± 10	641 ± 7	7.3 + 0.2

Figure 4-16 a), b), c) and d) detail DIC snapshots taken at different stages of deformation, namely during elastic deformation, macroscopic yielding, uniform plastic deformation and right before fracture, respectively, showing the strain distribution along the joint. During the elastic deformation stage (refer

to Figure 4-16 a)), the deformation is uniform over the welded joint and the maximum local strain is small. When macroscopic material yielding occurs (refer to Figure 4-16 b)), there is a significant increase in the maximum strain, ($\varepsilon \approx 1.1\%$), but the differentiation between the BM, HAZ and FZ is not obvious. When entering the uniform plastic deformation regime (refer to Figure 4-16 c)), significant stress concentration at the HAZ/FZ interface is observed, where a maximum local strain of 5 % is reached. Prior to fracture of the material (refer to Figure 4-16 d)), the BM, HAZ and FZ regions of the welded joint can be clearly distinguished, as the strain concentration at the HAZ/FZ interface is now significant. By combining this mechanical response information with the previous microstructure characterization, it can be inferred that the stress concentration observed in the strain map prior to failure is due to the joint reinforcement (refer to Figure 4-16 a)). Failure initiated at the weld toe propagating along the HAZ/FZ interface. Thus, the one reason for fracture occurring at this location is related to a stress concentration effect caused by the excess of material in the FZ. Although not discussed due to lack of available material, it is possible to further tune the welding process parameters to obtain smoother reinforcement profiles, which can then help to alleviate the stress concentration issues and aid in obtaining improved mechanical properties of the joint, especially in what concerns its ductility. Another responsible cause is the microstructural changes, this can be inferred from the hardness measurement results, to be more specific, after enter the HAZ, the material shows a tendency to soften until it reaches the minimum value of hardness. These softening effects cause the material to transfer the loading to these softened regions first during the deformation process until failure. Combined with the geometrical defects as mentioned above, the interaction of the two main reasons leads to the fracture eventually occurring at the weld toe.

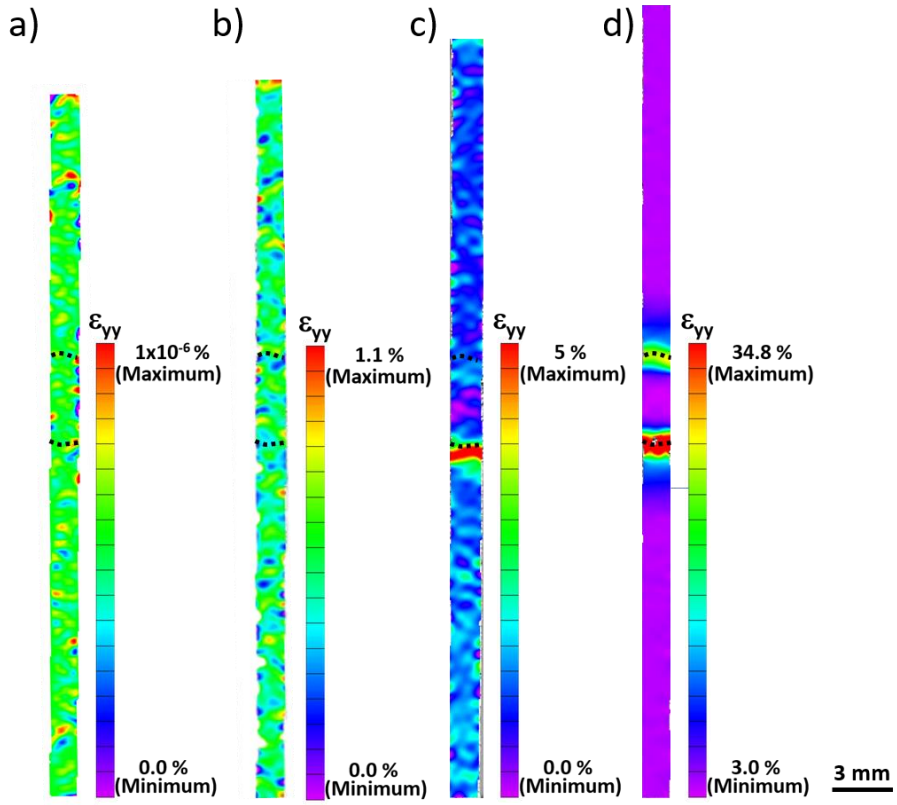

Figure 4-16. DIC snapshots obtained at different loading steps during: a) macroscopic elastic deformation; b) macroscopic yielding; c) uniform plastic deformation; and d) before joint fracture.

To gain a more detailed understanding of the mechanical behavior of the different regions over the welded joint during tensile testing, the raw DIC data was further processed to determine the stress-strain curves of the BM, HAZ, weld toe (fracture initiation location) and FZ. These results are shown in Figure 4-17, where the black, pink, red and blue lines represent the local tensile stress-strain curves for each of these four regions.

Each region shows different mechanical behavior, which is mainly caused by two factors. The first is due to changes in microstructure caused by the weld thermal cycle. The second is attributed to the shape-related defects due to the face/root reinforcement in the FZ which favors the occurrence of preferential stress concentrations.

Considering the total deformation imparted by each region, it is observed that the BM only deformed by ≈ 1.8% before joint failure occurred. This is related to the strain hardening experienced by the material prior to welding. Hence, the onset for plastic deformation to occur is delayed compared to the remaining softer regions of the joint. This means that there is a load partitioning effect, where the low hardness regions will be preferentially deformed during loading of the welded joint. Despite being the softer region, the strain in the FZ is only around 4.8 %. This significantly contrasts with the strains measured in the HAZ region (up to 16.8 %) and near the weld toe (32.0 %) where failure occurred. This is an apparent

contradiction when considering the local hardness and the likely stress distribution during mechanical loading. In fact, this is not surprised, since this is related to the addition of the ER410-NiMo filler metal which increases the effective cross-sectional area in the FZ (refer to Figure 4-16 a)) by comparison with welding processes without addition of filler material. Looking at the cross-sectional area of the FZ, it is observed that this region is almost three times larger than in the remaining joint, leading to a smaller force per unit area imparted by the FZ under the same external tensile loading. Consequently, the plastic deformation over the whole FZ region will be reduced, causing the amount of deformation in the softer FZ region to be lower than that in the HAZ region and near the weld toe site. However, the amount of deformation in the FZ region is still slightly higher than that of the BM (4.7 vs 1.8 %), which suggests that the significantly higher hardness in the BM (400 vs 125 HV0.5) prevails in resisting to plastic deformation. Conversely, the amount of deformation at the weld toe site reaches its maximum at fracture, approximately 32.0%, as a result of the stress concentration acting on the smaller cross section area and relatively softer region (compared to the BM).

Based on the stress-strain curves of the different regions of the joint shown in Figure 4-17, the load transfer behavior can also be predicted. Specifically, at the onset of deformation, the FZ is the softest region and takes on more load. When it starts to yield, the FZ and the weld toe site also consecutively yield, while the BM region is still only being elastically deformed due to the previous strain hardening. Theoretically, with further deformation, the load should be transferred to the BM, owing to the strain hardening occurring at the remaining regions. However, due to the presence of face and root reinforcement in the welded joint, stress concentration points are easily enabled thus promoting the preferential local deformation at the weld toe as shown in Figure 4-17. In addition, the microstructural changes as we can infer from the hardness distribution (refer to Figure 4-14) in the HAZ, weld toe and FZ, suggesting that the material in these regions are much softer than in the BM. Therefore, after the FZ, HAZ and weld toe have yielded, there is not a significant load transfer to the BM region.

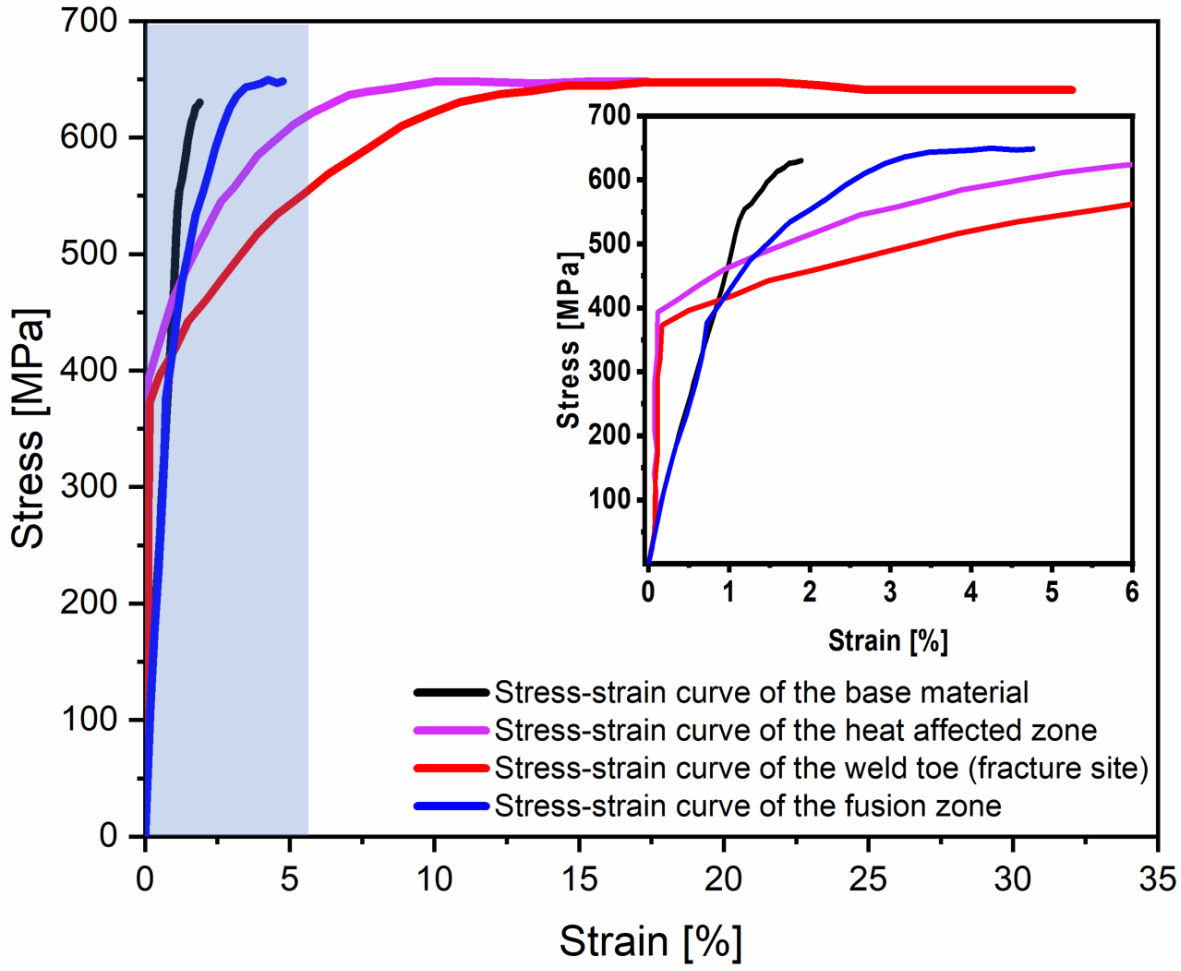

Figure 4-17. Tensile curves obtained from the DIC measurements for different regions across the joint: BM (black line), HAZ (pink line), weld toe (red line) and FZ (blue line). The light blue region is zoomed in the insert.

Figure 4-18 details a SEM image of fracture surface of the welded joint. It is well know that dimples are the primary feature associated to ductile fracture in polycrystalline metals in [182]. Here, a large number of dimples with various diameters were observed, which agrees well with the good plasticity of the welded joint, as detailed by the tensile and DIC data. Minor particles are observed sparsely distributed. These particles correspond to the previously identified Cr-Mn-based oxides [31].

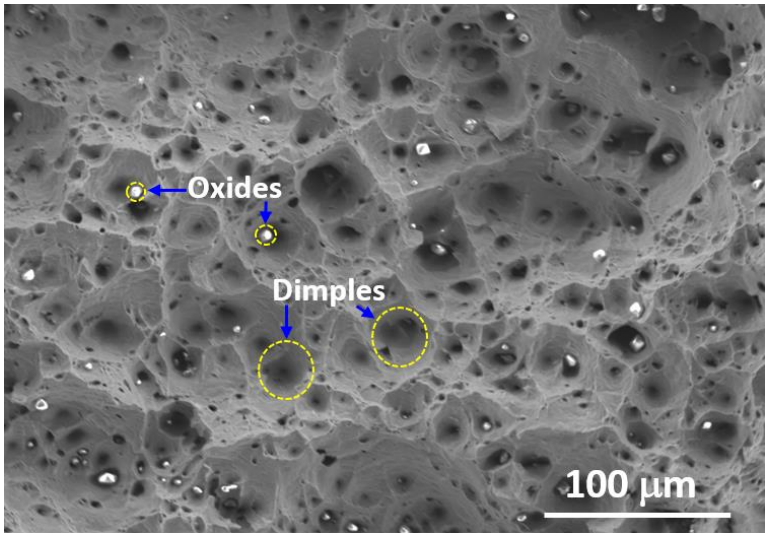

Figure 4-18. Fracture surface of the CoCrFeMnNi gas metal arc welded joint with ER410-NiMo filler.

4.2.1.4 Conclusions

In this work, GMAW of CoCrFeMnNi HEA using ER410-NiMo stainless steel filler wire was performed. By combining advanced material characterization, thermodynamic calculations, X-ray synchrotron diffraction and mechanical testing, a connection between the microstructure and mechanical properties of welded joints is established. The following main conclusions were drawn:

1) A gas metal arc welded joint of CoCrFeMnNi HEA using ER410-NiMo stainless steel filler wire was obtained eventually without welding defects.

2) The thermal cycle influenced the recrystallization and grain growth phenomena experienced in the HAZ, promoting different softening effects (in terms of magnitude). Particularly, in the low temperature HAZ there was only a moderate decrease in hardness, whereas in the high temperature HAZ an abrupt decay was observed. The composition change of the FZ was not conducive to a solid solution strengthening effect.

3) High energy synchrotron X-ray diffraction was used to determine the phase constituents within the FZ, while thermodynamic simulations were employed to predict the effect of different dilution ratios. A good agreement was obtained when considering C as a fast diffuser in the Scheil-Gulliver calculations.

4) Analysis of the FWHM evolution analysis along the joints revealed that the actual extension of the HAZ is slightly larger than that obtained considering both electron microscopy and microhardness measurements. This is due to recovery of the heavily cold rolled BM which occurs in the low temperature HAZ.

5) The gas metal arc welded CoCrFeMnNi joints with ER410-NiMo filler wire exhibited an increase in tensile strength (641 vs 519 MPa) but a slight decrease in elongation (7.3 vs 9.5 %) compared to gas tungsten arc welded CoCrFeMnNi joints without the addition of filler wire. The good strength and ductility of these joints open the door for the potential application of GMAW of CoCrFeMnNi HEAs for industrial-oriented applications.

6) Non-contact DIC was used to obtain local stress-strain curves for different regions of the joint, confirming the existence of preferential strain concentrations at the weld toe interface site where fracture initiates. The local mechanical response is in good agreement with microstructure features observed across the welded joint.

4.2.2 Gas metal arc welded CoCrFeMnNi joints with a 308 stainless steel

4.2.2.1 Microstructure evolution

Figure 4-19 a) depicts the EBSD map of the joint cross section, detailing a defect-free and full penetration joint. Distinctive microstructural features are observed across the joint, and these are discussed next. The BM experienced cold rolling prior to welding, and the grain structure is composed of pancake-like grains with a width of approximately 2 μm, as previously shown in [67]. Entering the HAZ (refer to Figure 4-19 b)), the pancake-like grains are replaced by equiaxed grains and the grain size increases to ≈ 15 μm (in the low temperature HAZ) and to ≈ 53 μm (in the high temperature HAZ). The above changes in microstructure and the coarsening of the grain structure are related to the weld thermal cycle, which resembles the effect of a low and high temperature heat treatment for a short time period. Closer to the BM, i.e., in the low temperature HAZ, recovery and recrystallization phenomena are predominant and justify the small equiaxed grains observed at this location. Closer to the FZ, i.e., in the high temperature HAZ, recrystallization but especially grain growth are the predominant solid-state phenomena, thus in good agreement with the larger grain size observed when approaching the fusion boundary.

Several $\sum 3$ twins were observed in the low temperature HAZ (refer to Figure 4-19 b) (middle)), which was induced by a combination the high prestored strain energy within the BM and the heat imposed to this region of the material during welding. Approaching the fusion boundary, the grain boundaries and annealing twin boundaries move rapidly during the grain growth process, which engulfs the original twin boundaries, leading to a gradual reduction in the fraction of $\sum 3$ twins until they fully disappear upon entering in the FZ. Here, fine equiaxed and columnar grains nucleate from the cold substrate (at the HAZ/FZ interface) with competitive growth towards the weld centerline. Moving away from the cold substrate toward the weld centerline there is preferential formation of coarse columnar grains (refer to Figure 4-19 a)), due to the reduction of the temperature gradient, G, to growth rate, R, product. Figure 4-19 b) (bottom) reproduces the evolution of KAM of the joint, while Figure 4-19 c) and d) detail the KAM

and Geometrically Necessary Dislocation (GND) values for different regions across the joint. The BM possesses the highest KAM and GND values due to the large plastic deformation resulting from the previously imposed cold rolling. However, upon the introduction of heat during welding, the stored strain energy arising from the cold rolling will aid on the solid-state transformations that were previously mentioned (recovery, recrystallization and grain growth), with the amount of necessary heat for these transformations to occur being lower with higher stored strain energy.

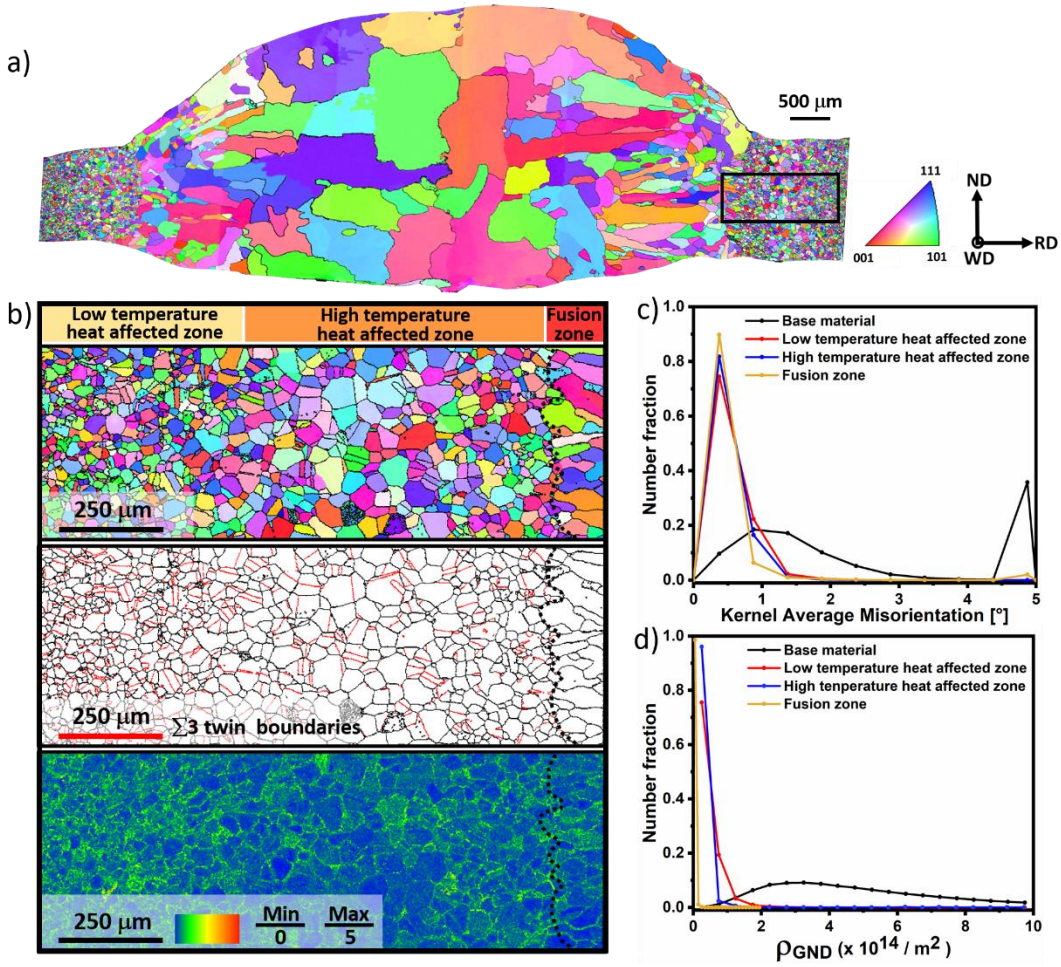

Figure 4-19. a) EBSD map of the gas metal arc welded CoCrFeMnNi joints with ER308LSi filler material; b) IPF, Σ3 boundaries and KAM (top, middle and bottom, respectively) EBSD maps of the HAZ1 up to the interface with the FZ; c) and d) variation of KAM and GND values with respect to the different regions of the joint, respectively.

4.2.2.2 High energy synchrotron X-ray diffraction

To further understand the impact of the welding process on the existing phases, high energy synchrotron X-ray diffraction was used to scan the sample. Representative X-ray diffraction patterns of the BM, heat affected and fusion zones are depicted in Figure 4-20. Most of the low intensity diffraction peaks correspond to Cr-Mn-based oxides and are observed all along the joint. These oxides are easily formed in the Co-Cr-Fe-Mn-Ni system due to potential contamination of the raw material and oxidation during

the casting process of the BM, as detailed in [170]. In the FZ, the higher temperatures experienced by the material further exacerbate the potential for oxidation to occur, which is aided by the strong affinity of both Cr and Mn with O [172], which explains the presence of these oxides at this location of the joint. Rietveld refinement of the diffraction data revealed that the oxides volume fraction in both the BM and HAZ is ≈ 2.5%, while in the FZ reaches ≈ 3.1%, with this increase justified by the extremely high temperatures developed in the FZ. In both the BM and HAZ (refer to Figure 4-20 a) and Figure 4-20 b), respectively) aside from the Cr-Mn oxides, these regions are composed by a disordered FCC phase, as typical of this material. In the FZ, the composition change induced by the addition of the 308 stainless steel filler material leads to present of other phases. In fact, aside from the previously identified disordered FCC phase and oxides, the FZ shows evidence of a disordered BCC (≈ 2.17%) and σ phases (≈ 0.77%).

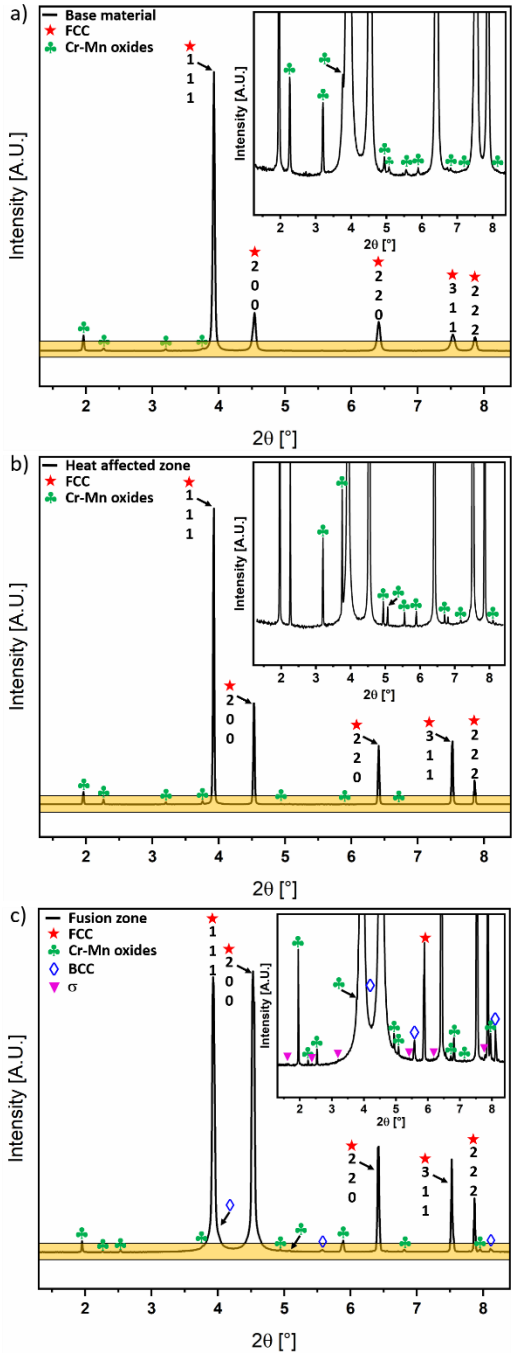

Figure 4-20. Representative diffraction patterns from the: a) BM; b) HAZ; d) FZ. The yellow boxes highlight the inserts used to detail the low intensity peaks captured.

4.2.2.3 Thermodynamic calculations

To further investigate the effect of dilution of the filler material on the solidification phases and solidification temperatures range, the Scheil-Gulliver model was used considering dilution steps of 1%. These results are detailed in Figure 4-21.

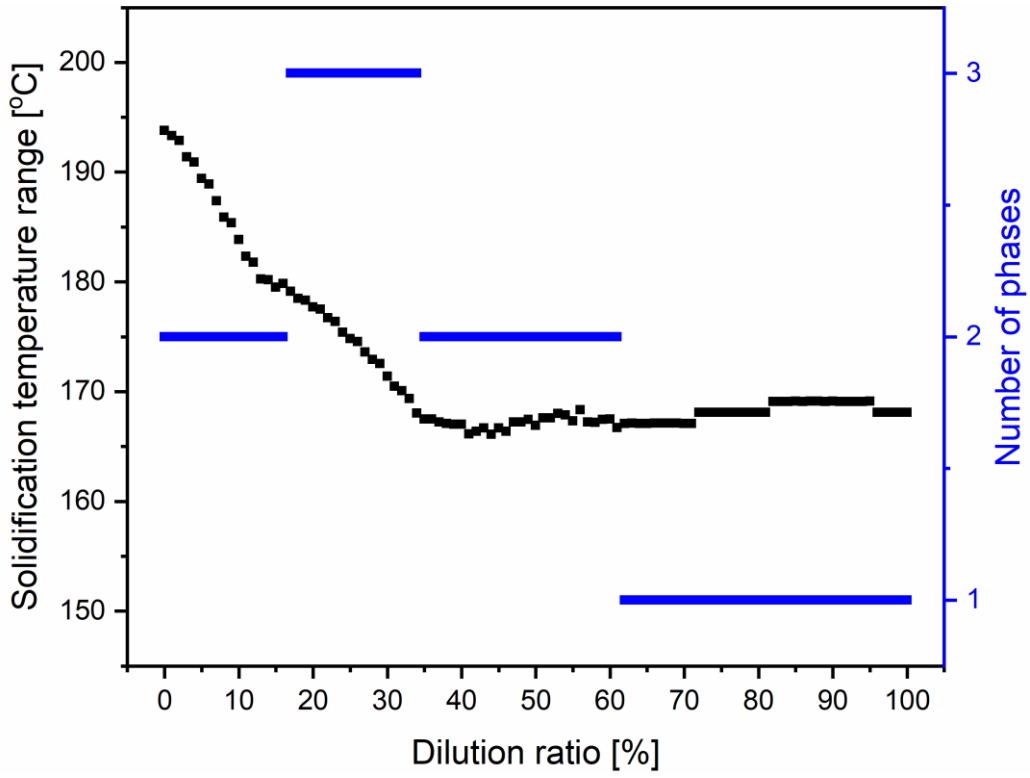

Figure 4-21. Thermodynamic calculations performed using the Scheil-Guliver model considering different dilution conditions as a function of number of existing phases at the end of solidification (blue lines) and solidification temperature range (black dots). A 0% dilution ratio corresponds to the 308 stainless steel filler, while a 100% dilution ratio corresponds to the CoCrFeMnNi BM.

When the dilution ratio ranges between 0 to 18% and 35 to 61%, the predicted solidification paths are Liquid + FCC → Liquid + BCC + FCC and Liquid + FCC → Liquid + FCC + σ, respectively. Thus, for these ranges of dilution, two phases are predicted to be formed. For the 19 to 34% range, FCC, BCC and σ phases are predicted, but equally contain two different solidification paths, Liquid + FCC → Liquid + BCC + FCC → Liquid + FCC + σ and Liquid + FCC → Liquid + BCC + FCC → Liquid + BCC + FCC + σ → Liquid + FCC + σ. When the dilution is above 60%, only FCC phase is predicted and the solidification path is Liquid → FCC. It is thus evident that the formation of σ and BCC phases are closely related to the dilution ratio: when the 308 filler is dominant, two (FCC and BCC) or three phases (FCC, BCC and σ) are expected in the FZ.

Although not shown here, the BCC phase is Fe- and Cr-rich, with its molar content ranging between 36.63 to 50.10% and 34.84 to 35.54%, respectively, depending on the dilution ratio. Since these

elements are predominant in the filler material, it is thus clear the role of dilution on the potential formation of the BCC phase. The formed σ phase will be rich in both Cr (37.41 to 42.29 at. %) and Fe (28.70 to 37.13 at. %), as well as in Mn (9.01 to 18.37 at. %), again, depending on the FZ dilution.

Attention must also be paid to Mo, which composes the 308 filler material. Mo can promote the transformation from a single FCC phase structure to a mixture of FCC and BCC phases, while favoring the formation of σ phase in the Co-Cr-Fe-Mn-Ni system [175,183]. From our thermodynamic calculations, molar percentages of 1.81 to 1.87% and 2.81 to 3.07% of Mo can promote the formation of BCC and σ phases, respectively. These thermodynamic predictions are validated by the diffraction data previously presented.

The solidification temperature range of fusion-based welded joints has a significant effect on the cracking susceptibility. As can be seen in Figure 4-21, the solidification temperature ranges from 154 to 171 °C. Although mixing of the BM and 308 filler wire changes the solidification temperature range of the molten pool, it does not vary considerably. Nevertheless, it still has a clear correlation with the number of phases being formed. In the relatively high solidification temperature range, only FCC or FCC + BCC is predicted, while FCC + σ are predicted in the lower solidification temperature range.

4.2.2.4 Mechanical behavior

Figure 4-22 a) and b) depict the hardness mapping of the welded joint and a line scan obtained at the middle height, respectively. Figure 4-22 c) presents the average grain size variation in the BM, HAZ and FZ.

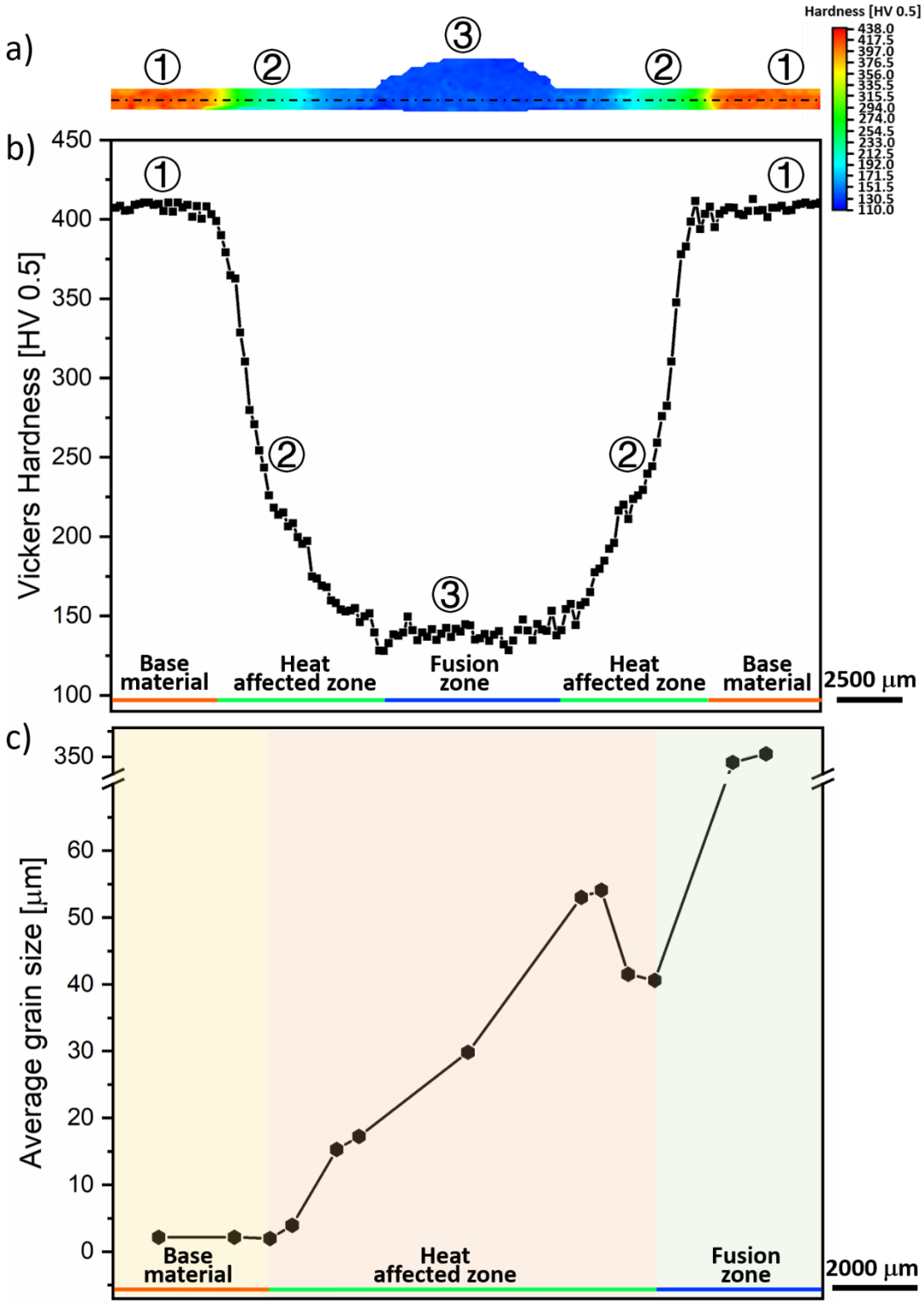

Figure 4-22. a) Microhardness map across the welded joint; b) microhardness profile obtained at the middle height of the joint (black dashed line in a); c) average grain size evolution across the joint.

The as-rolled BM has the highest hardness, averaging 408 HV0.5 (region 1). Upon entering the HAZ, a continuous decrease in hardness is observed when progressing toward the FZ interface. While in the

low temperature HAZ the hardness decreases to 408 HV0.5, in the high temperature side the drop is more significant to 151 HV0.5. This decrease in hardness is related to the effect of the weld thermal cycles on the microstructure condition, where recrystallization and grain growth promote to a decrease in hardness. Evidence of grain growth within the HAZ towards the fusion boundary is further evidenced in Figure 4-22 c) and is in good agreement with the hardness evolution detailed in Figure 4-22 a) and b). Upon entering in the FZ (region 3), the hardness reaches its lowest value at ≈ 142 HV0.5, which is similar to that commonly observed in cast CoCrFeMnNi alloys [155]. Thus, although BCC and σ are formed in this region, with σ typically being a strengthening phase [184], its low volume fraction (≈ 0.77%) and very large grain structure of the FCC phase is not conducive to an evident increase in hardness. Moreover, the modification of the chemical composition of the fusion, via dilution, is not strong enough to induce solid solution strengthening compared to the equiatomic CoCrFeMnNi HEA.

Figure 4-23 details the engineering stress-strain curve for the CoCrFeMnNi joints, and different DIC strain maps obtained at different stress/strain conditions. The yield strength, ultimate tensile strength and elongation of the welded joint were 225 MPa, 517 MPa and 8.4 %, respectively. While the elongation of the welded joint is only slightly lower than that of the BM [67] (≈ 8.4 vs ≈ 9.4 %), the tensile strength significantly decreases (≈ 517 vs ≈ 945 MPa).The relatively poorer mechanical performance of the welded joint compared to the BM, while still being able to be considered for structural applications, is explained considering both the microstructure features and DIC maps obtained: the FZ, with its lower hardness and extremely large grain size, will promote significant strain concentration, while in the non-welded material the load is more uniformly distributed. Owing to this strain concentration in the FZ, the remaining parts of the joint are less strained and the overall deformation sustained is lower than in the original BM. Nonetheless, the local strain experienced by the FZ can reach up to ≈ 75% suggesting that this region is highly ductile. Future work will first understand the mechanical behavior for the filler material alone, then remove the face/root refinement and compare the mechanical properties with and without refinement, and finally assess how different post-weld heat treatments can be used to improve the mechanical response of these welded joints.

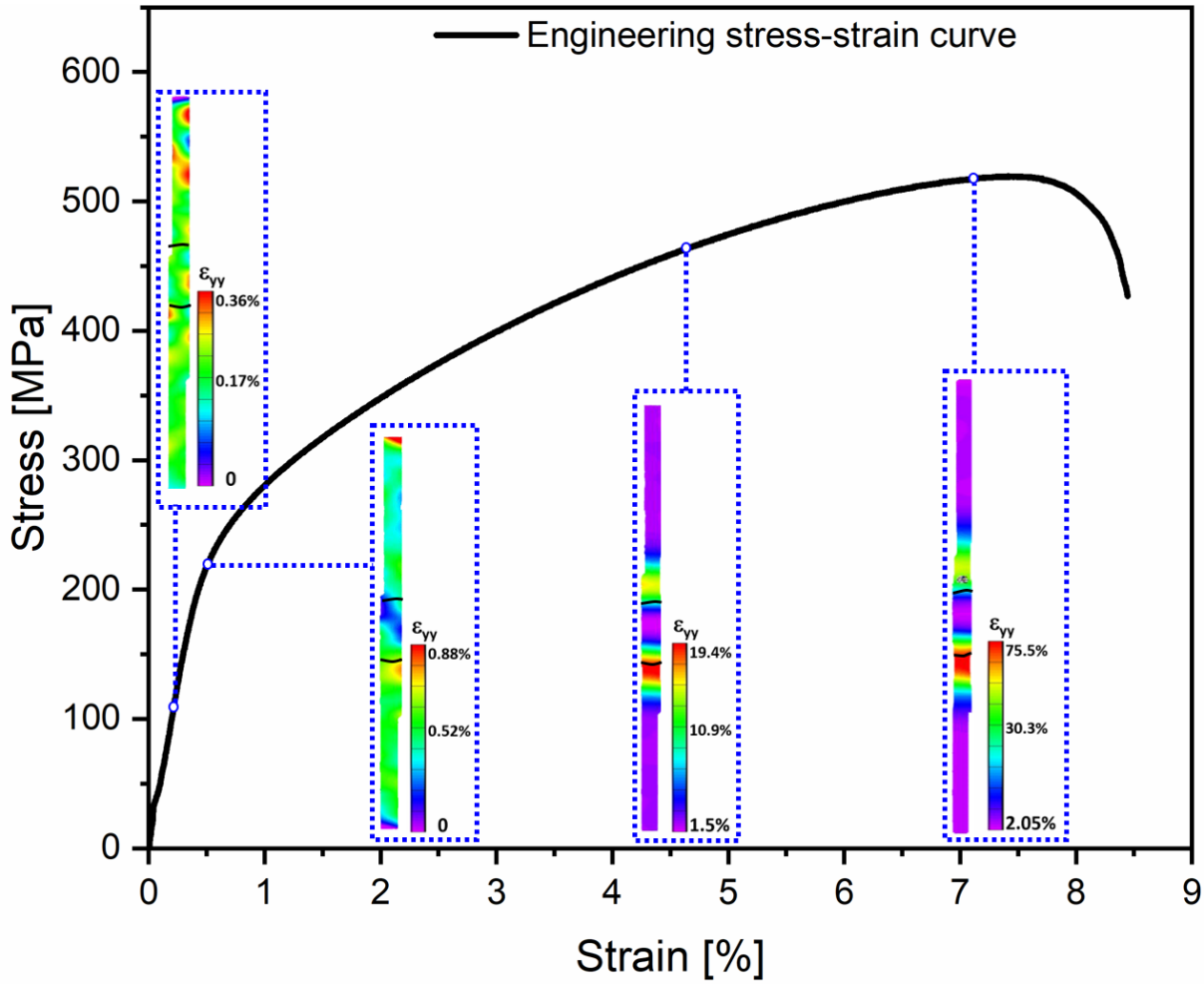

Figure 4-23. Engineering stress-strain curve of the gas metal arc welded CoCrFeMnNi joints with ER308LSi filler material, with DIC snapshots obtained at different loading steps during loading until failure.

4.2.2.5 Conclusions

This work combined advanced material characterization, thermodynamic simulations and mechanical testing to provide a comprehensive analysis of the microstructure evolution and mechanical properties of GMAW CoCrFeMnNi joints obtained with ER308LSi filler material. The results show that the prestored strain energy in the as-rolled BM and the weld thermal cycle are the main driving forces for recrystallisation and grain growth occurring in the HAZ, and in turn, such solid-state transformations are the direct causes for the hardness drop in this region. A chemical composition gradient caused by the dilution of the filler material is closely related to the phase structure that is formed in the FZ. Mechanical testing detailed that the joints can be considered for structural application, despite fracture occurred in the FZ region.

4.3 Benchmark of the effect of different filler materials on the microstructure features and mechanical properties of gas metal arc welded CoCrFeMnNi HEA

In this section a comparison between the microstructure features and mechanical properties detailed in chapters 4.2.1 to 4.2.2 will be summarized and compared to elucidate on the role of each filler material and its suitability for different structural applications.

From the perspective of microstructure, the chemical composition gradient caused by the dilution of the filler material is closely related to the phase structure that is formed in the FZ. And either the addition of ER308LSi stainless steel or ER410-NiMo stainless steel filler materials, the composition changes in both different FZ are not conducive to a solid solution strengthening. From the aspect of mechanical properties, gas metal arc welded CoCrFeMnNi joints with ER410-NiMo/ER308LSi filler wire exhibited an increase strength but a slight decrease in fracture strain compared to gas tungsten arc welded CoCrFeMnNi joints without the addiction of filler wire. Further comparing, the welded joint with ER410-NiMo filler wire shows lager ultimate strength (641 vs 520 MPa) and comparable fracture strain (7.5 vs 7.3%). Overall, the good strength and ductility of these joints open the door for the potential application for the potential applications of GMAW of CoCrFeMnNi HEAs for industrial-oriented application.

5.

MICROSTRUCTURE AND MECHANICAL PROPERTIES OF GAS TUNGSTEN ARC WELDED $AlCoCrFeNi_{2.1}$ JOINTS

5.1 Deformation mechanism of an eutectic $AlCoCrFeNi_{2.1}$ high entropy alloy probed by in-situ synchrotron X-ray diffraction

5.1.1 Introduction

HEAs, also known as multi-principal alloys, have attracted widespread interest in the field of materials science for their good thermal stability [185–187], high ductility and strength [188–191], and excellent corrosion resistance [192,193], since they were first proposed by Cantor et al. [1] and Yeh et al. [2] in 2004. Despite its complex composition, containing typically at least five principal elements [188], HEAs often exhibit simple crystal structures, with FCC and BCC being the most prevalent ones.

For single-phase HEAs with FCC structure, such as the equiatomic CoCrFeMnNi [194], $Fe_{40}Mn_{26}Ni_{27}Co_5Cr_2$ [195] and $Fe_{40}Mn_{40}Co_{10}Cr_{10}$ [196], the yield strength is almost always below 400 MPa (except if previous plastic deformation has been applied), although they reach elongations of more than 50%. For single BCC HEAs compositions, such as equiatomic NbMoTaW and VnbMoTaW [186], the yield strength can be above 1000 MPa, but the alloy plasticity is significantly reduced as compared to single FCC HEAs. In addition, the casting properties and compositional segregation of HEAs can further limit their practical applications [197,198].

One of the most sought-after challenges in metallurgical research concerns the ability to develop alloys with a good balance of strength and plasticity. This trade-off seems of be absent in single phase HEAs [149,199]. In order to solve this challenge and achieve simultaneous high strength and ductility, Lu et al. first proposed the concept of eutectic HEAs [200]. In their seminal work, an $AlCoCrFeNi_{2.1}$ HEA

consisting of soft and hard phases within a lamellar microstructure was developed. Subsequently, other eutectic HEAs such as $Fe_{20}Co_{20}Ni_{41}Al_{19}$ [201], $AlCrFeNiMo_{0.2}$ [202] and $Nb_{25}Sc_{25}Ti_{25}Zr_{25}$ [203] have emerged. However, among all currently available eutectic HEAs, the most studied is still the $AlCoCrFeNi_{2.1}$ composition. Of special relevance in this composition are its good thermophysical properties, including reduced solidification temperature range arising from the isothermal transition of the eutectic reaction of the alloy in its as-cast condition [202].

The potential for as-cast $AlCoCrFeNi_{2.1}$ eutectic HEAs as an engineering material for structural application has been studied by different research groups primarily focusing on two main aspects: the effect of thermomechanical treatments on the microstructure evolution and resulting properties [204–213]; dependence of the mechanical properties under service conditions [200,205,214–219]. In 2016, Wani et al. [220] performed for the first time thermomechanical processing on the $AlCoCrFeNi_{2.1}$ alloy, which included significant cold-rolling followed by multiple annealing treatments. It was shown, by electron microscopy characterization, that the as-cast microstructure was composed of a lamellar B2 BCC + $L1_2$ FCC microstructure. After thermomechanical processing, the ordered $L1_2$ become disordered, whereas no microstructural changes in the B2 BCC phase were observed. Bhattacharjee et al. [214] investigated the effect of low temperature tensile testing (from room temperature to 77 K) on the mechanical properties of an as-cast $AlCoCrFeNi_{2.1}$ alloy. Again, disordering of the $L1_2$ phase and subsequent transformation to a simple FCC phase was reported, whereas the B2 BCC phase remained unchanged. Moreover, the fracture strains were seen to be practically constant with decreasing testing temperature, while the tensile strength increased by ≈ 300 Mpa. Zhang et al. [219] performed high-temperature tensile tests on an as-cast $AlCoCrFeNi_{2.1}$ eutectic HEA composed of $L1_2$ FCC and B2 BCC phases, which exhibited good strength and high plasticity at high temperatures due to the simultaneous hardening and dynamic recrystallization during deformation. In addition to this, Guo et al. [217] studied, in-situ, the deformation response of a similar alloy over a wide temperature range (from 77 to 676 K) using neutron diffraction, highlighting the microstructural evolution of both phases. Finally, Lu et al. [221] investigated the mechanical behavior and microstructural evolution of both the FCC and B2 BCC phases at room and low temperatures.

It is worth noting that phase identification of the as-cast eutectic $AlCoCrFeNi_{2.1}$ HEA is predominantly performed by transmission electron microscopy (TEM). Moreover, several researchers have identified different phases in the as-cast $AlCoCrFeNi_{2.1}$ HEA. Some authors have identified disordered FCC and ordered B2 BCC phases [222–226], while others have identified ordered $L1_2$ FCC and B2 BCC phases [217,227–232], while some have simultaneously identified FCC, $L1_2$ FCC, B2 BCC and tetragonal σ phases [233]. Additionally, studies on the as-cast $AlCoCrFeNi_{2.1}$ eutectic HEA have been primarily focused on qualitatively exploring the mechanical properties of the alloy under different deformation conditions (e.g., low temperature [205,207,214,217] vs room [190,217,218] vs high temperature [209,217,219,220,227,229,232,234], and fatigue [235]). A comprehensive quantitative study of the deformation mechanisms of the different phases that exist in this alloy and their impact on the

macroscopic mechanical response is yet lacking, thus hampering full understanding of microstructure/properties relationships.

Here, we use in-situ high energy synchrotron X-ray diffraction to evaluate the micromechanical behavior and microstructure evolution of an as-cast $AlCoCrFeNi_{2.1}$ eutectic HEA during tensile deformation until failure. Aside from quantifying for the first time all phases that co-exist in the material, the contribution of each phase towards the mechanical strength of the alloy is determined and rationalized not only based on the dislocation density evolution but also on the impact of the lamellar structure. We also highlight the possibility to tune the strength/ductility response of eutectic HEAs by modifying the volume fractions of existing phases. Lattice strain measurements reveal the impact of the as-cast texture on the preferential deformation behavior of specific (h k l) planes.

5.1.2 Starting material

In this work, the previously described $AlCoCrFeNi_{2.1}$ eutectic HEA in the as-cast condition was used. The chemical composition of the material was detailed before in Table 3-1.

5.1.3 Results and discussion

5.1.3.1 Microstructural characterization and phase identification

Figure 5-1 shows the microstructure of the $AlCoCrFeNi_{2.1}$ eutectic high-entropy alloy in the as-cast state, (a) before tensile deformation, and (b) after the tensile test. Previous reports in the literature [233] indicate that the microstructure corresponding to the bright (light contrast) and dark (dark contrast) corresponds to the FCC and B2 BCC phases, respectively. Macroscopic measurements of the average interlamellar distances reveal subtle changes before and after deformation. Prior to mechanical loading, the average interlamellar distance of the FCC and B2 BCC phases were 2.41 ± 0.39 and 1.99 ± 0.34 µm respectively, which then changes to 2.97± 0.41 and 2.40 ± 0.21 µm. This corresponds to change of roughly 20 to 23 % for each phase, suggesting that the overall deformation is homogenous. The reason for this is related to the distinct mechanical behavior of both phases and to constraint effects induced by the hard B2 BCC phase over the soft FCC one, as it will be shown latter. It should be emphasized that these measurements were obtained at multiple distinct orientations to get an overall understanding of the interlamellar distance variation upon tensile testing.

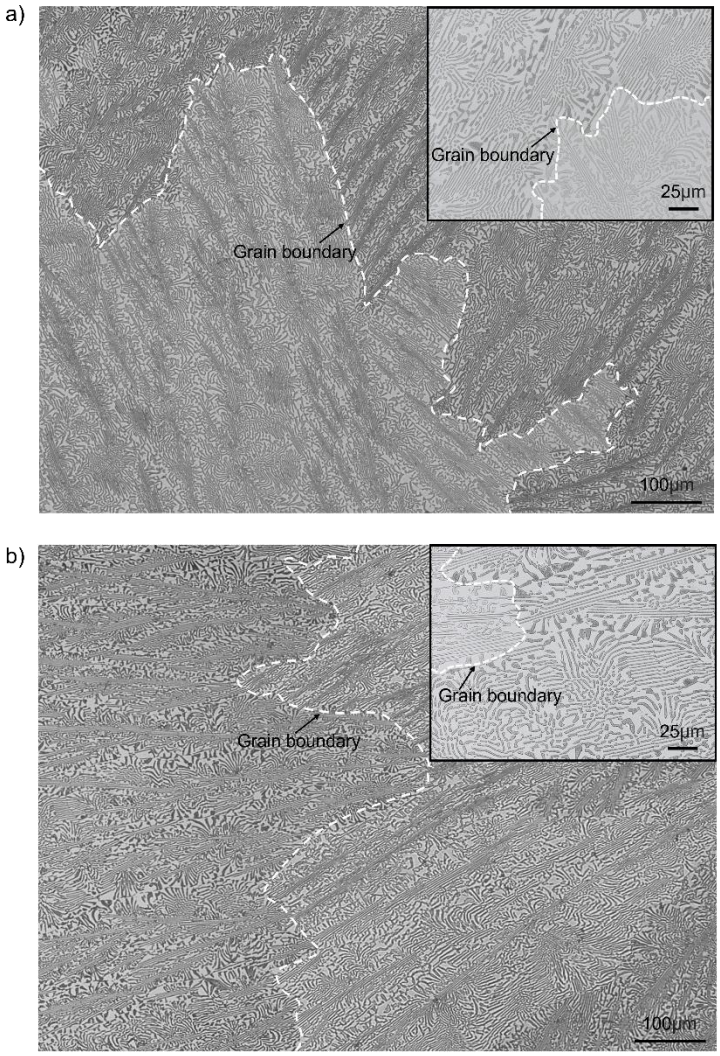

Figure 5-1. OM images of as-cast AlCoCrFeNi2.1 eutectic HEA: a) before tensile loading; b) after fracture. The inserts detail a close-up view of the lamellar structure.

Figure 5-2 details a superimposition of the synchrotron diffraction patterns obtained by full integration along the azimuthal angle for different stress/strain levels during tensile testing. The phase identification detailed in Figure 5-2 depicts that the as-cast $AlCoCrFeNi_{2.1}$ HEA is composed by a B2 BCC phase, a disordered FCC structure, an ordered FCC phase with $L1_2$ structure and also tetragonal phase, named as σ phase. The existing phases in the as-cast alloy are in excellent agreement with previous microstructural characterization performed using transmission electron microscopy on a similar alloy reported by Choudhuri et al. [233].

Of novelty within this work is the volume fraction quantification of the existing phases and determination of their lattice parameters. These results are detailed in Table 5-1. The volume fraction of the FCC phase is 65.5 % and within it exists the $L1_2$ FCC phase with a volume fraction of 0.7 %. As for the B2 BCC phase, a volume fraction of 32.7 % was determined and the σ phase, that is known to precipitate in the

B2 BCC matrix upon solidification of the alloy [233], has a volume fraction of 1.1 %. The measured lattice parameters for the two major phases that compose this eutectic alloy (disordered FCC and B2 BCC) are in good agreement with the work of Xiong et al. [236].

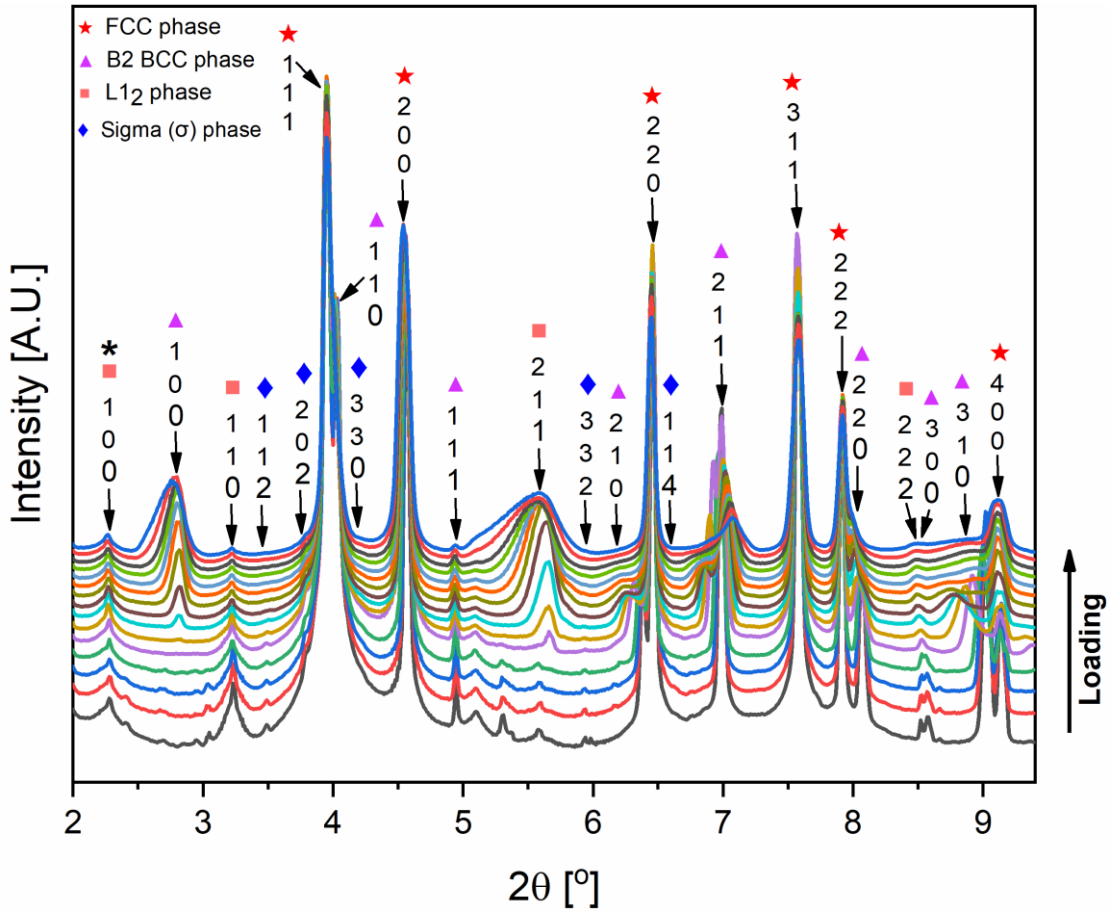

Figure 5-2. Superimposition of the diffraction patterns obtained after integration of the Debye-Scherrer rings along the full azimuthal angle. * Marks the superlattice reflection of (1 0 0) L12 FCC phase.

Table 5-1 – Refined lattice parameters and volume fraction of the existing phases in the as-cast AlCoCrFeNi2.1 HEA.

Phases	a [Å]	b [Å]	c [Å]	α [º]	β [º]	γ [º]	Space group	Volume fraction [%]
FCC	3.56232	a=b=c	a=b=c	90	90	90	Fm–3m	65.5
B2 BCC	2.85168	a=b=c	a=b=c	90	90	90	Pm–3m	32.7
$L1_2$ FCC	3.56219	a=b=c	a=b=c	90	90	90	Pm–3m	0.7
σ	8.1768	a=b	5.0185	90	90	90	P42/mnm	1.1

Confirmation of the presence of the $L1_2$ FCC phase is aided by the presence of a superlattice reflection of the (1 0 0) plane [237] (refer to Figure 5-2). Previously, σ phase was identified (but not quantified) in $AlCoCrFeNi_{2.1}$ HEAs [233,238,239] and this phase was also observed in an $Al_{0.5}CoCrFeMnNi$ alloy [240]. The ability to detect and quantify, for the first time, such low fraction phases ($L1_2$ FCC and σ phases) is related to the high signal-to-noise ratio enabled by high energy synchrotron X-ray diffraction. It should be noted that the lattice parameters of the σ phase present in the eutectic alloy are similar to those reported for a related phase that can form in equiatomic CoCrFeMnNi HEA [241].

5.1.3.2 Macroscopic mechanical behavior, stress partitioning and dislocation density evolution

Figure 5-3 details the engineering and true stress-strain curves (black and red lines, respectively), as well as the strain-hardening rate response (blue line) of the eutectic alloy. These results highlight that the $AlCoCrFeNi_{2.1}$ HEA in the as-cast condition has a combination of high strength and ductility. A tensile strength of 980 Mpa and an elongation to fracture of 13.1 % (true values) were measured. Macroscopically, the as-cast $AlCoCrFeNi_{2.1}$ HEA also exhibits extraordinary work-hardening behaviour by comparison with NiAl-based alloys [242] and with other conventional engineering alloys [243].

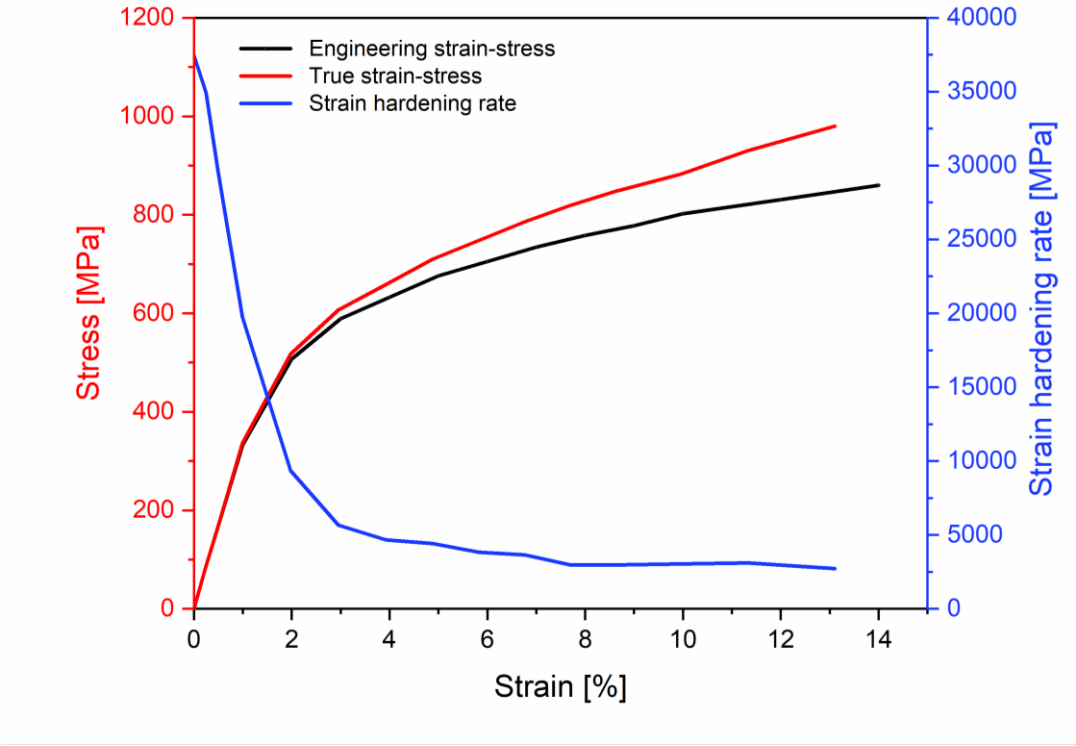

Figure 5-3. Tensile strain-stress curves and strain hardening behavior of the as-cast $AlCoCrFeNi_{2.1}$ HEA.

To clarify the contributions of the two major phases in the alloy towards the work hardening behavior, the stress partitioning between the disordered FCC and ordered B2 BCC phases during macroscopic loading was determined, as previously detailed in the experimental section. These results are depicted in Figure 5-4 and were obtained from the full azimuthal integrated data to evaluate the macroscopic mechanical response of both phases. From this data, it is evident that the macroscopic yield point of the material (≈ 333 Mpa and 1.5 % strain) corresponds to an abrupt point after which there is a significant stress redistribution between the FCC and B2 BCC phases. Comparing the individual stress-strain responses of the FCC and B2 BCC phases, it is perceptible that, within the elastic deformation regime, the FCC phase has a lower Young's modulus than the B2 BCC phase. The difference in elastic modulus between the hard B2 BCC and soft FCC phases ($E_{B2\ BCC} > E_{FCC}$) makes the FCC phase subjected to experience higher deformations for the same externally applied stress during macroscopic elastic deformation. Upon the initial yielding of the material, the stress partitioned to the B2 BCC phase (red line in Figure 5-4) presents a steep and continuous rise, while the stress imparted on by FCC phase only increases by ≈ 150 Mpa up until fracture, while for the B2 BCC phase the stress difference between the yielding start and fracture is of nearly ≈ 1600 Mpa.

Further analysis of Figure 5-4 suggests that yielding of the hard B2 BCC phase only starts to occur for a macroscopic strain of 3.5 %, after which a non-linear elastic response is observed. This behavior is also observed in the lattice strain evolution (refer to Figure 5-7 and subsequent discussion. Furthermore, a distinctive behavior between both phases is evident: the softer FCC phase has an almost negligible

work hardening behavior since after the onset for plastic deformation its phase stress remains almost unchanged. The same does not occur for the B2 BCC phase, where significant work hardening exists right after the end of the elastic deformation region. Therefore, it can be concluded that the macroscopic work hardening behavior of the as-cast $AlCoCrFeNi_{2.1}$ eutectic HEA is predominantly arising from the B2 BCC phase. It should be noticed that these phase stress calculations were made considering the (3 1 1) FCC and (2 1 1) B2 BCC planes, as these are less affected by intergranular stresses and can provide a more precise understanding of the load partitioning experienced by the material. Although significant differences between the FCC and B2 BCC phases are observed during plastic deformation, the same does not occur during macroscopic elastic loading where there is no evident load partitioning.

Another interesting point arising from the phase partitioning data concerns the possibility to tune the mechanical response of eutectic HEAs based on the volume fraction of both FCC and BCC phases. From this data, it clearly results that higher strength levels can be achieved by a material with higher volume fraction of the B2 BCC phase, whereas if lower strength but increased ductility is required then the volume fraction of the FCC phase must increase. The load partition and the higher stresses that are transferred to the B2 BCC phase also highlight that this is the strengthening phase for the present eutectic HEA. When considering the stress transferred to each phase and the respective volume fraction, the resulting curve (green line in Figure 5-4) is in good agreement with the macroscopic tensile behaviour of the alloy (black line in Figure 5-4).

To showcase the strengthening effect of the B2 BCC phase as a function of different volume fraction contents, Figure 5-5 was developed to further highlight the relative importance of each phase for the overall material strength. It should be emphasized that these calculations can only be used to evaluate the potential strength of the alloy and not its ductility.

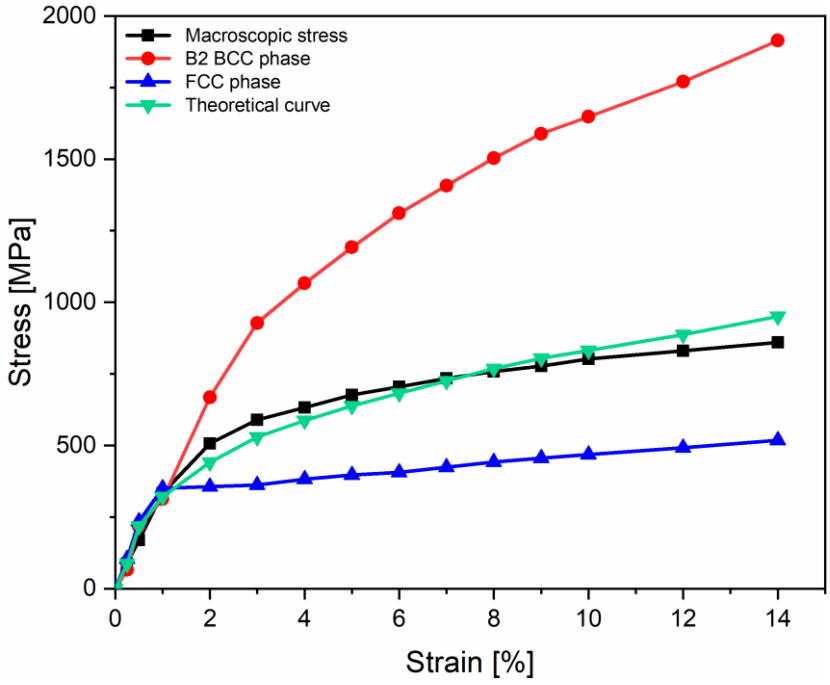

Figure 5-4. Stress partitioning of B2 BCC phase and disordered FCC phase during in-situ synchrotron tensile loading.

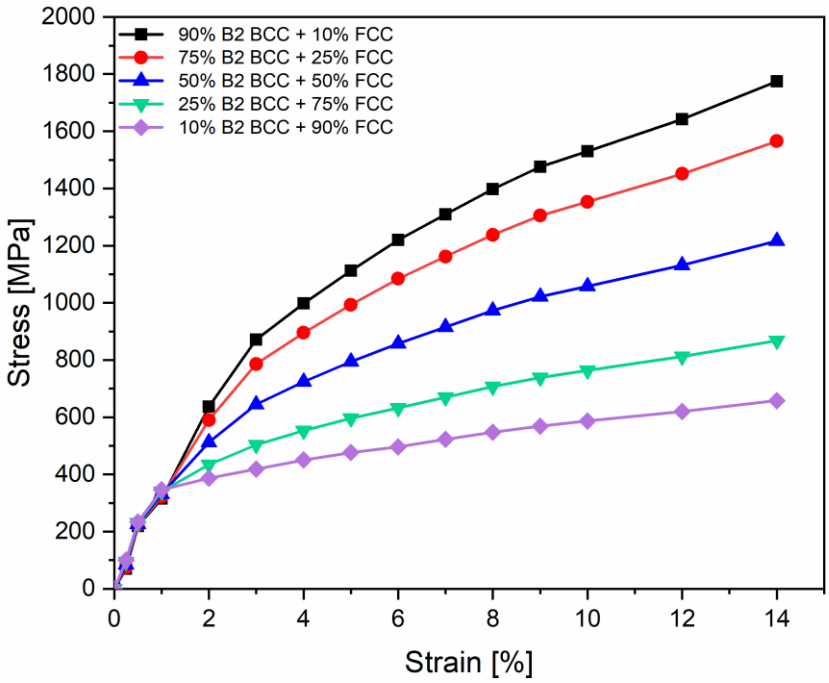

Figure 5-5. Calculated effect of different volume fractions of disordered FCC and ordered B2 BCC on the mechanical response of the eutectic HEA.

The dynamic evolution of the dislocation density in both disordered FCC and ordered B2 BCC phases is qualitatively analysed next. Figure 5-6 (a) depicts the average lattice strain as a function of

engineering strain for both FCC and B2 BCC phases, while Figure 5-6 (b) illustrates the dislocation density evolution. Figure 5-6 (c) details the strengthening effect promoted by the dislocation density evolution in both FCC and B2 BCC phases. From Figure 5-6 (a), it can be perceived the slightly higher ductility of the FCC phase when compared to the B2 BCC phase. These results, in combination with the stress partitioning data (Figure 5-4), further emphasize that the material strength is primarily controlled by the volume fraction of the B2 BCC phase, while its ductility can be regulated by the disordered FCC phase.

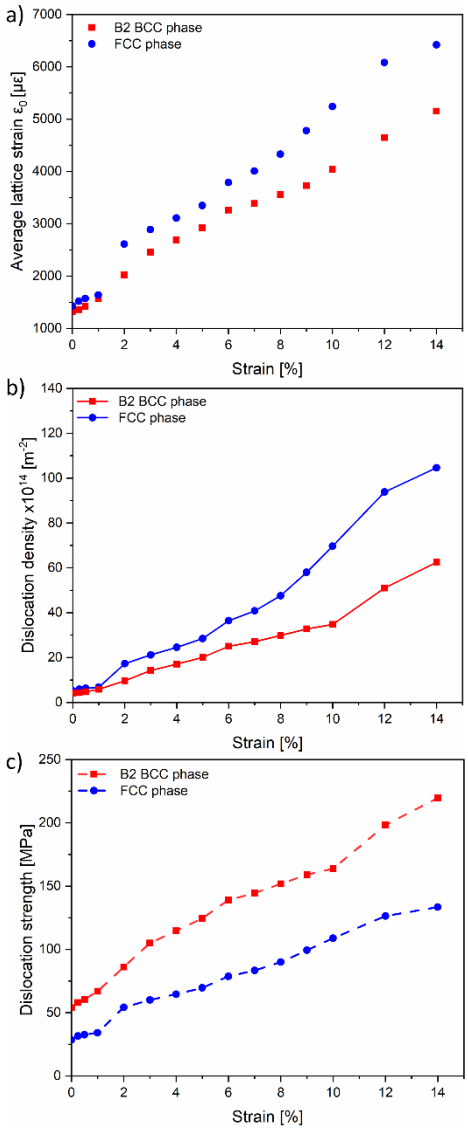

Figure 5-6. Evolution of: a) average lattice strain as a function of engineering strain; b): dislocation density evolution as a function of engineering strain; c): strengthening effect promoted by the dislocation density evolution.

In the as-received condition, i.e., prior to any mechanical loading, the dislocation density was similar for both phases, 5.2 x 10^{14} and 4.1 x 10^{14} m^{-2} for the FCC and B2 BCC, respectively. These dislocation

density values are within the order of magnitude for others HEAs, such as CoCrFeNi and CoCrFeMnNi, in their as-cast state and as-rolled state [244,245].

During the elastic deformation domain, the dislocation densities of both FCC and B2 BCC phases do not change significantly, but the dislocation density of the B2 BCC phase is always slightly below that of the FCC phase. This evolution is consistent with a similar variation trend exhibited in the phase stress partitioning in the elastic region ($\varepsilon < 1.5\%$), as previously shown in Figure 5-4.

When the applied strain increases above 1.5%, the material starts to deform plastically. The dislocation density of the FCC phase increases significantly to 1.9×10^{15} m^{-2}, while the B2 BCC phase only shows a moderate increase to 9×10^{14} m^{-2}. The reason for the difference in the evolution of dislocation density between these two phases is that under externally applied stresses, the plastic deformation of the eutectic alloy is activated in the FCC phase first due to the inherent soft nature of this phase (nanohardness of the FCC and B2 BCC phases of 5.8 ± 0.2 Gpa and B2 BCC = 9.7 ± 0.3 Gpa, respectively [214]). Therefore, when plastic deformation in the FCC phase is induced there is concomitant increase in the amount of dislocations that are formed, thus justifying the increased dislocation density over that of the BCC phase.

During the macroscopic plastic deformation regime, the dislocation density evolution in both phases tends to increase almost linearly up until fracture. However, the increased slope of the curve corresponding to the FCC phase highlights that the strengthening mechanism induced by generation and movement of dislocations is not as effective in promoting the strain hardening of the alloy. This is further elucidated in the evolution of the alloy strength induced by the variation of the dislocation density in both phases, as detailed in Figure 5-6. In fact, it is observed that the increase in alloy strength due to the dislocation density in the B2 BCC phase is significantly higher (≈ 100 MPa) of that caused by the increase in dislocation density in the FCC phase, even though this latter phase has always a higher dislocation density throughout the tensile test.

Due to the stress incompatibility between the FCC and B2 BCC phases which arises from their distinct mechanical behaviour (as shown in Figure 5-4), the soft FCC matrix plastically deforms first, leading to the proliferation and rearrangement of dislocation substructures, resulting in a substantial increase in dislocation density [204]. Plastic deformation of the hard B2 BCC phase is delayed until effective stress transfer to this phase occurs. At this time, the plastic deformation experienced by the B2 BCC phase results in an increase of the dislocation density, as previously shown in Figure 5-6 (c). In reality, plastic deformation of the soft FCC phase is constrained by the hard B2 BCC. The FCC phase cannot plastically deform in a free way, because of the lamellar structure of the eutectic phase: the hard B2 BCC acts as physical barrier to the deformation of the FCC phase. This leads to the formation of strain gradients across the FCC + B2 BCC eutectic structure [204]. It should be emphasized that such strain gradients will increase with proceeding deformation because of the distinct mechanical behaviour of the FCC and B2 BCC phases. In fact, the different mechanical properties of the FCC and B2 BCC phases are known

to generate a back-stress that can also increase the strength of the alloy [204]. The mechanism that promotes this back-stress is described next. The deformation of the soft FCC is constrained by the hard B2 BCC phase, which aids in the formation of strain gradients across both phases. More dislocations are formed in the FCC phase since this phase will always bear more plastic strain than the B2 BCC one. This continues to increase the strain gradient across the eutectic microstructure. Directly resulting from these strain gradients, there is an increase in the GND which then promotes a strength increase by the resulting back-stresses. Since the FCC phase is significantly more deformed and is also constrained by the B2 BCC phase during deformation it will necessarily generate more dislocations when macroscopic deformation is progressing, thus justifying the higher dislocation density across the tensile test. Such back-stress effects have been exemplified in the literature when developing similar eutectic HEAs possessing hierarchical microstructures [204]. There is final potential contributing factor to the alloy strength which is related to an ordering strengthening mechanism induced by the B2 phase.

5.1.3.3 Lattice strain evolution

Figure 5-7 depicts the evolution of the lattice strains for the (2 0 0), (3 1 1), (2 2 2) planes of FCC, (2 1 1), (1 1 0), (3 1 0) planes of B2 BCC and (1 0 0) planes of $L1_2$ FCC parallel (LD) and perpendicular (TD) to the LD. When the engineering stress is less than 333 MPa (corresponding to 1.5 % strain) the lattice strain of all planes has a linear response with the applied stress (refer to Figure 5-7 (a), (b) and (c)). This shows that up to this point the material in only being elastically deformed, thus in good agreement with the stress partitioning and tensile response of the eutectic alloy.

Linear fitting of the evolution of the lattice strain with the macroscopic stress for each lattice plane allows to determine the direction-dependent Young's modulus. Table 5-2 details the Young's modulus for all analyzed planes obtained in the LD, revealing strong elastic anisotropy. For the FCC phase, the (2 2 2) plane has the largest elastic modulus (265 GPa), whereas the (2 0 0) plane has the lowest with 108 GPa. This means that the (2 0 0) plane is the softest, while the (2 2 2) is the hardest. These results are in good agreement with previous work by Lu et al. on the $AlCoCrFeNi_{2.1}$ eutectic HEA [190]. As for the B2 BCC phase, the hardest plane was the (2 1 1), while the (3 1 0) is the softest (191 vs 108 GPa).

Another novelty of this work is the determination of the superlattice (1 0 0) plane elastic modulus for the $L1_2$ FCC phase which was calculated to be 222 GPa. Calculations for other planes were not performed owing to the extremely low intensity of the diffraction peaks and overlapping, which prevented an accurate implementation of the peak fitting procedure described in the experiment and methods section.

Attention is now paid to the lattice strain evolution when macroscopic plastic deformation starts to occur. When the material enters the plastic deformation stage, a nonlinear response for all lattice planes with increased applied stress gradually becomes more evident. The deviation from linearity, which corresponds to the onset for macroscopic plastic deformation, has been marked with a dashed horizontal line in Figure 5-7 a), b) and c) for the FCC, B2 BCC and $L1_2$ FCC phases. It has been

demonstrated that the separation of lattice strains in different phases or different grain families in the plastic region, indicates the occurrence of stress redistribution between different phases and grain families [246–248]. This is again in excellent agreement with the phase stress partitioning calculations previously shown in Figure 5-4. In this case, the internal stress is transferred from the soft phase or the soft grain family to their hard counterparts after plastic deformation in the soft domain.

Comparing the lattice strain distributions of the FCC and B2 BCC phases along the LD (refer to Figure 5-7 (b) and (d)), it can be observed that the lattice strains of all analyzed planes of the FCC phase start to deviate from a linear elastic response after the macroscopic yield point (333 MPa), which indicates that the FCC phase yields first than the B2 BCC phase as previously shown and discussed considering the macroscopic response of the alloy detailed in Figure 5-4. Also, the lattice strain of all analyzed planes of the B2 BCC phase is significantly larger than those of the FCC planes. For example, the maximum lattice strain of the (h k l) planes of the B2 BCC phase corresponded to the (3 1 0) lattice plane which is almost 8 times higher than the largest lattice (h k l) strain of FCC phase, which corresponded to the (2 0 0) plane. Quantitatively, this translates to a maximum lattice strain of ≈ 65000 με for the (3 1 0) B2 BCC plane and ≈ 8000 με for the (2 0 0) FCC plane. As for the TD, larger lattice strains are preferentially obtained in the analyzed B2 BCC planes. This behavior could indicate that preferential macroscopic deformation should be expected in the B2 BCC phase, which was not experimentally observed as previously shown. The reason that justifies the increased lattice strains for the analyzed B2 BCC planes is related to the preferential deformation in the two analyzed directions, i.e., parallel and perpendicular to the LD. In fact, this preferential deformation, which is governed by the material texture, depends on the spatial relationship between a certain (h k l) plane and the azimuthal angle. Although not shown here, when analyzing other azimuthal angle ranges (30º ± 7.5º, 45º ± 7.5º and 60º ± 7.5º) larger lattice strain deformations in the FCC planes were observed, thus further confirming the dependence of the lattice deformation with the azimuthal angle.

A closer look at the superlattice reflection of the (1 0 0) plane of the $L1_2$ FCC phase (refer to Figure 5-7 e) reveals near mirror-like behavior, with a maximum positive lattice strain of ≈ 8000 με developing along the LD and maximum negative lattice strain of ≈ 5000 με developing in the TD. Further observation of the lattice strain evolution of the (1 0 0) $L1_2$ FCC superlattice plane and the (2 0 0) FCC lattice plane under tensile loading, revealed that the two planes have similar deformation evolution (as shown in Figure 5-7 (a) aI(e)). $L1_2$ FCC phase coherently precipitates within the FCC matrix, thus is it expected that equivalent crystallographic planes behavior similarly. This is what is observed when directly comparing the (1 0 0) $L1_2$ FCC superlattice plane the (2 0 0) plane of the surrounding matrix. The interaction mechanism of secondary phases with dislocations usually includes dislocation cutting and Orowan looping mechanisms [249]. The interaction mechanism of the $L1_2$ phase as the secondary phase with dislocations during deformation is considered as dislocation cutting [219]. The dislocation cutting mechanism is mainly manifested by the dislocation cutting through the second phase and

deforming it along with the matrix phase. This explains why the $L1_2$ FCC phase has a similar deformation behavior of that of the FCC matrix phase.

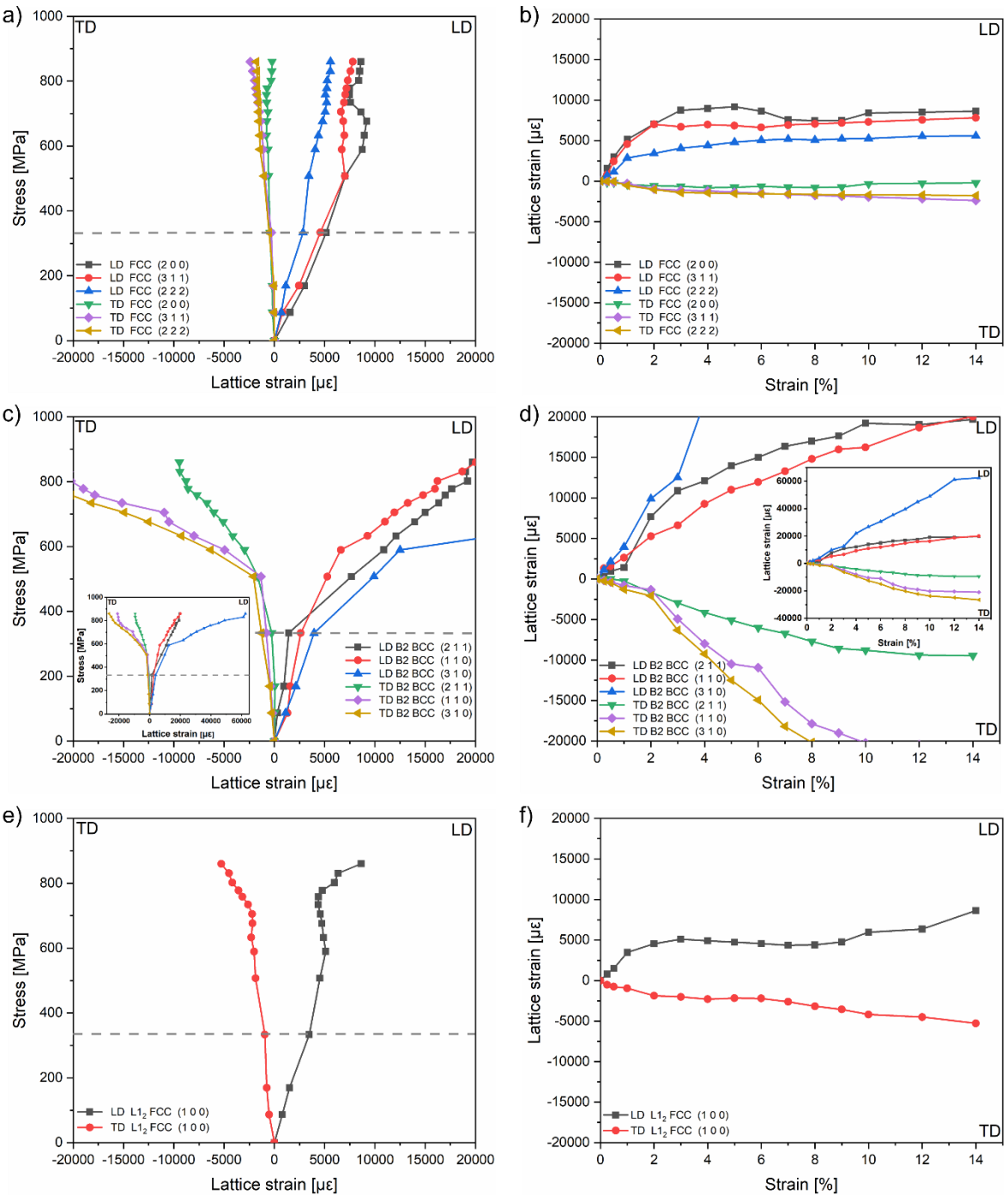

Figure 5-7. Lattice strain evolution along the LD and transverse direction (TD) as a function of applied stress (a, c, e) and strain (b, d, f) for FCC (a, b), B2 BCC (c, d) and L12 FCC phases (e, f). The dashed lines represent the onset for macroscopic plastic deformation.

Table 5-2 – Elastic modulus for different lattice planes of constituent phases in as-cast $AlCoCrFeNi_{2.1}$ HEA.

$L1_2$ FCC	FCC			B2 BCC		
E_{100} (GPa)	E_{200} (GPa)	E_{311} (GPa)	E_{222} (GPa)	E_{211} (GPa)	E_{110} (GPa)	E_{310} (GPa)
222	108	221	265	191	175	108

5.1.4 Conclusions

The micromechanical behavior of an as-cast $AlCoCrFeNi_{2.1}$ eutectic HEA during tensile deformation has been investigated by in-situ tensile testing at room temperature using high energy synchrotron X-ray diffraction. The phase constitution and respective volume fractions, phase stress partitioning, dislocation density evolution as well as the lattice strain evolution parallel and perpendicular to the LD were determined. The following major conclusions can be drawn:

Phase identification of the as-cast eutectic alloy revealed the presence of two FCC phases (one ordered and one disordered), an ordered BCC phase and tetragonal σ phase. These results contradict several works on the phase identification of the same eutectic alloy, which often misidentify the existing phases. The lattice parameters of all four phases were determined: i) FCC, a = b = c = 3.56232 Å; ii) B2 BCC, a = b = c = 2.85168 Å; iii) $L1_2$ FCC, a = b = c = 3.56219 Å; iv) σ, a = b = 8.1768 Å, c = 5.0185 Å.

Stress partitioning between the two major matrix phases, FCC and B2 BCC, revealed that upon the onset of plastic deformation the stress is primarily transferred to the hard B2 BCC phase. Moreover, plastic deformation of the hard B2 BCC phase is delayed until a macroscopic strain of 3.5% is achieved. We also highlight the possibility to tune the stress/strain response of eutectic HEAs by changing the volume fraction of the matrix phases.

The evolution of the dislocation density was seen to occur preferentially in the soft FCC phase. Nonetheless, the strength contribution resulting from the increase in dislocation density was calculated to be more significant in the B2 BCC phase, even though this phase has a smaller dislocation density than the FCC phase throughout the deformation.

Local deformation of the soft FCC phase is constrained by the hard B2 BCC phase, resulting in strain gradients across the lamellar structure. This strain gradients increase with further deformation resulting in the preferential generation of GND in the FCC phase, thus justifying the increase dislocation density despite the low stress partitioned to this phase.

The lattice strain evolution along the parallel and perpendicular directions to the loading in both cases, revealed that the analyzed (h k l) planes of the B2 BCC phase present a significantly larger lattice strain

that those of the FCC phase. This is related to the texture of the as-cast material which governs the deformation response of each (h k l) plane for specific azimuthal angles.

5.2 Gas tungsten arc welding of as-cast $AlCoCrFeNi_{2.1}$ eutectic high entropy alloy

5.2.1 Introduction

Based on the literature review presented in chapter 2.3.4.2 the current state of research on the weldability of $AlCoCrFeNi_{2.1}$ eutectic HEAs still relatively unknown. To bridge the afore-mentioned gap in literature (refer to chapter 2.3.4.2) in what concerns the weldability of HEAs, the as-cast $AlCoCrFeNi_{2.1}$ eutectic HEA was welded by GTAW for the first time. The microstructural evolution of the welded joints was investigated using light OM, SEM aided by EBSD, high energy synchrotron X-ray diffraction and thermodynamic simulations. Additionally, uniaxial tensile testing coupled with DIC and microhardness mapping were used to evaluate the mechanical properties of the welded joints. The microstructural evolution and resulting mechanical properties were systematically evaluated, unveiling the correlation between processing, microstructural and mechanical properties.

5.2.2 Starting material

Commercially pure Al, Co, Cr, Fe, Ni (99.9 wt. % for Al, Co and Ni and 99.5 wt. % for Cr and Fe) were used to cast the $AlCoCrFeNi_{2.1}$ eutectic HEA BM used in this work. Casting was performed using vacuum induction melting, with the ingot being remelted multiple times to ensure good chemical homogeneity. The dimensions of the sheets to be welded were $74 \times 25 \times 1.5$ mm^3.

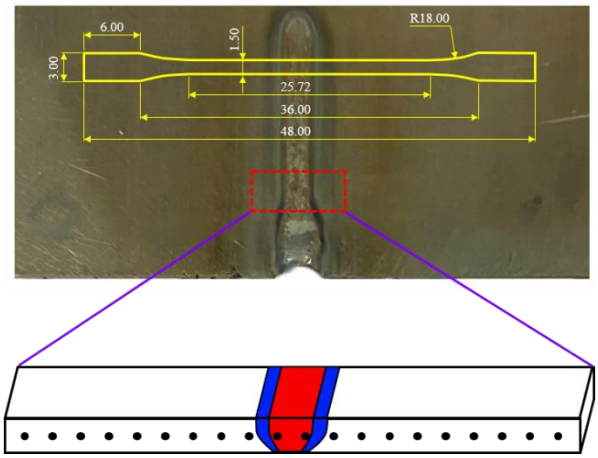

Figure 5-8. Macrograph of the welded joint (face side), white dimensions of the specimens obtained by EDM.

5.2.3 Results and discussion

5.2.3.1 Optical and electron microscopy

Figure 5-9 a) provides a cross-sectional view of the welded joint, while Figure 5-9 b), c) and d) show the light OM images of the BM, HAZ and FZ, respectively. Figure 5-9 e), f) and g) present detailed higher magnification electron microscopy images of the same regions. The different regions of the joints, i.e., BM, HAZ and FZ, in Figure 5-9 b), c) and d), respectively, can be clearly distinguished due to differences in microstructure. From Figure 5-9 a), it can be observed that the joint has full penetration without evidence of welding defects such as pores or solidification cracking.

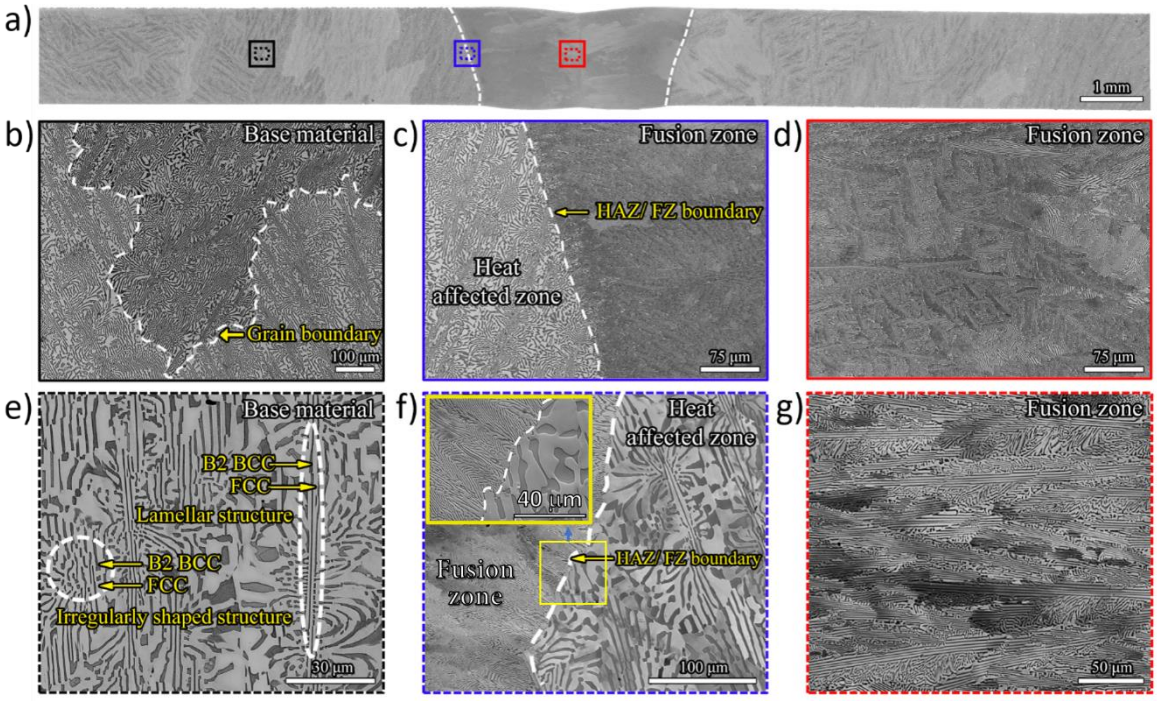

Figure 5-9. Light OM micrographs of the as-cast AlCoCrFeNi2.1 welded joint: a) overview of the weld cross-section; b) and e), c) and f), d) and g) are close-up views of the BM, HAZ and FZ near the boundary (HAZ/FZ), and FZ, respectively.

Further observation of the microstructure of the three representative regions is detailed next starting with the BM (refer to Figure 5-9 b) and e)). This region is mainly composed of ordered B2 BCC phase as well as of disordered FCC phase, as shown by the arrows marked in Figure 5-9 e). The contrast in color between the white and dark phases corresponds to the FCC and B2 BCC phases, respectively, which occurs due to elemental partitioning between both phases as confirmed by numerous researchers focusing on this alloy system [204,233,250]. In the magnified view (refer to Figure 5-9 e)), it can be observed that the BM contains both well-aligned and irregularly shaped lamellar structures.

The next region of interest corresponds to the HAZ (detailed in Figure 5-9 c) and f)), which experiences temperatures high enough to promote solid-state transformations. Compared to the initial eutectic microstructure in the BM, the FCC and B2 BCC phase structures are still observed. Moreover, the morphology of the eutectic structure remained unchanged. As documented later, changes induced at this region by the weld thermal cycle impact the nanoscale precipitates that can form in the $AlCoCrFeNi_{2.1}$ alloy.

The FZ experiences full melting, followed by a relatively fast and non-equilibrium solidification. The microstructure development in this region will largely depend on the alloy chemistry and how sensitive the material is to the off-equilibrium conditions of fusion-based welding processes [251,252]. The FZ microstructure is detailed in Figure 5-9 d) and g), and it can be observed that the lamella thickness of the FCC and B2 BCC phases shows a significant refinement, i.e., the lamella structure becomes thinner.

This difference in the lamellar thickness is related to the solidification conditions experienced during casting and welding: in casting the cooling rate is slower, which enables the development of relatively thicker lamellae, while the opposite occurs in arc-welding processes, where the higher cooling rate allows achieving a refined microstructure. The current observations coincide with the recent work of Zhang et al. using laser welding on the same alloy [50]. In addition, in the FZ boundary (refer to Figure 5-9 c) and f)), a refined grain structure is observed owing to the faster cooling rates enabled by the colder HAZ that act as a substrate from where solidification progresses toward the weld centerline. This is in good agreement with the solidification theory of metals [252–254], where grain growth tends to occur in an epitaxial mode along the direction opposite to the maximum temperature gradient at the solid/liquid interface, proceeding to the center of the FZ and having certain preferential orientations during solidification.

A more detailed crystallographic analysis of the welded joint microstructure was performed using EBSD, as detailed in Figure 5-10. Owing to the large size of the FZ and taking advantage of the microstructure symmetry along the weld centerline, the EBSD map was performed only in part of the FZ and only on one side of the HAZ and BM. From Figure 5-10, it can be determined that during the rapid cooling of the FZ, the grains of FCC and B2 BCC phase have different preferred growth directions, growing along the (101) and (001) directions, respectively. This seems inconsistent with the preferential growth along the (100) direction of cubic materials, but it is widespread in $AlCoCrFeNi_{2.1}$ eutectic HEAs [236,255]. This can be attributed to the fact that the eutectic HEA does not cross different phase regions during cooling [234]. Further observations reveal that the FZ is still dominated by a eutectic lamellar structure in the welded joint (see Figure 5-9 g)), indicating that the solidification rate in the FZ is insufficient to enable the $AlCoCrFeNi_{2.1}$ eutectic HEA to release itself from the eutectic growth. This is similar to the results previously reported by Zheng et al. [256] regarding the effect of different cooling rates on the solidification path of the as-cast $AlCoCrFeNi_{2.1}$ eutectic HEA, where different cooling rates significantly affect the solidification path. Moreover, depending on the potential composition changes in the FZ, the solidification microstructure may not be completely lamellar, but composed of FCC primary dendrites and of an FCC + B2 BCC eutectic structure (refer to Figure 5-9 f), g) and associated insert). The former is attributed to the competitive grain growth mechanism occurring during solidification [167], while the latter is attributed to the cooling conditions experienced during welding. This aspect will be further detailed when analyzing the thermodynamic calculations.

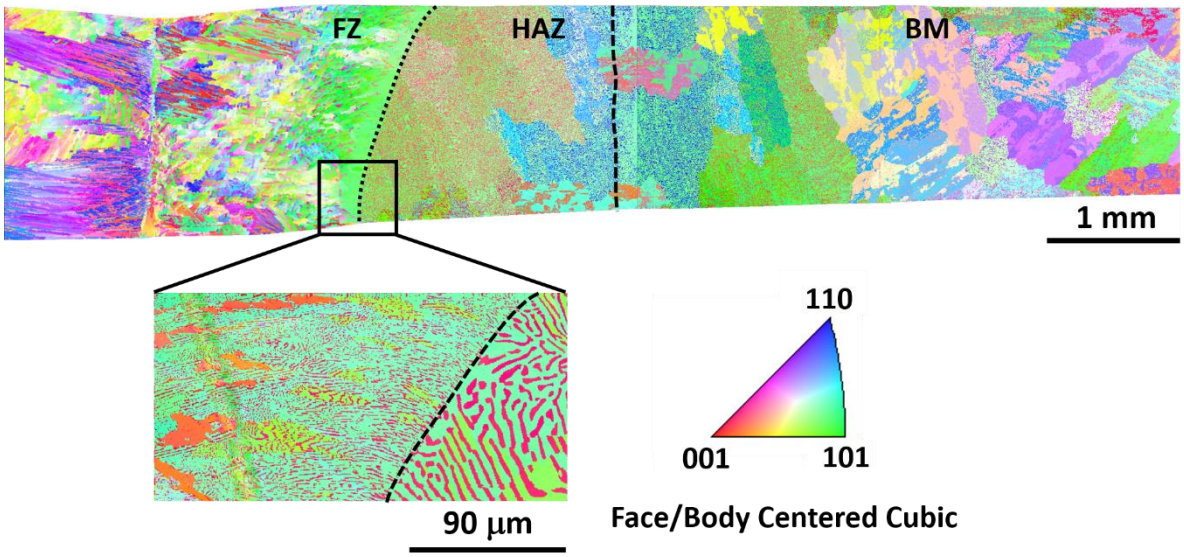

Figure 5-10. Electron backscattered diffraction images of the AlCoCrFeNi2.1 eutectic HEA welded joint.

It should be mentioned here that the above electron microscopy images did not reveal the presence of any precipitates due to limitation of resolution, although they exist, as it will be shown with the synchrotron X-ray diffraction data. In other words, the inability to detect these precipitates is related to their very low volume fraction and size. In addition to this, with EBSD it is not possible to distinguish between the disordered BCC and ordered B2 BCC phases, as they have the same crystallographic parameters. However, upon the use of high energy synchrotron X-ray diffraction both phases can be clearly distinguished, as will be detailed after.

To further elucidate the effect of welding thermal cycle on the thickness of the lamellae in the three different regions of the welded joint (BM, HAZ and FZ), Nano measurer 1.2 software was used. The average calculations are listed in Table 5-3.

Table 5-3 – Average interlamellar thickness evolution of eutectic FCC and B2 BCC phases in the welded joint of the as-cast $AlCoCrFeNi_{2.1}$ eutectic HEA (BM, HAZ and FZ).

Region	Average interlamellar thickness [μm]	
	FCC phase	B2 BCC phase
BM	3.27 ± 0.44	1.66 ± 0.57
HAZ	2.85 ± 0.36	1.95 ± 0.22
FZ	0.62 ± 0.18	0.25 ± 0.07

Comparing the eutectic lamellar thickness of the BM, HAZ and FZ, significant changes can only be observed in the FZ against the other two regions. Wani et al. [220] found that when the as-cast $AlCoCrFeNi_{2.1}$ eutectic HEA was treated at different annealing temperature between 800 and 1200°C (heat treatments that would partially correspond to the HAZ of the welded joint), there was no significant coarsening of the grains after annealing compared to the as-cast specimens due to slow diffusion and dual phase morphology of the eutectic HEA. Upon entering the FZ, the lamellar thickness of the FCC phase decreased to 0.62 ± 0.18 μm, while for the B2 BCC phase it decreased to 0.25 ± 0.07 μm. As detailed above, this refined grain structure is attributed to the faster cooling rate in the FZ compared to that experienced by the cast BM [257,258].

To clarify the effect of the weld thermal cycle on the partitioning of elements in the FZ, EDS mapping of the constituent elements (Al, Co, Cr, Fe and Ni) was performed as shown in Figure 5-11. The nominal composition of the BM, as well as the average chemical composition of the BM and FZ are further detailed in Table 5-4. It should be mentioned that the EDS results show that the proportion of the elements in the BM deviates from the alloy design, especially for Al, this being attributed to its low melting point and its partial burning during the casting process.

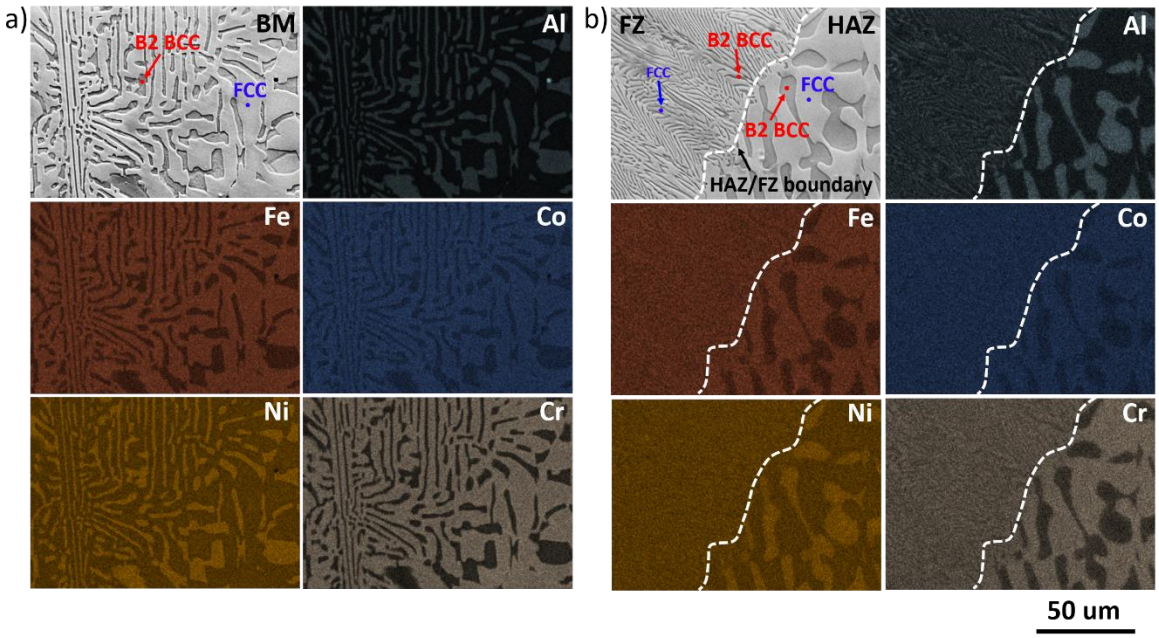

Figure 5-11. EDS mapping of the as-cast $AlCoCrFeNi_{2.1}$ eutectic HEA joint: a) BM; b) across the FZ and HAZ.

Table 5-4 – Chemical composition of the BM and FZ (at. %).

Region	Elements (at. %)				
	Al	Co	Cr	Fe	Ni
BM (Nominal)	16.39	16.39	16.39	16.39	34.44
BM (Averaged measured)	11.18	13.02	15.72	18.19	41.89
FZ (Averaged measured)	9.0	19.31	15.08	17.12	39.36

In the BM and HAZ, the FCC phase is mainly enriched in Co, Cr, and Fe, but depleted in Al and Ni. In opposition, the B2 BCC phase is mainly depleted in Co, Cr, and Fe, but abundant in Al and Ni, which is in line with previous works as detailed in [204,220]. Since among the constituent elements of the $AlCoCrFeNi_{2.1}$ eutectic HEA, Co, Cr, and Fe have a similar atomic radius and strong chemical compatibility, they have the tendency to form the disordered FCC phase [259], while the Al-Ni atomic pair has the largest negative mixing enthalpy, thus preferentially combining to form a Ni-Al type ordered B2 BCC phase [260]. Comparing the elemental maps obtained in both the HAZ and BM, it can be concluded that the welding peak temperature and duration in the former region is not enough to promote significant chemical differences between the major phases that exist in the material.

In the FZ, however, some changes exist. According to the theoretical model of Jackson and Hunt for rapid eutectic growth [261], the rapid solidification rate induced during welding can prevent the elemental partitioning and thus homogenize the material elemental composition, which is consistent with the recent work on laser welding of the same $AlCoCrFeNi_{2.1}$ eutectic HEA [50].

The nominal composition of the BM and that measured by EDS details key differences (refer to Table 5-3). It should be noted that the chemical composition given for the FZ is the average of multiple points taken across the FZ. The most significant difference concerns the loss of Al in the FZ, which is related to the significantly lower boiling (2519°C), vapor pressure (100 kPa) and vaporization heat (293 kJ/mol). It should be also mentioned that preferential loss of Al due to the high temperatures experienced by the melt pool will also be location-dependent: at the joint centerline, where the temperature is the highest, an increased Al loss is expected. Resulting from this Al loss in the FZ, there is some chemical redistribution of the remaining elements leading to an overall increase on the Co and Ni content in the FZ when compared to the as-cast BM.

5.2.3.2 High energy synchrotron X-ray diffraction

The microstructure of welded joints is strongly dependent on the peak temperature and cooling rate experienced by the material during welding. Moreover, the peak temperature and cooling rate varies with the distance to the center of the FZ [262]. To further support the above microstructure characterization, synchrotron X-ray diffraction was used to comprehensively analyze the phase structure evolution across the joint, including identification of precipitates and secondary phases. Representative individual diffraction patterns for each region are detailed in Figure 5-12 a), b), c) and d), representing the BM, HAZ1, HAZ2 and FZ, respectively. The lattice parameters of the different phases identified across the welded joint are detailed in Table 5-5.

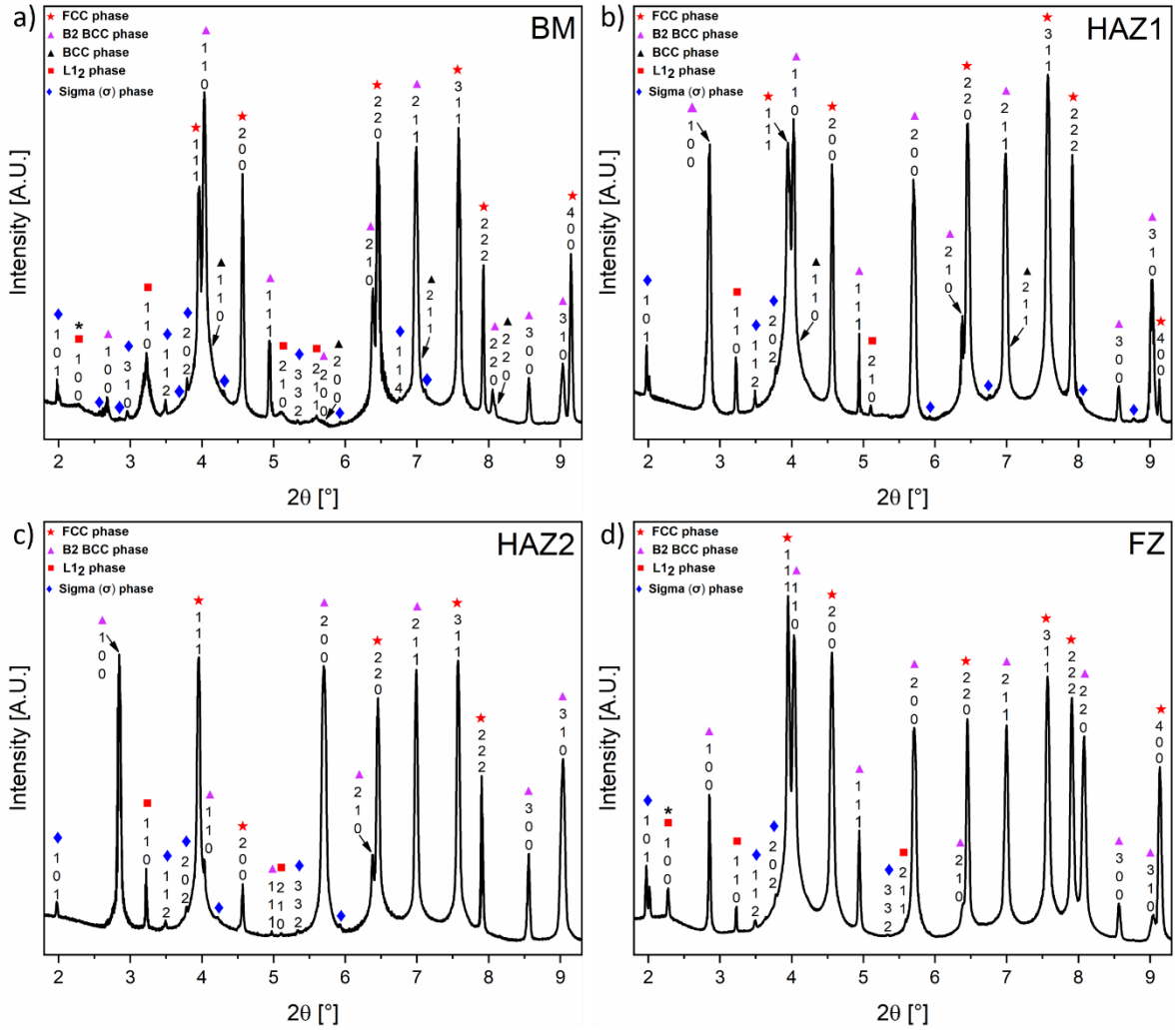

Figure 5-12. Individual synchrotron X-ray diffraction patterns of the AlCoCrFeNi2.1 eutectic HEA joint in: a) BM; b) HAZ1; c) HAZ2 and d) FZ.

Table 5-5 – Refined lattice parameters from BM, HAZ1, HAZ2 and FZ of the gas tungsten arc welded $AlCoCrFeNi_{2.1}$ eutectic HEA as obtained from high energy synchrotron X-ray diffraction.

Region	Phases				
	FCC	B2 BCC	BCC	$L1_2$	Sigma (σ)
BM	a=3.5702 Å	a=2.8594 Å	a=2.8431 Å	a=3.5574 Å	a=b=8.1768 Å; c=5.0185Å; $\alpha = \beta = \gamma = 90^o$
HAZ1	a=3.5705 Å	a=2.8592 Å	a=2.8430 Å	a=3.5571 Å	a=b=8.1761 Å; c=5.0187Å; $\alpha = \beta = \gamma = 90^o$
HAZ2	a=3.5714 Å	a=2.8587 Å	-	a=3.5693 Å	a=b=8.1683 Å; c=5.1702Å; $\alpha = \beta = \gamma = 90^o$
FZ	a=3.5701 Å	a=2.8593 Å	-	a=3.5573 Å	a=b=8.1771 Å; c=5.0179Å; $\alpha = \beta = \gamma = 90^o$

The phase identification from the high energy synchrotron X-ray diffraction data presented in Figure 5-12 a) indicates that the BM consists of the main phases that compose the lamellar (FCC and B2 BCC phases), as well as nanosized $L1_2$ FCC, disordered BCC and σ phases, as expected when the material is in the as-cast state [233].

The BM and HAZ1 possess all the same five phases: the FCC + B2 BCC phases that compose the eutectic microstructure, as well as nanoscale BCC, $L1_2$ FCC and σ phases. This is in good agreement with previous transmission electron microscopy work performed by Choudhuri et al. [233], where all these phases were identified except the σ phase. Although the σ phase was not identified in [233], the DFTEM results indicate that, besides the cluster-like $L1_2$ FCC nanosized phase, there still existed speckle-shaped precipitates in the $L1_2$ FCC matrix phase, with Choudhuri et al. not providing a specific phase identification for these specks. In combination with the results of the synchrotron data phase identification of the present work, it can be confirmed that these diffusely distributed speckle-like precipitates can be the now identified as σ phase.

When approaching the HAZ1 towards the FZ (HAZ2), no evidence of the BCC phase was noticed suggesting its dissolution into the material matrix owing to the higher temperatures experienced by this region during the welding process. The absence of this phase upon cooling to room temperature suggests that the cooling rate is not low enough to allow the precipitation of this phase as it occurs in the as-cast BM. The presence of this nanosized BCC phase in the as-cast $AlCoCrFeNi_{2.1}$ eutectic HEA is most likely due to the spinodal decomposition originating from compositional modulations in the B2 BCC phase matrix [220,263]. Wani et al. [220] found that water quenching after annealing at 800 ºC was sufficient to completely dissolve the nanosized BCC phase in the B2 BCC matrix while studying the effect of aging heat treatments on the same $AlCoCrFeNi_{2.1}$ eutectic HEA. This is consistent with the complete dissolution of the BCC phase observed in the HAZ2 region of the welded joint in the current work.

In the FZ, the detected phases include the FCC and B2 BCC phases that compose the eutectic microstructure, as well as $L1_2$ and σ nanosized phases. The previously observed disordered BCC phase is now absent, indicating that the solidification and cooling conditions experienced by this region of the joint prevented this phase to form.

It is important to mention here that the (100) superlattice reflections of the B2 BCC and $L1_2$ FCC phases detected by synchrotron X-ray diffraction data provide clear evidence for the ordered structures of these FCC and BCC phases. Indeed, these results are in good agreement with previous transmission electron microscopy work, where the same superlattice reflections were observed [233]. Besides this, there are additional diffraction peaks such as (110) and (210) in the ordered FCC phase compared to those of the disordered FCC phase, as marked in Figure 5-12. This is easily identified using synchrotron data, but is rarely reported in TEM characterization results.

The lattice parameters of the two matrix phases (FCC and B2 BCC) in the BM region obtained by Rietveld refinement are in good agreement with the data previously reported by Lozinko et al. [264], while the lattice constants of the nanosized phases (BCC, $L1_2$ and σ) are detailed for the first time in this work. Comparing the evolution of the lattice parameters of the FCC and B2 BCC phases, it can be observed a decrease towards the FZ for the later and the opposite behavior for the former. Since no distortion of the welded joints was observed, this behavior is the way for the material to accommodate the thermal strains that occur during welding. In fact, the maximum microstrain calculated for the welded joint occurs in the HAZ and takes the value of 330 με. This small microstrain can be attributed to the relatively slow cooling rate of the joint, owing to the large heat input typical of arc-based welding processes, which allows for the material to accommodate thermal strains more effectively upon cooling to room temperature.

Throughout the BM, heat affected and FZ the existing phases may vary. Moreover, to further quantify the changes in the volume fraction of each phase, Rietveld refinement was performed. The aim is to determine how the volume fraction of each phase varies across the welded joint. Since the thermal cycle

is location dependent, the peak temperature and permanence time at temperatures that can promote solid-state transformations will vary. Table 5-6 summarizes the phase volume fraction of the existing phases in different regions of the welded joint as determined by Rietveld refinement and by image processing using ImageJ software. Overall, there are no major deviations in the phase fraction results obtained from Rietveld refinement or by optical methods. Identification of the nanoscale phases by imaging methods was hindered by the lack of resolution of the techniques used, thus the need to complement this microstructure characterization with high energy synchrotron X-ray diffraction measurements. Synchrotron radiation as a non-destructive testing technique can then be used as a complementary characterization method alongside the optical aid electron microscopy which are destructive characterization tools. Moreover, with key advantages such as high photon flux and narrow beam spot sizes, it is possible to get bulk microstructure information with sufficient statistical significance for quantitative (and qualitative) characterization. A detailed analysis of the evolution of the phase volume fraction of the welded joints is presented next.

Table 5-6 – Volume fraction evolution of the FCC, B2 BCC, disordered BCC, $L1_2$ FCC and σ phases across the welded joint (BM, HAZ1, HAZ2 and FZ) as obtained by Rietveld refinement and light optical micrographs.

		Phase volume fraction [%]									
Phases		**FCC**		**B2 BCC**		**BCC**		**$L1_2$**		**Sigma (σ)**	
Method		**MAUD**	**ImageJ**	**MAUD**	**ImageJ**	**MAUD**	**ImageJ**	**MAUD**	**ImageJ**	**MAUD**	**ImageJ**
Region	BM	62.69	61.93	33.60	38.07	0.57	-	2.03	-	1.11	-
	HAZ 1	64.40	61.46	34.08	38.54	0.19	-	0.75	-	0.58	-
	HAZ 2	57.79	56.47	41.73	43.53	-	-	0.21	-	0.27	-
	FZ	86.62	84.06	12.79	15.94	-	-	0.38	-	0.21	-

The BM primarily consists of the eutectic-composing phases with 62.69 and 33.60 % of FCC and B2 BCC phases, respectively, which is consistent with measurements made with TEM by other researchers [226,233,265]. Due to the small size and scattered distribution of the nanosized phases that may compose this material, their quantification is difficult by conventional characterization means and, so far, no quantitative analysis has been reported. However, these nanoscale phases are clearly distinguished

in the low-noise diffraction data, as previously shown in Figure 5-12 a). The Rietveld refinement data shows that the volume fractions of the identified nanosized $L1_2$ FCC, BCC and σ phases were 2.03, 1.11 and 0.57 %, respectively.

Entering the HAZ1 region, the volume fraction of the eutectic phases does not significantly change compared to the non-affected BM. Moreover, this region still retains all the nanoscale phases identified in the BM, but there is a clear partial dissolution since the volume fractions of the $L1_2$ FCC, BCC and σ phases is reduced to 0.75, 0.19 and 0.58 %, respectively. Going toward the fusion boundary but still in the HAZ2, the phase volume fraction of the eutectic phases undergoes a subtle change, with the BCC phase starting to show a slight increase from 34.08 to 41.73 %, with a corresponding decrease in the volume fraction of the FCC phase from 64.40 to 57.79 %. As it will be shown in the microhardness plots, this volume fraction increase of the hard B2 BCC phase in the HAZ2 region will correspond to an increase in hardness (to be further assessed in the microhardness plots of Figure 5-16). Still in HAZ2 region, the higher peak temperatures and permanence time at temperatures where solid-state transformations can occur, further promotes dissolution of the nanoscale phases, with the BCC phase dissolving into the B2 BCC matrix (refer to Figure 5-12 c)).

A significant change in the volume fraction of the FCC and B2 BCC eutectic phases in the FZ is noted, with the volume fraction of the FCC phase increasing from 57.79 to 86.62 %, while the B2 BCC phase retained only 12.79 % after melting and rapid material solidification. However, from Figure 5-12 d), it can be observed that the diffraction peaks corresponding to the B2 BCC phase possess high intensity, which is likely due to the rapid solidification in the FZ promoting strong texture effects in the B2 BCC phase. The nanosized $L1_2$ FCC and σ phases formed in the FZ, although their volume fraction was slightly below than measured in the as-cast BM (0.38 and 0.21 %, respectively). Again, the fast cooling rate during welding can suppress the formation of these phases upon cooling, thus justifying the differences observed between the FZ and the as-cast BM.

5.2.3.3 CalPhaD-based calculations

The Scheil-Gulliver model was used to reproduce the solidification behavior and phase evolution of the FZ in the as-cast $AlCoCrFeNi_{2.1}$ eutectic HEA under non-equilibrium conditions. The high temperature of the melt pool induces elemental redistribution and promotes preferential loss of some elements due to evaporation, thus altering the starting nominal composition of the alloy. Therefore, to predict the solidification behavior more accurately in the FZ, the nominal alloy composition of the $AlCoCrFeNi_{2.1}$ eutectic HEA and the average elemental composition obtained by EDS measurements at multiple points in the FZ were used in the Scheil-Gulliver model to calculate the potential solidification pathways. It should be mentioned that the Scheil-Gulliver model simulation has three main assumptions [266]: 1) no back diffusion is considered in the solid phase; 2) diffusion in the liquid phase is extremely fast so that the liquid phase always has a homogeneous composition; and 3) phase equilibrium between liquid and solid phases is achieved at the local interface.

Figure 5-13 a) details the solidification pathway from the Scheil-Gulliver model using the nominal composition of the alloy, while Figure 5-13 b) considered the average FZ composition. From Figure 5-13 a), it can be seen that the solidification pathway obtained based on the standard eutectic composition has only the eutectic reaction, which can be described as Liquid → Liquid + FCC (Disordered) + B2 BCC (Ordered) reaction. However, the solidification pathway shown in Figure 5-13 b) occurs in two steps as follows: Liquid → Liquid + FCC (Disordered), and then followed by eutectic reaction of the remaining liquid, i.e., Liquid → Liquid + FCC (Disordered) + B2 BCC (Ordered).

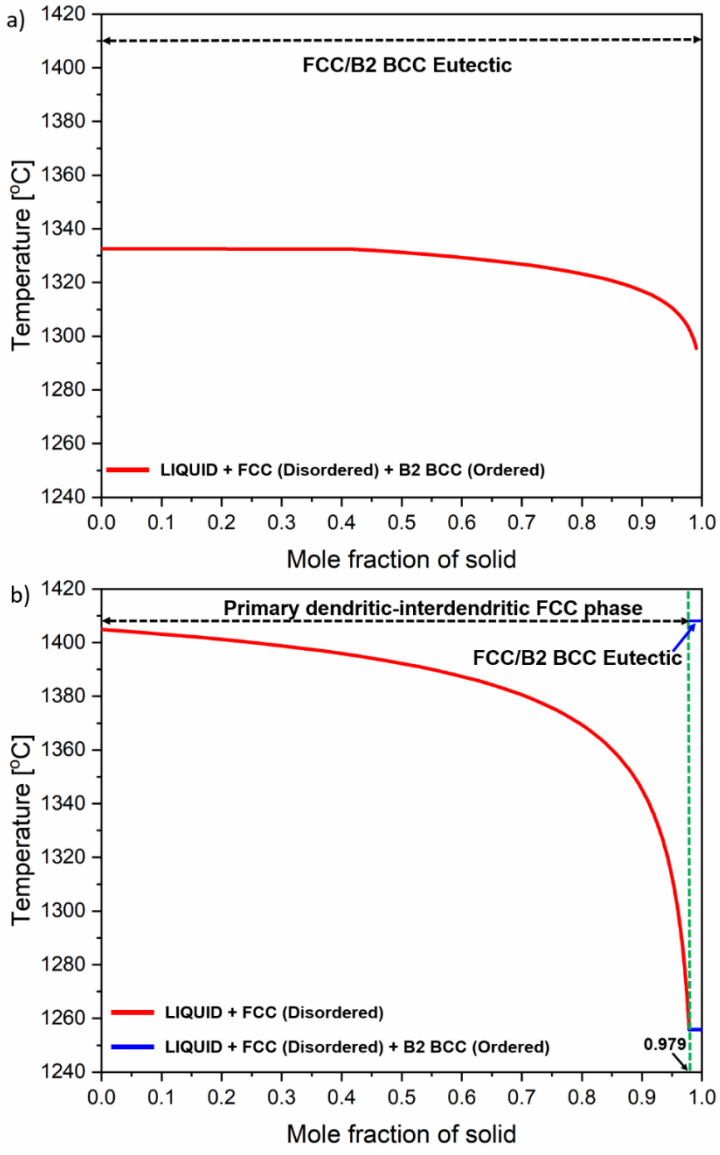

Figure 5-13. Scheil-Gulliver solidification pathway calculations using ThermoCalc (TCHEA 5.1 database) considering: a) nominal alloy composition; b) average FZ composition.

As can be seen from the observed dendritic FCC phase in the optical micrographs of the FZ (refer to Figure 5-9 f)), the solidification pathway of Figure 5-13 b), which considered the FZ average composition,

is more compatible with that experienced by this region of the joint. It is obvious that the elemental distribution in the FZ does deviates from the standard eutectic composition and can be described as a sub-eutectic FZ. Combined with the microstructural features of the FZ in Figure 5-9 f), it is expected that when the composition deviates from the standard eutectic composition, solidification of the primary dendritic FCC phase from the liquid starts at a temperature of 1410 ^{o}C, followed by the eutectic reaction at 1256 ^{o}C, producing a mixed lamellar structure of disordered FCC and ordered B2 BCC phases. Compared to the nominal composition of the alloy used, the solidification pathway changes significantly. However, based both on the nominal alloy composition (Figure 5-13 a)) and on the average elemental composition of the FZ measured by EDS (Figure 5-13 b)), the eutectic microstructure predicted by thermodynamic calculations is composed of disordered FCC and ordered B2 BCC phases, which is in good agreement with the eutectic phases determined by synchrotron X-ray diffraction measurements presented above. However, the small amount of nanosized $L1_2$ FCC and σ phases obtained by synchrotron X-ray diffraction in the FZ are not predicted by the Scheil calculations. This disagreement can be likely due to deviations is composition due to the possible presence of minor impurities in the starting materials used to cast the master alloy, thus promoting the formation of these phases.

The evolution of the elemental redistribution during non-equilibrium solidification is provided in Figure 5-14. Figure 5-14 a) reproduces the redistribution behavior of the elements in the dendritic and interdendritic FCC phase, as well as in the eutectic lamellar structure (FCC and B2 BCC phases). To distinguish the elemental partitioning in the FCC and B2 BCC phases among the eutectic lamellar structure, the evolution of each element in the B2 BCC phase is detailed in Figure 5-14 b), so that the variation of the elemental content in the eutectic FCC phase can be deduced and compared to the dendritic FCC phase.

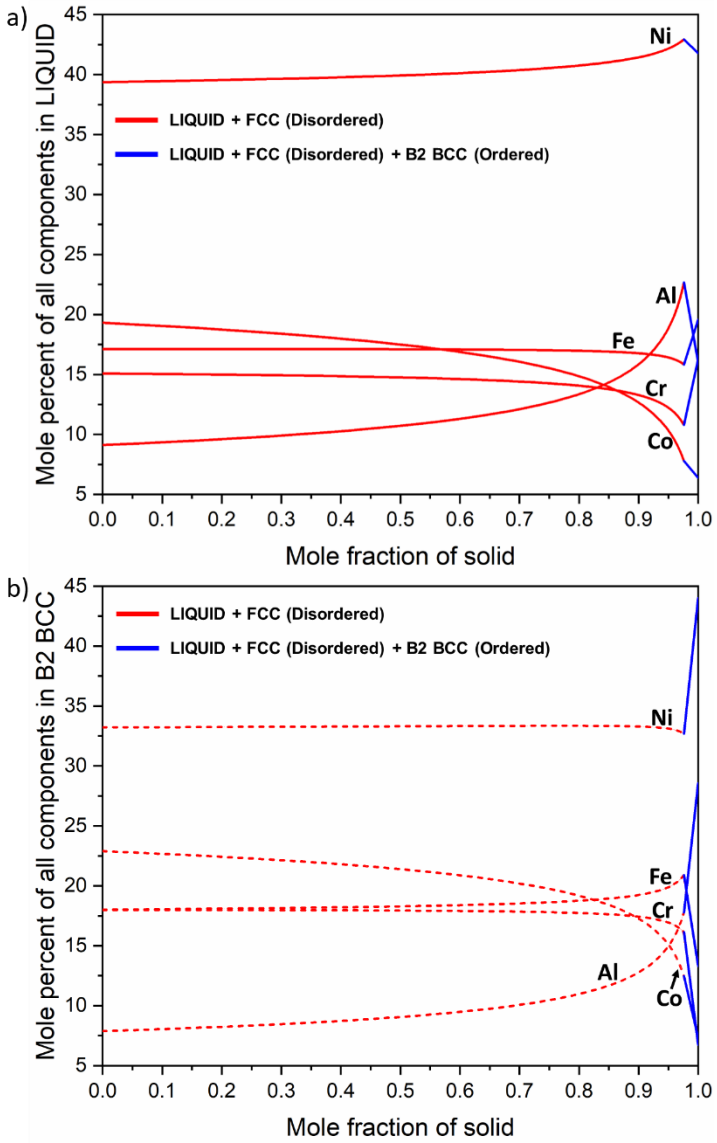

Figure 5-14. Elemental redistribution obtained from the Scheil-Gulliver calculations for the as-cast $AlCoCrFeNi_{2.1}$ HEA (considering the average FZ composition): a) composition in the liquid phase; b) composition in the B2 BCC phase.

In Figure 5-14 a), the red solid lines represent the elemental evolution in the dendrites, while the intersection between the red and blue solid lines correspond to the interdendritic composition. The blue solid lines denote the elemental partition in the FCC and B2 BCC phases of the eutectic lamellar structures. For a clearer analysis of the solidification process, the partition coefficient, k, is used to explain the chemical heterogeneity associated with solidification, being an indication of a given element to partition during solidification. k is expressed as the C_s/C_L ratio, where C_s is a given element content in the solid and C_L in the liquidus line. When the partition coefficient is above 1, it reflects the enrichment of a specific element in the interdendritic region, and conversely, when the partition coefficient is below 1, it indicates an increase in the concentration of that element in the dendritic region. When k approaches

1, it represents a homogeneous distribution of that element throughout the microstructure [267]. The evolution of the red solid line in Figure 5-14 a) shows that the partition coefficients for Al and Ni are larger than 1, especially for the Al, thus suggesting that the interdendritic region is enriched in these two elements. Especially due to the higher k of Al, the interdendritic space will be preferentially enriched in Al. Apart from this, Co, Cr and Fe all possess k values below 1, revealing that the dendritic region will be enriched in these elements. The predicted redistribution of the elements in the dendritic and interdendritic regions is consistent with that measured by EDS point scanning, as shown in Figure 5-15 b) and c). A more detailed analyzes and discussion of this EDS data will be given later.

The variation in the elemental composition in the B2 BCC phase is given by the blue solid line in Figure 5-14 b). It can be observed that from the onset of the eutectic reaction, both Ni and Al show a linear upward trend, while the remaining elements show a downward trend, which suggests that the B2 BCC phase is enrich in Ni and Al, while the FCC phase will be enriched in Co, Cr and Fe. Combined with the evolution of the blue solid line in Figure 5-14 a), it can be deduced that the eutectic FCC phase contains more Co, Cr and Fe than the B2 BCC phase.

To further verify the reliability of the thermodynamic calculations, Figure 5-15 b), c), d) and e) detail representative point compositional results of the dendritic (spot 1) and interdendritic (spot 2) regions, the FCC phase (spot 3) and the B2 BCC phase (spot 4) in the FZ, respectively, to further investigate the elemental differences within these different microstructures in the FZ and compare them with the thermodynamic calculations.

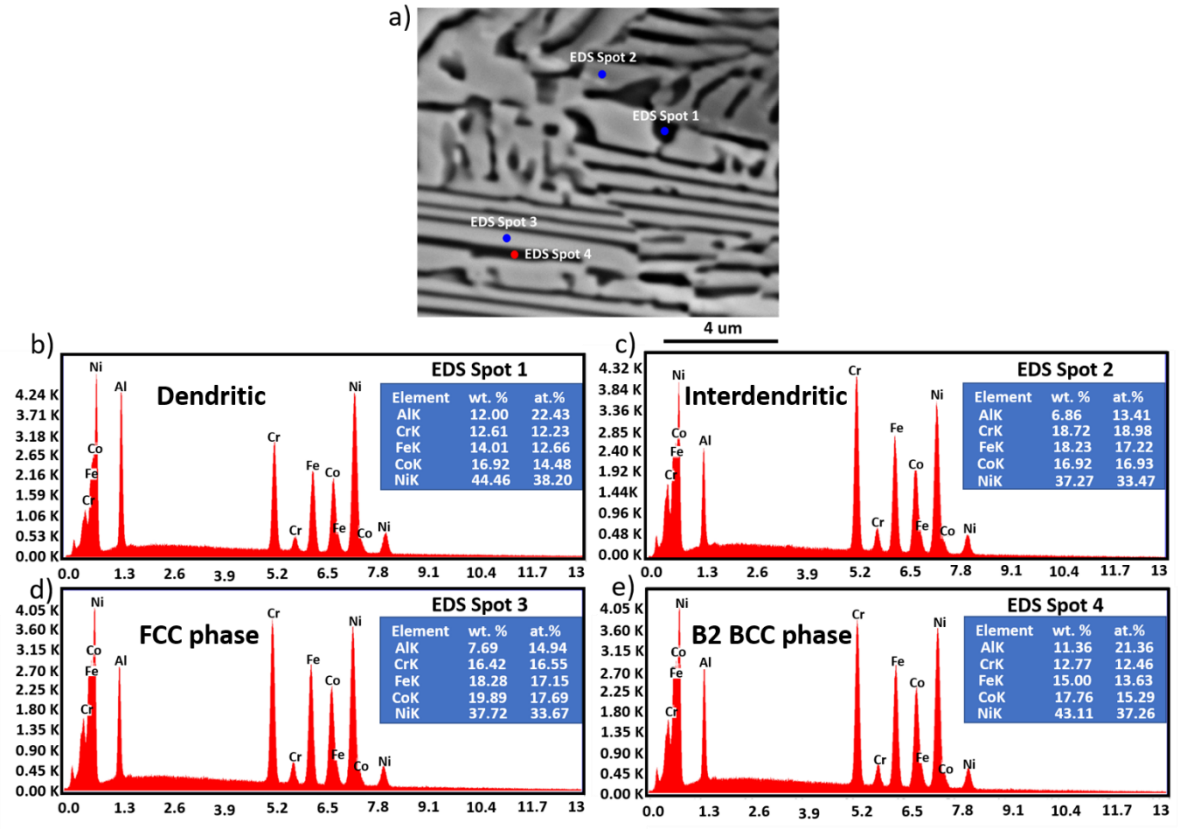

Figure 5-15. a): SEM micrograph along with the EDS point analysis in different region within the FZ; b to e) are EDS patterns and the resulting compositions of points 1 to 4, respectively.

Overall, the elemental segregation in the FZ is not significant, but there is still microsegregation. As can be seen from the thermodynamic calculations (refer to Figure 5-14), the FZ first forms as FCC dendrites, followed by the eutectic FCC + B2 BCC eutectic structure. A comparison of the results from the EDS point scans in Figure 5-15 b) and d) shows that, the composition of Co, Cr and Fe in the dendritic region are higher than that in the interdendritic space. Concomitantly, there is a preferential Al and Ni enrichment in the interdendritic space. The existence of these different composition domains can be attributed to microsegregation, which is commonly found in fusion-based welding processes, and depends heavily on the partition coefficient of each element in the liquid [268]. The obtained EDS measurements are consistent with the results calculated in this work using Scheil-Gulliver model, as previously shown and discussed in Figure 5-14. The occurrence of component microsegregation in dendritic structures obtained during rapid solidification was also observed in work of Güler et al. [269] for HEAs of the Al-Co-Cr-Fe-Ni-Ti system. For the eutectic structure, as expected, the FCC phase in the FZ contains preferentially enriched in Co, Cr and Fe than in the B2 BCC phase, but the opposite occurs for Ni and Al. This observation is, thus, in good agreement with the elemental distribution evolution calculated by the Scheil-Gulliver solidification model.

5.2.3.4 Microhardness and tensile properties

For evaluating the effect of the weld thermal cycle on the local strength of the joint, microhardness mapping was performed. Figure 5-16 a) details the microhardness mapping of the joint, while Figure 5-16 b) details the microhardness distribution obtained at mid height of the material.

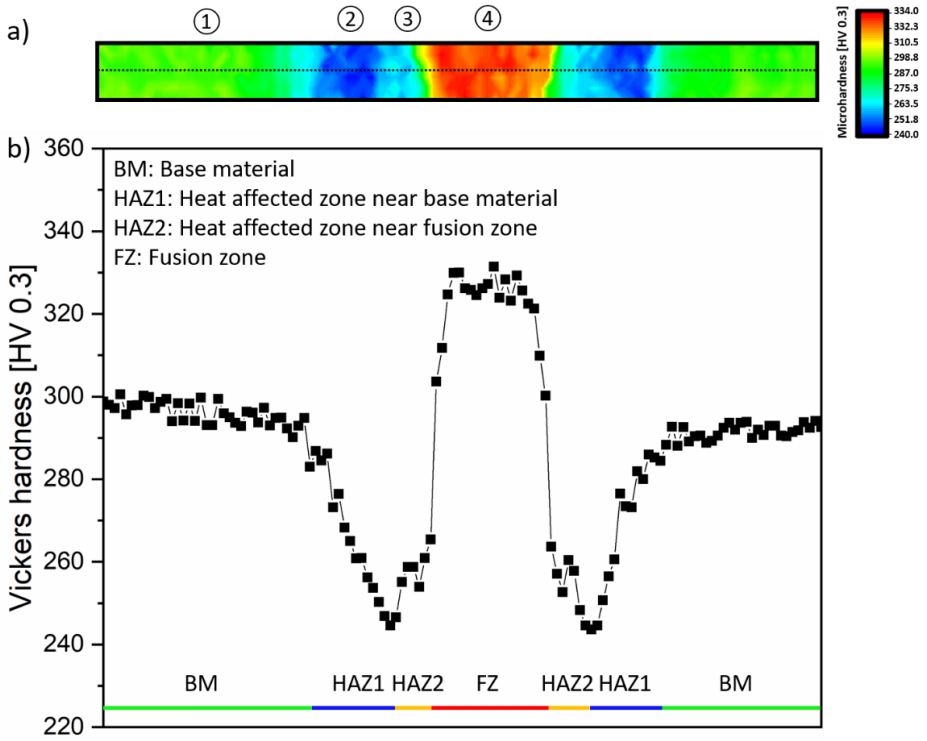

Figure 5-16. a) Microhardness map across the welded joint; b) Microhardness profile obtained at the mid height of the welded joint (black dotted line across the hardness map in a)).

Based on the evolution of the microhardness, four distinct regions within the welded joint are identified: the BM, the HAZ1, the HAZ2 and the FZ.

The BM hardness has a microhardness around 300 HV, which serves as the benchmark for comparison with the other regions of the joint. When entering in the HAZ (HAZ1 region), a clear downward trend to 242 HV in hardness is observed. From the previous microstructure characterization, it was observed that this region was similar to the as-cast BM. The only difference was the volume fraction of nanosized phases that existed in the FCC and B2 BCC eutectic phases (refer to Table 5-6). In fact, the decrease in the volume fraction of these nanosized phases can justify the decreased hardness of this region. Obviously, it is clear that the nanosized phases in the FCC and B2 BCC phases act as precipitation strengtheners, so that their (partial) dissolution will decrease the material strength. Xiong et al. [270] performed a quantitative analysis of the strengthening induced by the presence of the $L1_2$ FCC and BCC nanosized phases within the lamellar structure FCC and B2 BCC phases of the same material.

Their results showed that these nanosized phases increase the alloy strengthening while sacrificing ductility. Therefore, it can be deduced that when their dissolution occurs, this will lead to a reduction in hardness, which is consistent with the results of the current work. Still proceeding to the HAZ and approaching the FZ (HAZ2 region), there is a slight increase in hardness which is associated to the increase in the volume fraction of the hard B2 BCC phase, as previously observed from the synchrotron X-ray diffraction data.

Interestingly, the FZ shows a significant increase in hardness to 330 HV. This is mainly due to the considerable reduction in the lamellar thickness on this region over that observed in both the BM and HAZ (refer to Table 5-3), which is referred to as a grain refinement strengthening mechanism. The reduction in grain size increases the number of grain boundaries, which act as effective barriers to dislocation movement, thus increasing the accumulation of dislocations, supporting that grain boundary strengthening is also an auxiliary factor in this hardness increase. Miao et al. [260] previously reported that the nanosized phases and lamella thickness were the main factors influencing the hardness of eutectic HEAs. According to Miao's work, when the lamella thickness was reduced to 0.51 μm, the contribution of the phase interface was more important than that due to precipitation strengthening. Although the solidification conditions in the FZ resulted in a phase volume fraction of only about 10% for the hard B2 BCC phase, as well as slightly less volume fraction of the nanosized phases, the potential hardness losses are compensated by the strengthening induced due to grain refinement.

For the purpose of assessing the effect of welding on the mechanical behavior of the as-cast $AlCoCrFeNi_{2.1}$ eutectic HEA, tensile experiments were also performed. Figure 5-17 details representative engineering and true stress-strain curves obtained for both the BM (used as benchmark) and welded joint. The yield strength, ultimate tensile strength and elongation at fracture for each condition are detailed in Table 5-7.

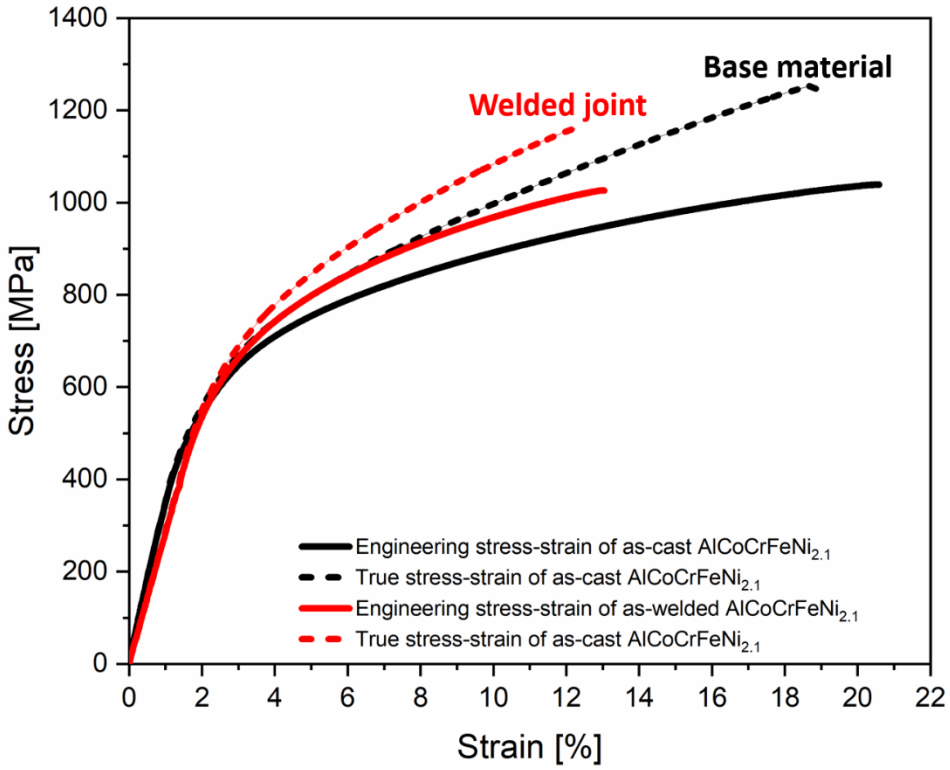

Figure 5-17. Representative tensile stress-strain curves of BM and as-welded as-cast $AlCoCrFeNi_{2.1}$ eutectic HEA at room temperature under the strain rate 10-3 s^{-1}.

Table 5-7 – Mechanical behavior of the BM and as-welded $AlCoCrFeNi_{2.1}$ eutectic HEA from tensile testing until failure.

Reference	Yield strength [MPa]	Ultimate tensile strength [MPa]	Fracture strain [%]
$AlCoCrFeNi_{2.1}$ BM	284 ± 8	1039 ± 5	20.6 ± 0.2
Welded joint	372 ± 12	1026 ± 10	13.0 ± 0.4

Comparing the tensile test results obtained in both different states, it is evident that the welding process modifies the mechanical properties of the material. The yield strength increases from ≈ 284 MPa in the as-cast state to ≈ 372 MPa in the as-welded material. This increase can be explained considering the strengthening effect induced by the refined lamellar structure of the FZ. However, compared to the as-cast material, the plasticity in the as-welded state decreases, with the elongation being reduced from ≈ 20.6 to ≈ 13.0 %. This decrease in ductility is attributed to the composite-like structure of the welded joint, where the different mechanical behavior of the BM, HAZ and FZ, will promote a different and

localized mechanical response across the joint as it will be shown with the DIC data. Fracture of the welded joints systematically occurred in the non-affected BM. Further analysis of the deformation of each region of the welded joint is detailed next considering the DIC data acquired. Here, it is worth mentioning that the properties of the BM used in this work are below those reported for other $AlCoCrFeNi_{2.1}$ eutectic HEAs [190], which can be due to the raw materials used, as well as the casting conditions.

Figure 5-18 was obtained considering the DIC data obtained during tensile testing. Each curve corresponds to one of the three key regions of any welded joint: BM, HAZ and FZ. From Figure 5-18, it can be seen that these three regions exhibit different yield strengths, which was already expected due to the microstructural changes induced by the weld thermal cycle. These results are in good agreement with what would be expected solely considering the microhardness measurements previously shown in Figure 5-16.

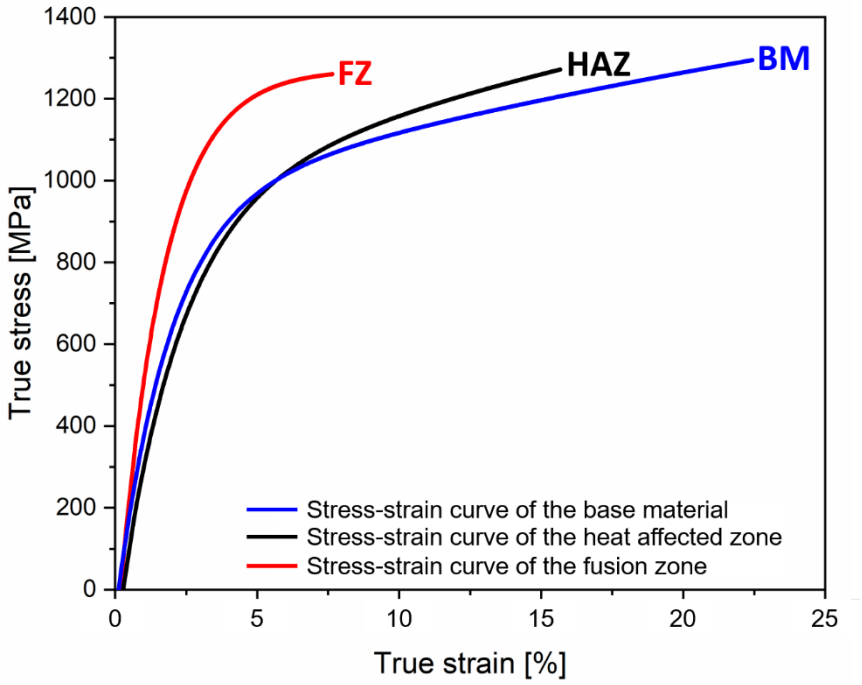

Figure 5-18. Tensile curves obtained from the DIC measurements for different regions: BM (blue line), HAZ (black line) and FZ (red line).

The strain in the FZ when failure of the joint occurred was only 7 %. The increased hardness and refined microstructure of this region will promote a preferential deformation in the softer regions of the welded joint, i.e., in the BM and HAZ. However, when the material fractured, the strain reached up to ≈ 22.0 and ≈ 15.8% in BM and HAZ, respectively, exhibiting a good ductility. The local deformation of the BM region is in good agreement with the bulk mechanical response of the BM specimen used to benchmark the mechanical properties against the welded joint. This also justifies why the overall joint ductility is reduced

as compared to the BM specimens: the composite nature of the welded joint promotes increased strain concentration at specific regions which eventually fail.

Purely considering the local tensile curves obtained by DIC of the three regions shown in Figure 5-18, it would be expected that fracture would occur in the softer HAZ, rather than in the BM. The systematic failure of the welded joints in the BM can be related to the relatively larger volume fraction of nanosized phases which can acts as stress concentrators. In the BM, there is a larger amount (relative to the HAZ) of dispersed and hard nanosized $L1_2$ FCC, BCC [271] and σ phases [272], which can aid in premature cracking development, ultimately leading to fracture in this region.

It is also possible to speculate on the load transfer behavior across the welded joint. Specifically, in the early stages of deformation, the HAZ, which is the softest zone, bears more of the loads first, and once it yields, the load starts to be transferred to the BM. With further deformation, the initially soft HAZ begins to harden, allowing the initially hard BM zone to accommodate more deformation and eventually fracture due to the presence of the dispersed nanosized precipitates.

To further clarify the fracture mechanism of the welded joints, post-mortem EBSD analysis was performed. Figure 5-19 a), b) and c) depict the EBSD KAM maps for the fracture area (BM region), the HAZ1, the HAZ2 and the FZ, respectively, while Figure 5-19 d) details the KAM values distribution for these four regions. KAM maps show the local misorientation across grains, which can be used to infer on the dislocation density: the change in color from blue to red indicates an increase in the KAM values, which is associated with increased misorientation and strain distortion in the material. The comparison of the KAM maps of these four regions in the fractured specimen reveals that the KAM values increase from the FZ to the non-affected BM. This suggests a larger strain imparted by the BM, while the FZ has accommodated the least amount of plastic deformation during the tensile deformation, owing to its refined grain structure. The associated higher dislocation density in the fractured region of the BM can be induced by the presence of preferential stress concentrator sites stress resulting from the presence of the dispersed and hard nanosized $L1_2$ FCC, BCC and σ phases contained in the BM.

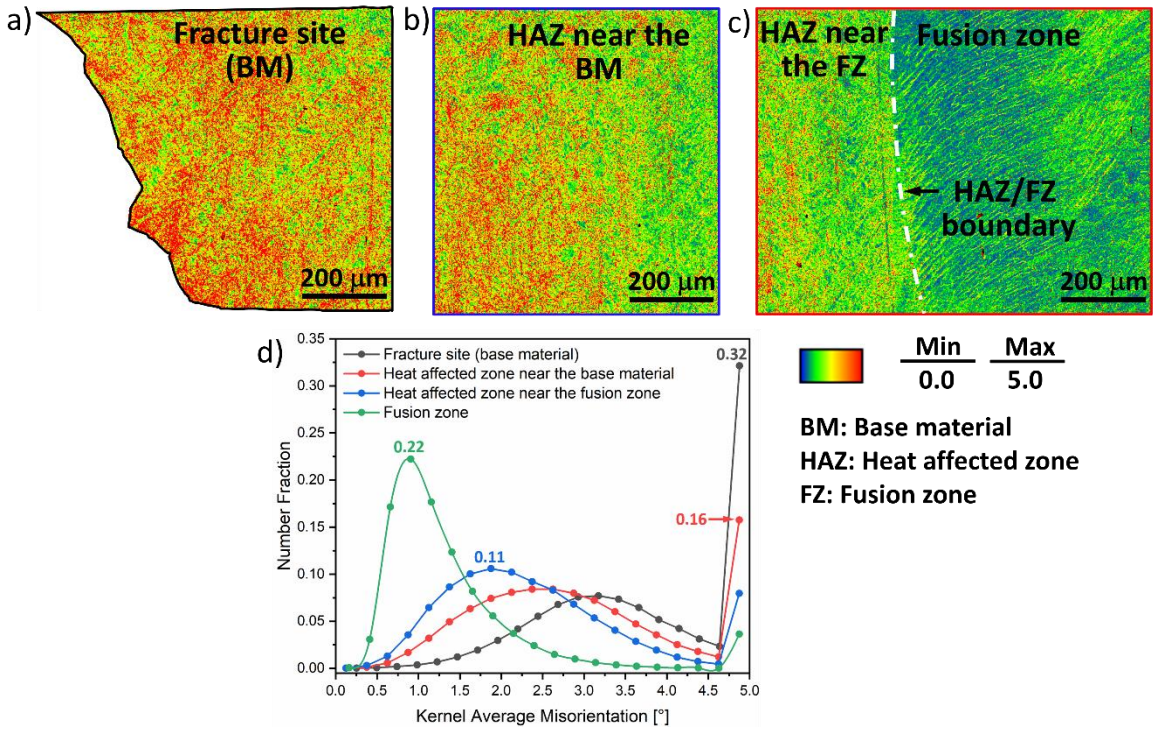

Figure 5-19. KAM maps of the fractured specimen considering different location across the joint: a) fracture site (BM); b) HAZ1 and c) HAZ2, as well as FZ. d) KAM values distribution in the analyzed regions.

The tensile fracture morphology of the gas tungsten arc welded joints of the $AlCoCrFeNi_{2.1}$ eutectic HEA was observed by SEM, as shown in Figure 5-20. As marked in Figure 5-20 c), the fracture has cleavage facets, as well as a large number of ductile dimples, disclosing a mixed fracture pattern of ductility and brittleness, but with significant predominance of the former. Further observations evidence that the cleavage facets generated by the brittle B2 BCC phase coexist within the dimples of the fracture surface. It can be inferred that during the tensile loading process, the soft FCC phase is significantly deformed and gradually thinned at the upward edge, and eventually the hard B2 BCC phase remains at the bottom of the ductile dimples due to the small amount of deformation sustained by this phase. Thus, the good strength/ductility synergy of the welded joint is attributed to the joint mechanical behavior of both the soft FCC and hard B2 BCC phases.

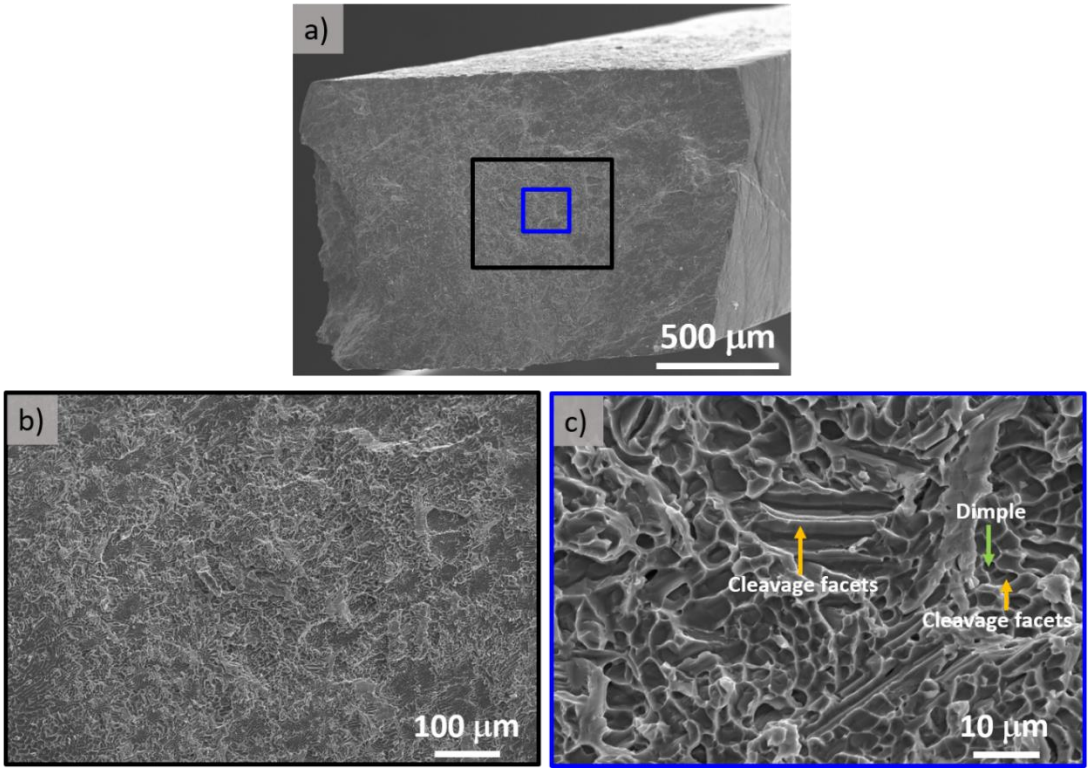

Figure 5-20. Fracture surface analysis of the as-cast $AlCoCrFeNi_{2.1}$ gas tungsten arc welded joint: a) overview; b) and c) close-up detailing brittle and ductile features.

5.2.4 Conclusions

This work investigated the effect of GTAW on the microstructure and mechanical properties of an as-cast $AlCoCrFeNi_{2.1}$ eutectic HEA combining advanced materials characterization and thermodynamic calculations. The following main conclusions can be drawn:

1) GTAW was able to successfully produce full penetration and defect-free welded joints, suggesting the potential of this fusion-based welding process to join these advanced engineering alloys.

2) High energy synchrotron X-ray diffraction was used to determine the existing phases across the joint, while CalPhaD simulations were used to predict the microstructure evolution.

3) The weld thermal cycle did not change the eutectic structure across the whole joint, although the volume fraction varied.

4) The HAZ evidenced softening in response to the weld thermal cycle, which is attributed to the partial dissolution of the nanosized phases that compose the starting alloy.

5) In the FZ, although the volume fraction of the hard B2 BCC phase is only ≈ 12 %, the existence of a significantly refined microstructure renders an increased hardness compared to the as-cast BM.

6) Mechanical testing of the joints showed that the yield strength of the joints was higher than that of the BM, whilst there was an obvious reduction in ductility. The fracture occurred in the BM, which is mainly due to the nanosized phases contained in the BM acting as stress concentrators.

6.

MICROSTRUCTURE AND MECHANICAL PROPERTIES OF GAS TUNGSTEN ARC WELDED $Fe_{42}Mn_{28}Co_{10}Cr_{15}Si_5$ JOINTS

6.1 Deformation mechanism of a metastable $Fe_{42}Mn_{28}Co_{10}Cr_{15}Si_5$ high entropy alloy probed in-situ with synchrotron X-ray diffraction

6.1.1 Introduction

HEAs were first discovered independently by Yeh et al. and Cantor et al. in 2004 [1,2]. At the beginning, focus was devoted to the development of single phase HEAs. However, it is difficult to design single phase HEAs that simultaneously possess a good combination of strength and plasticity [170,273]. In order to overcome the strength-ductility paradigm, TRIP [274,275], TWIP [60,276], or the combined activation of TWIP and TRIP [277] have become new concepts in the design of non-equiatomic HEAs in the recent years. Such HEAs containing TRIP and/or TWIP effects are generally referred to as metastable HEAs [278]. In addition, such metastable HEAs often introduce auxiliary strengthening mechanisms such as precipitation strengthening [57,58] and solid solution strengthening [279] which further increase the material strength.

The deformation mechanisms of metastable HEAs can be adjusted by the alloy SFE which is composition- and temperature-dependent [280]. When the SFE is above 45 mJ/m^2, the dominant deformation mode is dislocation slip. With a decrease in the SFE, the dislocation slip-dominated deformation mechanism gradually changes to TWIP (20 mJ/m^2 > SFE > 40 mJ/m^2) or TRIP (SFE < 15 mJ/m^2) [281]. The SFE values for the combined effect of TRIP and TWIP have also been reported to range between 13 mJ/m^2 and 18 mJ/m^2 [282,283]. Moreover, the SFE is key to changing the stability of the γ-f.c.c. matrix phase [62].

So far, most studies on the mechanical behavior of metastable HEAs have been primarily focused on advanced electron microscopy characterization [63,284–286], while only a few studies have used diffraction-based techniques to trace, in real time, the microstructure evolution and deformation mechanisms activation during deformation [146,287,288]. Specially for the optimized composition of $Fe_{42}Mn_{28}Co_{10}Cr_{15}Si_5$ developed by Nene et al. [62] there is still a significant gap on the microstructural evolution and assessment of the competing deformation mechanisms experienced by the alloy upon loading. Besides, the stress partitioning behavior, strengthening effects, lattice strain evolution, and the variation of the stacking fault probability with deformation are yet to be quantified.

In this study, the activation and changes in the deformation mechanisms of an as-cast $Fe_{42}Mn_{28}Co_{10}Cr_{15}Si_5$ metastable HEA during tensile deformation was evaluated in real time for the first time using high energy synchrotron X-ray diffraction. Stemming from the acquired diffraction data, the micromechanical behavior of the two main constituent phases of the alloy was determined. The TRIP and TWIP effects of the current studied material during tensile deformation and the onset for each to occur have been revealed and discussed. By quantifying the evolution of dislocation density and stacking faults, the strengthening contributions for the material strength have been elucidated for the first time. A detailed and comprehensive analysis of the diffraction data determined the relationship between the microstructure evolution and the alloy mechanical behavior, providing a deeper understanding of the different deformation mechanisms activated in TRIP/TWIP metastable HEAs.

6.1.2 Starting materials

The material used in this work was an as-cast non-equiatomic metastable $Fe_{42}Mn_{28}Co_{10}Cr_{15}Si_5$ (at. %) HEA, which was produced at the Sophisticated Alloys Inc. in Butler, PA, USA, by vacuum induced melting under an argon atmosphere [289]. The dimensions of the samples used for the in-situ synchrotron X-ray diffraction measured were detailed in Figure 3-4.

6.1.3 Results

6.1.3.1 Microstructure

Figure 6-1 a) and b) depict the microstructure of the metastable $Fe_{42}Mn_{28}Co_{10}Cr_{15}Si_5$ HEA before and after tensile deformation, respectively. After etching, a dual γ-f.c.c. / ε-h.c.p. microstructure is evidenced in both conditions. The bright and dark contrasting colors are related to the microstructural features of both phases.

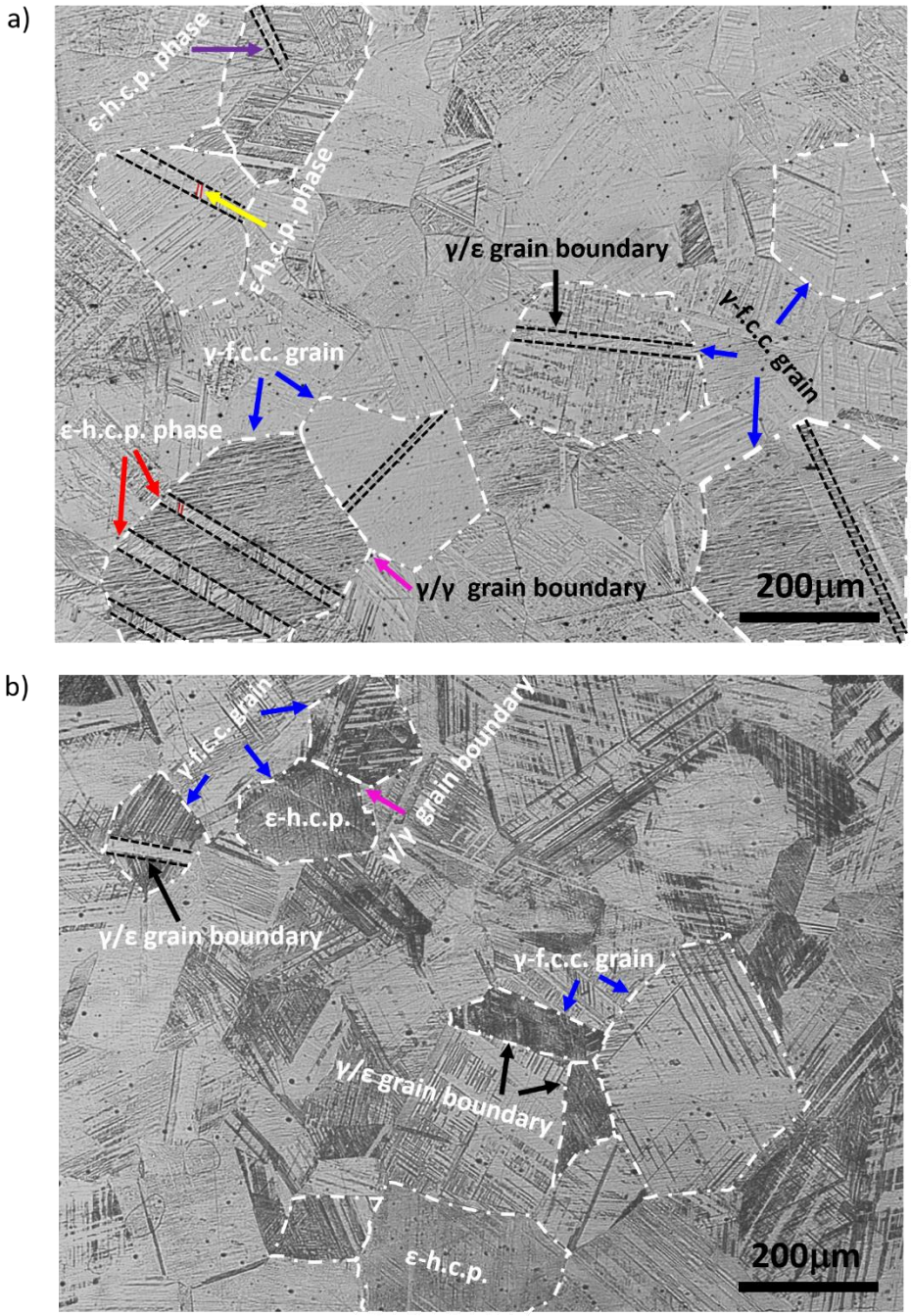

Figure 6-1. OM of the metastable $Fe_{42}Mn_{28}Co_{10}Cr_{15}Si_5$ HEA: a) before deformation and b) after fracture.

In order to compare changes on the average grain size of the γ-f.c.c. phase before and after deformation, Nano Measurer 1.2 software [290] was used. The γ-f.c.c. grain size decreases with increasing strain, from ≈ 184 to ≈ 150 μm (≈ 18 % reduction), indicating that imposed strain rate does not significantly refine the grain in the $Fe_{42}Mn_{28}Co_{10}Cr_{15}Si_5$ HEA. This behavior is unlike that observed for a $Fe_{50}Mn_{30}Co_{10}Cr_{10}$ HEA [62], suggesting the improved grain stability during mechanical behavior upon

the addition of Si. Qualitatively, it is also observed that the fraction of ε-h.c.p. phase in the fractured samples increased when compared to the as-received condition.

Figure 6-2 a) and b) depict the superimposition of the X-ray diffraction patterns of the metastable $Fe_{42}Mn_{28}Co_{10}Cr_{15}Si_5$ HEA during tensile deformation and the corresponding contour plots, respectively. The phases identified from these diffraction patterns are: γ-f.c.c., ε-h.c.p. as well as a tetragonal structure known as σ phase. This phase identification is in good agreement with the existing literature [291]. Further observation of the superimposed diffraction spectra in Figure 6-2 a), details that no new phases are formed upon loading until fracture.

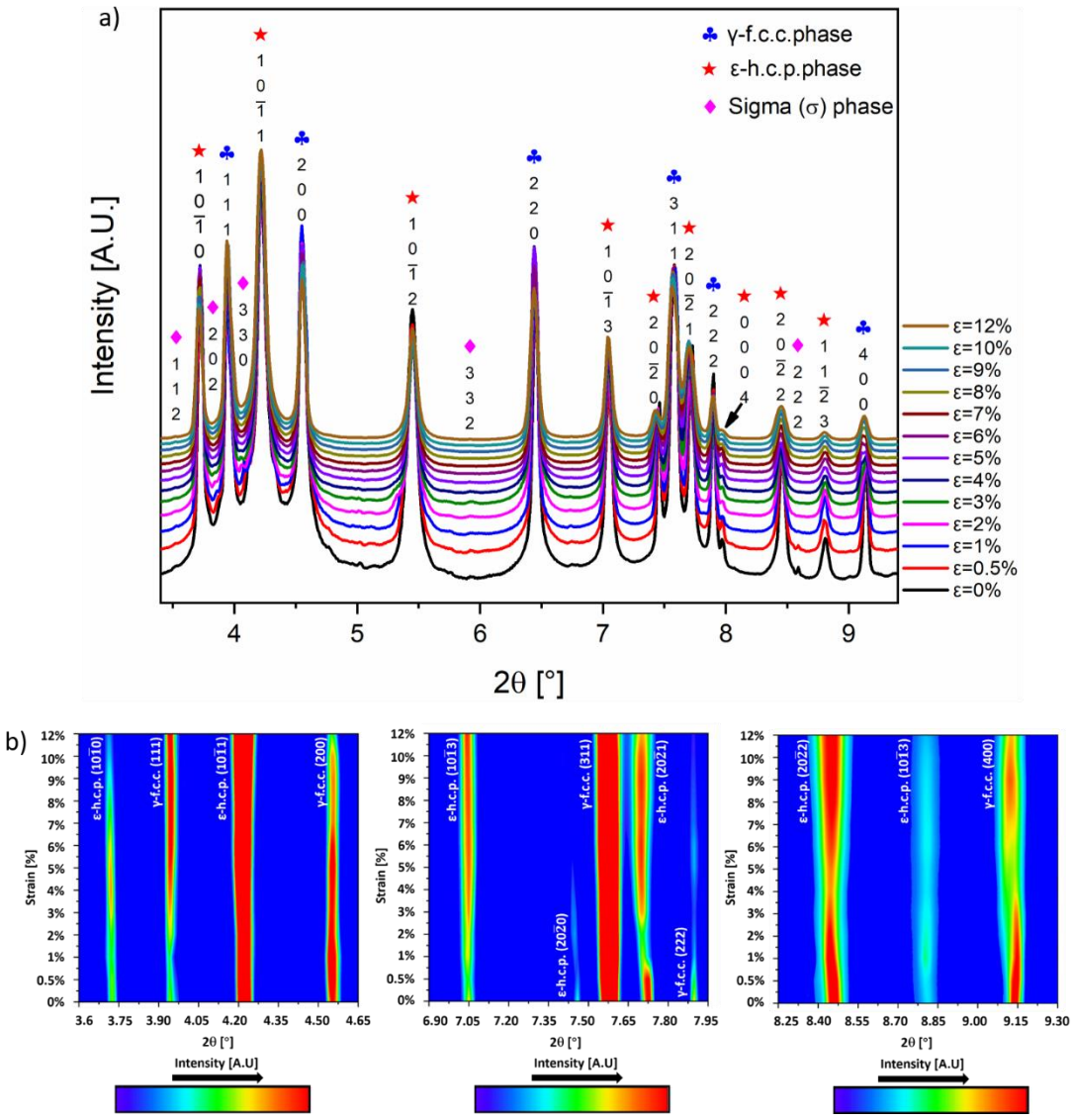

Figure 6-2. a) Superimposition of the 1D diffraction patterns, b) contour plots of specific diffraction ranges.

Figure 6-2 b) reveals the intensity evolution of different lattice planes of the γ-f.c.c. and ε-h.c.p. phases during tensile loading. Although the analysis of the superimposed diffraction patterns of Figure 6-2 a)

has led to the conclusion that no new phases were detected in the metastable $Fe_{42}Mn_{28}Co_{10}Cr_{15}Si_5$ HEA during deformation (refer to Figure 6-2 a), there are obvious changes in the diffracted intensity, indicating that transformation from γ-f.c.c. to ε-h.c.p. is occurring due to the TRIP effect [62]. Further observation of the evolution of the diffracted intensity of the γ-f.c.c. (400) and (222) peaks show a decrease in their intensity with increasing strain, while the intensity of the ε-h.c.p. $(10\bar{1}0)$ and $(20\bar{2}2)$ diffraction peaks increase significantly. This qualitative observation further suggests the increase in the volume fraction of the ε-h.c.p. phase during deformation at the expense of the γ-f.c.c. phase. The quantitative analysis of the evolution of the phase fractions of both γ-f.c.c. and ε-h.c.p. phases has been presented in the following section 5.1.3.2. The lattice parameters of the γ-f.c.c., ε-h.c.p. and σ phases before and after deformation, as obtained by Rietveld refinement, are shown in Table 6-1. The results of the lattice parameters of the γ-f.c.c. and ε-h.c.p. phases prior to loading are in good agreement with those reported by Sittiho et al. [289]. Regarding the σ phase, its lattice parameters are consistent with those previously determined using neutron diffraction in a $Fe_{42}Mn_{28}Co_{10}Cr_{15}Si_5$ alloy [291].

Table 6-1 – Refined lattice parameters of the ε-h.c.p., γ-f.c.c. and σ phases in the as-cast metastable $Fe_{42}Mn_{28}Co_{10}Cr_{15}Si_5$ HEA as obtained by Rietveld refinement.

Phases	ε-h.c.p. phase (Hexagonal: P63/mmc)			γ-f.c.c. phase (FCC: Fm/3m)	σ phase (Tetragonal P42/mnm)	
	$a_{\varepsilon\text{-h.c.p.}}$ (Å)	$c_{\varepsilon\text{-h.c.p.}}$ (Å)	c/a ratio	$a_{\gamma\text{-f.c.c.}}$ (Å)	a_σ (Å)	c_σ (Å)
Initial	2.525	4.102	1.625	3.578	8.831	4.800
Fracture	2.533	4.076	1.608	3.582	-	-

The c/a ratio before and after loading was also determined (refer to Table 6-1). Prior to loading, the as-cast $Fe_{42}Mn_{28}Co_{10}Cr_{15}Si_5$ HEA has a c/a ratio of approximately ≈ 1.625, which is significantly lower than the ideal value of ≈ 1.633 [105], but very close to that of the as-cast $Fe_{40}Mn_{20}Co_{20}Cr_{15}Si_5$ HEA (≈ 1.625) [105] and as-rolled $Fe_{42}Mn_{28}Co_{10}Cr_{15}Si_5$ (≈ 1.622) [289]. As expected, the c/a ratio in the present alloy is slightly higher than that reported by Bu et al. (≈ 1.616) for a duplex $Fe_{50}Mn_{30}Co_{10}Cr_{10}$ HEA [145]. This is related to the addition of Si, which is a ε-h.c.p. phase stabilizer, which promotes the increase of the c/a ratio, while the concomitant decrease of Mn, a γ-f.c.c. phase stabilizer, can decrease it. However, Si has a stronger effect (roughly 22 times higher) that that of Mn on the c/a ratio [105,106,292], thus justifying the change in the c/a ratio determined in this work.

Compared to the intrinsic c/a ratio of metals such as Ti or Mg that practically do not change during deformation [128], the c/a ratio of the metastable $Fe_{42}Mn_{28}Co_{10}Cr_{15}Si_5$ HEA decreases from ≈ 1.625 in

the initial state to ≈ 1.609 upon fracture, indicating that the ε-h.c.p. phase expands in the a-axis and compresses in the c-axis, revealing that the ⟨c + a⟩ slip system has a strong strain adaptation capability. This reduction in the c/a ratio during tensile deformation is also present in several other TRIP HEAs. However, there are variations in the magnitude of this decrease. For example, in a friction stir processed $Fe_{40}Mn_{20}Cr_{15}Co_{20}Si_5$ alloy there was a change from ≈ 1.619 to ≈ 1.588 in the fine grained region [146], while for a $Fe_{40}Mn_{20}Cr_{15}Co_{20}Si_5$ alloy prepared by laser powder bed fusion it decreased from ≈ 1.633 to ≈ 1.593 [293]. The variation of the c/a ratio of the ε-h.c.p. phase in TRIP HEAs is essentially a dependence of the lattice parameter on the texture and stress state caused by the variation of its volume. It is a function of the dislocation density and the volume of the ε-h.c.p. phase, which in turn indirectly affects the activation of the different slip systems of the ε-h.c.p. phase [105]. This mechanistic analysis has been discussed in detail in the Discussion section.

Table 6-2 details that the phase fractions of both γ-f.c.c., ε-h.c.p. and σ phases in the metastable $Fe_{42}Mn_{28}Co_{10}Cr_{15}Si_5$ HEA before deformation were ≈ 71%, ≈ 28% and ≈ 1%, respectively. After tensile fracture of the material, the γ-f.c.c. phase decreases to ≈ 17%, the ε-h.c.p. phase increases to ≈ 82%, while the σ volume fraction remained constant.

Before deformation, the existence of ≈ 28% of ε-h.c.p. phase is attributed to the addition of Si, which effectively increases the metastability of the γ-f.c.c. matrix phase, as Si is an ε-h.c.p. phase stabilizer [279,294,295]. Moreover, it has been suggested that maximum metastability of the γ-f.c.c. phase is obtained when 5 at. % Si is added [60], as also verified by thermodynamic calculations [62]. Specifically, the higher metastability of the γ-f.c.c. phase, the lower the value of the Gibbs free energy for the γ-f.c.c. to ε-h.c.p. transformation ($\Delta G_{\gamma-\text{f.c.c.}\rightarrow\,\varepsilon-\text{h.c.p.}}$) to occur, thus causing a greater driving force for the γ-f.c.c. to ε-h.c.p. transition, which ultimately corresponds to a reduction in the γ-f.c.c. phase fraction upon cooling to room temperature after casting.

In the current study the phase fraction volume transition which is defined as $(f^{b}_{\gamma-\text{f.c.c.}} - f^{a}_{\gamma-\text{f.c.c.}})/f^{b}_{\gamma-\text{f.c.c.}}$, with $f^{a}_{\gamma-\text{f.c.c.}}$ corresponding to phase volume fraction of γ-f.c.c. phase after (superscript a) tensile deformation and $f^{b}_{\gamma-\text{f.c.c.}}$ to the volume fraction of γ-f.c.c. phase before (superscript b) deformation, was also calculated. The phase volume fraction transition of the γ-f.c.c. matrix phase before deformation and after fracture is ≈ 75%, which is consistent with the findings of a high phase fraction transition for an as-cast $Fe_{42}Mn_{28}Co_{10}Cr_{15}Si_5$ HEA reported by Nene et al. using TEM [62]. In addition, it was previously reported that the conversion rate of the γ-f.c.c. phase in TRIP HEAs during tensile deformation is proportional to the work hardening rate [62]. As it will be shown later, the work hardening rate of the material studied in this work is significantly higher than that measured for a $Fe_{50}Mn_{30}Co_{10}Cr_{10}$ HEA [62], which naturally justifies the existence of a higher phase volume fraction conversion.

It is worth mentioning that the evolution of the phase volume fraction, lattice constants and c/a ratio in the metastable $Fe_{42}Mn_{28}Co_{10}Cr_{15}Si_5$ HEA during deformation have not been reported so far. By

combining high energy synchrotron X-ray radiation and refinement methods it is possible to quantify the micromechanical behavior of the HEA used in this work for the first time.

Table 6-2 – Volume fractions of ε-h.c.p. phase, γ-f.c.c. phase and σ phase in the as-cast metastable $Fe_{42}Mn_{28}Co_{10}Cr_{15}Si_5$, as obtained by Rietveld refinement.

	Volume fraction		
Phases	ε-h.c.p. phase	γ-f.c.c. phase	σ phase
Initial	28%	71%	1%
Fracture	82%	17%	1%

6.1.3.2 In-situ synchrotron tensile test

The engineering and true stress-strain curves (black and red lines, respectively) as well as the strain-hardening rate curve (blue line) during deformation of the metastable $Fe_{42}Mn_{28}Co_{10}Cr_{10}Si_5$ HEA are given in Figure 6-3. Based on the activation of a preferred deformation mode these curves can be divided into four stages, each one marked in Figure 6-3 with the letters A, B, C and D. Each region represents a qualitative change in the deformation mechanism based on the measured diffraction data. Here, it should be noted that the TRIP and TWIP effects mentioned below have been further assessed in the Discussion section.

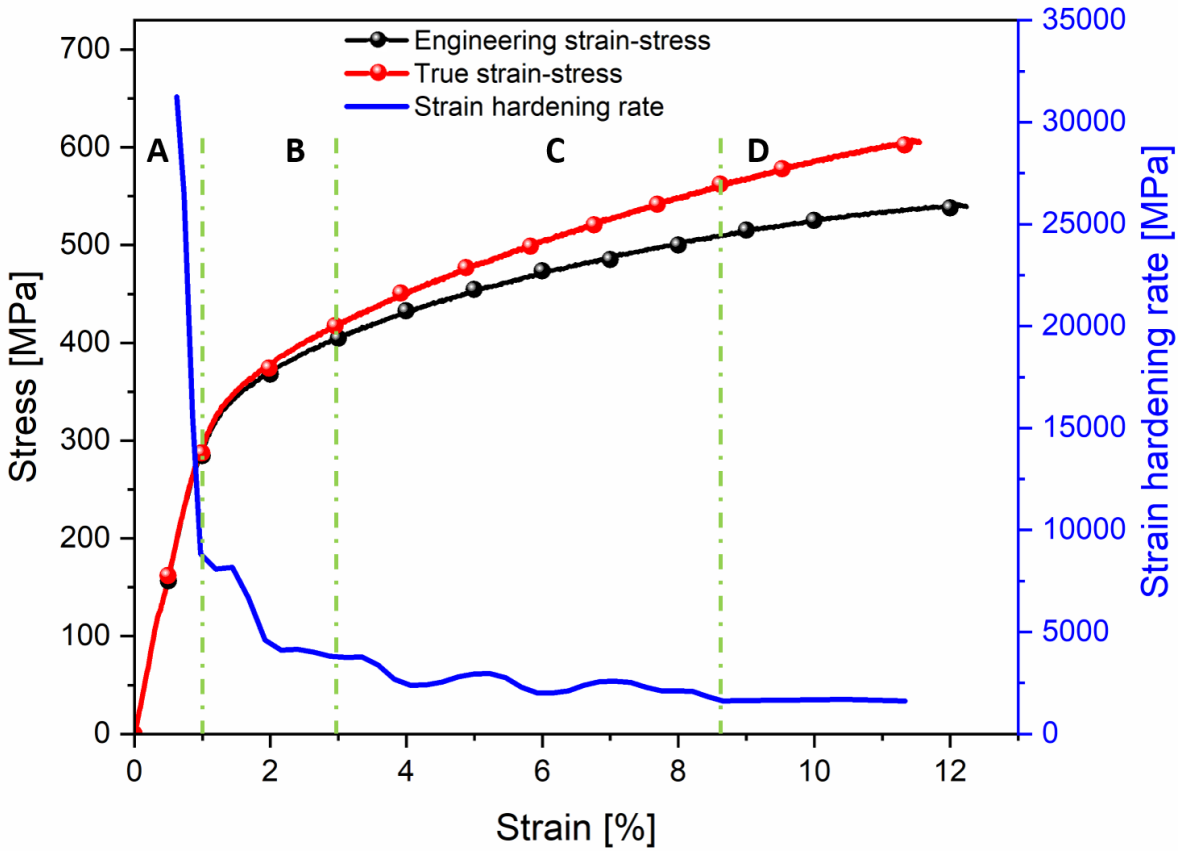

Figure 6-3. Engineering and true strain-stress curves and strain hardening rate of the as-cast metastable $Fe_{42}Mn_{28}Co_{10}Cr_{15}Si_5$ HEA tested at room temperature at a strain rate of 1 x 10^{-3} s^{-1}.

The uniform strain distribution between the metastable γ-f.c.c. phase and the resultant ε-h.c.p. phase in the $Fe_{42}Mn_{28}Co_{10}Cr_{15}Si_5$ HEA [62] resulted in a total elongation of ≈ 12% and an yield strength of ≈ 284 MPa. The observed elongation is related to the large number of deformation twins that appear during tensile deformation, as previously shown by TEM [289]. The large number of parallel twins generated during deformation can provide sufficient twinning interfaces in the high strain region (corresponding to stages C and D, as it has been described after), thus increasing the resistance to plastic deformation, and delaying the onset of necking. Similarly, TRIP, as a key deformation mechanism of the γ-f.c.c. phase, is primarily responsible for regulating the mechanical properties of the material through the associated phase transformation. When the γ-f.c.c. to ε-h.c.p. phase transformation occurs, there is a corresponding transformation strain which releases the stress concentration on the interface between the two phases, thus delaying the appearance of cracks [296,297]. In addition, the activated pyramidal < c + a > and < a > slip systems [145,298] and the c/a ratio change [146] in the ε-h.c.p. phase should also be responsible for the ductile behavior exhibited by the material.

Meanwhile, compared with the $Fe_{50}Mn_{30}Co_{10}Cr_{10}$ TRIP HEA [288], the yield strength is increased by nearly 100 MPa in the alloy used in this work. However, the elongation is only one third of that of the $Fe_{50}Mn_{30}Co_{10}Cr_{10}$ counterpart. This is attributed to the fact that the metastability of the matrix γ-f.c.c.

phase in the $Fe_{42}Mn_{28}Co_{10}Cr_{15}Si_5$ alloy is higher than that of $Fe_{50}Mn_{30}Co_{10}Cr_{10}$ HEA due to the addition of Si. The SFE is significantly reduced, which in turn increases the transformation rate from the soft γ-f.c.c. matrix phase to the hard ε-h.c.p. phase, thus increasing the yield strength of the material while sacrificing its ductility. With the emergence of the TRIP and TWIP effects, more slip systems and dislocations are activated and the interaction between dislocations provides a greater work-hardening capacity for the macroscopic deformation of the material. In addition, the existence of numerous grains and phase boundaries (as previously shown in Figure 6-1) impede and difficult dislocation movement and enhance the strain accommodation capacity, thus justifying the high degree of work hardening in this HEA.

Here, the material exhibits a higher sustained work-hardening behavior related to the higher metastability of the γ-f.c.c. matrix phase on one hand, and to the appearance of deformation twins on the other hand [62,299,300]. The high metastability can promote the phase transformation of γ-f.c.c. to ε-h.c.p., as well as the twinning of the ε-h.c.p. phase during deformation, which are called TRIP and TWIP effects, respectively. In addition to the fact that the ε-h.c.p. phase is significantly harder than the γ-f.c.c. phase [24,62,279,294,295,301,302], the formation of plasticity-induced twinning of the ε-h.c.p. phase further helps to accommodate more strain, which has a significant effect on the work hardening. In order to investigate the nature of the TRIP effect on the strain-hardening behavior, Nene et al. [275] compared two HEAs with and without Si added ($Fe_{40}Mn_{20}Co_{20}Cr_{15}Si_5$ and $Fe_{45}Mn_{20}Co_{20}Cr_{15}$, respectively). Their results showed that the addition of Si (which increases the instability of the matrix γ-f.c.c. phase) not only increased the yield strength and improved the ductility of the material, but also improved the material work-hardening. At the same time, the TWIP effect produces deformation twins that act as barriers to dislocation movement and, to some extent, provide the material with a continuous work-hardening capacity.

Overall, the high strength, ductility and work-hardening behavior exhibited by the metastable $Fe_{42}Mn_{28}Co_{10}Cr_{15}Si_5$ HEA studied in this study is mainly attributed to the γ-f.c.c. to ε-h.c.p. phase transformation and to deformation twinning initiated in the ε-h.c.p. phase due to the large deformation experienced, which is also observed in $FeMn_{30}Co_{10}Cr_{10}C_{0.5}$ [279], $Fe_{40}Mn_{40}Co_{10}Cr_{10}$ [196], $Al_{0.3}$CoCrFeNi and $Al_{0.7}$CoCrFeNi HEAs [303–305].

The strain-hardening rate curve (blue line) shows a different slope variation (unevenness) during macroscopic deformation. This slope variation is attributed to the superiority of TRIP or TWIP dominated deformation in the material over conventional dislocation plasticity [60,62,299,300,306–308]. In the case of materials where the deformation mechanism is by dislocation slip only, the strain hardening rate sharply drops after the onset of plastic deformation and remains almost constant with increasing strain [309–311], while for TWIP/TRIP dominated deformation there are observable variations in the strain hardening rate after the onset of plastic deformation. Thus, in other words, this change in slope during tensile testing is associated with a shift from a dislocation-dominated to a multi-mechanism-dominated deformation condition. Indeed, this multi-stage work-hardening behavior is common in low SFE alloys

that exhibit secondary deformation mechanisms [62,275,285,286]. Based on the evolution of the deformation mechanisms in the material during loading, the strain hardening rate is divided into four stages, labelled with the letters A, B, C, and D, which has been discussed in detail in section 6.1.4.

6.1.3.3 Phase stress partitioning

To further investigate the influence of the constituent phases in the metastable $Fe_{42}Mn_{28}Co_{10}Cr_{15}Si_5$ HEA on the continuous work-hardening behavior exhibited by the material, synchrotron X-ray was used to trace in real-time the dynamic stress distribution between the two dominant constituent phases: γ-f.c.c. and ε-h.c.p. The detailed procedure for the calculation was previously described in section 3.5.1.2.2 and the results are shown in Figure 6-4. The stress imparted by γ-f.c.c. and ε-h.c.p. phases varies dynamically at different stages of deformation (as shown by the markings A, B, C and D in Figure 6-4). The solid blue curve is the true stress-strain curve of the HEA studied in this work; the dashed blue line is the theoretical stress-strain curve of the material, which was calculated using the mixing law for multiphase materials [312], using the phase volume fractions of the γ-f.c.c. and ε-h.c.p. phases obtained at different loading steps. The black and red dashed lines are used as the representative stresses imparted by γ-f.c.c and ε-h.c.p. phases due to the load partitioning, which was obtained from the (311) and $(10\bar{1}2)$ lattice planes of γ-f.c.c. and ε-h.c.p. phases, respectively, using the von Mises criterion. The orange and green overlays refer to the range of stresses partitioned between the γ-f.c.c. and ε-h.c.p. phases during loading process. The upper and lower limits for each phase correspond to the stiffest and softest lattice planes, respectively, which were determined based on the elastic modulus of each lattice plane analyzed.

In this work, for the γ-f.c.c. phase structure, the Youngs modulus of the (111), (211) and (311) planes follow the order $E_{111} > E_{311} > E_{211}$ (further information will be detailed in section 6.1.5 corresponding to the lattice strain evolution). Thus, the upper and lower limits of the green area that make up the γ-f.c.c. phase stress range were calculated using the (111) and (211) γ-f.c.c. planes, respectively. Similarly, for the ε-h.c.p. phases structure we have $E_{(1011)} > E_{(10\text{-}12)} > E_{(10\text{-}13)}$, which also coincides with observations done in [146]. The upper and lower limits of the corresponding ε-h.c.p. phase stress range (orange region) were then calculated from the $(10\bar{1}1)$ and $(10\bar{1}3)$ ε-h.c.p. planes, respectively.

Two key features are worth mentioning from the results depicted in Figure 6-4: i) the ε-h.c.p. phase bears significantly more stress than the γ-f.c.c. phase, and ii) macroscopic yielding and phase yielding do not coincide. In fact, macroscopic yielding of the alloy occurs at 287 MPa, whereas the γ-f.c.c. phase yields prematurely at 261 MPa, which contrasts to the 367 MPa for yielding of the ε-h.c.p. phase. These aspects will be detailed and clarified in the Discussion section. It should be noted that, unless otherwise stated, all stress values detailed in the text correspond to true stress values.

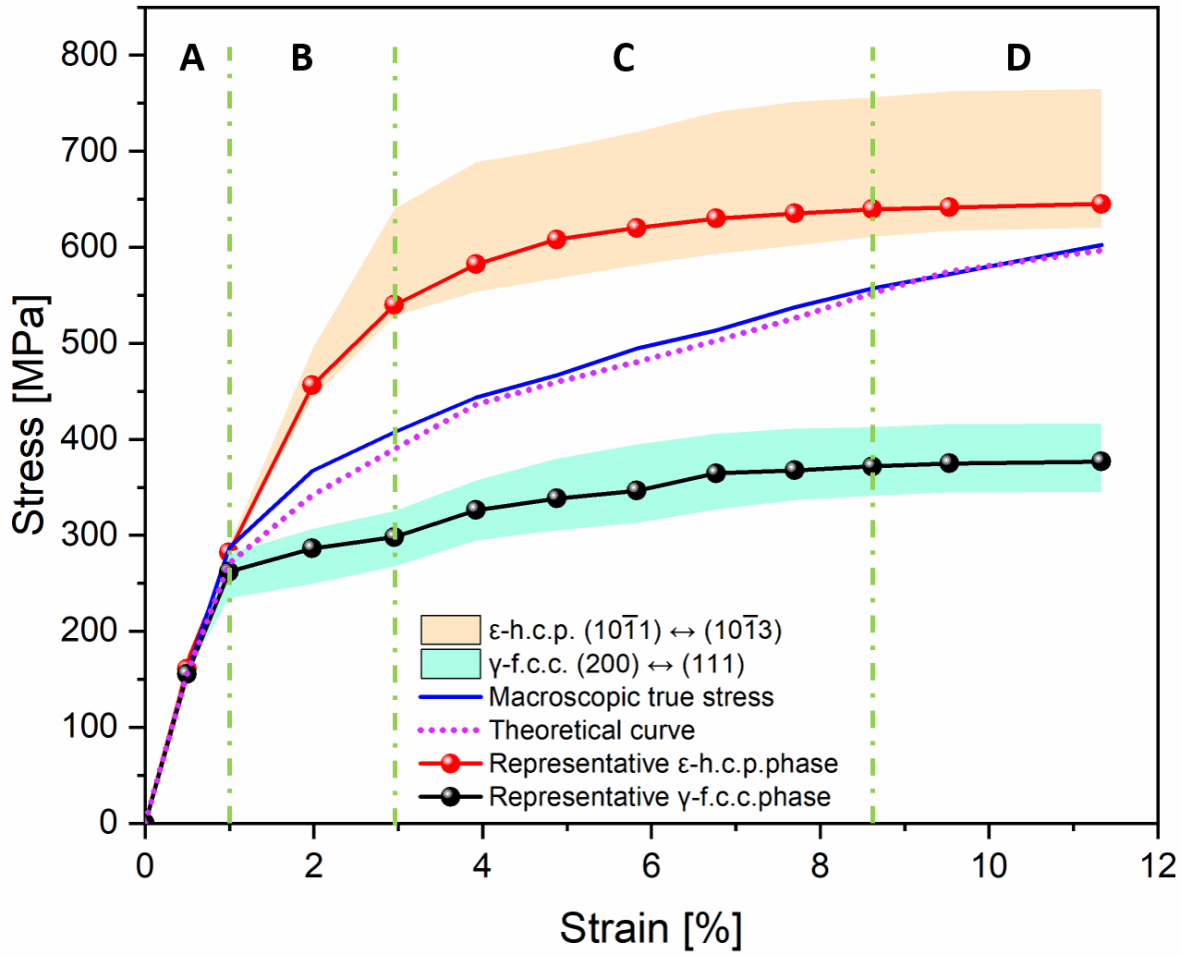

Figure 6-4. Stress partitioning between γ-f.c.c. and ε-h.c.p. phases as a function of applied strain in the as-cast metastable $Fe_{42}Mn_{28}Co_{10}Cr_{15}Si_5$ HEA.

6.1.3.4 Volume fraction and transformation volume evolution

The results depicted in Figure 6-4 in combination with the qualitative evolution of the diffraction patterns of Figure 6-2 a) suggest the importance of the phase change in the dynamic stress partitioning process. To further explore the phase transformation and its kinetics, the real-time evolution of the γ-f.c.c. (black line) and ε-h.c.p. (red line) phase fractions as well as associated transformation volume changes were determined (refer to Figure 6-5 a) and b), respectively).

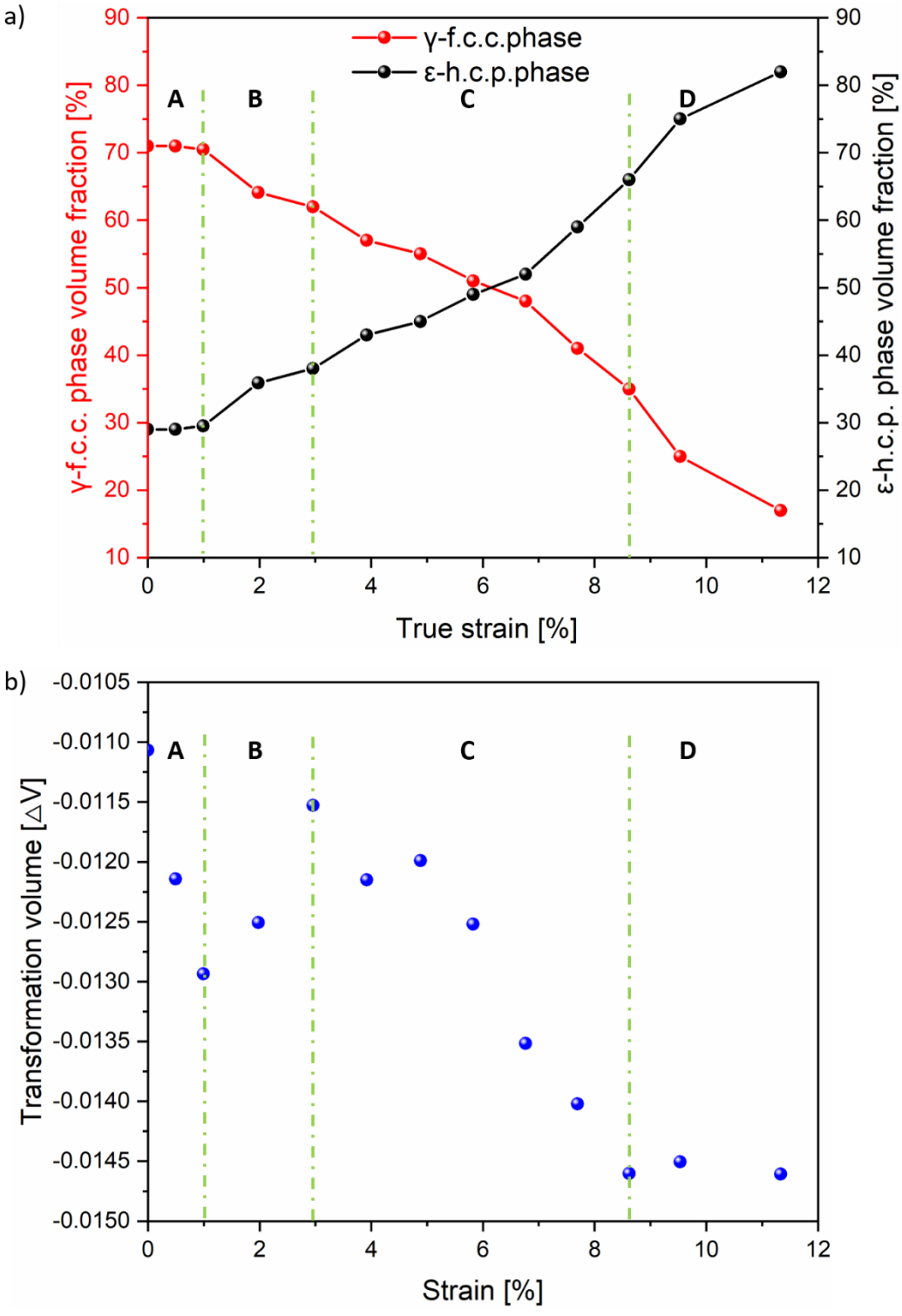

Figure 6-5. Evolution of a) γ-f.c.c. and ε-h.c.p. phase volume fractions in the as-cast metastable $Fe_{42}Mn_{28}Co_{10}Cr_{15}Si_5$ HEA, and b) evolution of the transformation volume.

Except for stage A, which corresponds to the macroscopic elastic deformation, it can be perceived that transformation of γ-f.c.c. to ε-h.c.p. phase is occurring throughout the entire tensile test until failure.

However, the conversation rate in each stage changes owing to the different predominant deformation mechanisms. This will be further highlighted and detailed in the Discussion section. As for the evolution of the transformation volume, an overall decrease is observed during tensile loading. Again, the magnitude of the transformation volume change is dependent on the primary deformation mechanism experience by the material as it will be evidenced.

6.1.3.5 Average microstrain, dislocation density, stacking faults probability and stacking faults interspacing evolution

Figure 6-6 reproduces in detail the dynamic evolution of the average microstrain (ε_0) and dislocation density of the as-cast $Fe_{42}Mn_{28}Co_{10}Cr_{15}Si_5$ metastable HEA along the LD, TD, as obtained from full azimuthal integration. Comparing the average microstrain obtained from the two principal directions (refer to Figure 6-6 a and c)), it can be found that the average microstrain is only slightly larger along LD than along TD, which suggests the homogeneity of the deformation in the material during the loading process. Also, regardless of the orientation considered (LD, TD or full azimuthal), the average microstrain of the ε-h.c.p. phase starts to exceed that of the γ-f.c.c. phase after the TWIP effect has been triggered (stage C). Interestingly, the dislocation density of the γ-f.c.c. phase in the analyzed orientations is significantly larger than that in the ε-h.c.p. phase, as shown in Figure 6-6 b), c) and f). It is worth mentioning that the average microstrain (refer to Figure 6-6 e)) and the dislocation density (refer to Figure 6-6 f)) obtained by full azimuthal integration can be treated as an average distribution over the whole material. For this reason, focus is given on the average microstrain and dislocation density obtained from full azimuthal integration to investigate the dynamic evolution of these in the cast $Fe_{42}Mn_{28}Co_{10}Cr_{15}Si_5$ metastable HEA during the loading process.

The dynamic evolution of both the average strain and dislocation density obtained from the full azimuthal integrations for both γ-f.c.c. to ε-h.c.p. phases during tensile deformation are detailed in Figure 6-6 e and f), respectively. As can be seen from Figure 6-6 e), the average microstrain in both the γ-f.c.c. and ε-h.c.p. phases (red and black dotted lines, respectively) in the metastable $Fe_{42}Mn_{28}Co_{10}Cr_{15}Si_5$ HEA increases with the increasing tensile stress. The higher the average lattice strain, the more plastic deformation is imparted by each phase. As-cast Al-containing and Cu-containing HEAs ($Fe_{39}Mn_{20}Co_{20}Cr_{15}Si_5Al_1$ and $Fe_{38.5}Mn_{20}Co_{20}Cr_{15}Si_5Cu_{1.5}$) experienced a similar phenomenon of increase of the average lattice strain with deformation [105]. Overall, a similarity can be perceived in the evolution profile of the average lattice strain between the two phases, although the change in magnitude for each phase is different. An interesting finding is the difference in the average lattice strain evolution between the two phases: the average lattice strain in the "hard" ε-h.c.p. phase starts to exceed that of the "soft" γ-f.c.c. phase from stage C. This is related to the activation of non-basal plane < c + a > slip and deformation twinning modes in the ε-h.c.p. phase, both of which are essential for strain accommodation in the material [105,313,314].

From Figure 6-6 f), it can be found that the dislocation density evolution in the γ-f.c.c. and ε-h.c.p. phases during the tensile process is also dependent on the deformation mechanism (stages A to D) experienced by the material. The dislocation density shows an increasing trend with increasing tensile loading in both the γ-f.c.c. and ε-h.c.p. phases, which is similar with the results of the dislocation density evolution measured in a friction stir processed $Fe_{39}Mn_{20}Co_{20}Cr_{15}Si_5Al_1$ HEA [105]. Moreover, the dislocation density in the γ-f.c.c. phase is always above that in the ε-h.c.p. phase. This is fundamental for the TRIP effect to be activated and proceed during continuous material deformation and will be further detailed in the Discussion section.

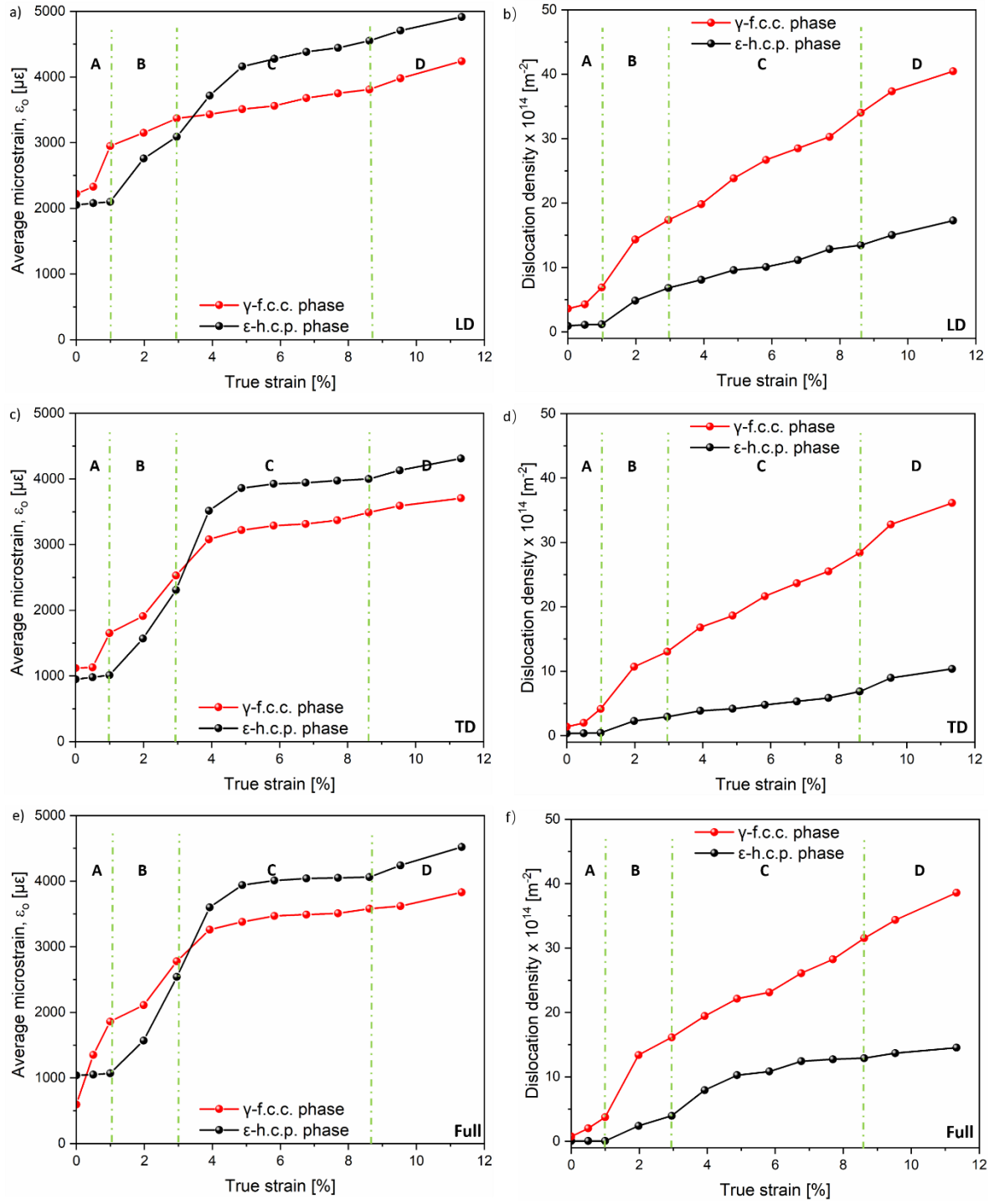

Figure 6-6. a), c) and e) Evolution of the average microstrain, ε_0, as a function of true engineering strain along LD, TD, and full azimuthal integration, respectively; b), d) and e) dislocation density as a function of engineering strain along LD, TD, and full azimuthal integration, respectively.

The introduction of nanoscale stacking faults provide a barrier to dislocation movement and increase the strength of the material without sacrificing plasticity, thus making stacking faults highly attractive for improving the mechanical properties of the metastable HEA. Therefore, to further investigate the

dynamic evolution response of staking faults during tensile deformation, the contribution of these microstructural features to the material work-hardening behavior and the origin of macroscopic strength and ductility needs to be properly understood. Figure 6-7 reproduces the evolution of the stacking faults interspacing, L_{sf}, and stacking faults probability, P_{sf}, the latter being a measure of deformation faulting which is defined as the probability of finding a deformation fault between any two layers in the γ-f.c.c. stacking sequence, with tensile strain.

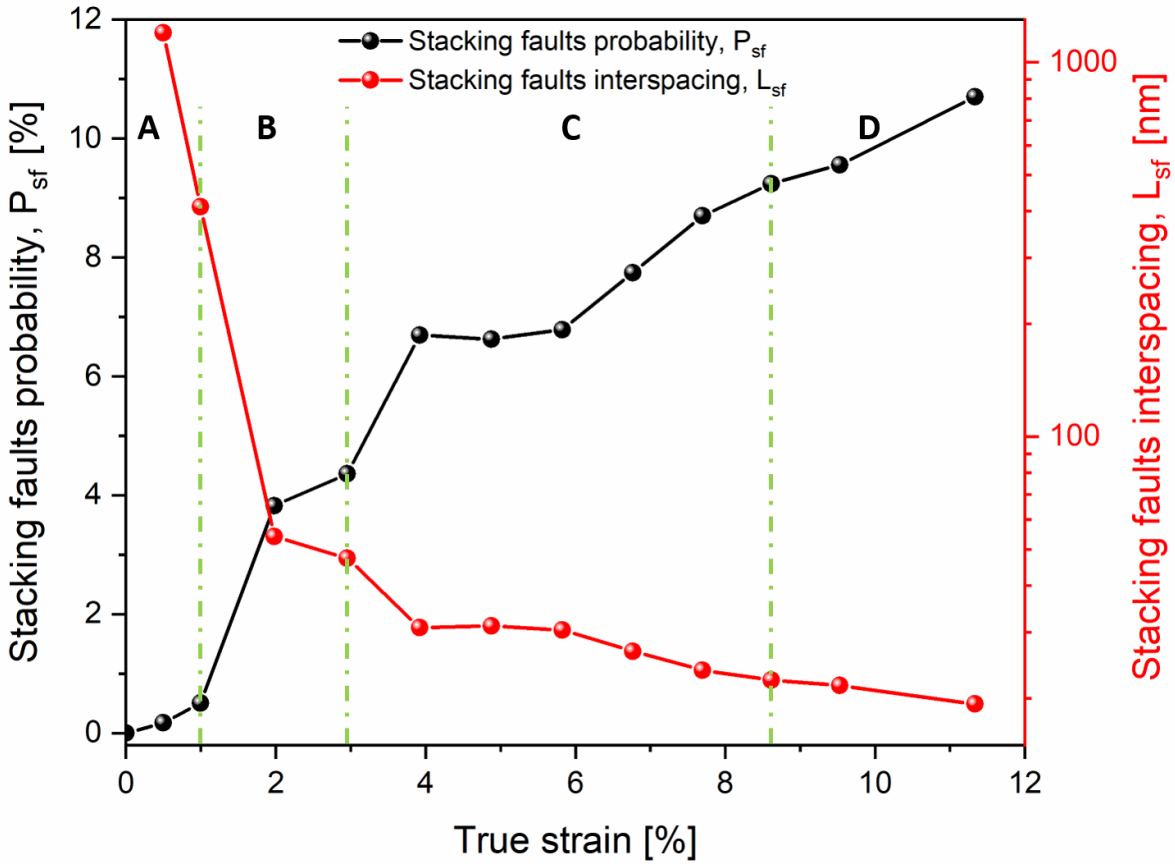

Figure 6-7. Evolution of stacking faults probability, Psf, and stacking faults interspacing, Lsf.

The strengthening contributions arising from dislocations in both phases as well as due to the stacking faults in the γ-f.c.c. phase were calculated as detailed in section 6.1.3.9 and these results are detailed in section 6.1.4.2.

6.1.3.6 Intensity evolution

Gharghouri et al. [315] reported that in-situ neutron diffraction can be used to study the propagation of deformation twinning, by tracing the characteristic intensity variations of certain (hkl) diffraction reflections corresponding to the "parent grains" (i.e., grains undergoing deformation twinning) and the "twinned" (i.e., twinned parent grains) crystal families. Synchrotron X-ray diffraction can be used for the same purpose, and this was used to further investigate the deformation mechanisms within the ε-h.c.p.

phase of the as-cast $Fe_{42}Mn_{28}Co_{10}Cr_{15}Si_5$ HEA. Specifically, the variation in the diffracted intensity of certain ε-h.c.p. planes along the longitudinal and traverse directions, LD and TD, during tensile loading was used to demonstrate the onset of TWIP as well as the evolution and transition of single-twinning (by tensile twinning) to multi-twinning (with the onset of compression twinning).

In terms of the microscopic mechanisms of twinning, three factors affect the type of twinning in the ε-h.c.p. phase, i) c/a ratio, ii) type of loading, and iii) crystal orientation [316]. The c/a ratio must be below the ideal value of 1.633 for twinning to occur. The type of loading is related to the imposition of tensile or compression, or in more complex cases, with multiaxial loadings. Evaluation of different crystal orientations enables to determine if the twinning deformation is tensile or compressive in nature. In fact, the $(10\bar{1}2)$ plane can be used to evaluate the onset of tensile twinning, while $(10\bar{1}3)$ and $(10\bar{1}1)$ planes can be used to record compression twinning. ε-h.c.p. grains are difficult to compress along the c-axis, thus the orientation of the c-axis with respect to the LD determines the type of twinning, which is activated within a single family of grains, especially the type of twinning modes, i.e., tensile, or compressive, and its range.

Here, we use synchrotron X-ray diffraction to reveal the onset and range of TWIP in the metastable $Fe_{42}Mn_{28}Co_{10}Cr_{15}Si_5$ HEAs by quantitatively analyzing the diffraction intensity evolution of several differently oriented ε-h.c.p. grains. Figure 6-8 a), c), e) and g) depict the normalized diffracted intensities of the $(10\bar{1}1)$, $(10\bar{1}2)$ and $(10\bar{1}3)$ ε-h.c.p. planes along the LD and TD during tensile loading as a function of the true stress. Figure 6-8 b), d), f) and h) show the above-mentioned diffraction intensities of the same ε-h.c.p. grains as a function of true tensile strain along the LD and TD during tensile deformation. Note that the initial value of the normalized diffracted intensity, I_0, corresponds to the peak intensity of the analyzed with no load imposed. It is clear that within stages A and B there are no evident changes, in opposition to what occurs in stages C and D. As it will be shown in section 6.1.4.2.3, this is related to the activation of tensile and compression twinning.

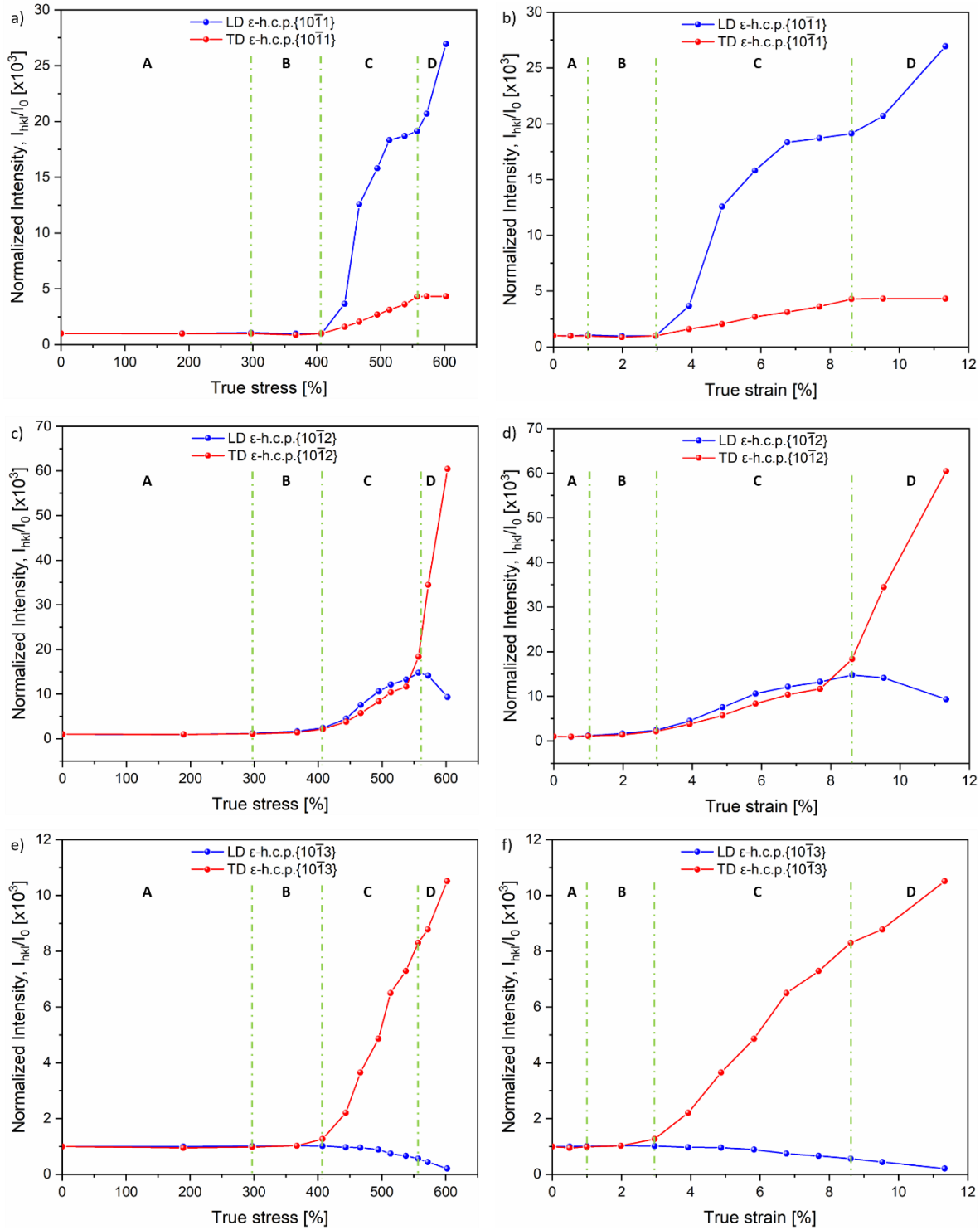

Figure 6-8. Normalized diffraction intensity evolution of the different ε-h.c.p. planes along LD and TD as a function of, a) true stress, and b) true strain.

6.1.3.7 Lattice strain evolution

Evaluating the lattice strain evolution along different directions during macroscopic loading can provide insights into the micromechanical behavior and load-dependent response of the phases that constitute the metastable $Fe_{42}Mn_{28}Co_{10}Cr_{15}Si_5$ HEA. Moreover, the (hkl)-dependent behavior can provide information on the load partitioning between different lattice planes and how this is affected by both TWIP and TRIP effects. Figure 6-9 a) and b) depict the evolution of lattice strain as a function of true stress (refer to Figure 6-9 a)) and true strain (refer to Figure 6-9 b)) for the (111), (200) and (311) γ-f.c.c. planes along the LD and TD. Similarly, Figure 6-9 c) and d) display the mechanical response of the $(10\bar{1}0)$, $(10\bar{1}1)$, $(10\bar{1}2)$ and $(10\bar{1}3)$ ε-h.c.p. planes along the LD and TD in relation to the true stress (refer to Figure 6-9 c)) and the true strain (refer to Figure 6-9 d)). The lattice strain evolution in each plane was divided into the same A, B, C, and D stages which mark different predominant deformation modes experienced by the material, as described in detail in section 6.1.4.2.2.

For both phases a positive lattice strain developed along LD and a negative lattice strain developed along TD, the latter being due to the Poisson effect. It is also observed that the soft planes for the γ-f.c.c. and ε-h.c.p. phases are the (200) and $(10\bar{1}0)$, respectively, while the stiffest are the (111) and the $(10\bar{1}3)$. Moreover, it can be observed that the lattice strain evolution experiences significant changes when transitioning from one stage to another in both phases. This is related to deformation slip, TRIP and/or TWIP being the main deformation mechanisms occurring at a given loading step, as it will be discussed in section 6.1.4.2.2.

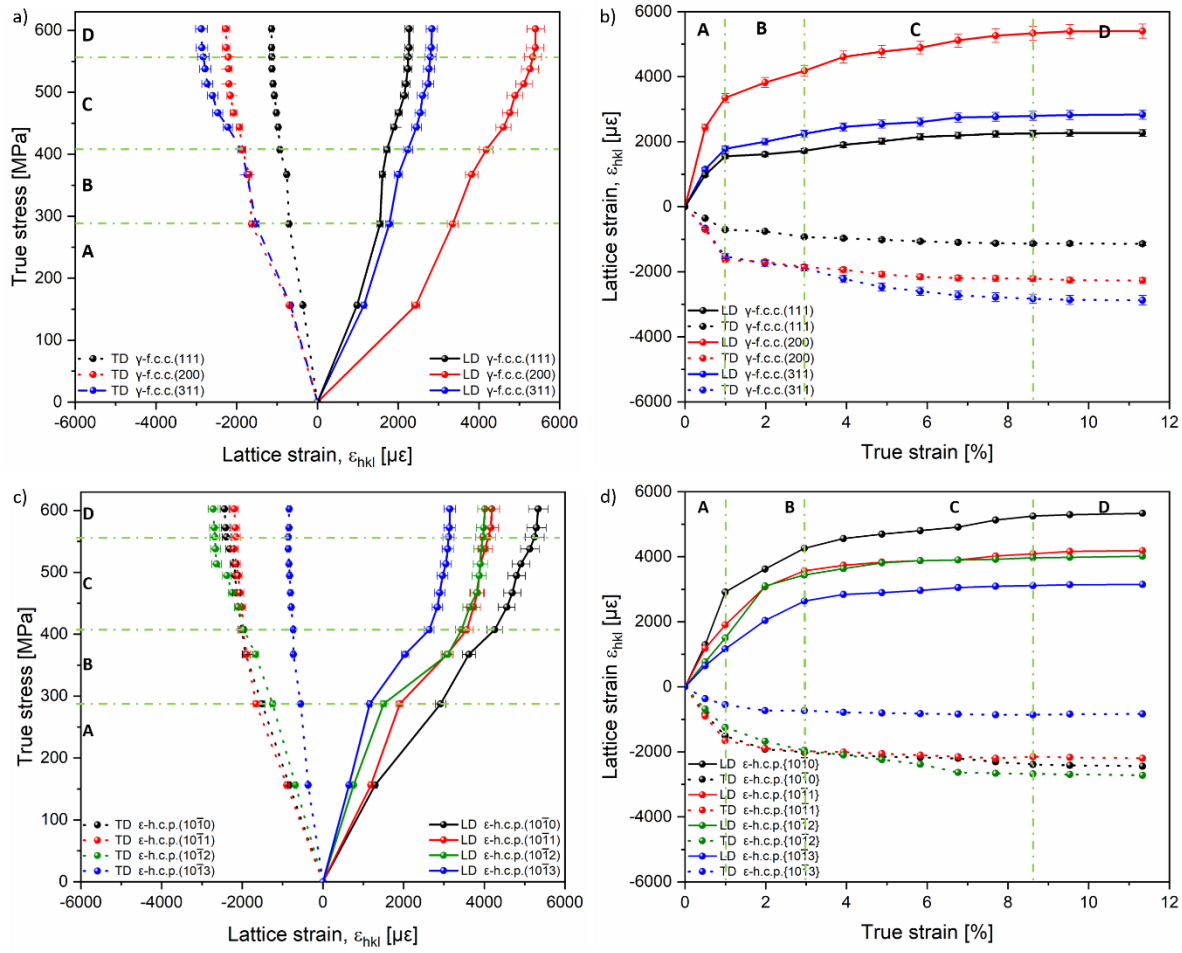

Figure 6-9. Lattice strain evolution along the LD and TD as a function of applied true stress (a, c) and true strain (b, d) for γ-f.c.c. (a, b) and ε-h.c.p. phases (c, d).

6.1.3.8 c/a ratio evolution

To explore the various deformation modes in the ε-h.c.p. phase of the currently studied $Fe_{42}Mn_{28}Co_{10}Cr_{15}Si_5$ metastable HEA, the changes in the ε-h.c.p. phase lattice parameters, $a_{\varepsilon\text{-h.c.p.}}$ and $c_{\varepsilon\text{-h.c.p.}}$, during the tensile deformation are shown in Figure 6-10 a). Figure 6-10 b) provides details on the variation of the ε-h.c.p. c/a ratio with increasing applied tensile loading. During tensile deformation at room temperature and a fixed strain rate, the decrease in the ε-h.c.p. c/a ratio with applied tensile loading is attributed to lattice expansion along the a-axis and compression along the c-axis. This is reflected in the lattice constants evolution, where the ε-h.c.p. phase lattice parameter a and c tend to increase (from 2.525 Å to 2.533 Å) and decrease (from 4.104 Å to 4.078 Å), respectively, as shown in Figure 6-10 a). Frank et al. [146] performed in-situ neutron diffraction analysis of a $Fe_{40}Mn_{20}Cr_{15}Co_{20}Si_5$ HEA under tensile deformation, and found that the ε-h.c.p. c/a ratio decreased from 1.619 to 1.588 with increasing strain, reporting that this decrease was due to the activation of the non-basal pyramidal < c + a > slip system and to deformation twinning that can accommodate strain along the c-axis at larger strain levels. The processing and deformation dependence of the ε-h.c.p. c/a ratio in TRIP HEAs was

also observed in our metastable $Fe_{42}Mn_{28}Co_{10}Cr_{15}Si_5$ HEA, where a reduction in the ε-h.c.p. c/a ratio from 1.625 to 1.609 was observed (refer to Figure 6-10 b). Depending on the c/a ratio, the ε-h.c.p. phase can deform not only via basal slip, but also on a number of non-basal slip carriers, which will help to accommodate more strain, and also enable to overcome the strength-ductility paradigm. This is completely different from most conventional ε-h.c.p. structural alloys such as Mg, where their ε-h.c.p. phase c/a ratio remains almost constant during deformation, and thus only pure basal < a > slip occurs [128,317], which is one of the reasons why these alloys are prone to possess lower plasticity.

Bu et al. [145] revealed that there were three types of slip planes in a $Fe_{50}Mn_{30}Co_{10}Cr_{10}$ HEA during tensile deformation using in-situ TEM tensile experiments. These included basal < a > slip, prismatic < c > slip and pyramidal < c + a > slip. Sinha et al. [105] studied the ε-h.c.p. c/a ratios by comparing five HEAs, ($Fe_{44}Mn_{28}Co_{10}Cr_{15}Si_3$, $Fe_{42}Mn_{28}Co_{10}Cr_{15}Si_5$, $Fe_{40}Mn_{20}Co_{20}Cr_{15}Si_5$, $Fe_{39}Mn_{20}Co_{20}Cr_{15}Si_5Al_1$ and $Fe_{38.5}Mn_{20}Co_{20}Cr_{15}Si_5Cu_{1.5}$), showing that the influence of the ε-h.c.p. c/a ratio is attributed to a combination of chemistry, responsive phase evolution, elastoplastic deformation characteristics and transformation volume change.

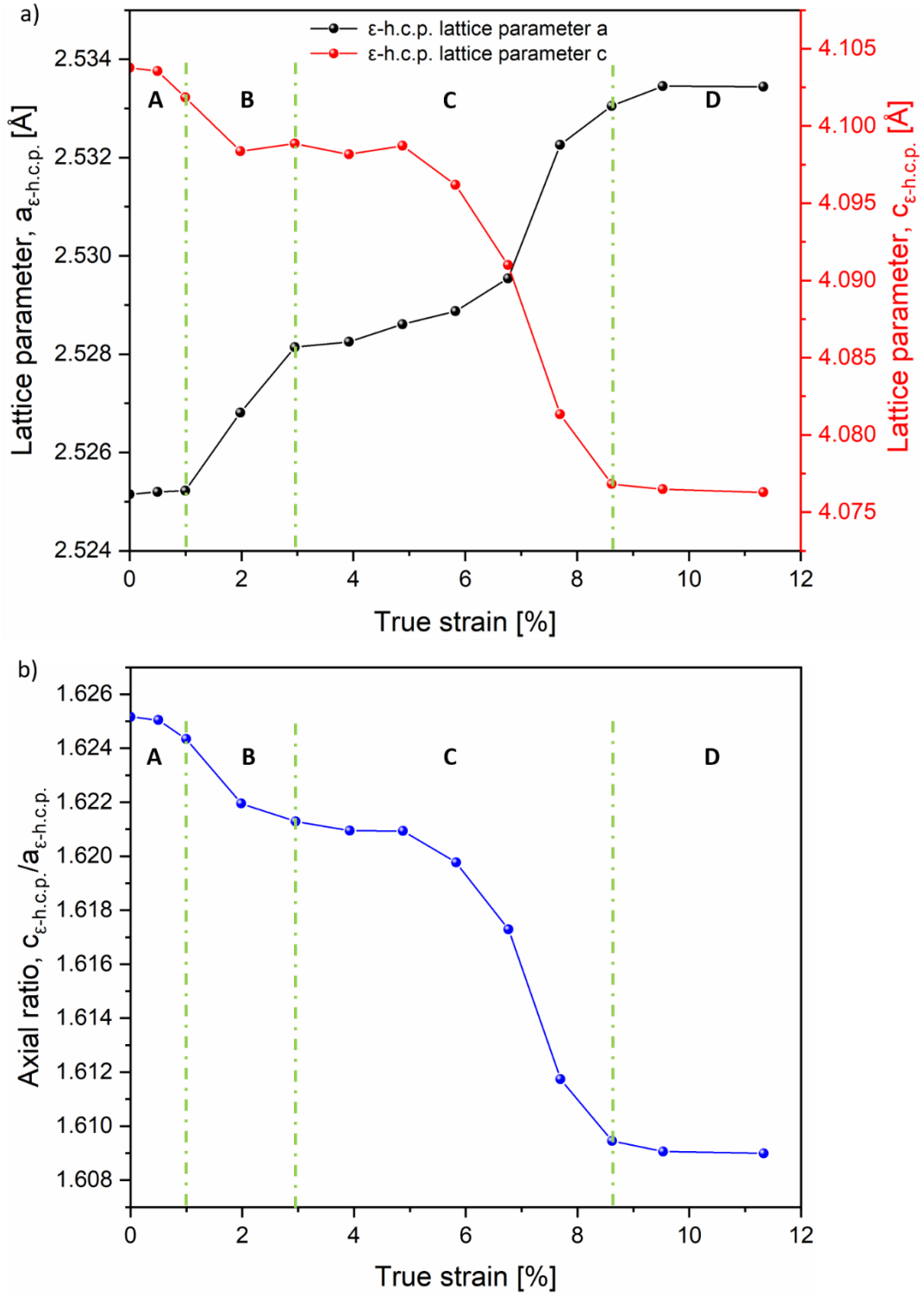

Figure 6-10. a) Evolution of a and c lattice parameters in the ε-h.c.p. phase as a function of true strain, and b) deformation induced decrease in the c/a ratio of the ε-h.c.p. phase in the metastable $Fe_{42}Mn_{28}Co_{10}Cr_{15}Si_5$ HEA.

Figure 6-11 shows the evolution of the lattice parameter a of the γ-f.c.c. phase during tensile loading. These data were mainly used to calculate the volume transition generated by the phase transformation

of γ-f.c.c. to ε-h.c.p. phase, whose results are shown in Figure 6-5 b). The evolution of the γ-f.c.c. lattice shows varying degrees of growth with increased tensile loading. It is within stage C, where the phase transformation rate is the highest (refer to Figure 6-5 a)), that there is a more pronounced increase. The different trends within each deformation stage will be detailed in the Discussion section 6.2.3.4.

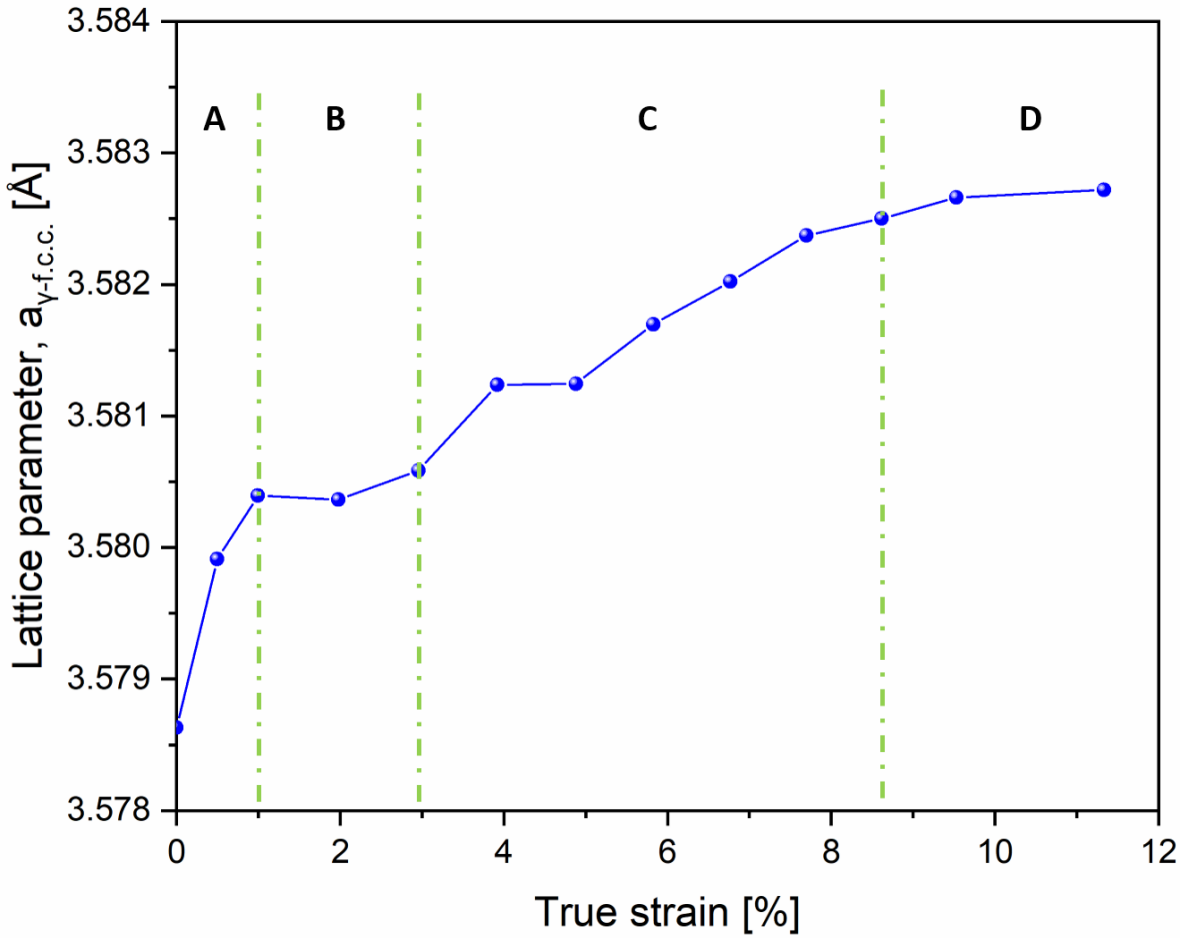

Figure 6-11. Evolution of lattice parameter a of the γ-f.c.c. phase with the true strain in the metastable $Fe_{42}Mn_{28}Co_{10}Cr_{15}Si_5$ HEA.

6.1.3.9 Strengthening contributions

In Figure 6-12, the black, red, and blue dotted lines represent the dislocation strengthening of the ε-h.c.p. ($\sigma_{\varepsilon\text{-h.c.p. DIS}}$) and γ-f.c.c. ($\sigma_{\gamma\text{-f.c.c. DIS}}$) phases, as well as the stacking faults strengthening of the γ-f.c.c. phase ($\sigma_{\gamma\text{-f.c.c. SF}}$), respectively. The dashed and solid orange lines detail the calculated strengthening contribution (σ_{Calc}) and the macroscopic tensile stress-strain response (σ_{Macro}), respectively. It should be mentioned that the orange dashed line is the linear summation of all the strengthening contributions. Moreover, the difference between σ_{Macro} and σ_{Calc}, is defined here as σ_{Extra} which represents the strengthening contributions arising from, i) solid solution strengthening, ii) precipitation strengthening due to the presence of σ phase, and iii) the Hall-Petch strengthening

resulting from changes in the interface spacing. These contributions are not quantified as these are expected to remain constant during tensile deformation of the metastable HEA.

Since the dislocation density in both γ-f.c.c. and ε-h.c.p. phases, and the amount of stacking faults in the γ-f.c.c. phase vary significantly during deformation (refer to Figure 6-6 b and Figure 6-7 b), it is possible to define the calculated stress, σ_{Calc}, in the currently studied $Fe_{42}Mn_{28}Co_{10}Cr_{15}Si_5$ HEA as follows,

$$\sigma_{Calc} = \sigma_{\gamma-\text{f.c.c. DIS}} + \sigma_{\varepsilon-\text{h.c.p. DIS}} + \sigma_{\gamma-\text{f.c.c. SF}}, \tag{6-1}$$

where $\sigma_{\gamma\text{-f.c.c. DIS}}$ and $\sigma_{\varepsilon\text{-h.c.p. DIS}}$ are the strengthening contributions in both the γ-f.c.c. and ε-h.c.p. due to dislocations, while $\sigma_{\gamma\text{-f.c.c. SF}}$ is the contribution of the stacking faults generated in the γ-f.c.c. phase. The difference between the macroscopic stress imparted by the alloy, σ_{Macro}, and σ_{Calc} is defined by σ_{Extra} as detailed in Equation (6-2) and encompasses the other strengthening contributions that are kept constant during tensile loading of the alloy,

$$\sigma_{Extra} = \sigma_{Macro} - \sigma_{Calc}. \tag{6-2}$$

Overall, the evolution of the three major strengthening contributions ($\sigma_{\gamma\text{-f.c.c. DIS}}$, $\sigma_{\varepsilon\text{-h.c.p. DIS}}$ and $\sigma_{\gamma\text{-f.c.c. SF}}$) that change during loading exhibit all a continuous increase with increasing deformation. However, depending on the deformation mechanism that is predominant at a given time (stages A to D) will modify the magnitude of each strengthening contribution. These aspects will be further detailed in section 6.1.4.2. In terms of the magnitude of the strengthening contribution, the dislocation strengthening contribution of the γ-f.c.c. phase is the highest. The strengthening effect induced by dislocations and stacking faults within the ε-h.c.p. phase are of similar magnitude with one another.

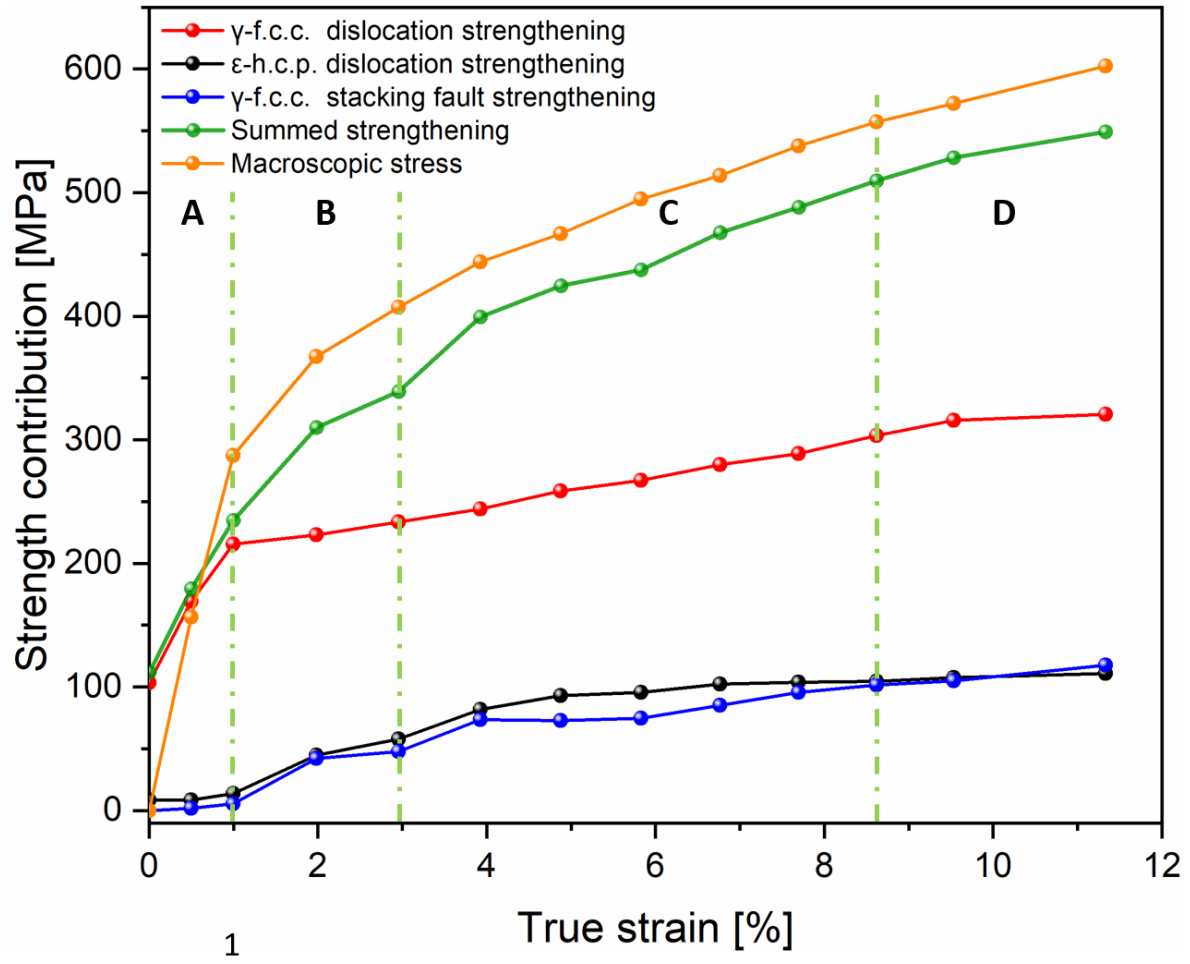

Figure 6-12. Evolution of the strengthening contributions of γ-f.c.c. and ε-h.c.p. phases as a function of true strain.

6.1.3.10 Fracture surface analysis

Fractography was performed on the as-cast $Fe_{42}Mn_{28}Co_{10}Cr_{15}Si_5$ HEA to evaluate the fracture surface morphology, which is shown Figure 6-13. The overview image in Figure 6-13 a) details both ductile and brittle features, although the former predominated. Figure 6-13 b) details a ductile-like fracture morphology with high density of dimples corroborating the good degree of plastic deformation that the alloy was able to sustain. In opposition Figure 6-13 c) details a cleavage-like fracture morphology indicative of brittle failure in this region.

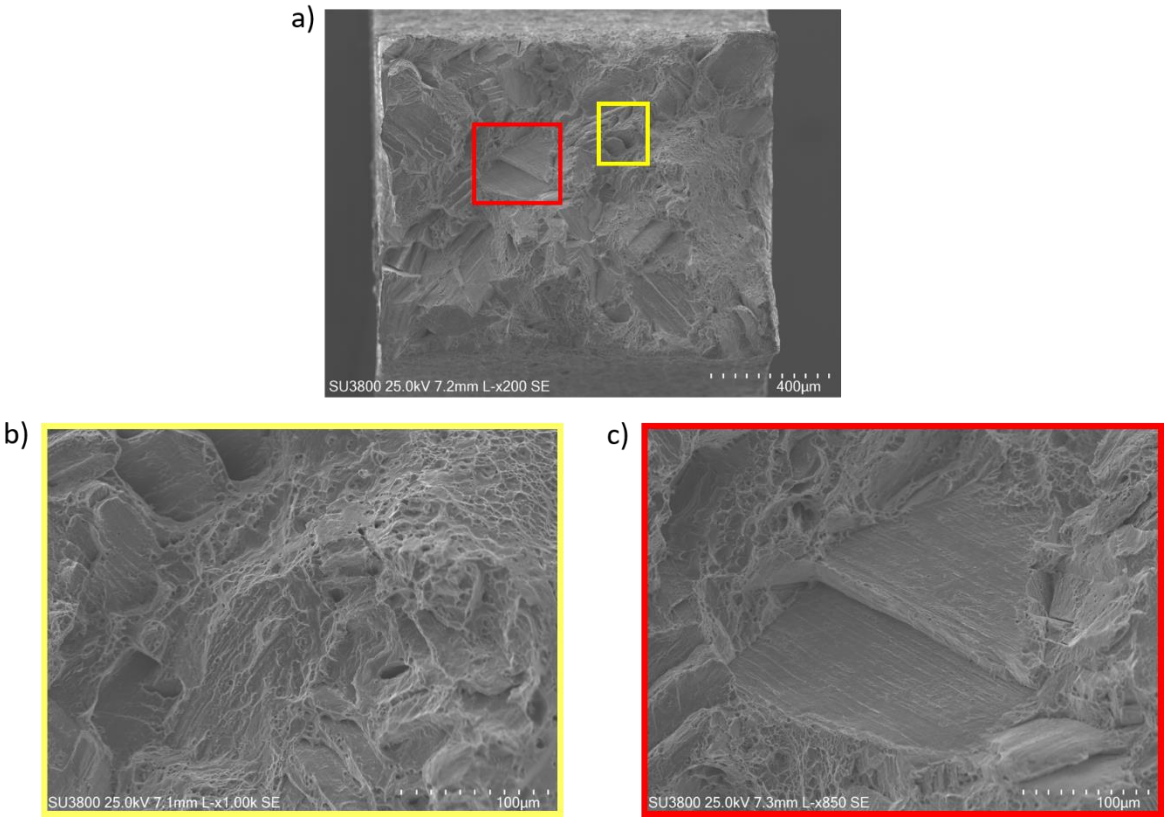

Figure 6-13. Fracture surface of the metastable $Fe_{42}Mn_{28}Co_{10}Cr_{15}Si_5$ HEA: a): an overview of fracture surface of welded joint; b) and c) close-up detailing the ductile and brittle characteristics.

6.1.4 Discussion

Leveraged on the results and descriptions presented in the previous section, we now focus on detailing and discussing the microstructure evolution of the metastable $Fe_{42}Mn_{28}Co_{10}Cr_{15}Si_5$ HEA. A full section is devoted to the analysis of the four deformation stages (A to D) to clearly highlight the predominant deformation mechanism during each loading step.

6.1.4.1 Microstructure characterization and phase identification

As observed in Figure 6-1, the γ-f.c.c. grains are divided by laths of ε-h.c.p. in various directions. Further observation of the microstructural features presented in Figure 6-1, show that these lath morphologies are limited to a single grain and no cross-over to other grains occurs. This will generate γ-f.c.c. / ε-h.c.p. boundaries (shown by black arrows), which combined with the γ-f.c.c. / γ-f.c.c. grain boundaries (shown by pink arrows) and ε-h.c.p. / ε-h.c.p. boundaries (pointed by yellow arrows) can improve the material work-hardening by pilling up of dislocations and staking faults. The ε-h.c.p. / ε-h.c.p. boundaries are formed by pairs of ε-h.c.p. laths that intersect each other. Moreover, some of the ε-h.c.p. laths do not fully cross a γ-f.c.c. single grain where they originate from, as shown by the purple arrow, indicating that incomplete growth of certain laths occurred.

The coexistence of multiple boundaries in the microstructure of the metastable $Fe_{42}Mn_{28}Co_{10}Cr_{15}Si_5$ alloy is observed prior and after tensile loading. To the thermally stable ε-h.c.p. phase that exists in the material prior to loading (refer to Figure 6-1 a)), it is observed the massive formation of strain-induced ε-h.c.p. phase due to TRIP, which generated significantly more interfaces during tensile loading (refer to Figure 6-1 b)). Concomitant with the larger amount of ε-h.c.p. phase being formed due to TRIP, there is also a dramatic decrease in the lath spacing, which is also aided by TWIP [24,64,279,295,318].

Further observation from the superimposed diffraction spectra in Figure 6-2 a), details that no new phases other than the γ-f.c.c., ε-h.c.p. and σ phases are formed upon loading until fracture. The γ-f.c.c. and ε-h.c.p. phases are the dominant structures, with a volume fraction prior to loading of 71% and 28%, respectively, which is consistent with the phase constitution measured via EBSD by Nene et al. [62] and with X-ray diffraction by Sittiho et al. [289]. In HEAs of the Fe-Mn-Co-Cr system, the addition of Si and Cr increases the tendency for σ phase to precipitate [275,319]. Nene et al. detected the presence of Fe- and Cr-rich σ with a tetragonal structure in a rolled $Fe_{42}Mn_{28}Co_{10}Cr_{15}Si_5$ HEA [291], which is consistent with the current phase identification.

The phase fraction measured at the end of the tensile loading (refer to Table 6-2) revealed a significant increase of ε-h.c.p. (up to 82 %) at the expense of γ-f.c.c. (decreasing to 17 %), which is indicative of the TRIP effect and in good agreement with the qualitative evaluation of the superimposed diffraction data of Figure 6-2 and OM analysis of Figure 6-1. The dynamic evolution of the phase fraction during tensile loading will be discussed in section 6.1.4.2.2.

6.1.4.2 Deformation mechanisms

Based on the changes of the deformation mechanisms in the as-cast $Fe_{42}Mn_{28}Co_{10}Cr_{15}Si_5$ HEA during tensile loading it is possible to identify four distinct deformation regimes. These were marked by the letters A ($\varepsilon < 1.0\%$), B ($1.0\% < \varepsilon < 3.0\%$), C ($3.0\% < \varepsilon < 7.7\%$) and D ($\varepsilon > 7.7$ %), matching to the various trigger stress points for the onset of distinct deformation mechanisms. The trigger stress points for each stage are 0, 287, 407 and 557 MPa, for stages A to D, respectively, and in each the following deformation mechanisms are active, stage A) elastic deformation and dislocation slip in the γ-f.c.c. phase, stage B) dislocation slip + TRIP, stage C) dislocation slip + TRIP + TWIP (single twinning mode), and stage D) dislocation slip + TRIP + TWIP (multiple twinning modes). A detailed discussion for each stage is presented next.

6.1.4.2.1 Stage A – macroscopic elastic deformation

Stage A, corresponding to low strain regime in Figure 6-3 ($\varepsilon < 1.0$ %), encompasses the macroscopic elastic deformation of the material. During stage A, there is almost no divergence in the load distribution of the main constituent phases of the $Fe_{42}Mn_{28}Co_{10}Cr_{15}Si_5$ HEA, as shown in Figure 6-4. The stress imparted by both γ-f.c.c. and ε-h.c.p. phases grow linearly with increasing load. A closer look shows that the γ-f.c.c. phase structure yields first at about 261 MPa (lower than the macroscopic material yield point

284 MPa), while the ε-h.c.p. phase showed no signs of yielding at stage A. One thing that is important to note is that the yielding stresses of different lattice planes will necessarily vary, as it will be discussed in detail in section 6.1.3.7. Here, we are only analyzing the phase-dependent macroscopic response, as shown by the red and black dotted lines of Figure 6-4. Therefore, when there is macroscopic evidence of material yielding, the γ-f.c.c. phase has already yielded, while the ε-h.c.p. phase is still in the elastic deformation stage, and part of the load begins to be transferred from the soft γ-f.c.c. phase to the hard ε-h.c.p. phase. 284 MPa not only corresponds to the macroscopic yield point of the HEA, but also marks the onset for the γ-f.c.c. → ε-h.c.p. phase transformation (refer to Figure 6-5), which will be analyzed in the next section. This changes the stress-strain response of the material, which are consistent with the basic features of the TRIP deformation mechanism [320], promotes significant stress redistribution after the yield point. Therefore, besides the soft and hard behaviors of the γ-f.c.c and ε-h.c.p. phases, which influence the stress partitioning, the formation of the plastically-induced ε-h.c.p. phase from the metastable γ-f.c.c. also requires continuous stress increase to promote plastic deformation and continue the TRIP effect, thus ensuring intergranular and interphase stress coordination in the microstructure [321,322], which is also the reason why the ε-h.c.p. phase can maintain continuous hardening [323].

Stage A is dominated by perfect dislocation slip due to the γ-f.c.c. phase premature yielding. In fact, as it was shown in section 6.1.3.5, resulting for the early yielding of the γ-f.c.c. phase in stage A, there is a concomitant increase in the dislocation density (from 7.3×10^{13} to 3.7×10^{14} m^{-2}). On the other hand, since the ε-h.c.p. phase is only elastically deformed (its yielding occurs at 287 MPa), there is no change in the dislocation density of this phase (which is kept at 3.8×10^{13} m^{-2}). The increase in dislocation density in the γ-f.c.c. phase can help in the nucleation of the ε-h.c.p. phase upon the imposition of macroscopic plastic deformation [324,325]. This stage is also controlled by the evolution of dislocation density without formation of twins. In fact, dislocation entanglement and twinning do not occur, but perfect dislocation slip and overlapping stacking faults often appear [326].

In stage A, the stacking faults probability increases from ≈ 0.17 to ≈ 0.52% during macroscopic elastic deformation and a significant reduction in the stacking faults interspace was determined. As the strain increases, the L_{sf} decreases sharply from ≈ 1199 to ≈ 411 nm, which in combination with the increase in stacking faults probability serves to demonstrate that stacking faults are being formed during macroscopic elastic deformation of the material. More importantly, the presence of stacking faults and the reduction in their interspacing can reduce the free path for dislocation movement. Therefore, the increase of stacking faults probability and decrease of stacking faults interspacing will facilitate the effective accumulation of dislocations in the γ-f.c.c. phase [309,327] leading to an increase in the dislocation density within the macroscopic elastic regime, which will eventually facilitate the TRIP effect. Thus, it can be stated that stage A is mainly controlled by the perfect dislocation slip of the γ-f.c.c. phase, as well as overlapping of stacking faults without occurrence of twinning [326] The fact that TRIP does not occur upon yielding of the macroscopic material is related to the need for the accumulation of

stacking faults during stage A, which will act as nuclei for the strain-induced transformation that will take place in stage B.

The onset for macroscopic plastic deformation and entry in stage B is the trigger point for the TRIP effect to occur. Prior to that, the transformation of f.c.c. and ε-h.c.p. does not occur, as also evidenced by the constant volume fraction of both phases in this stage (refer to Figure 6-5 a). The phase transformation kinetics of γ-f.c.c. to ε-h.c.p. is mainly determined by the applied stress and by the existence (or not) of plastic deformation. Moreover, it is well known that the nucleation and growth of the ε-h.c.p. phase is accomplished by a large number of stacking faults [328,329].

In the $Fe_{42}Mn_{28}Co_{10}Cr_{15}Si_5$ HEA, the γ-f.c.c. phase acts as the soft phase regulating the ductility of the material. Considering the average microstrain evolution of both phases (refer to Figure 6-6 e), it can be observed that deformation is primarily accommodated by the γ-f.c.c. phase, with a negligible change in the ε-h.c.p. phase which can be justified by the soft and hard nature of both phases, respectively. Before effective load transfer to the hard ε-h.c.p. phase occurs, the deformation is primarily being accommodated by the γ-f.c.c. phase, promoting the formation of stacking faults and dislocations.

The normalized diffraction intensity of the ε-h.c.p. phase along both the LD and TD in stage A details no changes for the selected diffraction planes (refer to Figure 6-8), which is related to the pure elastic deformation and perfect dislocation slip of this phase in stage A. The non-splitting of diffracted intensity in both the TD and LD reveals that no twinning of the ε-h.c.p. grains occurs in the stage A. These findings provide a basis for exploring the slip mechanisms of the ε-h.c.p. phase based on the c/a ratio which is discussed next.

The ε-h.c.p. c/a ratio is almost practically constant (1.625 vs 1.624) in stage A as seen in Figure 6-10. It is well known that the ε-h.c.p. c/a ratio is closely related to the slip system [330]. When the ε-h.c.p. c/a ratio is greater than the ideal value of 1.633, mainly basal < a > slip is the dominant in plastic deformation mechanism. In contrast, when the c/a ratio is lower than the ideal value of 1.633, the probability for the non-basal pyramidal < c + a > slip being dominant is higher. Moreover, c/a ratios below the ideal value also aids in the development of twinning as a deformation mechanism. Throughout this stage, although the ε-h.c.p. phase c/a ratio is lower than ideal value, the basal < a > slip and non-basal pyramidal < c + a > slip have not been activated at this stage. Such is related to the pure elastic deformation experienced by the ε-h.c.p. in stage A and explains the low increase in the average microstrain, as well as the constant dislocation density (see Figure 6-6).

Based on the above analysis, during the macroscopic elastic loading, the main deformation mechanism is dislocation slip which occurs in the γ-f.c.c. phase that yields prematurely at 261 MPa. The ε-h.c.p. phase remains elastically deformed, leading to the differences in the evolution of the average microstrain and dislocation density among both phases.

6.1.4.2.2 Stage B – onset of TRIP

When the material enters stage B (1.0% < ε < 3.0%) the deformation mechanism is dominated by the TRIP effect, i.e., the phase transition from γ-f.c.c. to the ε-h.c.p. takes place, as it can be evidenced by the evolution of the phase volume fraction in Figure 6-5 a). It is well known that TRIP is the main deformation mechanism regulator in the γ-f.c.c. phase, aside from dislocation slip [60,62,279,314]. In this study, the trigger point for the onset of TRIP corresponds to the macroscopic yield strength of 287 MPa. There is a significant decrease in the rate of decline of the strain hardening rate during this stage (refer to Figure 6-3). The ups and downs of the strain-hardening curve in stage B can be explained by two concurring effects: the transformation of γ-f.c.c. to ε-h.c.p. and the nucleation of twins, which will trigger TWIP in stage C. This nucleation of twins is expected to occur mainly at the plateau regions of stage B [331].

Throughout stage B, the phase stress partitioning evolution in the γ-f.c.c. phase has a small increase in its hardening rate after yielding, as shown in Figure 6-4, which is mainly attributed to the phase transformation that introduces new phase boundaries in the γ-f.c.c. matrix, thereby reducing the mean free path for dislocation movement. This results in a sharp increase in dislocation density at this stage as shown in Figure 6-6 f), increasing the storage capacity of dislocations and hence the hardening behavior. The ε-h.c.p. phase exhibits a more significant work-hardening behavior than the γ-f.c.c., thus having a greater impact on the macroscopic work-hardening behavior exhibited by the studied metastable HEA. As it can be seen, the macroscopic work-hardening behavior exhibited by the material in stage B (blue curve) is mainly attributed to TRIP effect and dislocation slip (refer to Figure 6-4).

Upon the onset of TRIP and within stage B, the γ-f.c.c. phase volume fraction decreased from 71 to 62%, while the ε-h.c.p. increased by the corresponding amount. The lower SFE of the metastable $Fe_{42}Mn_{28}Co_{10}Cr_{15}Si_5$ HEA facilitates the occurrence of partial dislocations and phase transformation rather than conventional deformation by dislocation slip [62]. The onset for TRIP occurs slightly after yielding of γ-f.c.c. phase (281 vs 261 MPa, respectively). This suggests that an excess driving force (in the form of plastic deformation) is necessary for the metastability of the γ-f.c.c. to allow the formation of new ε-h.c.p. phase. This extra driving force also arises from the stacking faults that are accumulated still during macroscopic plastic deformation as shown in Figure 6-7.

The stacking faults probability, P_{sf}, shows a sudden increase (from 0.52 to 4.36%) during stage B. The physical meaning of a stacking fault probability of 4.36% implies the existence of 43.6 stacking faults among 1000 layers on average in the (111) planes [332]. This abrupt increase in the P_{sf} is related to the transformation from γ-f.c.c. to ε-h.c.p. which requires a significant increase in stacking faults, as these act as nucleation sites for the new ε-h.c.p. phase to form. The stacking faults that are continuously being generated provide an additional support for the continuous nucleation of ε-h.c.p. phase [291,333]. This suggests that the plastic deformation of the as-cast $Fe_{42}Mn_{28}Co_{10}Cr_{15}Si_5$ HEA during tensile deformation is mainly regulated by the Shockley partial dislocations, producing large amounts of

stacking faults [128]. Compared to NiCoCr [334], FeCoNiCr [335] and $Fe_{20}Co_{30}Ni_{10}Cr_{20}Mn_{20}$ alloys [138], the metastable $Fe_{42}Mn_{28}Co_{10}Cr_{15}Si_5$ HEA under study has an increased stacking faults probability rate, which is attributed to its lower SFE [336]. In other words, the smaller the SFE, the greater the possibility for stacking faults to form. Accordingly, the rate of decline of the stacking faults interspacing, L_{sf}, in stage B becomes relatively lower compared to stage A (refer to Figure 6-7). Frank et al. [337] pointed out that this reduction in L_{sf} is related to the onset of the phase transition. The continued and significant decrease of L_{sf} in both stages A and B, contrasts with the sudden increase in the dislocation density of the γ-f.c.c. phase indicating that the smaller L_{sf} promotes dislocation accumulation in this phase, which ultimately contributes to an increase in the material strength.

From a crystallographic aspect, the γ-f.c.c. to ε-h.c.p. transformation is accomplished by Shockley partial shear a/6 <1 1 2> of every {111} lattice plane in the matrix γ-f.c.c. phase [296,338,339]. In other words, the stacking faults in the γ-f.c.c. phase are formed by the gliding of the Shockley partials of the 1/6 <1 1 2> Burgers vector [176,177]. Evidently, the core of ε-h.c.p. formation is stacking faults, but this is controlled by the movement of the Shockley partial dislocations [342]. In this work, when the applied stress reaches 287 MPa (macroscopic yield point), the shear stress required for inducing partial dislocation motion is reached, which triggers the onset of TRIP. When the applied strain increases from 2 to 3.0 %, the phase transformation rate starts to decrease, which is related to the nucleation of tensile twins in the ε-h.c.p. grains which will then promote the TWIP effect in stage C.

Although the γ-f.c.c. has already yielded and undergoes phase transformation in stage B, its phase volume fraction is still dominant (as shown in Figure 6-5 a). As for the ε-h.c.p. phase, it starts to be plastically deformed in stage B. In fact, yielding of this phase occurs at the same stress level as the material yielding and above the yielding of the γ-f.c.c. phase (287 vs 261 MPa, respectively). Based on the volume fractions of the γ-f.c.c. and ε-h.c.p. phases at this stage and on the evolution of the average microstrain, it is evident that the γ-f.c.c. phase continues to act as the soft phase regulating the plastic deformation of the material.

During stage B, the dislocation density of both phases is drastically modified. The dislocation density in the γ-f.c.c. phase increases significantly from 3.7×10^{14} to 1.61×10^{15} m^{-2}, which is almost four times higher than the increase in dislocation density in the ε-h.c.p. phase from 4.9×10^{13} to 3.94×10^{14} m^{-2}. Moreover, the variation in the dislocation density of the ε-h.c.p., which did not occur in stage A, further confirms that plastic deformation of this phase started to occur.

The sustained transformation of γ-f.c.c. to ε-h.c.p. requires large amounts of stacking faults, which makes the dislocation activity in the γ-f.c.c. phase to become even more important. As mentioned above, dislocations will encounter stacking faults, which are additional pinning sites to block dislocation motion. Meanwhile, the large number of phase boundaries created by the phase transformation further adds additional barriers to dislocation slip. This also justifies the increased accumulation of dislocations in the γ-f.c.c. phase. In addition to this, the premature yielding of the γ-f.c.c. phase will cause further

deformation imparted by this phase leading to the accumulation of more dislocations [204]. The average microstrain evolution of the f.c.c. phase (refer to Figure 6-6 e)) also corroborates this: the average microstrain is higher in the γ-f.c.c. phase than in -h.c.p. phase, which as a product of plastic deformation correlates well with the higher dislocation density exhibited by the γ-f.c.c. phase, thus justifying the remarkable growth in the dislocation density of this phase in stage B.

Sinha et al. have proposed that the ε-h.c.p. phase dislocation density is a function of the ε-h.c.p. phase fraction and the c/a ratio [105]. In our work, the increase in the volume fraction of the ε-h.c.p. phase due to the phase transformation was shown in Figure 6-5, which can be used to explain the increase in the ε-h.c.p. phase dislocation density in stage B. Furthermore, considering that the pre-existing thermally induced ε-h.c.p. phase was not yet plastically deformed until a stress of 287 MPa is reached, the increase in ε-h.c.p. phase dislocation arises from both plastic deformation of the thermally induced ε-h.c.p. as well as that being formed due to the TRIP effect. In fact, it is differences in the dislocation densities of the thermally stable and strain-induced ε-h.c.p. phase [343]. However, with synchrotron X-ray diffraction, it is only possible to get an overall quantification of the dislocation density in this phase without considering its nature (thermal- vs strain-induced).

The predominant deformation mechanisms in stage B can be further elucidated based on the variation of the diffracted intensity of the selected ε-h.c.p. planes in both the TD and LD (refer to Figure 6-8). From the above analysis, it was shown that the ε-h.c.p. phase starts to be plastically deformed during stage B. However, no splitting on the diffracted intensity along LD and TD is expected, and this is demonstrated in Figure 6-8. Splitting of the diffracted intensity would mean that twinning was occurring. Thus, the fact that deformation twinning was not yet activated indicates that the ε-h.c.p. phase starts to be dominated by the basal <a> slip, instead of the non-basal pyramidal $< c + a >$ slip, although the c/a ratio of the ε-h.c.p. phase is below the ideal value and shows signs of slow decrease.

To be more specific, the material began to yield upon entering in stage B and a slow decrease in the c/a ratio from 1.624 to 1.621 occurs. In this stage, the ε-h.c.p. phase begins to deform plastically under a stress of 287 MPa. By default, the ε-h.c.p. c/a ratio should continue to follow the same trend of the previous stage, but as the γ-f.c.c. phase yields the transformation to ε-h.c.p. phase is induced while plastic deformation of ε-h.c.p. phase also occurs. Therefore, a change in the c/a ratio starts to occur in order to accommodate the volume change variation resulting from the phase transformation (refer to Figure 6-5 b), and lattice distortion induced by plastic deformation of both phases. However, as the phase fraction transformation is only of 9 % (see Figure 6-5 a), the resulting volume fraction transformation is also small (see Figure 6-5 b), leading to only a minor decrease in the c/a ratio of the ε-h.c.p. phase. Thus, combining the analysis of the intensity evolution in ε-h.c.p. phase during the deformation of stage B, it can be concluded that basal $< a >$ is the dominant slip mechanism for this phase.

In summary, during stage B two main deformation mechanisms are present: TRIP and dislocation slip. While the γ-f.c.c. phase experiences both dislocation slip and TRIP, the ε-h.c.p. phase only experiences basal < a > slip.

6.1.4.2.3 Stage C – onset of tensile twinning

In stage B, with the onset of TRIP there was also the nucleation of twins. Stage C (3.0% < ε < 7.7%) marks the onset of twinning in the ε-h.c.p. grains, while the γ-f.c.c. to ε-h.c.p. transformation is also occurring. Thus, the main deformation mechanisms at this stage are TRIP and TWIP, in addition to deformation slip, enabling for more plastic deformation of the material. In this region, the strain hardening rate curve exhibits a wave-like shape, which is attributed to the activation of tensile twinning and nucleation of compression twins, with the latter being a preceding step for the activation of a secondary twinning system. The valleys, which appear on the strain hardening rate curve, imply a reduction in the rate of incipient twin formation [326], as well as the nucleation of compression twins which will be described in section 6.1.4.2.4.

The stress partitioning evolution in stage C, where both γ-f.c.c. and ε-h.c.p. phases have already undergone large plastic deformation, shows more marked differences than in stage B. The phase transformation rate from the γ-f.c.c. matrix to ε-h.c.p. is further accelerated in this stage (refer to Figure 6-5 a)), causing the stacking faults interspacing L_{sf} to further decrease with increasing stress (as shown in Figure 6-7). Moreover, the dislocation build-up necessary for the TRIP effect to be manifested also results in a persistent small-amplitude strain hardening in the γ-f.c.c. matrix phase. However, the deformation- and thermally-induced ε-h.c.p. phase carry almost 1.5 times more stress than the γ-f.c.c. phase, which is attributed to the load transfer to the harder ε-h.c.p. and to the activation of tensile twinning.

The continued change in the volume fraction transformation from γ-f.c.c. to ε-h.c.p. proves that the TRIP deformation mechanism is still progressing. Moreover, the phase transformation rate continues to increase slightly compared to stage B. This is attributed to a combination of multiple deformation mechanisms: tensile twinning triggered in the ε-h.c.p. grains, phase transformation and dislocation slip. A stress of 407 MPa marks the trigger point for twinning and enables the TWIP deformation mechanism, as shown in Figure 6-8.

Considering Figure 6-8, it was observed that the normalized diffraction intensities of the three selected grain families of the ε-h.c.p. phase start to change dramatically over TD and LD. The evolution of the normalized diffraction intensity of the ε-h.c.p. $(10\bar{1}2)$ oriented grains along TD and LD has a similar trend, however, there is a diametrically opposite evolution for the normalized diffraction intensity in both directions among the $(10\bar{1}3)$ and $(10\bar{1}1)$ orientated grains. Fu et al. [288] used neutron diffraction to evaluate TWIP in a $Fe_{50}Mn_{30}Co_{10}Cr_{10}$ HEA and noted that the splitting behavior of the diffracted intensities along TD and LD is evidence of the presence of deformation twinning, which is associated with significant lattice reorientation. Furthermore, the onset for this splitting marks the stress point at

which deformation twinning is activated. Recently, Polatidis et al. [278] combined in-situ synchrotron X-ray diffraction with EBSD to demonstrate once again that the splitting behavior of the normalized diffraction intensity along both TD and LD is indeed caused by the presence of deformed twins in the ε-h.c.p. grains. Moreover, distinction between tensile and compression twinning can be evidenced by considering the evolution of the diffracted intensity along LD and TD for the $(10\bar{1}2)$, $(10\bar{1}1)$ and $(10\bar{1}3)$ oriented grains. Considering Figure 6-8, it can be observed that the abrupt splitting of the normalized diffraction intensity of the $(10\bar{1}3)$ oriented grains over the TD and LD confirms onset of the $(10\bar{1}2)$ tensile twinning.

It should be mentioned that, unlike deformation slip, twinning causes an abrupt reorientation of the crystal structure [344–346], and that two factors affect the deformation twinning modes: i) the critical resolved shear stress (CRSS), which refers to the tensile or compression component parallel to the c-axis of the deformed grain; ii) the Schmid factor, which describes the orientation of the grains with respect to the direction of the applied stress [347]. Usually, tensile twinning in the $(10\bar{1}2)$ grains occurs with a rotation of about 86.3° with respect to the "parent grain", while the compression twinning in the $(10\bar{1}1)$ grains has a rotation of around 56.2° [348]. The lower CRSS required for tensile twinning (between 2 and 2.8 MPa) [349], compared to the CRSS required for compression twinning (between 76 and 153 MPa) [350], is the main reason for the preferential and premature activation of $(10\bar{1}2)$ tensile twinning. Although the CRSS between $(10\,\bar{1}\,1)$ tensile twins and $(10\,\bar{1}\,2)$ compression twins are significantly different, twin crystals with two different deformation modes can also occur in the same grain [351]. Therefore, in order to further assess the deformation twinning modes that are present in the three selected grain families, the normalized diffraction intensity trends in both TD and LD were used for further comparative analysis.

On closer inspection of the ε-h.c.p. $(10\bar{1}3)$ oriented grains (refer to Figure 6-8 e and f), the normalized diffraction intensity increases sharply along TD and only decreases slightly along LD, while the other oriented grain families do not change significantly in the TD direction. Considering that tensile twins are easily activated during tensile deformation due to the relatively low CRSS, it can be deduced that the increase in the normalized diffraction intensity of $(10\bar{1}3)$ oriented grains along TD is caused by the lattice reorientation of the $(10\,\bar{1}\,2)$ tensile twinning in the $(10\,\bar{1}\,3)$ oriented "parent grain" reorientated by approximately 86.5°. The $(10\bar{1}2)$ tensile twinning after lattice reorientation of 86.3° is now nearly parallel to the TD of the $(10\bar{1}3)$ oriented "parent crystal" grains, revealing that the c-axis of the ε-h.c.p. $(10\bar{1}3)$ oriented "parent crystal" grain is nearly parallel to LD. In other words, the $(10\bar{1}3)$ oriented "parent grain" has a higher Schmidt factor. Thus, it can be determined that the $(10\bar{1}3)$ oriented grains favor the activation tensile twinning due to the high Schmid factor [352].

In contrast, the normalized diffracted intensity of the $(10\bar{1}1)$ oriented grains continues to increase along the LD, while in the TD the increase is significantly more reduced, suggesting that the twinned $(10\bar{1}3)$

oriented grains are most likely to become the LD of the $(10\bar{1}1)$ oriented grains. In other words, the ε-h.c.p. $(10\bar{1}3)$ oriented grains are in a $\approx 90°$ azimuthal relationship with the ε-h.c.p. $(10\bar{1}1)$ oriented grains.

Deformation twinning is now an active deformation mechanism in stage C and occurs first on the ε-h.c.p. $(10\bar{1}3)$ oriented grains. This conclusion echoes that the non-basal pyramidal < c + a > slip system is activated aided by the change in the c/a ratio. In addition, twinning formation is strongly influenced by the local stress state or strain distribution, and it can be inferred that the accumulation of a large number of dislocations in the ε-h.c.p. phase will act as stress concentrators, being this the main reason for the activation of twinning.

Compared to stage B, the lattice distortion increases in stage C (refer to Figure 6-10). The lattice parameters in the ε-h.c.p. phase change significantly in this stage, with the lattice constant $a_{\varepsilon\text{-h.c.p.}}$ expanding from 2.528 to 2.533 Å and the lattice constant $c_{\varepsilon\text{-h.c.p.}}$ shrinking from 4.099 to 4.077 Å, resulting in a sharp decrease in the c/a ratio (from 1.621 to 1.609). At this stage, plastic deformation of the ε-h.c.p. phase is more predominant as a way for the material to accommodate more strain. Moreover, pyramidal < c + a > slip gradually replaces the basal < a > slip and starts to dominate the ε-h.c.p. phase slip mechanism, since the activity of pyramidal < c + a > slip is strongly dependent on the ε-h.c.p. c/a ratio. The lower the ε-h.c.p. phase c/a ratio, the less favorable the basal < a > slip is, thus facilitating the activation of the pyramidal < c + a > slip [105]. In other words, at large deformations, the pyramidal < c + a > slip has a higher Schmid factor, and is the deformation mode that can accommodate more strain along the c-axis [105].

The combined effect of pyramidal < c + a > slip and deformation twinning are essential to accommodate the high c-axis strain and the associated work-hardening behavior of the ε-h.c.p. phase. Sinha et al. [105] have reported that the c/a ratio in HEAs undergoing phase transformation varies with processing and deformation, which is attributed to the dependence of the ε-h.c.p. phase lattice parameters on the microstructure and stress state due to transformation volume changes, which matches with the results derived in the present work. Moreover, from the evolution of the γ-f.c.c. and ε-h.c.p. volume fractions, shown in Figure 6-5 a), it is clear that the faster phase transformation rate in stage C allows for the ε-h.c.p. phase to become predominant, resulting in significant volume contraction (as shown in Figure 6-5 b). Thus, it is evident that the change in c/a ratio is also a product of the volume transition induced by the phase transformation. Furthermore, unlike basal < a > slip, the non-basal pyramidal < c + a > slip system dominated the ε-h.c.p. phase slip mechanism which not only helps to achieve kinematically compatible deformation, but is also the most efficient way to generate dislocation sources, resulting in significant dislocation multiplication [145], which is consistent with the high dislocation density observed in stage C of Figure 6-6 f).

The average microstrain of the constituent phases change significantly during this stage. In fact, in stage C, there is an inversion in the evolution of the average microstrain, where the ε-h.c.p. phase now experiences more average microstrain than the γ-f.c.c. phase. The onset of twinning in the ε-h.c.p. can

justify the increased average microstrain experienced by this phase. Moreover, the evolution of the γ-f.c.c. phase average microstrain for true strains above 4 % suggests that due to its soft nature, it will follow the same variation in average microstrain as that experienced by the ε-h.c.p phase, which is ultimately imposed by the cooperative movement with the soft and hard phases.

The phase stress partitioning of Figure 6-4 shows that the ε-h.c.p. phase now bears more load than the γ-f.c.c. phase, while the higher deformation accommodated (refer to Figure 6-6 e) occurs as a result of twinning deformation experienced by the ε-h.c.p phase. It is evident that although the ε-h.c.p. phase is a “hard” phase structure, further promotion of strain accommodation can be achieved with the combined assistance of multiple deformation mechanisms such as deformation twinning and < c + a > pyramidal slip as mentioned before. These multiple deformation mechanisms are also responsible for the ductility of the material, proving that the ε-h.c.p. phase mentioned above plays a crucial role in regulating of the plastic deformation of the metastable HEA after macroscopic yielding.

The combined existence of TRIP and TWIP in stage C promotes the increase of phase boundaries, providing a high-density source for dislocation accumulation, leading to a rapid increase in the dislocation density. The dislocation density within the γ-f.c.c. phase evolved from 1.61 x 10^{15} to 3.15 x 10^{15} m^{-2}, while for the ε-h.c.p. phase it grew from 3.94 x 10^{14} to 1.29 x 10^{15} m^{-2}.

Compared to the low dislocation density contained in γ-f.c.c. grains in medium-Mn steels [353], which also experience TWIP, the high dislocation density in the γ-f.c.c. grains found in the metastable $Fe_{42}Mn_{28}Co_{10}Cr_{10}Si_5$ HEA under study plays a crucial role in enhancing its mechanical stability [95]. Dislocations can act as barriers for the sliding of the ε-h.c.p. phase interfaces, thus stabilizing the γ-f.c.c. grains [354]. Also, the larger amount of hard ε-h.c.p. induced by TRIP protects the γ-f.c.c. grains from experience excessive deformation [355], but still allowing for the phase transformation to occur. Meanwhile, the high stress and elastic strain fields caused by the high dislocation density can effectively reduce the ε-h.c.p. phase nucleation barriers, and increase the necessary driving force for the phase transformation [325,356,357]. In other words, the high dislocation density can increase the transformation rate of γ-f.c.c. to ε-h.c.p. phase, which is consistent with the high phase transformation rate of stage C detailed in Figure 6-5 a). The twin boundaries introduced at this stage can also reduce the mean free motion path for dislocations and cause dislocation plugging, thus increasing the dislocation density of the ε-h.c.p. phase. This is in good agreement with the moderate increase in the dislocation density observed for the ε-h.c.p. phase.

To summarize the following deformation mechanisms are occurring in stage C: dislocation slip and TRIP for the γ-f.c.c. phase; tensile twinning and < c + a > pyramidal slip for the ε-h.c.p. phase.

6.1.4.2.4 Stage D – onset of compression twinning

Finally, for true strains above 7.7 %, the material enters in stage D where the deformation mechanisms encompass a combination of TRIP, TWIP as well as dislocation slip, which results in an almost constant

strain hardening rate. This is attributed to the widespread occurrence of nanoscale twins in the γ-f.c.c. grains and the formation of new boundaries induced by the TRIP and TWIP effects that limit the free travel of dislocations upon macroscopic loading [326].

A closer look at the stress-partition evolution detailed in Figure 6-4, reveals that there is a tendency for the saturation of the strain hardening rate for both phases. For the ε-h.c.p. phase, the imparted stress is almost approaching that of the macroscopic stress behavior of the material due to the massive transformation of γ-f.c.c. to ε-h.c.p. and due to the multiple-twinning effects and dislocation interactions that primarily occur in this phase, indicating that the work hardening of ε-h.c.p. phase dominates the deformation behavior of the alloy studied in this work. For the γ-f.c.c. phase, the saturation in the strain hardening is caused by the formation of a large amounts of ε-h.c.p. phases through TRIP in the material, which generates new grain boundaries and thus limits the movement of dislocations within and to the γ-f.c.c. phase.

A slightly increase in the phase transformation rate at this stage compared to stage C, demonstrates the continuous occurrence of the TRIP effect, which started from the onset of macroscopic yielding and persists until material failure (refer to Figure 6-5 a). Two reasons may justify the variation of the phase transformation rate at this stage. The first one is related to a activation effect due to the high dislocation density in the γ-f.c.c. phase (refer to Figure 6-6 f)) under large strains in this stage [342,358,359]. In stage D, the magnitude of the stacking faults interspacing, L_{sf}, is only 19.31 nm (refer to Figure 6-7), with the smaller dislocation slipping path providing evidence for the high dislocation density accumulation. Moreover, the regions in the γ-f.c.c. phase with higher dislocation density (which can act as stress concentrators), when transformed to the ε-h.c.p. phase will promote stress relaxation, further activating more slip systems and allowing for more stress and strain to be imparted by the material. The second reason for this is related to the stress redistribution at the grain and phase boundaries. Figure 6-5 b) shows that compressive stresses develop upon tensile testing, which is primarily related to the phase transformation and deformation of the γ-f.c.c. phase. The phase transformation will initiate at the γ-f.c.c. phase grain boundaries, where dislocations tend to primarily pile up increasing the strain energy required for the phase transformation to occur. However, a relaxation effect on these high stress concentration regions occurs upon TRIP [360,361]. This will reduce the stresses required for the phase transformation and have a retarding effect on the nucleation of the new ε-h.c.p. phase. The interaction between the two factors discussed above lead to an incomplete phase transformation prior to failure in the metastable γ-f.c.c. phase, ultimately resulting in 19% of residual γ-f.c.c. phase. A similar phenomenon for the phase transformation dynamics at high strains was observed by Fu et al. in a $Fe_{50}Mn_{30}Co_{10}Cr_{10}$ HEA [288].

Overall, the stress partitioning evolution from stage A to D, suggests that the metastable $Fe_{42}Mn_{28}Co_{10}Cr_{15}Si_5$ HEA can perform load redistribution during tensile loading through a series of different and competing deformation mechanisms. Moreover, the contributions of each deformation mechanism during macroscopic tensile loading varies and promotes a dynamic stress distribution

behavior between both phases in the different deformation stages. Specifically, there is a large difference in the stress partitioning between the γ-f.c.c. and ε-h.c.p. phases, with the ε-h.c.p. phase bearing 1.2 to 1.5 times more stress than the γ-f.c.c. phase. Again, this value varies with the preferential deformation mechanism at different stages, but TRIP always plays a dominant role in the stress partitioning. Similar behavior to that has been shown in duplex stainless steels [312]. As revealed by Muránsky et al. [320] and Fu et al. [288], an essential feature of TRIP is the significant stress redistribution and demonstrates the importance of dynamic load distribution in the bulk hardening behavior [297,362]. Moreover, it contributes to improve the mechanical properties of the material.

In this stage, the occurrence of twinning in the ε-h.c.p. phases (refer to Figure 6-8) and the higher phase volume fraction (refer to Figure 6-5 a)) allow the average microstrain of the ε-h.c.p. phase under to increase at a higher rate than the γ-f.c.c. phase, which plays a role in regulating the plastic deformation of the material.

The dislocation densities of both γ-f.c.c. and ε-h.c.p. phases continues to increase until fracture. In fact, the rate of increase is similar to that of the stage C, which is in good agreement with the similar transformation rate of the γ-f.c.c. to ε-h.c.p. phase observed in both stages C and D. The dislocation density of the γ-f.c.c. phase increased from 3.15 x 10^{15} to 3.85 x 10^{15} m^{-2}, while for the ε-h.c.p. phase it grew from 1.25 x 10^{15} to 1.49 x 10^{15} m^{-2}. The increase in dislocation density in the γ-f.c.c. phase probably originates from the release of a large amount of dislocations from the moving ε-h.c.p. / γ-f.c.c. heterogeneous interface during the ongoing phase transformation [357]. It should be noted that the volume fraction of the ε-h.c.p. phase at this stage is already as high as 81% (as shown in Figure 6-5), and the softer γ-f.c.c. phase is constrained by the surrounding harder ε-h.c.p. phase, which can lead to long-range back stress [325,363]. This back stress can prevent/difficult the dislocation source from emitting more dislocations.

The amount of new ε-h.c.p. phase formed by phase transformation is to some extent related to stacking faults probability, P_{sf}, and stacking faults interspacing, L_{sf}, since the new ε-h.c.p. phase nucleates at sites in γ-f.c.c. phase with a large density of stacking faults. In addition to this, the evolution of the dislocation density in the γ-f.c.c. phase is related to the plastic deformation but also to the formation and accumulation of stacking faults in the γ-f.c.c. phase, as these act as barriers against the movement of the dislocations, resulting in a reduction of the average free path of the dislocation movement and consequently causing the plugging of dislocations.

Regarding the evolution of the stacking faults probability, P_{sf}, and stacking faults interspacing, L_{sf}, in stage D, the P_{sf} is increasing at an approximately constant state with increasing deformation, suggesting that if the material has a sufficiently low stacking faults energy, thus significant accumulation of stacking faults can occur even at room temperature and low strain rates, as in the case of the current work. Upon fracture, the P_{sf} reaches ≈ 10.7%, which is significantly higher than that measured for a CrMnFeCoNi HEA (≈ 1.5%) [364], indicating that the lower the stacking faults energy, the higher the corresponding

P_{sf}. It is important to mention here that, the the P_{sf} is generally correlated with the amount of ε-h.c.p. phase, as this phase is formed by the ordering of dense stacking faults. The increase of the P_{sf} in the γ-f.c.c. phase means that more stacking faults are being formed and accumulated in this phase. These stacking faults act as nucleation sites for the transformation from γ-f.c.c. phase to ε-h.c.p. phase. Thus, the evolution of the P_{sf} is directly linked with the phase transformation kinetics upon loading. This is evident when comparing the steady increasing trend of the γ-f.c.c. to ε-h.c.p. transformation in both stage C and D (refer to Figure 6-5) and a similar trend in the evolution of the P_{sf} (refer to Figure 6-7). From stage C onwards, the reduction in L_{sf} is further slowed until it enters stage D, where the change in L_{sf} is found to reach a saturation plateau, at approximately 19 nm. A similar saturation response is observed in numerous alloys such as hot-rolled Co-Cr-Mo alloy, Mg alloy [128,144] as well as in $Fe_{40}Mn_{20}Cr_{15}Co_{20}Si_5$ HEAs [337]. The reduction of the L_{sf} during plastic deformation not only promotes an increase in the dislocation density, but also strengthens the material as evidenced in both Mg alloys [144] and $Fe_{40}Mn_{20}Cr_{15}Co_{20}Si_5$ HEAs [337].

Alongside with TRIP, multiple twinning modes (tensile and compression twinning modes) are now fully activated. Severe lattice reorientation leads to a dramatic change in the normalized diffracted intensity, as evidenced by the clear splitting behavior diffracted data in Figure 6-8 a) and b). The normalized intensity of ε-h.c.p. $(10\bar{1}1)$ oriented grains decreases along the TD and increases sharply along the LD, while the normalized intensity of ε-h.c.p. $(10\bar{1}2)$ and $(10\bar{1}3)$ oriented grains exhibits an opposite evolution, showing an opposite evolutionary trend along TD and LD. Fu et al. have reported that a similar normalized diffraction intensity splitting behavior was observed in a TRIP $Fe_{50}Mn_{30}Co_{10}Cr_{10}$ HEA when it was subjected to large tensile plastic deformation, and attributed this to the activation of compression twinning and multiple-twin systems [288]. As can be seen from stage C in Figure 6-8 a) and b), the c-axis of ε-h.c.p. $(10\bar{1}1)$ oriented grains are perpendicular to the loading axis (LD) and therefore the c-axis is compressed, which means that the ε-h.c.p. $(10\bar{1}1)$ oriented grains are favorable to the formation of compression twins. The source of the CRSS required for compression twinning formation arises the high local stress concentration resulting from the saturation of both the phase transformation (as shown in Figure 6-4) as well as the high dislocation density (as shown in Figure 6-6 f)). The formation of compression twins in the ε-h.c.p. $(10\bar{1}1)$ oriented grains allow for an ≈ 56.2° lattice reorientation, which is consistent with previous findings [146,288]. Frank et al [146] pointed out that the compression twinning of ε-h.c.p. $(10\bar{1}1)$ grains can also be predicted by a decrease in the normalized diffraction intensity along TD and an increase along LD. The increase in the diffraction intensity of the ε-h.c.p. $(10\bar{1}2)$ oriented grains along the LD is the result of dislocation slipping [288]. The rarely reported ε-h.c.p. $(10\bar{1}3)$, on the other hand, is regarded as evidence of compression twinning action, and the orientation deviations were confirmed by Fu et al. [288] using EBSD.

The lattice parameters of the ε-h.c.p. phase, $a_{\varepsilon\text{-h.c.p.}}$ and $c_{\varepsilon\text{-h.c.p.}}$, reach to practically constant values in stage D (as shown in Figure 6-10 a)), which results in a saturation behavior of the c/a ratio. Nonetheless, the main slip mechanism of the ε-h.c.p. phase in this stage is still dominated by non-basal pyramidal <

c + a > slip system, while basal slip is almost suppressed. To accommodate the higher macroscopic tensile strain, both tensile and compression twins are active at this stage (refer to Figure 6-8). The saturation behavior seen in the c/a ratio stems from the high ε-h.c.p. phase volume fraction ($V_{\varepsilon\text{-h.c.p.}} \approx$ 81% in stage D), causing the soft γ-f.c.c. phase to be surrounded by the hard ε-h.c.p. phase, which can make the plastic deformation of the γ-f.c.c. phase and the TRIP effect difficult at this stage. This effect also translates into a saturation of the transformation volume, as shown in Figure 6-5 b). In conclusion, when designing structural materials based on ε-h.c.p. phase structures, tuning of the c/a structural parameters should be performed so that the < c + a > slip system is preferentially activated. This can render the development of highly ductile materials, while still exhibiting good mechanical strength.

From the comprehensive discussion presented from section 6.1.4.2.1 to section 6.1.4.2.4, the main deformation mechanisms experienced by the metastable $Fe_{42}Mn_{28}Co_{10}Cr_{15}Si_5$ HEA were detailed. These are schematically represented in Figure 6-14 and are summarized as follows: stage A experiences dislocation slip in the γ-f.c.c. phase; stage B possesses dislocation slip and TRIP of the γ-f.c.c., while basal < a > slip occurs on the ε-h.c.p. phase; stage C is characterized by dislocation slip and TRIP of γ-f.c.c. phase, with the onset of tensile twinning and non-basal pyramidal < c + a > slip in the ε-h.c.p. phase; finally in stage D, to same deformation mechanisms observed in stage C there is the addition of compression twinning in the ε-h.c.p. phase.

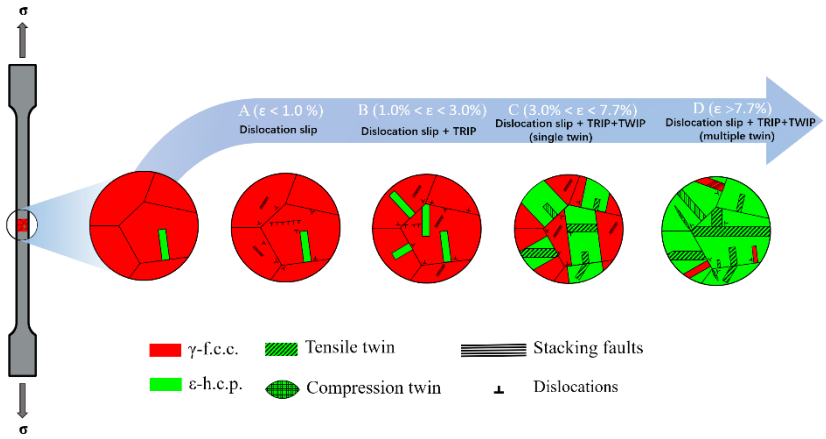

Figure 6-14. Schematic diagram of the deformation mechanisms in the as-cast $Fe_{42}Mn_{28}Co_{10}Cr_{15}Si_5$ metastable HEA during tensile loading.

The schematic of lattice reorientation during tensile and compression twinning is shown in Figure 6-15 and can be used to support the previous discussion on the onset of these twinning modes and their identification for the diffracted data of specific ε-h.c.p. phase planes. Figure 6-15 a) shows a $(10\bar{1}3)$ oriented grain with its c-axis parallel to the LD, which facilitates the formation of tensile twins by lattice reorientation 86.3° of the "parent grain" $(10\bar{1}3)$. $(10\bar{1}3)$ oriented grains are transformed into $(10\bar{1}1)$ oriented grains after the $(10\bar{1}2)$ tensile twinning occurs. In other words, $(10\bar{1}3)$ oriented grains have high probability to become the $(10\bar{1}1)$ oriented grain after tensile twinning occurs. The $(10\bar{1}1)$ oriented grains

are prone to compressive twinning because their c-axis is close to TD, and their lattice reorientation schematic is shown in Figure 6-15 b), where these compression twins are formed by a 57.2° lattice reorientation of the $(10\bar{1}1)$ parent grain.

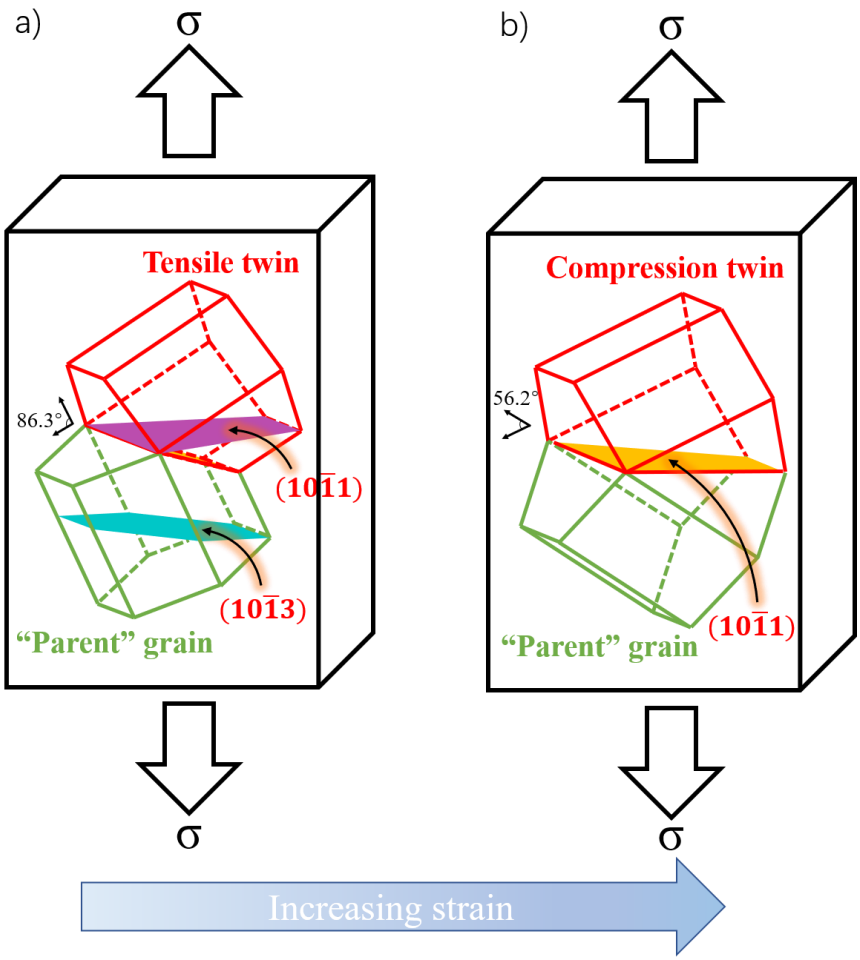

Figure 6-15. Schematic representation of the lattice reorientation occurring with increasing strain. a) 86.3° reorientation of the tensile twin relative to the parent $(10\bar{1}3)$ oriented grain; b) 56.2° reorientation of the compression twin relative to the parent $(10\bar{1}1)$ orientated grain.

6.1.5 Lattice strain evolution

The lattice strain evolution is not only able to show the amount of deformation imparted by each phase but, more importantly, is able to reflect the load transfer among different grain families. The lattice strain evolution in the $Fe_{42}Mn_{28}Co_{10}Cr_{15}Si_5$ metastable HEA which was previously shown in Figure 6-9 is analyzed next.

During the macroscopic elastic deformation (stage A), the lattice strain of each lattice plane of both γ-f.c.c. and ε-h.c.p. phases increases almost linearly with the applied stress. However, the slope of this

variation, which related to the plane stiffness varies between different crystallographic orientations, revealing anisotropy in the mechanical response.

Softer lattice planes will first bear the applied stress until their yielding occurs, upon which load transfer to harder planes takes place. This load transfer and partitioning behaviors ensures the uniform plastic deformation of the material. The Young's modulus of the analyzed γ-f.c.c. and ε-h.c.p. phases along the LD were determined by linear fitting in the macroscopic elastic deformation region. For the γ-f.c.c. it follows that $E_{\gamma-\text{f.c.c.}(111)}$ > $E_{\gamma-\text{f.c.c.}(311)}$ > $E_{\gamma-\text{f.c.c.}(200)}$, which reveals that the γ-f.c.c. (111) plane is the hardest, while the (200) plane is the softest. These results are consistent with the soft and hard responses exhibited by the f.c.c. lattice planes observed in some single-phase [364,365] and dual-phase HEAs [146,217,366]. For the ε-h.c.p. phase structure, $E_{\varepsilon-\text{h.c.p.}\ (10\bar{1}3)} > E_{\varepsilon-\text{h.c.p.}\ (10\bar{1}2)} > E_{\varepsilon-\text{h.c.p.}\ (10\bar{1}1)}$. Frank et al. [146] previously studied a metastable $Fe_{40}Mn_{20}Cr_{15}Co_{20}Si_5$ HEA by neutron diffraction in which the ε-h.c.p. phase $(10\bar{1}1)$ was the softest and the ε-h.c.p. $(10\bar{1}3)$ was the hardest plane, thus in good agreement with the current results. For reference, the Young's modulus for the analyzed crystallographic planes obtained along LD are summarized in Table 6-3. It should be mentioned here that the lattice strains in the γ-f.c.c. and ε-h.c.p. lattice planes are both positive in the LD and, conversely, negative in the TD, this behavior being expected due the Poisson's effect [367,368].

Table 6-3 – Elastic modulus for different lattice planes of constituent phases in as-cast $Fe_{42}Mn_{28}Co_{10}Cr_{15}Si_5$ metastable HEA.

γ-f.c.c. plane (GPa)			ε-h.c.p. plane (GPa)			
$E_{(111)}$	$E_{(200)}$	$E_{(311)}$	$E_{(10\bar{1}0)}$	$E_{(10\bar{1}1)}$	$E_{(10\bar{1}2)}$	$E_{(10\bar{1}3)}$
182 ± 1.9	108 ± 1.7	158 ± 1.8	117 ± 1.1	149 ± 1.3	191 ± 8.1	247 ± 0.4

When entering stage B, where macroscopic plastic deformation of the material starts to occur all analyzed planes exhibit a deviation to the previous linear response suggesting their yielding. However, the associated lattice strain is dependent on the crystal orientation vs LD relationship [244]. For example, in stage B the developed lattice strain is higher for the softest plane, and lower for the stiffer one.

The same behavior is noticed for the ε-h.c.p. phase. The four different lattice planes $(10\bar{1}0)$, $(10\bar{1}1)$, $(10\bar{1}2)$ and $(10\bar{1}3)$ of ε-h.c.p. phase, which are dominated by the basal < a > slip in stage B, all have a tendency for increasing the imparted lattice strain along LD, but with different magnitudes (1342, 1663, 1933 and 1478 με, respectively). The trend in the evolution of lattice strain also highlights that the ε-h.c.p. phase starts to bear more stresses, due to the premature yielding and soft nature of the γ-f.c.c., thus promoting a stress relaxation effect in this phase [288]. However, it should be emphasized that this stress relaxation arises from both the load partitioning to the ε-h.c.p. phase but also due to the TRIP effect.

When entering stage C, the lattice strain developed in the ε-h.c.p. is significantly reduced in magnitude when compared to stage B. This is related to a saturation of the work-hardening behavior of the different lattice planes resulting from the massive plastic deformation imparted by the material. This effect is further exacerbated in stage D, where the increase in lattice strain as function of stress or strain is almost negligible. The saturation is occurring in both phases and is primarily related to the high dislocation density (refer to Figure 6-6 f)).

6.1.6 Strengthening contributions

Dislocation slip has always been of interest as a common deformation mechanism among both γ-f.c.c. and ε-h.c.p. phases, while TRIP is an additional deformation mechanism in the γ-f.c.c. phase. However, studies on the stacking faults strengthening effect in HEAs are scarce. A comprehensive analysis of the different dislocation strengthening contributions of the γ-f.c.c. and ε-h.c.p. phases, as well as the stacking faults strengthening contribution in the γ-f.c.c. phase was previously shown in Figure 6-7.

In the macroscopic elastic deformation stage A ($\varepsilon < 1\%$), which is dominated by dislocation slip of the γ-f.c.c., the intrinsic dislocation strengthening contribution from the ε-h.c.p. phase due to dislocation is approximately 5 MPa, which contrasts with the 104 MPa (with further increase up to 215 MPa in stage A) of the γ-f.c.c. phase. This significant difference is rooted to the distribution of dislocation density in both phases (see Figure 6-6 f)). Throughout stage A, the stacking faults strengthening contribution from the γ-f.c.c. phase increase is only of 5 MPa.

In the plastic deformation stage B ($1\% < \varepsilon < 3\%$), where the deformation mechanism is dominated by TRIP and dislocation slip, the dislocation strengthening contributions of the γ-f.c.c. and ε-h.c.p. phase increase from 215 to 233 MPa and from 14 MPa to 58 MPa, respectively. Based on the magnitude of the strengthening contribution, the dislocation strengthening contribution in the γ-f.c.c. phase is almost four times larger than that in the ε-h.c.p. phase. The reason for this difference is related to the dislocation density contained in both phases ($\rho_{\gamma\text{-f.c.c. phase}} \approx 1.61 \times 10^{15}$ m^{-2} and $\rho_{\varepsilon\text{-h.c.p. phase}} \approx 3.94 \times 10^{14}$ m^{-2}, as shown in Figure 6-6 f)). Regarding the contribution of the stacking faults in the γ-f.c.c. phase to the material flow stress, it increases from 5 MPa to 48 MPa, which is near a 10-fold increase compared to stage A. In fact, this is directly related to the amount of stacking faults accumulated (refer to Figure 6-7). Specifically, it can be seen from Equation (3-42) that there are two main factors affecting the strengthening due to stacking faults, one being the strengthening factor, K_{sf}, which is a constant, and the other being the stacking faults interspacing L_{sf}, which evolves under tensile deformation as shown in Figure 6-7. Therefore, the dynamic evolution of the stacking faults contribution is only dependent on the L_{sf}. Thus, the evolution of the stacking faults strengthening contribution during this stage coincides well with the variation of L_{sf} depicted Figure 6-7. In addition to this, Frank et al. [369] have reported that stacking faults strengthening is associated with the γ-f.c.c. to ε-h.c.p. phase transformation as well as to the work-hardening behavior, and that an increase in the stacking faults strengthening contribution corresponds to the onset of the phase transformation, which is again in good agreement with the results of the current study. In this work, the γ-f.c.c. to ε-h.c.p. phase transformation is triggered at 284 MPa, which corresponds to the point where there is a sudden increase in the stacking fault probability (refer to Figure 6-7).

During stage C ($3\% < \varepsilon < 7.7\%$) where the deformation mechanism comprised TRIP, TWIP and dislocation slip, the dislocation strengthening contribution from γ-f.c.c. phase grows gradually from 233 to 304 MPa and from 58 to 105 MPa for the ε-h.c.p. phase. From Figure 6-12, it is observed that the dislocation strengthening contributions in both γ-f.c.c. and ε-h.c.p. phase show a continuous increasing trend and the incremental rate is larger than in stages A and B. However, in stage C, the contribution of the dislocation strengthening from the γ-f.c.c. phase is only two times larger than that arising from the ε-h.c.p. phase. This as expected, since the transformation from γ-f.c.c. to ε-h.c.p. promotes the appearance of ε-h.c.p. with higher dislocation density than the thermally-induced one. The large transformation rate (as shown in Figure 6-5 a)) at this stage also further contributes to the strengthening by the stacking faults in the γ-f.c.c. phase from 48 to 102 MPa.

Finally, when entering stage D (ε > 7.7%), it can be found that the evolution of the dislocation strengthening contribution from both γ-f.c.c. and ε-h.c.p. phases, as well as the stacking faults strengthening contribution from γ-f.c.c. phase, are approaching a saturated state and remain almost constant. This stems from the saturation of dislocation density and stacking faults interspacing, L_{sf}, as detailed in Figure 6-6 f) and Figure 6-7. The maximum strengthening contribution arising from dislocations in both the γ-f.c.c. and ε-h.c.p. phases reaches 321 and 111 MPa, respectively, while the stacking faults strengthening further contributed to 118 MPa to the material strength. Overall, it is shown that the dislocation strengthening contribution is the main source of the high strength of the present metastable HEA.

In summary, it is shown that there are two major sources of contribution to the flow stress in the as-cast $Fe_{42}Mn_{28}Co_{10}Cr_{15}Si_5$ HEA studied in this work. One is dislocation-dislocation interactions, where the dislocation strengthening contribution from the γ-f.c.c. phase is significantly higher than that in the ε-h.c.p. phase. The reason for this is the reduction in the average free path for dislocation movement resulting from the large amount of stacking faults and decrease in the stacking faults interspacing in the γ-f.c.c. phase, which greatly contributes to the dislocation hardening effect. The other source is the stacking faults strengthening in the γ-f.c.c. phase, which is necessary for the phase transformation to occur, as stacking faults are the preferential sites for the ε-h.c.p. phase nucleation. However, its strengthening effect is significantly lower than that caused by dislocations. It should be mentioned that this is the first time that a quantitative analysis of the evolution of the strengthening contributions of a metastable HEA of the Fe-Mn-Co-Cr system is performed using high energy synchrotron X-ray diffraction. This provides a comprehensive understanding of how the microstructure evolution experienced by the alloy modifies the predominant deformation mechanisms and how these contribute to the strength and ductility of the material, which can be useful to overcome the traditional strength-ductility paradigm with implications for the design of advanced structural alloys.

Through the above analysis of the strengthening mechanisms experienced by metastable $Fe_{42}Mn_{28}Co_{10}Cr_{15}Si_5$ HEA during tensile loading are schematically depicted in Figure 6-16. Here, Figure 6-16 a) refers to the dislocation strengthening in the γ-f.c.c. phase, $\sigma_{\gamma\text{-f.c.c. DIS}}$; Figure 6-16 b) details the stacking faults strengthening in the γ-f.c.c. phase, $\sigma_{\gamma\text{-f.c.c. SF}}$; while Figure 6-16 c) points to dislocation strengthening in the ε-h.c.p. phase, $\sigma_{\varepsilon\text{-h.c.p. DIS}}$. The core of these strengthening mechanisms lays in the reduction of the mean free path of dislocations, Λ, resulting in the piling up of dislocations.

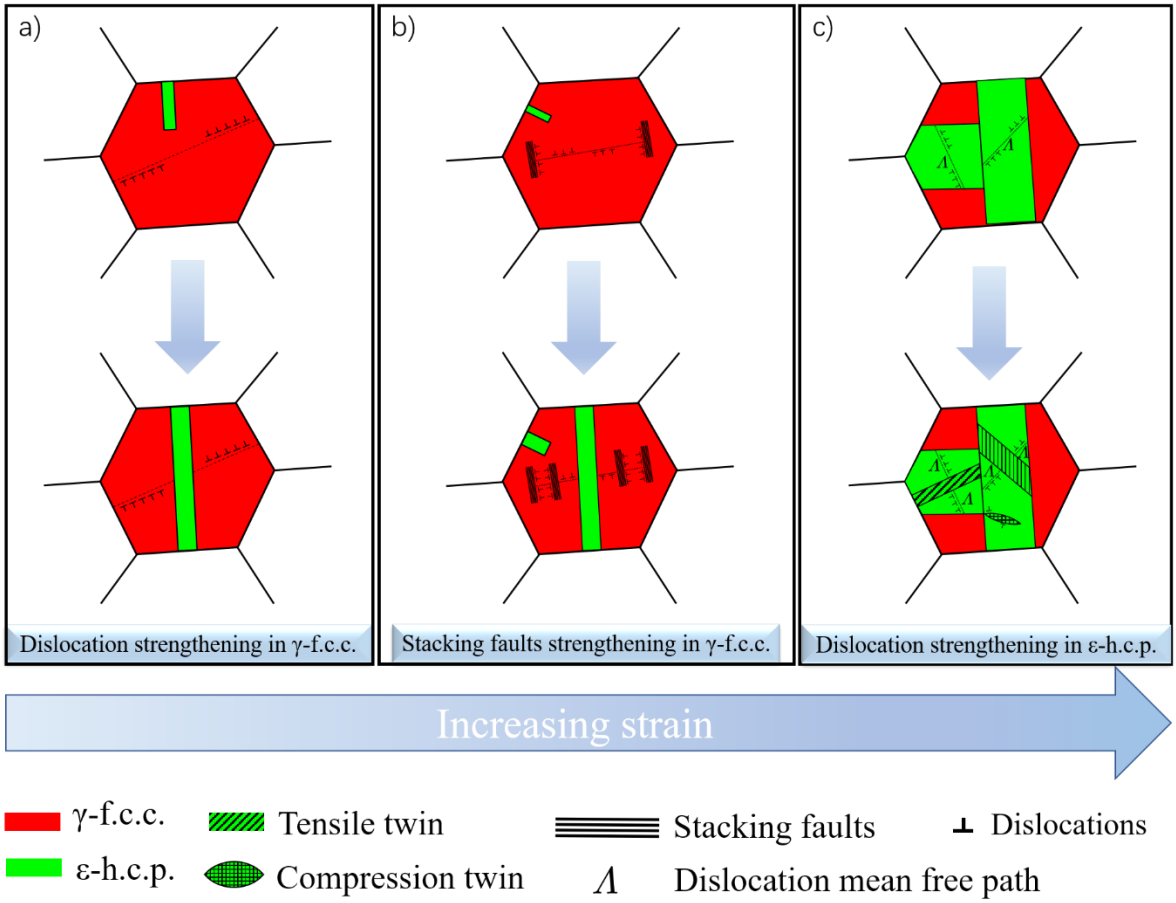

Figure 6-16. Schematic representation of the strengthening mechanisms in the as-cast $Fe_{42}Mn_{28}Co_{10}Cr_{15}Si_5$ metastable HEA upon tensile loading.

6.1.7 Conclusions

In this thesis, the deformation mechanisms and micromechanical behavior of an as-cast $Fe_{42}Mn_{28}Co_{10}Cr_{15}Si_5$ metastable HEA was investigated by in-situ synchrotron X-ray diffraction. The microstructure evolution was qualitatively and quantitatively assessed, based on multiple features including phase volume fraction, c/a ratio, average microstrain and lattice strain, for example. Stress partitioning and redistribution between the γ-f.c.c. and ε-h.c.p. phases was seen to be linked to the active deformation mechanisms of the alloy at a given loading step.

Yielding of the soft γ-f.c.c. phase was seen to occur prior to yielding of the hard ε-h.c.p., with the latter occurring in parallel to macroscopic yielding. Upon entering the plastic deformation region, the hard ε-h.c.p. phase bears significantly more stress than the γ-f.c.c. phase. The onset of TRIP occurred slightly after plastic deformation of the γ-f.c.c. phase suggesting the need for an excess driving force for the transformation to occur. This excessive driving force was in the form of stacking faults accumulation. TWIP occurred at larger stresses levels compared to TRIP (407 vs 287 MPa, respectively). Tensile

twinning was first activated due to the lower critical resolved shear stress, and prior to material failure compression twining was evidenced.

The four identified deformation regimes were characterized by different actuating deformation mechanisms: stage A had dislocation slip occurring in the γ-f.c.c. phase; stage B had dislocation slip and TRIP on the γ-f.c.c. and basal < a > dislocation slip on the ε-h.c.p.; stage C had the same deformation mechanisms for the γ-f.c.c., but non-basal < c + a > dislocation slip and tensile twinning were activated on the ε-h.c.p. phase; finally, in stage D there was the addition of compression twinning to the ε-h.c.p. phase, while the other mechanisms were kept active.

The strengthening contributions were also quantified. It was determined that the dislocation strengthening from the γ-f.c.c. phase was larger than that induced by dislocations in the ε-h.c.p. phase. Moreover, the magnitude of the strengthening contribution due to stacking faults in the γ-f.c.c. phase was similar to that arising from dislocations in the ε-h.c.p. phase.

The results presented in this work can be of interest for the design of dual-phase alloys with good strength-ductility balance.

6.2 Gas tungsten arc welding of as-cast $Fe_{42}Mn_{28}Co_{10}Cr_{15}Si_5$ metastable high entropy alloy

6.2.1 Introduction

Extensive literature [370,371] shows that the most widely studied HEA, the equiatomic and f.c.c. single phase CoCrFeMnNi alloy, possesses high ductility, but relatively low mechanical strength which prevents its use in several practical applications. Recent developments in the field of non-equiatomic HEAs with tunable phase stability have led to breaking the strength-plasticity barrier by triggering TWIP and TRIP effects simultaneously, improving both strength and ductility [301]. Based on this design concept, Nene et al. [62] examined the impact of Si addition to the Fe-Mn-Co-Cr system on the metastability of the γ-f.c.c. phase, showing that the addition of 5 at. % Si was able to achieve a maximum metastability of the γ-f.c.c. phase. This allowed to develop an alloy with an optimized metastable microstructure with a composition of $Fe_{42}Mn_{28}Co_{10}Cr_{15}Si_5$ (at. %).

Welding is one of the most effective metal processing methods that is utilized in a wide range of industrial applications when it comes to structural engineering, including automobile, aerospace, and marine industries. Considering the relevance of HEAs as potential structural engineering materials, welding will

become increasingly necessary to construct complex shaped structures or to combine their properties with those of other materials. Therefore, to ensure the feasibility of using these new advanced alloys in real-life applications, their weldability needs to be addressed.

Up to now, most studies on TWIP/TRIP metastable HEAs have primarily focused on their thermo-mechanical processing, phase formation characterization, assessment of mechanical properties, as well as physical and chemical performances [60,279,295,372,373]. Weldability of TWIP/TRIP metastable HEAs has been addressed in only two reports, both using friction stir welding [374,375]. Thus, weldability studies for metastable high entropy alloys considering fusion-based welding methods have not yet been reported.

The work presented here is the first to use gas tungsten arc welding to weld an as-cast TWIP/TRIP $Fe_{42}Mn_{28}Co_{10}Cr_{15}Si_5$ metastable HEA for the purpose of obtaining and discussing new data for the widespread applications of these advanced engineering alloys. To determine how the weld thermal cycle affects the evolution of microstructure across the entire joint, a combination of electron microscopy, high-energy synchrotron X-ray diffraction analysis and thermodynamic calculations were used. In addition, further clarification of the processing/microstructure relationship was achieved by using tensile testing and microhardness mapping. Through multiscale and comprehensive characterizations of these novel materials, a deeper understanding of the correlation between processing, microstructure, and mechanical properties is gained paving the way for their wide application in a variety of fields.

6.2.2 Starting material

The material used in this work was an as-cast non-equiatomic metastable $Fe_{42}Mn_{28}Co_{10}Cr_{15}Si_5$ (at. %) HEA, which was produced at Sophisticated Alloys Inc. in Butler, PA, USA, by vacuum induced melting in an argon atmosphere [376]. Prior to welding, sheets with a thickness of 1.5 mm were cut into 80 × 40 mm^2 parts. Afterwards, the welding specimens were cleaned with acetone and ethanol to ensure that there were no potential contaminations on the joining surfaces.

6.2.3 Results and discussion

6.2.3.1 Microstructure evolution

Figure 6-17 a) provides a cross-sectional view of the as-cast $Fe_{42}Mn_{28}Co_{10}Cr_{15}Si_5$ gas tungsten arc welded joint. There, it can be observed that the welding parameters that were selected enabled a full penetration joint to be formed. A closer inspection of the cross section shows that there are no visible defects, such as pores or cracks. To clearly image representative microstructural features, optical microscopy images of the BM, HAZ, boundary of HAZ/FZ, as well as the FZ are detailed in Figure 6-17 b1), b2), b3) and b4), respectively. Besides, scans of the same regions taken at high magnifications

using electron microscopy are shown in Figure 6-17 c1), c2), c3) and c4), respectively. The boundaries of the HAZ/FZ are indicated by red dashed lines, as shown in Figure 6-17 a).

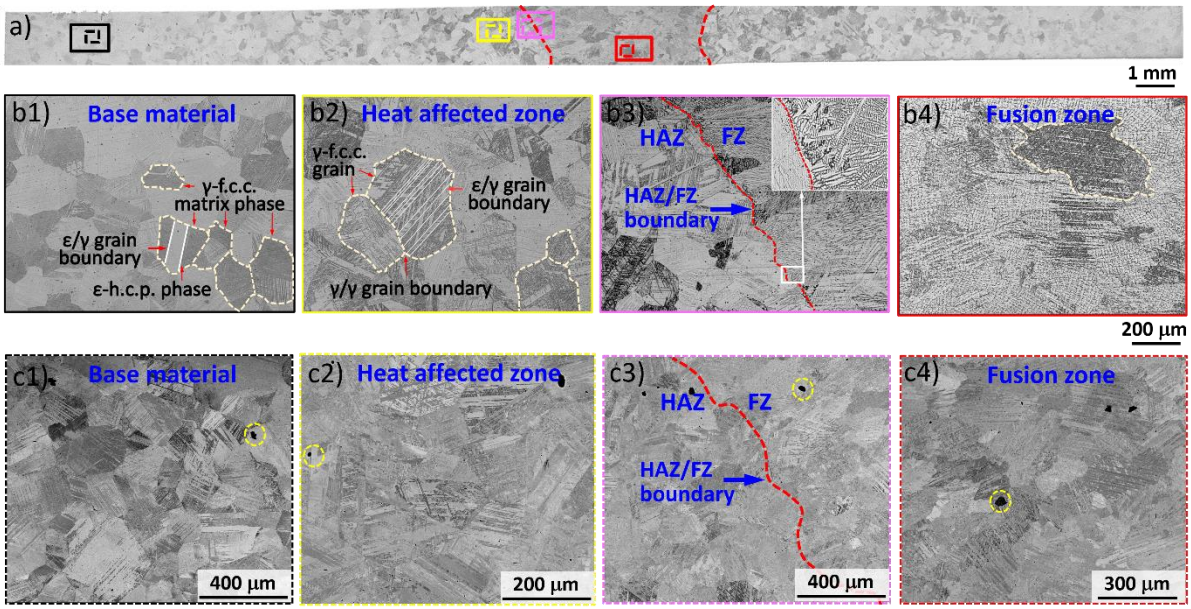

Figure 6-17. a): a cross-sectional view of the welded joint; b1) and c1), b2) and c2), b3) and c3), c4) and d4) are close-up views of optical/electron microscopy for the BM, HAZ, boundary of HAZ/FZ, FZ, respectively.

Overall, a dual γ-f.c.c. / ε-h.c.p. microstructure is evidenced across the welded joint. The bright and dark contrasting colors are related to the microstructural features of both phases. A further detailed description will follow with respect to the microstructure that exists over the four typical regions of a welded joint, beginning with the so-called BM. This region mainly consists of two phases: a γ-f.c.c. matrix phase and ε-h.c.p. phase. In the γ-f.c.c. matrix phase, the ε-h.c.p. phase forms within it and mainly exhibits a block-shaped morphology, as indicated by the red arrows in Figure 6-17 b1). Here, it is important to mention that the initial ε-h.c.p. phase formed was thermally induced upon cooling from the casting process used to obtain the starting BM. Entering in the HAZ (refer to Figure 6-17 b2)), the microstructure is found to retain the dual γ-f.c.c. / ε-h.c.p. phases, with the parent γ-f.c.c. phase appearing to be partitioned by laths of ε-h.c.p. phase that cross-cut individual grains, and filled with compact laths, as marked by the white solid line in Figure 6-17 b2).

Ahmed et al. [284] previously provided an interesting insight on how the inter-lath spacing (i.e., the distance between ε-h.c.p. laths) evolves. They conducted an examination of the ε-h.c.p. laths morphologies under different annealing conditions and found that the variations in the average interlath spacing is consistent with the trends in the ε-h.c.p. phase volume fraction, where the increased volume fraction of the ε-h.c.p. phase will lead to an increase in the density of ε-h.c.p. laths. This will be further discussed in the next section when evaluating the volume fraction changes across the welded joint. Moreover, from the BM (Figure 6-17 b1)) to the HAZ (Figure 6-17 b2)), a clear increase in grain size is

evident as a result of the increased local peak temperature and permanence at high temperatures where solid-state phenomena, such as grain growth, can occur. This is a typical feature of fusion-based welding processes.

The HAZ/FZ boundary is clearly observed in Figure 6-17 c3), because of the significant differences in the microstructures that exist in each region. These changes are attributed to the different weld thermal cycles experienced at each location, where the HAZ remains in the solid state, while in the FZ there is melting followed by solidification. Specifically, when weld solidification occurs, epitaxial nucleation is then triggered under the support of the cold HAZ, which serves as a substrate, and then grain growth ensues in accordance with the direction of the maximum temperature gradient in the FZ. Here, at the edge of the FZ, a fine dendritic structure is observed as a result of the fast-cooling rate enabled by the previously cold HAZ. Then, grains will start to grow towards the weld centerline (refer to Figure 6-17 c3) and associated insert), which is consistent with the solidification theory that is used during fusion-based welding processes [252]. While moving away from the HAZ/FZ boundary towards the weld centerline, the grain structure formed is mainly composed of finer equiaxed grains (refer to Figure 6-17 b4) whose formation is controlled by the degree of constitutional undercooling, i.e., the ratio of the temperature gradient, G, to the solidification rate, R, with a low G/R ratio being beneficial in promoting the formation of equiaxed grains [377].

Interestingly, the four regions of the welded joint evidence, according to the high magnification electron microscopy images, minor black spots (marked by yellow dashed circles), and most of them are concentrated on the phase boundaries, resembling welding defects such as pores and voids. However, EDS measurements detail that these spots correspond to the presence of Si-Mn-rich σ phase. This identification is corroborated by both synchrotron X-ray diffraction measurements, as well as thermodynamic calculations all of which will be further discussed in subsequent sections.

Figure 6-18 a) details the EBSD map of the gas tungsten arc welded $Fe_{42}Mn_{28}Co_{10}Cr_{15}Si_5$ joint. Owning to the large dimensions of the joint and symmetry along the weld centerline, as observed in the optical micrograph of Figure 6-17 a), only half of the joint is shown. In addition, the IPF (top) and KAM (bottom) of the BM (Figure 6-18 b)), HAZ (Figure 6-18 c)) and FZ (Figure 6-18 d)) are also shown.

In the FZ, large columnar grains are observed (refer to Figure 6-18 a)), which results from grain growth starting on the pre-existing solid material, where a large thermal gradient exists promoting the formation of fine grain structure at the edge of the FZ. As mentioned before, the growth of grains tends to follow a direction perpendicular to the solid-liquid interface, the direction of the maximum temperature gradient, and nucleation is preferentially initiated at the cold substrate, producing fine dendritic grains at that point, as previously shown in Figure 6-17 b3). However, when the solidification proceeds toward the weld centerline, competitive growth between grains will induce certain specific orientations, where grain growth will be facilitated if they are aligned more favorably with the heat flow. Here, during the rapid cooling of the FZ, the IPF map demonstrates that the preferential growth direction of the γ-f.c.c. and ε-

h.c.p. phases is along the (001) and (0001) orientations, respectively, which is line with the easy growth directions for these crystal structures [378].

Figure 6-18 b), c), and d) (bottom) illustrate the KAM maps of the BM, HAZ, and FZ, respectively. Generally, point to point measurements of local misorientation of grains in the surrounding microstructure define a KAM map. To further evaluate the variation of the KAM values across the welded joint, Figure 6-18 f) details the average KAM values for different regions. Comparing the KAM maps (Figure 6-18 b), c), and d) (bottom)) and values Figure 6-18 f)) in different regions, it is evident that the local deformation over the whole welded joint is quite low.

Based on the calculations made from multiple EBSD maps, Figure 6-18 e) provides the variation of the average grain size of the γ-f.c.c. phase in different regions of the welded joint. It should be noted that the values of the measured γ-f.c.c. grain size refers to the size of the whole matrix grains, which may contain the ε-h.c.p. laths. In the BM region, there is an average grain size of approximately 47.5 μm. Then, the average grain size increases to around 54.2 and 57.9 μm when entering the HAZ and FZ, respectively. It is well known that the HAZ near the BM and HAZ near the FZ, are expected to exhibit different microstructure features owing to the differences in both peak temperature and permanence time at which solid-state transformations can occur. Although grains are visible to grow in the HAZ, the minor growth observed can be attributed to the material's high thermal stability, which inhibits massive grain growth to occur.

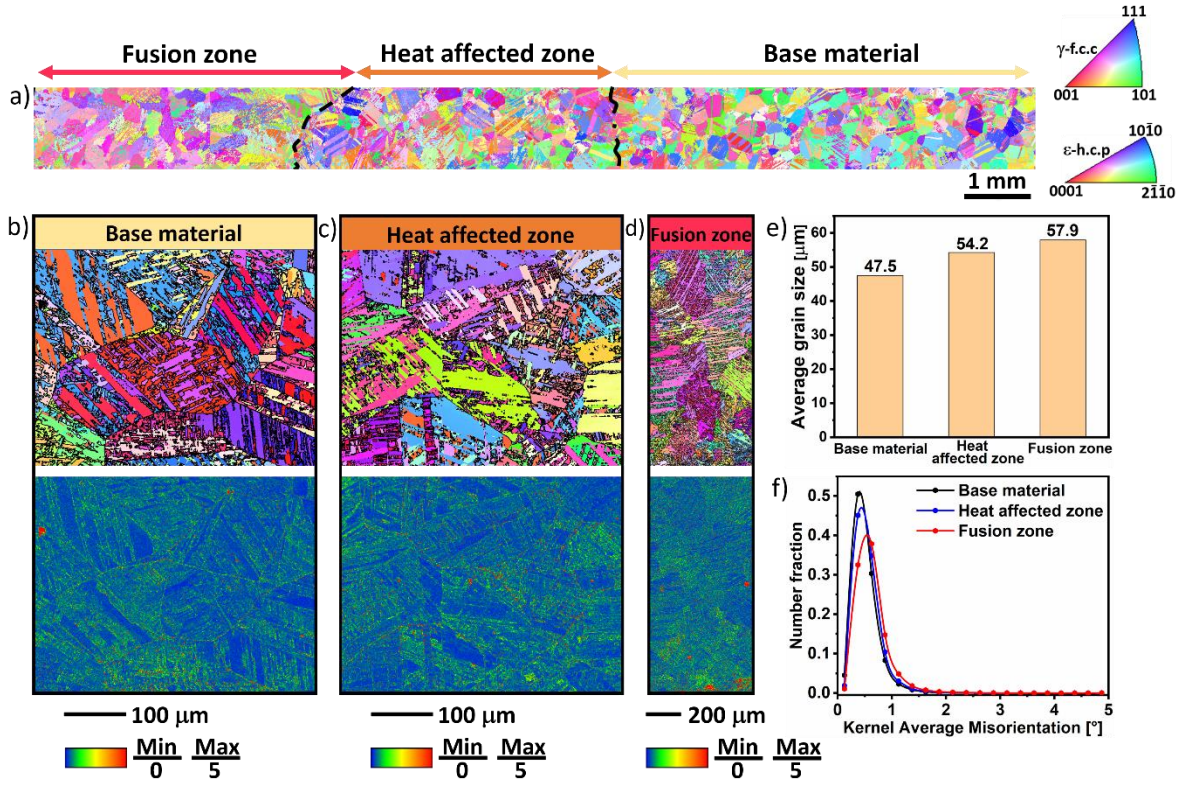

Figure 6-18. a) EBSD map of the gas tungsten arc welded $Fe_{42}Mn_{28}Co_{10}Cr_{15}Si_5$ joint; IPF map (top), KAM map (middle) and phase map (bottom) of b) BM region, c) HAZ and d) FZ; e) and f) variation of the average grain size and KAM values with respect to the different regions of the joint, respectively.

Figure 6-19 b) details an EDS map performed near the boundary of the HAZ/FZ for the main elements of the present HEA (Fe, Mn, Co, Cr and Si), which was used to study the homogeneity of the chemical composition of the material. The white dashed line corresponds to the boundary between the HAZ and FZ. In the HAZ, the chemical composition of Co, Cr, Fe, Mn and Si is well distributed in the ε-h.c.p. and γ-f.c.c. phases, without any segregation being observed, which is due to the fact that both the peak temperature during the welding and period at high temperatures in this region are insufficient to promote observable chemical contrast between the γ-f.c.c. and ε-h.c.p. phases. Within the FZ, elemental redistribution is a typical feature associated to the solidification of fusion-based welding process. Here, all elements are evenly distributed, suggesting that the high cooling rate during welding is beneficial for suppressing macroscopic elemental segregation.

To further present the local trends of different elements, Figure 6-19 c) details an EDS line scan performed along the yellow dashed line of Figure 6-19 a). From the elemental distribution curve of Figure 6-19 c), there is no significant fluctuations that exist for all the elements in the HAZ. Taken as a whole, all elements are uniformly distributed in the HAZ and FZ. This homogeneous distribution of elements is common in metastable HEAs [60,279], unlike for Mn-containing steels [379,380], which exhibit a distinct chemical gradient across phase boundaries.

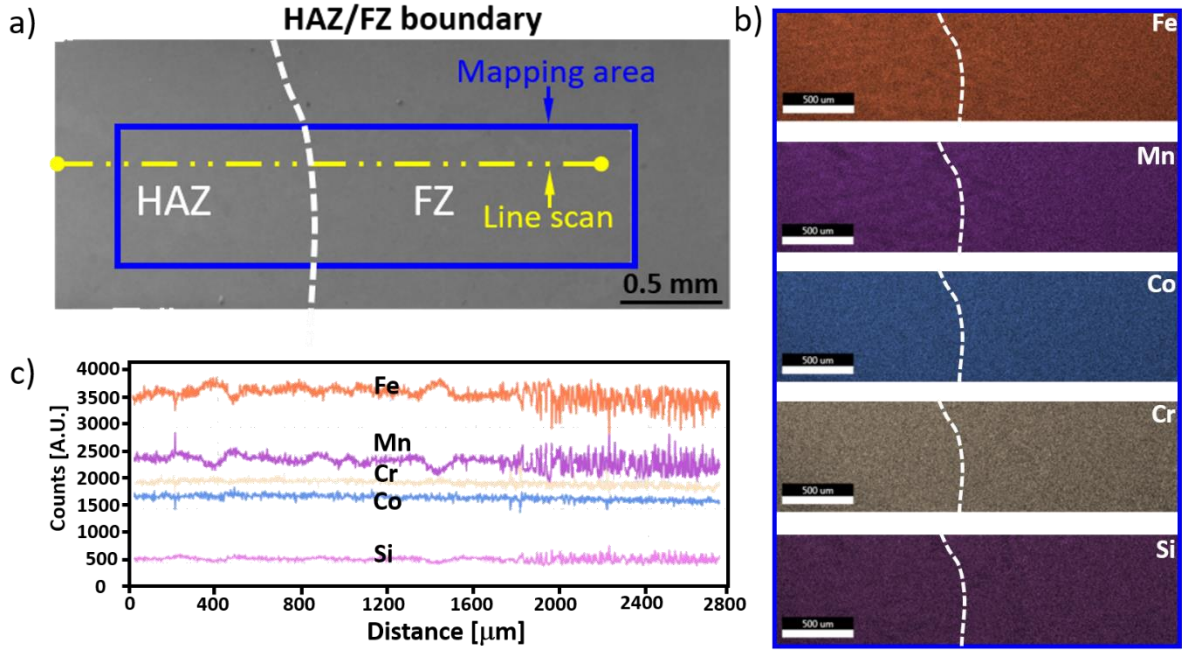

Figure 6-19. a) Scanning electron microscopy (SEM) micrograph along with an energy-dispersive X-ray spectroscopy (EDS) line scan (yellow line) and area scan (blue box) near the HAZ/FZ boundary; b) EDS area mapping, with the analyzed region corresponding to the blue box of Figure 6-18 a); c) EDS line scan along the yellow dashed line in Figure 6-18 a).

6.2.3.2 High energy synchrony X-ray diffraction

The high photon flux and fast acquisition rate of synchrotron X-ray diffraction make it an ideal technique for advanced materials characterization. Additionally, it is capable of working in transmission mode, and the spot size is significantly smaller than when using laboratory X-ray sources. Therefore, it offers the possibility of probing processed materials at the micro- to mesoscale where microstructural modifications occur, which would not be distinguished by conventional characterization approaches [381]. Here, this technique was employed to further probe the microstructure starting from the BM and passing through the HAZ and FZ until it reached the other side of the BM. Figure 6-20 a) presents the superimposition of the diffraction patterns over the entire welded joint. The extension of the BM, HAZ and FZ were determined and marked accordingly. To further compare phases that exist in the various regions of the welded joint, and to understand how the weld thermal cycle affects the microstructure, representative diffraction patterns of each location with the corresponding phase identification are shown in Figure 6-20 b), c) and d), for the BM, HAZ and FZ, respectively.

Overall, X-ray diffraction peaks assigned to γ-f.c.c., ε-h.c.p. and σ phases exist in the BM (Figure 6-20 b)), HAZ (Figure 6-20 c)) and FZ (Figure 6-20 c)), confirming that the gas tungsten arc welded $Fe_{42}Mn_{28}Co_{10}Cr_{15}Si_5$ joint possess the same phase structure throughout. All of the phases matched well with those previously determined using optical microscopy (refer to Figure 6-17) except for σ phase,

which is also well in line with the works of Gupta et al. [375] and Sittiho et al. [376], when performing friction stir welding of this metastable HEA. The presence of this dual-phase microstructure in both the HAZ and FZ, reveals that the thermally induced γ-f.c.c. → ε-h.c.p. martensitic transformation cannot be completely kinetically inhibited by the thermal cycle experienced by these regions during the welding process [382]. For the σ phase, EDS analysis (refer to Figure 6-21) will be utilized to prove the existence of this nanosized phase. Here, it is important to mention that the description of the thermally induced γ-f.c.c. → ε-h.c.p. martensitic transformation, which will be explained further in the next section when considering the thermodynamic calculations.

Attention is now devoted to the representative X-ray diffraction patterns for three distinct regions of the joint. First, the as-cast $Fe_{42}Mn_{28}Co_{10}Cr_{15}Si_5$ BM exhibited the dual γ-f.c.c. + ε-h.c.p. phase structure (Figure 6-20 b)), which is in line with previous reports [62]. The formation and presence of σ phase is discussed next. In HEAs of the Fe-Mn-Co-Cr system, the addition of Si and Cr increases the risk of hard and brittle σ phase formation [275]. However, the current work did not find any Cr-Si-rich particles, but rather Mn- and Si-rich particles. Frank et al. [337] previously found similarly shaped fine particles in the as-cast state of the same material, which was also detected to be rich in both Si and Mn as determined by atom probe tomography. The authors named it as “Si phase” based on its elemental richness without determining its crystal structure. Here, the microstructure characterization of the BM, combining electron microscopy and synchrotron X-ray diffraction, allows to identify that those Si-Mn-rich precipitates are indeed σ phase with a tetragonal structure. The small intensity diffraction peaks of this phase are marked with blue triangles in Figure 6-22. As it will be shown in the next section, this observation is in good agreement with the thermodynamic calculations that predict the formation of a Si-Mn-rich phase upon solidification (refer to Figure 6-21).

Entering the HAZ (Figure 6-20 c)), all previously identified phases (γ-f.c.c., ε-h.c.p. and σ) were detected, suggesting that the weld thermal cycle failed to alter the phase structure in this region. Finally reaching the FZ, the phase identification shown in Figure 6-20 d) indicates that the solidification and cooling conditions experienced by the joint region cannot prevent the same phases to be formed. It should be mentioned here that, although the weld thermal cycle is insufficient to change the existing phases in the current joint, it does alter their volume fraction, which will be further discussed below.

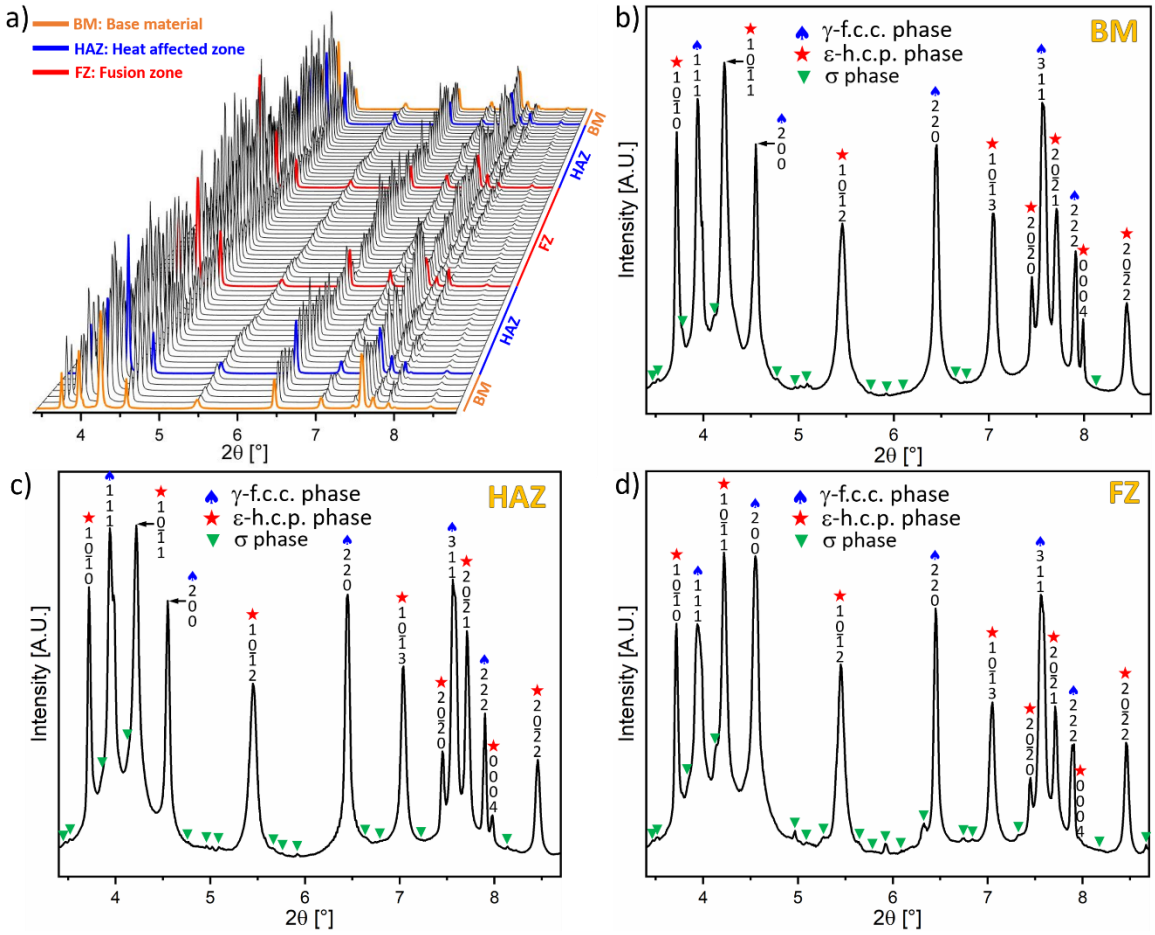

Figure 6-20. a) Superimposed X-ray diffraction patterns of across the welded joint; b), c) and d) are representative diffraction patterns from the BM, HAZ and FZ, respectively.

To quantitatively analyze of how the weld thermal cycle influenced the volume fraction of γ-f.c.c., ε-h.c.p. and σ phases across the welded joint, Rietveld refinement was performed on the synchrotron X-ray diffraction data and these results are detailed in Table 6-4.

Table 6-4. Volume fraction evolution of γ-f.c.c., ε-h.c.p. and σ phases across the welded joint (BM, HAZ and FZ) as obtained by Rietveld refinement.

	Phase volume fraction [%]		
	γ-f.c.c. phase	ε-h.c.p. phase	σ phase
BM	≈ 60.1	≈ 38.7	≈ 1.2
HAZ near the BM	≈ 51.3	≈ 47.8	≈ 0.9
HAZ near the HAZ/FZ boundary	≈ 48.4	≈ 51.9	≈ 0.7
FZ	≈ 73.2	≈ 24.4	≈ 2.5

As expected, the as-cast $Fe_{42}Mn_{28}Co_{10}Cr_{15}Si_5$ HEA showed the γ-f.c.c. phase being dominant in the dual-phase microstructure [62] with the phase distribution being ≈ 60.1% of γ-f.c.c. phase, and ≈ 38.7% of the ε-h.c.p. phase. The phase fraction obtained here is consistent with the findings presented by Nene et al. [62]. These authors developed the present HEA with a metastable γ-f.c.c. dominant microstructure based on the concept of Gibbs free energy change required for the martensitic transformation of γ-f.c.c. → ε-h.c.p. Specifically, they modified the metastability of the γ-f.c.c. phase by increasing the Cr content and by adding Si. The Si-Mn-rich σ phase had a volume fraction of approximately ≈ 1.2%. The phase quantification of all existing phases in this alloy is first reported in this work. Indeed, the calculated volume fraction of the existing phases in the BM can be considered as the phase volume fraction that should originate from an equilibrium-like solidification.

The HAZ is the region of the welded joint where the temperature experienced allows for solid-state phase transformation to occur while remaining in the same state, i.e., grain growth. Interestingly, there is a significant change in the phase volume fraction of the γ-f.c.c. and ε-h.c.p. phases in this region the the phase volume fraction of the γ-f.c.c. and ε-h.c.p. phases in this region changed significantly. Specifically, the γ-f.c.c. phase volume fraction decreased compared to the BM (from ≈ 60.1 % to ≈ 51.3 and ≈ 48.4 %, with the two latter values corresponding to the low and high temperature HAZ, respectively), and correspondingly, an increase in the volume fraction of the ε-h.c.p. phase was observed (from ≈ 38.7 % to ≈ 47.8 and ≈ 51.9%). Generally, there are two ways that can trigger the γ-f.c.c. → ε-h.c.p. transformation. One is via the TRIP mechanism [383], the other is via a thermally-induced phase transformation [384]. In the current work, it is evident that the phase fraction of the ε-

h.c.p. phase increases from the BM to the HAZ. Here, the newly formed ε-h.c.p. laths in the HAZ are related to the thermally induced γ-f.c.c. → ε-h.c.p. martensitic phase transformation during the welding process, and not to the TRIP effect as the eventual thermal strains that can develop during the process are not high enough to enable this mechanism. To justify that the increase in the ε-h.c.p. phase fraction was not related to the TRIP effect, KAM values (refer to Figure 6-18 f)) were used to evaluate the relationship between regions with high dislocation density and/or with a high local strain. Moreover, welding residual stresses have a correlation with the distribution of the KAM values [385], especially for welding of thin sheets, as it was demonstrated by Mitra et al. [386]. To be more specific, in Figure 6-18 f), only minimum variations in the average KAM values across the welded joint exist, with 0.375°, 0.451° and 0.625° for the BM, HAZ and FZ, respectively, which allows to infer the minimal residual strain/stress within the welded joint induced by the weld thermal cycle. Thus, the low residual stress/strain deduced from the KAM analysis, justifies the reasonableness of the hypothesis that the ε-h.c.p. transformation from the parent γ-f.c.c. occurred by a thermal-induced process, rather than by a deformation-assisted one. In conclusion, the γ-f.c.c. to ε-h.c.p. martensitic phase transformation that occurs in the HAZ is attributed to an allotropic transformation during cooling [387], i.e., the migration and rearrangement of atoms during the cooling process.

In other words, variations in both the local cooling rate and on the grain size affect the phase stability in metastable HEAs, where the higher cooling rates enhances the stability of the high temperature γ-f.c.c. phase while the large grains aid in stabilizing the ε-h.c.p. phase [388]. The reason for the increased volume fraction of the ε-h.c.p. phase in the HAZ is due to the thermal cycle experienced by the material. The maximum temperature at which the ε-h.c.p. phase is stable is 425 ºC [62]. Hence, any region of the material that experiences temperatures above this will transform to γ-f.c.c. However, within the HAZ, the distance to the heat source will influence both the peak temperature, as well as the associated cooling rate, leading to a gradient in the fraction of γ-f.c.c. and ε-h.c.p. across this region which impacts the local mechanical properties, as it will be shown latter. However, as detailed before, grain coarsening, as it occurs going from the BM to the fusion boundary, will promote the ε-h.c.p. stability, favoring the γ-f.c.c. to ε-h.c.p. martensitic phase transformation. Thus, two concurring effects, grain size and cooling rate, will compete towards the stability of the γ-f.c.c. or the ε-h.c.p. phases. Since the phase fraction of ε-h.c.p. phase increases within the HAZ, despite the existence of higher cooling rates near the fusion boundary that would tend to stabilize the γ-f.c.c. phase, it can be stated that the increase in grain size at this region of the welded joint will dominate in what concerns the phase evolution, promoting a stabilization of the ε-h.c.p. instead.

In what matters σ phase, there is a partial dissolution, as its volume fraction is reduced from 1.2 % in the BM to 0.9 % in the HAZ and then to 0.7 % when approaching to the FZ boundary. This is mainly due to the higher temperatures and residence time at temperatures promoting this occurrence and was expected since the melting point of this phase approaches ≈ 1045 ºC, as determined from

thermodynamic calculations, meaning that when approaching the FZ boundary its phase fraction is expected to decrease.

It is well known that the FZ is the region of a welded joint that undergoes melting and fast, non-equilibrium solidification. Here, a significant change in the phase volume fraction of both γ-f.c.c. and ε-h.c.p. phases is noted, with the volume fraction of the γ-f.c.c. phase increasing from 60.1 % (in BM) to 73.2 %, while the ε-h.c.p. phase retained only 24.4 %. This is mainly ascribed to the higher cooling rate in the FZ compared to that experienced during casting of the present BM [389]. Specifically, for metastable HEAs with low stacking fault energy, as the present material, γ -f.c.c. and ε-h.c.p. phases are the stable phases at high and low temperatures, respectively [274]. The volume fraction of the ε-h.c.p. phase is strongly dependent on the cooling rate [384]. Thus, in the FZ, the thermally-induced γ-f.c.c. to ε-h.c.p. martensitic transformation could be kinetically inhibited due to the faster cooling rate observed during welding than during casting, enabling to retain more metastable γ-f.c.c. phase. Thus, the variation in the volume fraction of γ-f.c.c. and ε-h.c.p. phases in the FZ compared to the BM suggests that the cooling rate is the primary reason affecting the extent of the γ-f.c.c. to ε-h.c.p. martensitic phase transformation in this metastable HEA. It is worth mentioning here that, in Figure 6-20 d), the X-ray diffraction peaks corresponding to the ε-h.c.p. phase possess high intensity, similar to that of the γ -f.c.c. phase, which is due to the strong texture effect in the ε-h.c.p. phase promoted by the rapid solidification in the FZ, rendering a highly oriented grain structure. For the σ phase, it can be observed that an increased volume fraction exists in the FZ compared to the remaining regions of the joint (≈ 2.5 for the FZ, ≈ 0.9 % for the HAZ and ≈ 1.2 % for the BM). This phenomenon occurs as a result of the addition of Si that leads to the Si-Mn-rich σ phase being generated directly from the rapid solidification of the melt pool at the end of the solidification (more details on this will be provided when discussing the thermodynamic data of Figure 6-21), which is consistent with the findings reported by Nene et al. whom used thermodynamic calculations to investigate the effect of Si on the σ phase formation [275]. In addition, another Si-Mn-rich σ phase may appear at lower temperatures (≈ 400 ºC under low cooling rates [390]) as observed in the cast condition. These two precipitated σ phase are generated at different times during the solidification and cooling processes and share the same tetragonal crystal structure, but their chemical composition slightly differs, causing the final phase volume fraction of this phase, as measured in the FZ, to be higher compared to the that determined in both the HAZ and BM. This is further evidenced by the higher peak intensity of σ phase as shown in X-ray diffractogram of Figure 6-20 d)).

6.2.3.3 Thermodynamic calculations

In order to gain a better understanding of the solidification process that occurs in the FZ, the Scheil-Gulliver model was used to implement and predict the solidification pathway and phases formation in the FZ by considering the non-equilibrium solidification conditions. As determined by EDS measurements, the average FZ composition (35% Fe, 23% Mn, 17% Co, 19% Cr and 6% Si, at. %) was

used for these thermodynamic calculations. Besides, a nominal composition of the material was also taken into account (42% Fe, 28% Mn, 10% Co, 15% Cr and 5% Si, at. %) to perform the same calculations.

Although not shown here, when comparing the non-equilibrium solidification diagrams obtained with the two different compositions it was found that the solidification pathway, as well as the phases formed, are practically the same. As a matter of fact, the only subtle differences between the two (average vs nominal compositions) are the temperatures of the solidus and liquidus as well as the temperature at which the σ phase begins to form. Thus, here, only the non-equilibrium solidification pathway obtained considering the average measured composition of the FZ is analyzed, as shown in Figure 6-21.

As can be clearly seen in Figure 6-21, the solidification path takes place in two steps as follows: Liquid → Liquid + γ-f.c.c., then followed by γ-f.c.c. and σ phases being formed from the remaining liquid. When using the average FZ composition, the solidus and liquidus temperatures were determined to be 1256 and 951 °C, respectively, whereas the range for σ formation occurred between 1045 and 951 °C. For reference, the liquidus, solidus and σ formation temperatures are 1223, 915, 932 and 916 °C when using the nominal composition of the material. It is worth noting that there is no trace of the ε-h.c.p. phase during the solidification process presented in Figure 6-21. In fact, the ε-h.c.p. phase previously detected in the FZ by synchrotron X-ray diffraction data (refer to Figure 6-20 d)) and optical microscopy (refer to Figure 6-17), did not form directly from the liquid, but rather occurred during a solid-state phase transformation upon further cooling after solidification was finished. This again proved the previous assumption that the variation of the γ-f.c.c. and ε-h.c.p. phases volume fraction in the HAZ and FZ are the result of a thermally induced γ-f.c.c. → ε-h.c.p. martensitic phase transformation.

According to these thermodynamic calculations, the σ phase that formed during non-equilibrium solidification was enriched in both Si and Mn. Furthermore, EDS data details that these small particles observed in the FZ are also enriched in both Si and Mn (see Figure 6-22), which further validates these thermodynamic calculations. This will be discussed in detail next.

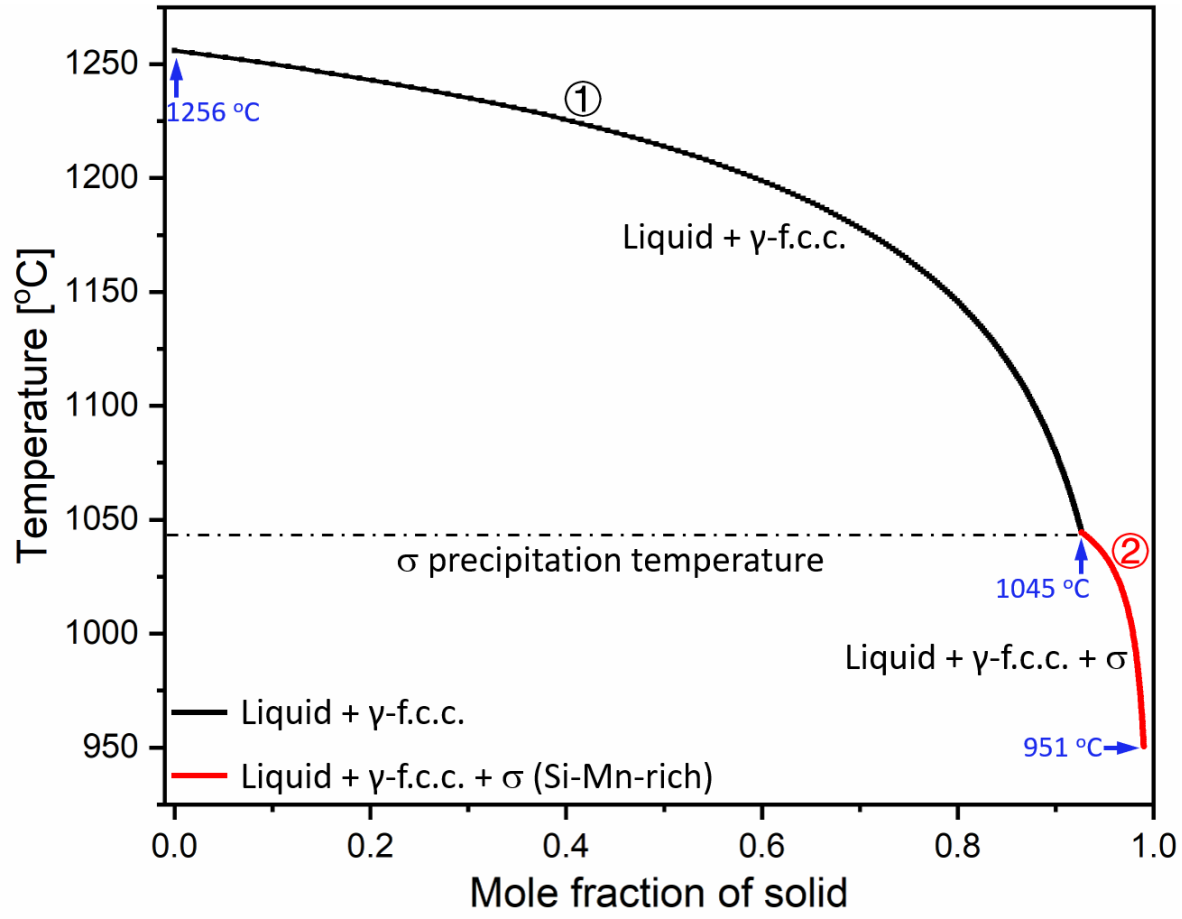

Figure 6-21. Solidification path calculations using Scheil-Gulliver model in ThermoCalc (TCHEA 5.1 database) considering the average FZ composition.

The EDS mapping of the constituent elements (Fe, Mn, Co, Cr and Si) was conducted to further investigate the composition distribution of the fine black particles that can be observed in the FZ, which are shown in the SEM images of Figure 6-22 with white ellipses. These EDS data confirms that these black particles are enriched in both Mn and Si, suggesting that these two elements had the most significant tendency to cluster [291]. Interestingly, in the present work, Mn and Si were also the elements with the most significant discrepancies in electronegativity [391] in the Fe-Mn-Co-Cr-Si system. Nene et al. [62] previously used atom probe tomography reconstruction to identify short-range clusters by nearest neighbor analysis of the particles that appeared in the same Fe-Mn-Co-Cr-Si metastable HEA. The observed elemental clustering is consistent with the current work observations, i.e., the particles being Si-Mn-rich. In conclusion, the Si-Mn-rich particles detected by EDS matched with the thermodynamically predicted σ phase enrichment of these two elements (refer to Figure 6-21), thus validating the accuracy of the thermodynamic predictions.

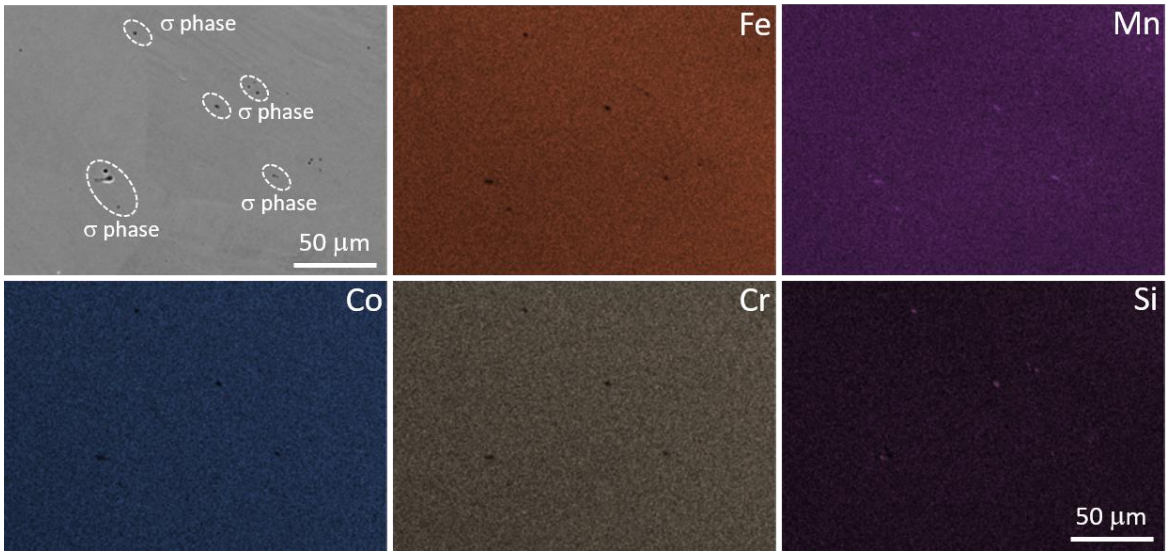

Figure 6-22. SEM image and corresponding EDS mapping near particles of σ phase in the FZ.

6.2.3.4 Mechanical behavior

As shown in Figure 6-23, microhardness measurements were performed across the welded joint to further evaluate how the weld thermal cycle and local material microstructure effected the local material strength. The color change in the hardness mapping presented in Figure 6-23 a) identified three typical regions of the welded joint: the blue, green and red colors represent the BM, HAZ and FZ, respectively, and these regions have been marked by a different number each. Besides, a representative trend of the hardness variation along the joint, obtained at mid height, is detailed in Figure 6-23 b).

From Figure 6-23 b), a significant difference in hardness was found among the BM (≈ 221 HV0.3), HAZ (ranging from ≈ 225 to ≈ 262 HV0.3) and FZ (≈ 275 HV0.3). As can be seen, the hardness in the region of the BM is the lowest of all, whereas the HAZ has an increasing trend in hardness value when compared to the BM. The increase in hardness in the HAZ when moving towards the fusion boundary is mainly due to a higher phase volume fraction of the hard ε-h.c.p. phase, which increases similarly along the HAZ (refer to Table 6-4). Previously, Hou et al. [392] and Shayasultanov et al. [393] reported that the hardness of the ε-h.c.p. phase is approximately three times higher than that of the γ-f.c.c. phase in such metastable HEAs. From the BM region, entering into the HAZ, the average grain size of the matrix γ-f.c.c. increases from 47.5 μm (BM) to 54.2 μm (HAZ), which should result in a minor hardness decrease following the Hall-Petch relationship. However, not only the grain size difference is small, but the volume fraction of the ε-h.c.p. phase has a more significant and profound impact on the material hardness. Thus, although there is an increase in the grain size when approaching the fusion boundary, the observed increase in hardness is due to the higher ε-h.c.p. phase fraction, which promotes a strengthening along the HAZ.

One interesting feature is the hardness distributions in the FZ. If purely looking at the volume fractions of γ-f.c.c. (73.2%) and ε-h.c.p. (24.4%) phases, it would be expected that a smaller hardness would exist at this region, owing to the domination of a soft γ-f.c.c. microstructure. In contrast, the FZ showed a maximum value of hardness over the whole joint, which was mainly due to the very refined subgrain structure of the γ-f.c.c. and ε-h.c.p. product phase (≈ 2 μm) induced by the rapid solidification of the FZ, and the consequent introduction of fine grain strengthening. Thus, although the volume fraction of ε-h.c.p. phase is lower in the FZ, the significant grain refinement is enough to significantly increase the material hardness at this location.

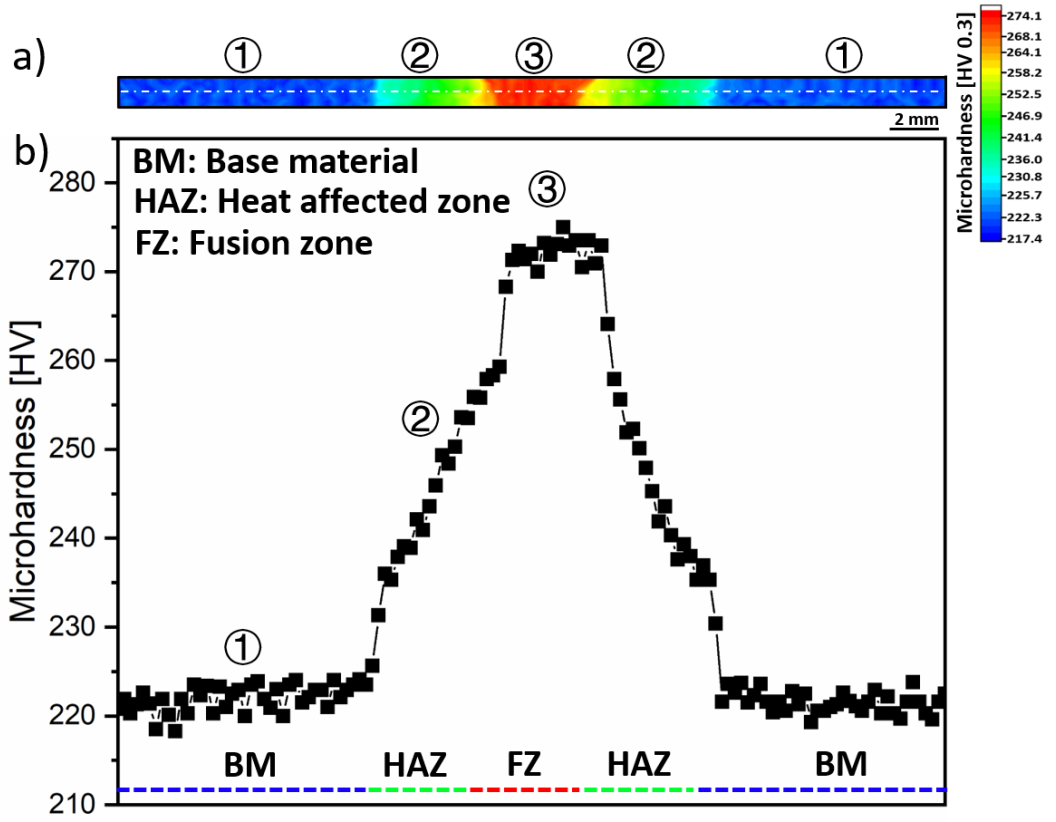

Figure 6-23. a) Microhardness map across the welded joint; b) Microhardness profile obtained at the mid height of the welded joint (white dashed line across the hardness map in a).

To assess the mechanical performance of the welded joints, and compare them with the BM, uniaxial tensile testing until failure was carried out on both gas tungsten arc welded $Fe_{42}Mn_{28}Co_{10}Cr_{15}Si_5$ joints, as well as the as-cast $Fe_{42}Mn_{28}Co_{10}Cr_{15}Si_5$ BM.

provides the stress-strain curves for the as-welded joints (blue curve) and as-cast BM (red color). Detailed information on the mechanical properties of the materials discussed above can be found in Table 6-5. Overall, there is a decrease in the strength and ductility of the weld joints compared to the BM. More specifically, the yield strength, ultimate tensile strength and maximum elongation of the BM are ≈ 440 MPa, ≈ 790 MPa and ≈ 9.8% respectively, while for the welded joints these values are ≈ 400

MPa, ≈ 615 MPa and ≈ 6.6%. Although less performing than the original base materials both in terms of the ultimate strength and ductility, the joint still exhibits interesting mechanical properties, with potential for being considered for structural applications. Observation of the macroscopic features of the fracture of the joints, revealed that failure occurred in the FZ. The larger amount (relative to the BM and HAZ) of dispersed and hard nanosized σ phase that was determined to exist in this region can justify the fracture location. Moreover, the nearly twice volume fraction of σ phase that exists in the FZ, which can act as the stress concentrators, trigger the crack initiation and subsequent development, can also contribute to the premature failure of the joint as well as its location.

Theoretically, TWIP and TRIP effects occur during the deformation of metastable HEAs, which can improve the strength and ductility of the material [60,295]. However, based on the final mechanical behavior of the welded joint in the current work (refer to Figure 6-24), it can be speculated that the large amount of nanosized σ phase distributed in the FZ triggers localized stress concentrations and cracking sources, causing the joints to fracture prematurely and not allowing the TWIP and TRIP effects to take full exploit their advantages in improving the mechanical properties of the material. Hence, future work will be primarily focused on how to improve the mechanical properties of the current welded joint by using the post-weld heat treatments.

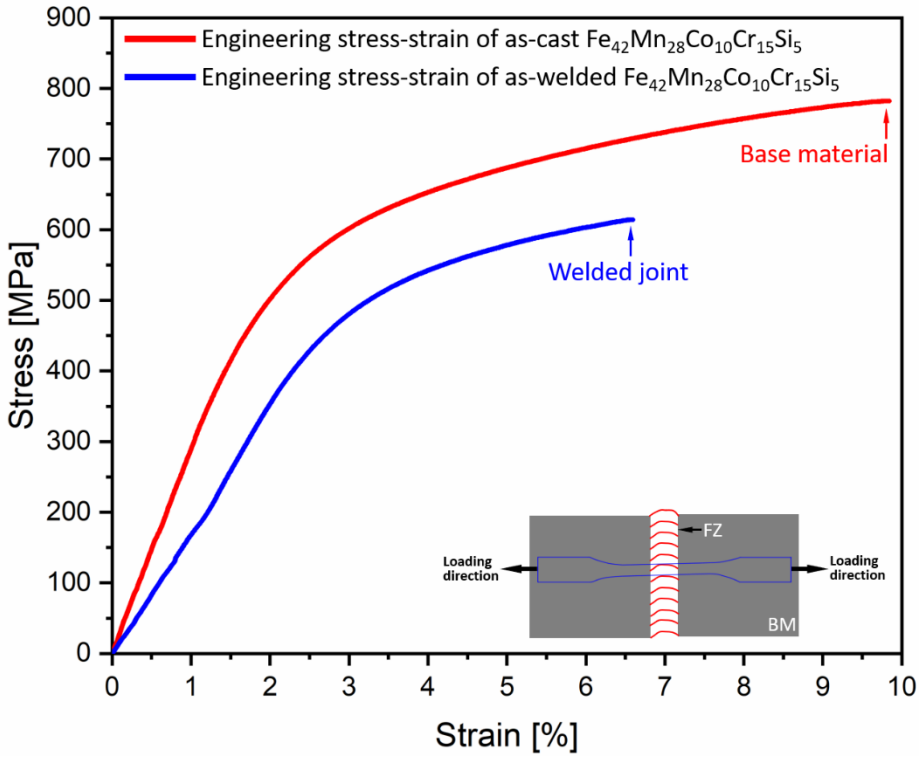

Figure 6-24. Representative tensile stress-strain curves of BM and as-welded as-cast $Fe_{42}Mn_{28}Co_{10}Cr_{15}Si_5$ metastable HEA at room temperature under a strain-rate 10-3 s^{-1}.

Table 6-5. Summary of tensile properties of BM, gas tungsten arc welded $Fe_{42}Mn_{28}Co_{10}Cr_{15}Si_5$ joints.

	Yield strength [MPa]	Ultimate tensile strength [MPa]	Fracture strain [%]
BM	≈ 440	≈ 790	≈ 9.8
Welded joints	≈ 400	≈ 615	≈ 6.6

To further explore the fracture mode as well as to determine the fracture origin, the tensile fracture morphology of the as-welded joints of $Fe_{42}Mn_{28}Co_{10}Cr_{15}Si_5$ metastable HEA were observed by SEM, as shown in Figure 6-25. Figure 6-25 a) details the overview of the fracture surface with Figure 6-25 b) and Figure 6-25 c) detailing zoomed in images of specific features observed. Interestingly, an intergranular fractured surface was observed, as shown in Figure 6-25 b). This implies that slip location is helpful in facilitating the development of damage along the grain boundaries [394]. As marked in Figure 6-25 c), evidence of cleavage fractures and dimples reveal a mixed brittle and ductile fracture morphologies.

Normally, localized plasticity in metastable HEAs can promote intergranular cracking mechanisms [395]. Considering that the hard nanosized σ phase was mainly distributed near the phase boundaries (refer to Figure 6-18), it can be deduced that the stress concentration induced by the σ phase activates localized plastic deformation at the grain boundaries, which aids in crack initiation occurring near the boundaries, and eventually the fracture occurs along the grain boundaries. In addition, the brittle ε-h.c.p. phase induced by the TRIP effect during tensile loading, tends to nucleate and grow near the grain boundaries, further reducing the ductility at the grain boundaries and serves as an auxiliary mechanism for localized plastic deformation. Thus, the analysis of the fracture mechanism further validates the previous hypothesis that the higher volume fraction of the hard nanosized σ phase in the FZ is the main reason for inducing premature failure in this region of the welded joint.

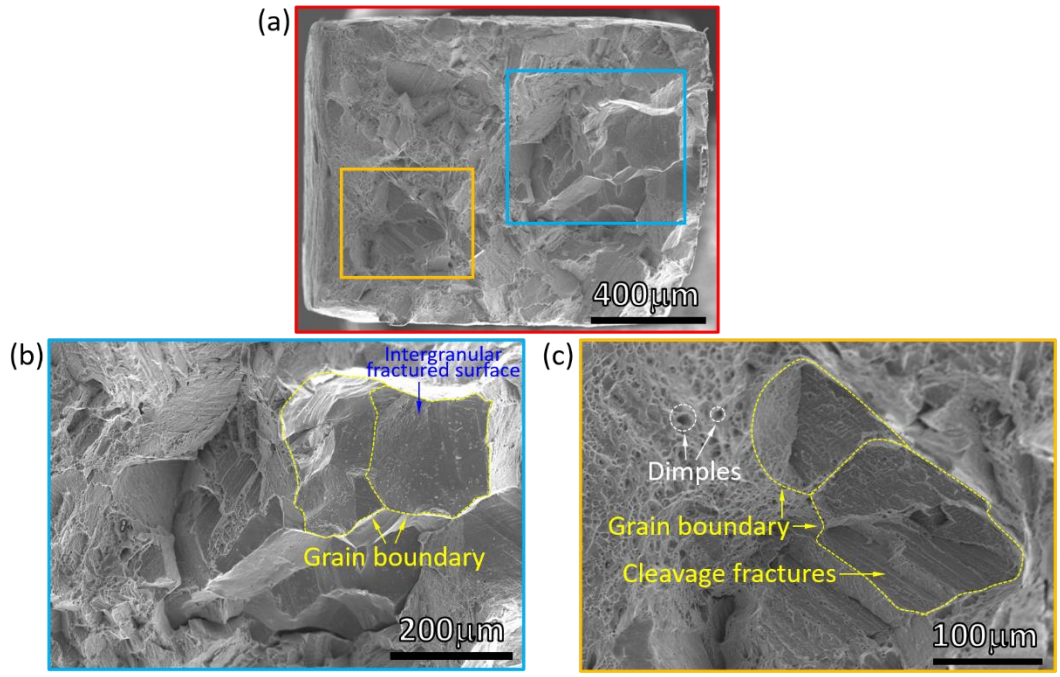

Figure 6-25. Fracture surface analysis of the as-cast $Fe_{42}Mn_{28}Co_{10}Cr_{15}Si_5$ gas tungsten arc welded joint: a) overview; b) and c) close-up detailing ductile-and brittle-like features.

6.2.4 Conclusions

A combination of advanced materials characterization and thermodynamic calculations was used to investigate the how gas tungsten arc welding affects the microstructure and mechanical properties of an as-cast $Fe_{42}Mn_{28}Co_{10}Cr_{15}Si_5$ metastable high entropy alloy. In conclusion, the following main points can be made:

1) Overall, there were no weld defects detected in the joints, which exhibited a good weldability.

2) The γ-f.c.c. to ε-h.c.p. phase transformation in the HAZ and FZ does not occur due to the TRIP effect triggered by the weld thermal strains, but rather due to a thermally-induced martensitic phase transformation during the cooling process.

3) Competition between grain size and locally varying cooling rates where seen to influence the phase stability across the HAZ.

4) Microstructure characterization, combining electron microscopy and synchrotron X-ray diffraction determined that Si-Mn-rich precipitates are σ phase with a tetragonal structure, which in good agreement with the thermodynamic calculations used to predict the solidification pathway.

5) The cooling rate is the primary reason affecting the extent of γ-f.c.c. to ε-h.c.p. martensitic phase transformation in the FZ.

6) Although the phase volume fraction of hard ε-h.c.p. significantly reduced in the FZ, the refine grain size of this phase promoted a significant strengthening effect at this location.

7) The joints have a lower strength and ductility compared to the original BM but can still be considered for structural applications owing to their good mechanical performance.

7.

CONCLUSIONS AND FUTURE WORK

7.1 Introduction

This Chapter presents the main findings of the overall research work and determines the future directions for further research. The major findings obtained in this works are briefly summarized and the significance of the research performed is put in evidence. Suggestions for future work are also provided to further expand the knowledge on the weldability of HEAs.

7.2 Conclusions

The primary goal of this work was to study the weldability of different HEAs systems (Co-Cr-Fe-Mn-Ni system, Al-Co-Cr-Fe-Ni system, and Fe-Mn-Co-Cr-Si system) by using GTAW and GMAW methods, establishing the correlations between the processing-microstructure-properties, and eventually provide new data for more massive implementation of these advanced engineering alloys.

In this section, the most relevant conclusions are summarized.

CoCrFeMnNi HEA:

- Sound and defect-free GMAW CoCrFeMnNi joints were obtained using 308 and 410 stainless steels filer materials.
- Suitability of using filler materials for joining CoCrFeMnNi HEAs is demonstrated owing to the good mechanical properties exhibited by the welded joints.
- This allows inferring that the addition of filler materials for welding HEAs is a viable method for the widespread use of these novel materials towards their implementation in structural applications.
- Recrystallization followed by grain growth were the primary causes behind HAZ softening.
- Existing phases predicted by thermodynamic calculations were in good agreement with those observed in the FZ and were seen to be dependent on the dilution ratio.
- Stress concentration at the weld toe caused by the face/root reinforcement is a dominant factor contributing to failure of welded joints.

$AlCoCrFeNi_{2.1}$ eutectic HEA:

1) Deformation mechanisms of a eutectic $AlCoCrFeNi_{2.1}$ HEA probed by in-situ synchrotron X-ray diffraction
    - The two major phases, a soft disordered FCC and a hard ordered B2 BCC, were observed to exhibit a stress partitioning effect which can be used to modulate the mechanical response of the material based on the relative volume fraction of each phase.
    - Dislocation density analysis revealed that the soft FCC phase had a significantly higher dislocation density right after the onset of plastic deformation. This is attributed to the existence of strain gradients across the lamellar structure, where the hard B2 BCC prevents free deformation of the FCC phase.
    - Despite the increase of the dislocation density in the soft FCC phase, calculations of the strengthening effects induced by the generation of dislocations are more significant in the hard B2 BCC phases, as this phase is primarily responsible for the strengthening increase in the alloy.
    - Lattice strain analysis across two principal directions (parallel and perpendicular to the loading axis) reveals that for these specific orientations there is a preferential deformation of the hard FCC planes which can be related to the as-cast texture and its impact on the deformation response of specific lattice planes at distinct orientations.
2) Study on the GTAW of as-cast $AlCoCrFeNi_{2.1}$ eutectic HEA
    - No welding defects were observed in the gas tungsten arc welded $AlCoCrFeNi_{2.1}$ joints.
    - The FZ exhibits a higher hardness due to a refined interlamellar thickness.
    - Good agreement between experimentally observed phases and those predicted by thermodynamic calculations.
    - The welded joints present a good strength/ductility balance

$Fe_{42}Mn_{28}Co_{10}Cr_{15}Si_5$ HEA:

1) Study on the deformation mechanism of a metastable $Fe_{42}Mn_{28}Co_{10}Cr_{15}Si_5$ HEA probed by in-situ with synchrotron X-ray diffraction
    - The dual-phase γ-f.c.c. / ε-h.c.p. microstructure on the deformation response of the alloy plays a critical role the deformation mechanisms that develop in the material during tensile loading.
    - The different deformation modes, slip, TRIP, and TWIP, were seen to initiate at different loading stresses and then overlap.
2) Study on the GTAW of as-cast $Fe_{42}Mn_{28}Co_{10}Cr_{15}Si_5$ metastable HEA
    - Gas tungsten arc welding of as-cast $Fe_{42}Mn_{28}Co_{10}Cr_{15}Si_5$ metastable high entropy alloys is successfully performed for the first time.
    - Defect-free joints with good mechanical behavior were obtained.
    - The γ-f.c.c. to ε-h.c.p. martensitic phase transformation that occurs in the HAZ is attributed to an allotropic transformation during cooling.
    - A large volume fraction of hard σ phase distributed in the FZ is a dominant factor contributing to failure of welded joints.
    - Arc-based welding techniques are suitable for welding these novel advanced engineering alloys.

7.3 Future work

This work mainly focused on fusion-based welding of HEAs. However, one key issue during the arc-based welding of HEAs is the large hardness drop of the FZ due to the presence of a large columnar grain structure. Thus, there is a need to develop processing strategies capable of controlling grain growth and modifying the FZ microstructure. Methods to reduce grain size usually involve the addition of nano or micron sized powders to facilitate nucleation within the FZ, thereby promoting grain refinement. This method has been used for a variety of critical engineering materials, such as steels and titanium alloys, but not for welded joints in HEAs.

Thus, in the future, the role of nano and micron sized powders additions on the microstructure and mechanical properties of CoCrFeMnNi, $AlCoCrFeNi_{2.1}$, and $Fe_{42}Mn_{28}Co_{10}Cr_{15}Si_5$ HEAs (or others) should be addressed. Here, powders, such as TiB_2, TiC, and TiN, can be potential materials of choice as thy have been already used with success in other materials. Advanced microstructure and mechanical characterization will be performed to understand the role of different powders on the welded joint. A correlation between the microstructure, welding conditions, and mechanical performance should then be established.

The role of post-weld heat treatments on the microstructure and mechanical response of the welded joints is also a key point that should be explored further. Here, optimization of the post-weld heat treatment conditions should be performed in order to further increase the mechanical response of the welded joints.

Finally, exploring other welding processes namely solid-state ones as friction stir welding, should be attempted to determine their suitability for advanced materials joining of these novel engineering alloys.

BIBLIOGRAPHY

[1] B. Cantor, I.T.H. Chang, P. Knight, A.J.B. Vincent, Microstructural development in equiatomic multicomponent alloys, Materials Science and Engineering: A. 375–377 (2004) 213–218. https://doi.org/10.1016/j.msea.2003.10.257.

[2] J.-W. Yeh, S.-K. Chen, S.-J. Lin, J.-Y. Gan, T. Chin, T.-T. Shun, C. Tsau, S.-Y. Chang, Nanostructured High-Entropy Alloys with Multiple Principal Elements: Novel Alloy Design Concepts and Outcomes, Advanced Engineering Materials. 6 (2004) 299–303. https://doi.org/10.1002/adem.200300567.

[3] J.G. Lopes, J.P. Oliveira, A Short Review on Welding and Joining of High Entropy Alloys, Metals. 10 (2020) 212. https://doi.org/10.3390/met10020212.

[4] W. Zhang, P.K. Liaw, Y. Zhang, Science and technology in high-entropy alloys, 61 (2018) 2–22.

[5] Y.F. Ye, Q. Wang, J. Lu, C.T. Liu, Y. Yang, High-entropy alloy: challenges and prospects, Materials Today. 19 (2016) 349–362. https://doi.org/10.1016/j.mattod.2015.11.026.

[6] J. Yeh, Alloy Design Strategies and Future Trends in High-Entropy Alloys, JOM. 65 (2013) 1759–1771. https://doi.org/10.1007/s11837-013-0761-6.

[7] S. Jiang, L. Shao, T.-W. Fan, J.-M. Duan, X.-T. Chen, B.-Y. Tang, Elastic and thermodynamic properties of high entropy carbide (HfTaZrTi)C and (HfTaZrNb)C from ab initio investigation, Ceramics International. 46 (2020) 15104–15112. https://doi.org/10.1016/j.ceramint.2020.03.045.

[8] H. Liu, L. Syama, L. Zhang, C. Lee, C. Liu, Z. Dai, Q. Yan, High-entropy alloys and compounds for electrocatalytic energy conversion applications, SusMat. 1 (2021) 482–505. https://doi.org/10.1002/sus2.32.

[9] L.M. Martyushev, V.D. Seleznev, Maximum entropy production principle in physics, chemistry and biology, Physics Reports. 426 (2006) 1–45. https://doi.org/10.1016/j.physrep.2005.12.001.

[10] J.-W. Yeh, Recent progress in high-entropy alloys, Annales de Chimie Science Des Matériaux. 31 (2006) 633–648. https://doi.org/10.3166/acsm.31.633-648.

[11] J. Dąbrowa, M. Zajusz, W. Kucza, G. Cieślak, K. Berent, T. Czeppe, T. Kulik, M. Danielewski, Demystifying the sluggish diffusion effect in high entropy alloys, Journal of Alloys and Compounds. 783 (2019) 193–207. https://doi.org/10.1016/j.jallcom.2018.12.300.

[12] A.N. Chaudhari, K. Dixit, G.S. Bhatia, B. Singh, P. Singhal, K.K. Saxena, Welding Behaviour of Duplex Stainless Steel AISI 2205: AReview, Materials Today: Proceedings. 18 (2019) 2731–2737. https://doi.org/10.1016/j.matpr.2019.07.136.

[13] American Welding Society (AWS), Standard Welding Terms and Definitions, United States of America, 2010.

[14] T.N. George, A centenary lecture: The concept of homoeomorphy, Proceedings of the Geologists' Association. 73 (1962) 9–64. https://doi.org/10.1016/S0016-7878(62)80017-0.

[15] N. Nguyen, Thermal Analysis of Welds, Applied Mechanics Reviews. 57 (2004) B34–B34. https://doi.org/10.1115/1.1849178.

[16] X. Wang, J. Huang, Y. Huang, D. Fan, Y. Guo, Investigation of heat transfer and fluid flow in activating TIG welding by numerical modeling, Applied Thermal Engineering. 113 (2017) 27–35. https://doi.org/10.1016/j.applthermaleng.2016.11.008.

[17] A. Służalec, Theory of Thermomechanical Processes in Welding, Springer Netherlands, Dordrecht, 2005. https://doi.org/10.1007/1-4020-2991-8.

[18] Z. Wu, S.A. David, D.N. Leonard, Z. Feng, H. Bei, Microstructures and mechanical properties of a welded CoCrFeMnNi high-entropy alloy, Science and Technology of Welding and Joining. 23 (2018) 585–595. https://doi.org/10.1080/13621718.2018.1430114.

[19] M.-G. Jo, H.-J. Kim, M. Kang, P.P. Madakashira, E.S. Park, J.-Y. Suh, D.-I. Kim, S.-T. Hong, H.N. Han, Microstructure and mechanical properties of friction stir welded and laser welded high entropy alloy CrMnFeCoNi, Metals and Materials International. 24 (2018) 73–83. https://doi.org/10.1007/s12540-017-7248-x.

[20] H. Nam, C. Park, C. Kim, H. Kim, N. Kang, Effect of post weld heat treatment on weldability of high entropy alloy welds, Science and Technology of Welding and Joining. 23 (2018) 420–427. https://doi.org/10.1080/13621718.2017.1405564.

[21] N. Kashaev, V. Ventzke, N. Stepanov, D. Shaysultanov, V. Sanin, S. Zherebtsov, Laser beam welding of a CoCrFeNiMn-type high entropy alloy produced by self-propagating high-

temperature synthesis, Intermetallics. 96 (2018) 63–71. https://doi.org/10.1016/j.intermet.2018.02.014.
[22] Z. Wu, S.A. David, Z. Feng, H. Bei, Weldability of a high entropy CrMnFeCoNi alloy, Scripta Materialia. 124 (2016) 81–85. https://doi.org/10.1016/j.scriptamat.2016.06.046.
[23] Z. Wu, S.A. David, Z. Feng, H. Bei, Weldability of a high entropy CrMnFeCoNi alloy, Scripta Materialia. 124 (2016) 81–85. https://doi.org/10.1016/j.scriptamat.2016.06.046.
[24] S.S. Nene, K. Liu, M. Frank, R.S. Mishra, R.E. Brennan, K.C. Cho, Z. Li, D. Raabe, Enhanced strength and ductility in a friction stir processing engineered dual phase high entropy alloy, Scientific Reports. 7 (2017) 16167. https://doi.org/10.1038/s41598-017-16509-9.
[25] Y. Lu, X. Zhang, H. Wang, C. Kan, F. Zhang, P. Dai, H. Wang, Investigation of microstructure, texture, and mechanical properties of FeCoNiCrMn high entropy alloy during drive friction welding, Materials Characterization. 189 (2022) 111959. https://doi.org/10.1016/j.matchar.2022.111959.
[26] Y. Hu, Y. Niu, Y. Zhao, W. Yang, X. Ma, J. Li, Friction stir welding of CoCrNi medium-entropy alloy: Recrystallization behaviour and strengthening mechanism, Materials Science and Engineering: A. 848 (2022) 143361. https://doi.org/10.1016/j.msea.2022.143361.
[27] J.-Y. Lin, Z.-H. Lai, T. Otsuki, H.-W. Yen, S. Nambu, Gradient microstructure and interfacial strength of CoCrFeMnNi high-entropy alloy in solid-state ultrasonic welding, Materials Science and Engineering: A. 825 (2021) 141885. https://doi.org/10.1016/j.msea.2021.141885.
[28] J.P. Oliveira, A. Shamsolhodaei, J. Shen, J.G. Lopes, R.M. Gonçalves, M. de Brito Ferraz, L. Piçarra, Z. Zeng, N. Schell, N. Zhou, H. Seop Kim, Improving the ductility in laser welded joints of CoCrFeMnNi high entropy alloy to 316 stainless steel, Materials & Design. 219 (2022) 110717. https://doi.org/10.1016/j.matdes.2022.110717.
[29] H. Nam, S. Yoo, J. Lee, Y. Na, N. Park, N. Kang, GTA Weldability of Rolled High-Entropy Alloys Using Various Filler Metals, Metals. 10 (2020) 1371. https://doi.org/10.3390/met10101371.
[30] H. Nam, S. Yoo, J.W. Ha, B. Lee, S. Song, Y. Na, N. Kang, Enhancement of tensile properties of gas tungsten arc welds using Cu-coated CoCrFeMnNi filler and post–weld heat treatment, Journal of Materials Research and Technology. 19 (2022) 4857–4866. https://doi.org/10.1016/j.jmrt.2022.07.023.
[31] H. Nam, S. Park, N. Park, Y. Na, H. Kim, S.-J. Yoo, Y.-H. Moon, N. Kang, Weldability of cast CoCrFeMnNi high-entropy alloys using various filler metals for cryogenic applications, Journal of Alloys and Compounds. 819 (2020) 153278. https://doi.org/10.1016/j.jallcom.2019.153278.
[32] H. Nam, B. Moon, S. Park, N. Kim, S. Song, N. Park, Y. Na, N. Kang, Gas tungsten arc weldability of stainless steel 304 using CoCrFeMnNi filler metals for cryogenic applications, Science and Technology of Welding and Joining. 27 (2022) 33–42. https://doi.org/10.1080/13621718.2021.1996851.
[33] K. Maeda, A. Niitsu, H. Morito, K. Shiga, K. Fujiwara, In situ observation of grain boundary groove at the crystal/melt interface in Cu, Scripta Materialia. 146 (2018) 169–172. https://doi.org/10.1016/j.scriptamat.2017.11.039.
[34] H. Do, S. Asadi, N. Park, Microstructural and mechanical properties of dissimilar friction stir welded CoCrFeMnNi high entropy alloy to STS304 stainless steel, Materials Science and Engineering: A. 840 (2022) 142979. https://doi.org/10.1016/j.msea.2022.142979.
[35] N.K. Adomako, G. Shin, N. Park, K. Park, J.H. Kim, Laser dissimilar welding of CoCrFeMnNi-high entropy alloy and duplex stainless steel, Journal of Materials Science & Technology. 85 (2021) 95–105. https://doi.org/10.1016/j.jmst.2021.02.003.
[36] H. Nam, S. Park, S.H. Shim, Y.-S. Na, N. Kim, S. Song, S.I. Hong, N. Kang, Enhancement of Tensile Properties Applying Phase Separation with Cu Addition in Gas Tungsten Arc Welds of CoCrFeMnNi High Entropy Alloys, SSRN Electronic Journal. 220 (2022) 114897. https://doi.org/10.2139/ssrn.4044644.
[37] M.J. Yao, K.G. Pradeep, C.C. Tasan, D. Raabe, A novel, single phase, non-equiatomic FeMnNiCoCr high-entropy alloy with exceptional phase stability and tensile ductility, Scripta Materialia. 72–73 (2014) 5–8. https://doi.org/10.1016/j.scriptamat.2013.09.030.
[38] Y.J. Zhou, Y. Zhang, Y.L. Wang, G.L. Chen, Solid solution alloys of AlCoCrFeNiTix with excellent room-temperature mechanical properties, Applied Physics Letters. 90 (2007) 181904. https://doi.org/10.1063/1.2734517.
[39] I.S. Wani, T. Bhattacharjee, S. Sheikh, Y.P. Lu, S. Chatterjee, P.P. Bhattacharjee, S. Guo, N. Tsuji, Ultrafine-Grained AlCoCrFeNi 2.1 Eutectic High-Entropy Alloy, Materials Research Letters. 4 (2016) 174–179. https://doi.org/10.1080/21663831.2016.1160451.

[40] S.G. Ma, S.F. Zhang, M.C. Gao, P.K. Liaw, Y. Zhang, A Successful Synthesis of the CoCrFeNiAl0.3 Single-Crystal, High-Entropy Alloy by Bridgman Solidification, JOM. 65 (2013) 1751–1758. https://doi.org/10.1007/s11837-013-0733-x.
[41] D. Li, C. Li, T. Feng, Y. Zhang, G. Sha, J.J. Lewandowski, P.K. Liaw, Y. Zhang, High-entropy Al0.3CoCrFeNi alloy fibers with high tensile strength and ductility at ambient and cryogenic temperatures, Acta Materialia. 123 (2017) 285–294. https://doi.org/10.1016/j.actamat.2016.10.038.
[42] P. Ding, A. Mao, X. Zhang, X. Jin, B. Wang, M. Liu, X. Gu, Preparation, characterization and properties of multicomponent AlCoCrFeNi2.1 powder by gas atomization method, Journal of Alloys and Compounds. 721 (2017) 609–614. https://doi.org/10.1016/j.jallcom.2017.06.020.
[43] R. John, A. Karati, J. Joseph, D. Fabijanic, B.S. Murty, Microstructure and mechanical properties of a high entropy alloy with a eutectic composition (AlCoCrFeNi2.1) synthesized by mechanical alloying and spark plasma sintering, Journal of Alloys and Compounds. 835 (2020) 155424. https://doi.org/10.1016/j.jallcom.2020.155424.
[44] M.H. Asoushe, A.Z. Hanzaki, H.R. Abedi, B. Mirshekari, T. Wegener, S.V. Sajadifar, T. Niendorf, Thermal stability, microstructure and texture evolution of thermomechanical processed AlCoCrFeNi2.1 eutectic high entropy alloy, Materials Science and Engineering: A. 799 (2021) 140012. https://doi.org/10.1016/j.msea.2020.140012.
[45] Y. Dong, X. Gao, Y. Lu, T. Wang, T. Li, A multi-component AlCrFe2Ni2 alloy with excellent mechanical properties, Materials Letters. 169 (2016) 62–64. https://doi.org/10.1016/j.matlet.2016.01.096.
[46] P. Li, H. Sun, S. Wang, X. Hao, H. Dong, Rotary friction welding of AlCoCrFeNi2.1 eutectic high entropy alloy, Journal of Alloys and Compounds. 814 (2020) 152322. https://doi.org/10.1016/j.jallcom.2019.152322.
[47] T. Wang, M. Komarasamy, S. Shukla, R.S. Mishra, Simultaneous enhancement of strength and ductility in an AlCoCrFeNi2.1 eutectic high-entropy alloy via friction stir processing, Journal of Alloys and Compounds. 766 (2018) 312–317. https://doi.org/10.1016/j.jallcom.2018.06.337.
[48] P. Li, S. Wang, Y. Xia, X. Hao, H. Dong, Diffusion bonding of AlCoCrFeNi2.1 eutectic high entropy alloy to TiAl alloy, Journal of Materials Science & Technology. 45 (2020) 59–69. https://doi.org/10.1016/j.jmst.2019.10.041.
[49] P. Li, H. Sun, S. Wang, Y. Xia, H. Dong, G. Wen, H. Zhang, Diffusion bonding of AlCoCrFeNi2.1 eutectic high entropy alloy to GH4169 superalloy, Materials Science and Engineering: A. 793 (2020) 139843. https://doi.org/10.1016/j.msea.2020.139843.
[50] M. Zhang, D. Wang, L. He, X. Ye, W. Zhang, Laser beam welding of AlCoCrFeNi2.1 eutectic high-entropy alloy, Materials Letters. 308 (2022) 131137. https://doi.org/10.1016/j.matlet.2021.131137.
[51] S.S. Nene, M. Frank, P. Agrawal, S. Sinha, K. Liu, S. Shukla, R.S. Mishra, B.A. McWilliams, K.C. Cho, Microstructurally flexible high entropy alloys: Linkages between alloy design and deformation behavior, Materials & Design. 194 (2020) 108968. https://doi.org/10.1016/j.matdes.2020.108968.
[52] D. Wei, X. Li, J. Jiang, W. Heng, Y. Koizumi, W.-M. Choi, B.-J. Lee, H.S. Kim, H. Kato, A. Chiba, Novel Co-rich high performance twinning-induced plasticity (TWIP) and transformation-induced plasticity (TRIP) high-entropy alloys, Scripta Materialia. 165 (2019) 39–43. https://doi.org/10.1016/j.scriptamat.2019.02.018.
[53] Z. Li, K.G. Pradeep, Y. Deng, D. Raabe, C.C. Tasan, Metastable high-entropy dual-phase alloys overcome the strength–ductility trade-off, Nature. 534 (2016) 227–230. https://doi.org/10.1038/nature17981.
[54] X. Gao, Y. Lu, J. Liu, J. Wang, T. Wang, Y. Zhao, Extraordinary ductility and strain hardening of Cr26Mn20Fe20Co20Ni14 TWIP high-entropy alloy by cooperative planar slipping and twinning, Materialia. 8 (2019) 100485. https://doi.org/10.1016/j.mtla.2019.100485.
[55] J. Su, D. Raabe, Z. Li, Hierarchical microstructure design to tune the mechanical behavior of an interstitial TRIP-TWIP high-entropy alloy, Acta Materialia. 163 (2019) 40–54. https://doi.org/10.1016/j.actamat.2018.10.017.
[56] E. Polatidis, S. Shukla, J. Čapek, S. Van Petegem, N. Casati, R.S. Mishra, Unveiling the interplay of deformation mechanisms in a metastable high entropy alloy with tuned composition using synchrotron X-ray diffraction, Materials Today Communications. 30 (2022) 103155. https://doi.org/10.1016/j.mtcomm.2022.103155.
[57] A. V Ayyagari, B. Gwalani, S. Muskeri, S. Mukherjee, R. Banerjee, Surface degradation

mechanisms in precipitation-hardened high-entropy alloys, Npj Materials Degradation. 2 (2018) 33. https://doi.org/10.1038/s41529-018-0054-1.
[58] J.Y. He, H. Wang, H.L. Huang, X.D. Xu, M.W. Chen, Y. Wu, X.J. Liu, T.G. Nieh, K. An, Z.P. Lu, A precipitation-hardened high-entropy alloy with outstanding tensile properties, Acta Materialia. 102 (2016) 187–196. https://doi.org/10.1016/j.actamat.2015.08.076.
[59] Z. Li, Y. Chen, G. Fang, Y. Li, Multivariate assessment and attribution of droughts in Central Asia, Scientific Reports. 7 (2017) 1316. https://doi.org/10.1038/s41598-017-01473-1.
[60] Z. Li, K.G. Pradeep, Y. Deng, D. Raabe, C.C. Tasan, Metastable high-entropy dual-phase alloys overcome the strength–ductility trade-off, Nature. 534 (2016) 227–230. https://doi.org/10.1038/nature17981.
[61] K. Gurumoorthy, M. Kamaraj, K.P. Rao, A.S. Rao, S. Venugopal, Microstructural aspects of plasma transferred arc surfaced Ni-based hardfacing alloy, Materials Science and Engineering: A. 456 (2007) 11–19. https://doi.org/10.1016/j.msea.2006.12.121.
[62] S.S. Nene, M. Frank, K. Liu, R.S. Mishra, B.A. McWilliams, K.C. Cho, Extremely high strength and work hardening ability in a metastable high entropy alloy, Scientific Reports. 8 (2018) 9920. https://doi.org/10.1038/s41598-018-28383-0.
[63] K. Liu, S.S. Nene, M. Frank, R.S. Mishra, Effect of Strain Rate on Deformation Response of Metastable High Entropy Alloys Upon Friction Stir Processing, Metallurgical and Materials Transactions A. 51 (2020) 5043–5048. https://doi.org/10.1007/s11661-020-05927-6.
[64] S.S. Nene, M. Frank, K. Liu, S. Sinha, R.S. Mishra, B.A. McWilliams, K.C. Cho, Corrosion-resistant high entropy alloy with high strength and ductility, Scripta Materialia. 166 (2019) 168–172. https://doi.org/10.1016/j.scriptamat.2019.03.028.
[65] S. Shukla, T. Wang, M. Frank, P. Agrawal, S. Sinha, R.A. Mirshams, R.S. Mishra, Friction stir gradient alloying: A novel solid-state high throughput screening technique for high entropy alloys, Materials Today Communications. 23 (2020) 100869. https://doi.org/10.1016/j.mtcomm.2019.100869.
[66] S. Shukla, T. Wang, M. Frank, P. Agrawal, S. Sinha, R.A. Mirshams, R.S. Mishra, Friction stir gradient alloying: A novel solid-state high throughput screening technique for high entropy alloys, Materials Today Communications. 23 (2020) 100869. https://doi.org/10.1016/j.mtcomm.2019.100869.
[67] J.P. Oliveira, T.M. Curado, Z. Zeng, J.G. Lopes, E. Rossinyol, J.M. Park, N. Schell, F.M. Braz Fernandes, H.S. Kim, Gas tungsten arc welding of as-rolled CrMnFeCoNi high entropy alloy, Materials & Design. 189 (2020) 108505. https://doi.org/10.1016/j.matdes.2020.108505.
[68] A.P. Hammersley, S.O. Svensson, M. Hanfland, A.N. Fitch, D. Hausermann, Two-dimensional detector software: From real detector to idealised image or two-theta scan, High Pressure Research. 14 (1996) 235–248. https://doi.org/10.1080/08957959608201408.
[69] T. Degen, M. Sadki, E. Bron, U. König, G. Nénert, The HighScore suite, Powder Diffraction. 29 (2014) S13–S18. https://doi.org/10.1017/S0885715614000840.
[70] B.H. Toby, R.B. Von Dreele, GSAS-II : the genesis of a modern open-source all purpose crystallography software package, Journal of Applied Crystallography. 46 (2013) 544–549. https://doi.org/10.1107/S0021889813003531.
[71] K.-T. Chen, T.-J. Wei, G.-C. Li, M.-Y. Chen, Y.-S. Chen, S.-W. Chang, H.-W. Yen, C.-S. Chen, Mechanical properties and deformation mechanisms in CoCrFeMnNi high entropy alloys: A molecular dynamics study, Materials Chemistry and Physics. 271 (2021) 124912. https://doi.org/10.1016/j.matchemphys.2021.124912.
[72] H.T. Jeong, H.K. Park, K. Park, T.W. Na, W.J. Kim, High-temperature deformation mechanisms and processing maps of equiatomic CoCrFeMnNi high-entropy alloy, Materials Science and Engineering: A. 756 (2019) 528–537. https://doi.org/10.1016/j.msea.2019.04.057.
[73] M. Patnamsetty, M.C. Somani, S. Ghosh, S. Ahmed, P. Peura, Processing map for controlling microstructure and unraveling various deformation mechanisms during hot working of CoCrFeMnNi high entropy alloy, Materials Science and Engineering: A. 793 (2020) 139840. https://doi.org/10.1016/j.msea.2020.139840.
[74] C.C. Tasan, Y. Deng, K.G. Pradeep, M.J. Yao, H. Springer, D. Raabe, Composition Dependence of Phase Stability, Deformation Mechanisms, and Mechanical Properties of the CoCrFeMnNi High-Entropy Alloy System, JOM. 66 (2014) 1993–2001. https://doi.org/10.1007/s11837-014-1133-6.
[75] B.H. Toby, R.B. Von Dreele, GSAS-II : the genesis of a modern open-source all purpose crystallography software package, Journal of Applied Crystallography. 46 (2013) 544–549.

https://doi.org/10.1107/S0021889813003531.
[76] J. Shen, Z. Zeng, M. Nematollahi, N. Schell, E. Maawad, R.N. Vasin, K. Safaei, B. Poorganji, M. Elahinia, J.P. Oliveira, In-situ synchrotron X-ray diffraction analysis of the elastic behaviour of martensite and H-phase in a NiTiHf high temperature shape memory alloy fabricated by laser powder bed fusion, Additive Manufacturing Letters. 1 (2021) 100003. https://doi.org/10.1016/j.addlet.2021.100003.
[77] Y. Shi, S. Li, T.L. Lee, X. Hui, Z. Zhang, R. Li, M. Zhang, S. Kabra, Y.-D. Wang, In situ neutron diffraction study of a new type of stress-induced confined martensitic transformation in Fe22Co20Ni19Cr20Mn12Al7 high-entropy alloy, Materials Science and Engineering: A. 771 (2020) 138555. https://doi.org/10.1016/j.msea.2019.138555.
[78] P. Shi, R. Li, Y. Li, Y. Wen, Y. Zhong, W. Ren, Z. Shen, T. Zheng, J. Peng, X. Liang, P. Hu, N. Min, Y. Zhang, Y. Ren, P.K. Liaw, D. Raabe, Y.-D. Wang, Hierarchical crack buffering triples ductility in eutectic herringbone high-entropy alloys, Science. 373 (2021) 912–918. https://doi.org/10.1126/science.abf6986.
[79] L. Ma, L. Wang, Z. Nie, F. Wang, Y. Xue, J. Zhou, T. Cao, Y. Wang, Y. Ren, Reversible deformation-induced martensitic transformation in Al0.6CoCrFeNi high-entropy alloy investigated by in situ synchrotron-based high-energy X-ray diffraction, Acta Materialia. 128 (2017) 12–21. https://doi.org/10.1016/j.actamat.2017.02.014.
[80] N. Jia, Z.H. Cong, X. Sun, S. Cheng, Z.H. Nie, Y. Ren, P.K. Liaw, Y.D. Wang, An in situ high-energy X-ray diffraction study of micromechanical behavior of multiple phases in advanced high-strength steels, Acta Materialia. 57 (2009) 3965–3977. https://doi.org/10.1016/j.actamat.2009.05.002.
[81] M. Zhang, H. Chen, Y. Wang, S. Wang, R. Li, S. Li, Y.-D. Wang, Deformation-induced martensitic transformation kinetics and correlative micromechanical behavior of medium-Mn transformation-induced plasticity steel, Journal of Materials Science & Technology. 35 (2019) 1779–1786. https://doi.org/10.1016/j.jmst.2019.04.007.
[82] N.R. Jaladurgam, A. Lozinko, S. Guo, T.-L. Lee, M. Hörnqvist Colliander, Temperature dependent load partitioning and slip mode transition in a eutectic AlCoCrFeNi <math altimg="si11.svg"> <msub> <mrow/> <mrow> <mn>2.1</mn> </mrow> </msub> </math> high entropy alloy, Materialia. 17 (2021) 101118. https://doi.org/10.1016/j.mtla.2021.101118.
[83] A.M. Korsunsky, S.P. Collins, R.A. Owen, M.R. Daymond, S. Achtioui, K.E. James, Fast residual stress mapping using energy-dispersive synchrotron X-ray diffraction on station 16.3 at the SRS, Journal of Synchrotron Radiation. 9 (2002) 77–81. https://doi.org/10.1107/S0909049502001905.
[84] S.H. Gu, V. Nicolas, A. Lalis, N. Sathirapongsasuti, R. Yanagihara, Complete genome sequence and molecular phylogeny of a newfound hantavirus harbored by the Doucet's musk shrew (Crocidura douceti) in Guinea, Infection, Genetics and Evolution. 20 (2013) 118–123. https://doi.org/10.1016/j.meegid.2013.08.016.
[85] G.. Williamson, W.. Hall, X-ray line broadening from filed aluminium and wolfram, Acta Metallurgica. 1 (1953) 22–31. https://doi.org/10.1016/0001-6160(53)90006-6.
[86] A. Khorsand Zak, W.H. Abd. Majid, M.E. Abrishami, R. Yousefi, X-ray analysis of ZnO nanoparticles by Williamson–Hall and size–strain plot methods, Solid State Sciences. 13 (2011) 251–256. https://doi.org/10.1016/j.solidstatesciences.2010.11.024.
[87] G.K. Rane, D. Apel, U. Welzel, E.J. Mittemeijer, The microstructural evolution and thermal stability of nanocrystalline ball-milled Ni–15 at.% W powder, Journal of Materials Research. 28 (2013) 873–886. https://doi.org/10.1557/jmr.2012.442.
[88] X. Wang, L. Li, J. Qu, W. Tao, Microstructure and mechanical properties of laser metal deposited AlSi10Mg alloys, Materials Science and Technology. 35 (2019) 2284–2293. https://doi.org/10.1080/02670836.2019.1674022.
[89] H. Adachi, Y. Karamatsu, S. Nakayama, T. Miyazawa, M. Sato, T. Yamasaki, Elastic and Plastic Deformation Behavior Studied by *In-Situ* Synchrotron X-ray Diffraction in Nanocrystalline Nickel, MATERIALS TRANSACTIONS. 57 (2016) 1447–1453. https://doi.org/10.2320/matertrans.MH201505.
[90] Y. Miyajima, S. Okubo, T. Miyazawa, H. Adachi, T. Fujii, In-situ X-ray diffraction during tensile deformation of ultrafine-grained copper using synchrotron radiation, Philosophical Magazine Letters. 96 (2016) 294–304. https://doi.org/10.1080/09500839.2016.1218563.
[91] J.Y. He, H. Wang, H.L. Huang, X.D. Xu, M.W. Chen, Y. Wu, X.J. Liu, T.G. Nieh, K. An, Z.P. Lu, A precipitation-hardened high-entropy alloy with outstanding tensile properties, Acta Materialia. 102 (2016) 187–196. https://doi.org/10.1016/j.actamat.2015.08.076.

[92] J. Joseph, N. Stanford, P. Hodgson, D.M. Fabijanic, Understanding the mechanical behaviour and the large strength/ductility differences between FCC and BCC AlxCoCrFeNi high entropy alloys, Journal of Alloys and Compounds. 726 (2017) 885–895. https://doi.org/10.1016/j.jallcom.2017.08.067.
[93] T. Xiong, W. Yang, S. Zheng, Z. Liu, Y. Lu, R. Zhang, Y. Zhou, X. Shao, B. Zhang, J. Wang, F. Yin, P.K. Liaw, X. Ma, Faceted Kurdjumov-Sachs interface-induced slip continuity in the eutectic high-entropy alloy, AlCoCrFeNi2.1, Journal of Materials Science & Technology. 65 (2021) 216–227. https://doi.org/10.1016/j.jmst.2020.04.073.
[94] S. UKAI, T. OKUDA, M. FUJIWARA, T. KOBAYASHI, S. MIZUTA, H. NAKASHIMA, Characterization of High Temperature Creep Properties in Recrystallized 12Cr-ODS Ferritic Steel Claddings, Journal of Nuclear Science and Technology. 39 (2002) 872–879. https://doi.org/10.1080/18811248.2002.9715271.
[95] B.B. He, B. Hu, H.W. Yen, G.J. Cheng, Z.K. Wang, H.W. Luo, M.X. Huang, High dislocation density–induced large ductility in deformed and partitioned steels, Science. 357 (2017) 1029–1032. https://doi.org/10.1126/science.aan0177.
[96] H.Y. Yasuda, K. Shigeno, T. Nagase, Dynamic strain aging of Al 0.3 CoCrFeNi high entropy alloy single crystals, Scripta Materialia. 108 (2015) 80–83. https://doi.org/10.1016/j.scriptamat.2015.06.022.
[97] S.-I. Baik, S.-Y. Wang, P.K. Liaw, D.C. Dunand, Increasing the creep resistance of Fe-Ni-Al-Cr superalloys via Ti additions by optimizing the B2/L21 ratio in composite nano-precipitates, Acta Materialia. 157 (2018) 142–154. https://doi.org/10.1016/j.actamat.2018.07.025.
[98] N. Yi, Y. Cao, Y.-M. Liu, W.-L. Dai, H.-Y. He, K.-N. Fan, Highly Efficient Ni–Ce–O Mixed Oxide Catalysts via Gel-coprecipitation of Oxalate Precursors for Catalytic Combustion of Methane, Chemistry Letters. 34 (2005) 108–109. https://doi.org/10.1246/cl.2005.108.
[99] P.W. Stephens, Phenomenological model of anisotropic peak broadening in powder diffraction, Journal of Applied Crystallography. 32 (1999) 281–289. https://doi.org/10.1107/S0021889898006001.
[100] L. Lutterotti, D. Chateigner, S. Ferrari, J. Ricote, Texture, residual stress and structural analysis of thin films using a combined X-ray analysis, Thin Solid Films. 450 (2004) 34–41. https://doi.org/10.1016/j.tsf.2003.10.150.
[101] H.-R. Wenk, L. Lutterotti, S. Vogel, Texture analysis with the new HIPPO TOF diffractometer, Nuclear Instruments and Methods in Physics Research Section A: Accelerators, Spectrometers, Detectors and Associated Equipment. 515 (2003) 575–588. https://doi.org/10.1016/j.nima.2003.05.001.
[102] C.E. Tommaseo, J. Devine, S. Merkel, S. Speziale, H.-R. Wenk, Texture development and elastic stresses in magnesiowűstite at high pressure, Physics and Chemistry of Minerals. 33 (2006) 84–97. https://doi.org/10.1007/s00269-005-0054-x.
[103] X. Li, D.L. Irving, L. Vitos, First-principles investigation of the micromechanical properties of fcc-hcp polymorphic high-entropy alloys, Scientific Reports. 8 (2018) 11196. https://doi.org/10.1038/s41598-018-29588-z.
[104] E. Rybacki, A. Reinicke, T. Meier, M. Makasi, G. Dresen, What controls the mechanical properties of shale rocks? – Part I: Strength and Young's modulus, Journal of Petroleum Science and Engineering. 135 (2015) 702–722. https://doi.org/10.1016/j.petrol.2015.10.028.
[105] S. Sinha, S.S. Nene, M. Frank, K. Liu, P. Agrawal, R.S. Mishra, On the evolving nature of c/a ratio in a hexagonal close-packed epsilon martensite phase in transformative high entropy alloys, Scientific Reports. 9 (2019) 13185. https://doi.org/10.1038/s41598-019-49904-5.
[106] N. Stanford, D.P. Dunne, Effect of Si on the reversibility of stress-induced martensite in Fe–Mn–Si shape memory alloys, Acta Materialia. 58 (2010) 6752–6762. https://doi.org/10.1016/j.actamat.2010.08.041.
[107] S. AGNEW, D. BROWN, C. TOME, Validating a polycrystal model for the elastoplastic response of magnesium alloy AZ31 using in situ neutron diffraction, Acta Materialia. 54 (2006) 4841–4852. https://doi.org/10.1016/j.actamat.2006.06.020.
[108] M.L. Young, J.D. Almer, M.R. Daymond, D.R. Haeffner, D.C. Dunand, Load partitioning between ferrite and cementite during elasto-plastic deformation of an ultrahigh-carbon steel, Acta Materialia. 55 (2007) 1999–2011. https://doi.org/10.1016/j.actamat.2006.11.004.
[109] N.R. Jaladurgam, A. Lozinko, S. Guo, T.-L. Lee, M. Hörnqvist Colliander, Temperature dependent load partitioning and slip mode transition in a eutectic AlCoCrFeNi2.1, Materialia. 17 (2021) 101118. https://doi.org/10.1016/j.mtla.2021.101118.

[110] S. Gao, T. Yoshimura, W. Mao, Y. Bai, W. Gong, M. Park, A. Shibata, H. Adachi, M. Sato, N. Tsuji, Tensile Deformation of Ultrafine-Grained Fe-Mn-Al-Ni-C Alloy Studied by In Situ Synchrotron Radiation X-ray Diffraction, Crystals. 10 (2020) 1115. https://doi.org/10.3390/cryst10121115.
[111] P. Hirsch, D. Cockayne, J. Spence, M. Whelan, 50 Years of TEM of dislocations: Past, present and future, Philosophical Magazine. 86 (2006) 4519–4528. https://doi.org/10.1080/14786430600768634.
[112] I. Groma, T. Ungár, M. Wilkens, Asymmetric X-ray line broadening of plastically deformed crystals. I. Theory, Journal of Applied Crystallography. 21 (1988) 47–54. https://doi.org/10.1107/S0021889887009178.
[113] I. Gutierrez-Urrutia, J.A. del Valle, S. Zaefferer, D. Raabe, Study of internal stresses in a TWIP steel analyzing transient and permanent softening during reverse shear tests, Journal of Materials Science. 45 (2010) 6604–6610. https://doi.org/10.1007/s10853-010-4750-7.
[114] Z.Y. Liang, Y.Z. Li, M.X. Huang, The respective hardening contributions of dislocations and twins to the flow stress of a twinning-induced plasticity steel, Scripta Materialia. 112 (2016) 28–31. https://doi.org/10.1016/j.scriptamat.2015.09.003.
[115] E. Snoeck, B. Warot, H. Ardhuin, A. Rocher, M.. Casanove, R. Kilaas, M.. Hÿtch, Quantitative analysis of strain field in thin films from HRTEM micrographs, Thin Solid Films. 319 (1998) 157–162. https://doi.org/10.1016/S0040-6090(97)01113-9.
[116] R.A. Renzetti, H.R.Z. Sandim, R.E. Bolmaro, P.A. Suzuki, A. Möslang, X-ray evaluation of dislocation density in ODS-Eurofer steel, Materials Science and Engineering: A. 534 (2012) 142–146. https://doi.org/10.1016/j.msea.2011.11.051.
[117] D. Akama, T. Tsuchiyama, S. Takaki, Change in Dislocation Characteristics with Cold Working in Ultralow-carbon Martensitic Steel, ISIJ International. 56 (2016) 1675–1680. https://doi.org/10.2355/isijinternational.ISIJINT-2016-140.
[118] K.D. Rogers, P. Daniels, An X-ray diffraction study of the effects of heat treatment on bone mineral microstructure, Biomaterials. 23 (2002) 2577–2585. https://doi.org/10.1016/S0142-9612(01)00395-7.
[119] M.H. Yoo, J.R. Morris, K.M. Ho, S.R. Agnew, Nonbasal deformation modes of HCP metals and alloys: Role of dislocation source and mobility, Metallurgical and Materials Transactions A. 33 (2002) 813–822. https://doi.org/10.1007/s11661-002-0150-1.
[120] H. Cheng, H.Y. Wang, Y.C. Xie, Q.H. Tang, P.Q. Dai, Controllable fabrication of a carbide-containing FeCoCrNiMn high-entropy alloy: microstructure and mechanical properties, Materials Science and Technology. 33 (2017) 2032–2039. https://doi.org/10.1080/02670836.2017.1342367.
[121] L. Song, X. Hu, L. Wang, A. Stark, D. Lazurenko, U. Lorenz, J. Lin, F. Pyczak, T. Zhang, Microstructure evolution and enhanced creep property of a high Nb containing TiAl alloy with carbon addition, Journal of Alloys and Compounds. 807 (2019) 151649. https://doi.org/10.1016/j.jallcom.2019.151649.
[122] K. Venkateswarlu, A. Chandra Bose, N. Rameshbabu, X-ray peak broadening studies of nanocrystalline hydroxyapatite by Williamson–Hall analysis, Physica B: Condensed Matter. 405 (2010) 4256–4261. https://doi.org/10.1016/j.physb.2010.07.020.
[123] Y.T. Prabhu, K.V. Rao, V.S.S. Kumar, B.S. Kumari, X-Ray Analysis by Williamson-Hall and Size-Strain Plot Methods of ZnO Nanoparticles with Fuel Variation, World Journal of Nano Science and Engineering. 04 (2014) 21–28. https://doi.org/10.4236/wjnse.2014.41004.
[124] G. Dini, R. Ueji, A. Najafizadeh, S.M. Monir-Vaghefi, Flow stress analysis of TWIP steel via the XRD measurement of dislocation density, Materials Science and Engineering: A. 527 (2010) 2759–2763. https://doi.org/10.1016/j.msea.2010.01.033.
[125] S. Kumari, D. Singh, P.K. Giri, Strain Anisotropy in Freestanding Germanium Nanoparticles Synthesized by Ball Milling, Journal of Nanoscience and Nanotechnology. 9 (2009) 5231–5236. https://doi.org/10.1166/jnn.2009.1138.
[126] N.J. Vickers, Animal Communication: When I'm Calling You, Will You Answer Too?, Current Biology. 27 (2017) R713–R715. https://doi.org/10.1016/j.cub.2017.05.064.
[127] Y. Wang, B. Liu, K. Yan, M. Wang, S. Kabra, Y.-L. Chiu, D. Dye, P.D. Lee, Y. Liu, B. Cai, Probing deformation mechanisms of a FeCoCrNi high-entropy alloy at 293 and 77 K using in situ neutron diffraction, Acta Materialia. 154 (2018) 79–89. https://doi.org/10.1016/j.actamat.2018.05.013.
[128] K. Yamanaka, M. Mori, S. Sato, A. Chiba, Stacking-fault strengthening of biomedical Co–Cr–Mo alloy via multipass thermomechanical processing, Scientific Reports. 7 (2017) 10808.

https://doi.org/10.1038/s41598-017-10305-1.
[129] F.F. Lavrentev, Y.A. Pokhil, Relation of dislocation density in different slip systems to work hardening parameters for magnesium crystals, Materials Science and Engineering. 18 (1975) 261–270. https://doi.org/10.1016/0025-5416(75)90179-2.
[130] F.F. Lavrentev, The type of dislocation interaction as the factor determining work hardening, Materials Science and Engineering. 46 (1980) 191–208. https://doi.org/10.1016/0025-5416(80)90175-5.
[131] R. Xiong, H. Peng, T. Zhang, J.W. Bae, H.S. Kim, Y. Wen, Superior strain-hardening by deformation-induced nano-HCP martensite in Fe–Mn–Si–C high-manganese steel, Materials Science and Engineering: A. 824 (2021) 141864. https://doi.org/10.1016/j.msea.2021.141864.
[132] W.R. Pereira, H. Kloos, S.B. Crawford, J.G. Velásquez-Melendez, L.F. Matoso, R.T. Fujiwara, G.G.L. Cançado, P.T. LoVerde, R. Correa-Oliveira, A. Gazzinelli, Schistosoma mansoni infection in a rural area of the Jequitinhonha Valley, Minas Gerais, Brazil: Analysis of exposure risk, Acta Tropica. 113 (2010) 34–41. https://doi.org/10.1016/j.actatropica.2009.09.001.
[133] Y. Shi, S. Li, T.L. Lee, X. Hui, Z. Zhang, R. Li, M. Zhang, S. Kabra, Y.-D. Wang, In situ neutron diffraction study of a new type of stress-induced confined martensitic transformation in Fe22Co20Ni19Cr20Mn12Al7 high-entropy alloy, Materials Science and Engineering: A. 771 (2020) 138555. https://doi.org/10.1016/j.msea.2019.138555.
[134] H. Cheng, H.Y. Wang, Y.C. Xie, Q.H. Tang, P.Q. Dai, Controllable fabrication of a carbide-containing FeCoCrNiMn high-entropy alloy: microstructure and mechanical properties, Materials Science and Technology. 33 (2017) 2032–2039. https://doi.org/10.1080/02670836.2017.1342367.
[135] Z. Li, C.C. Tasan, K.G. Pradeep, D. Raabe, A TRIP-assisted dual-phase high-entropy alloy: Grain size and phase fraction effects on deformation behavior, Acta Materialia. 131 (2017) 323–335. https://doi.org/10.1016/j.actamat.2017.03.069.
[136] T. Holden, D.W. Brown, B. Clausen, H. Suzuki, Search for Evidence of Stacking Faults in Austenitic Stainless Steel Alloys by Neutron Diffraction, Materials Science Forum. 652 (2010) 129–132. https://doi.org/10.4028/www.scientific.net/MSF.652.129.
[137] D.B. Miracle, O.N. Senkov, A critical review of high entropy alloys and related concepts, Acta Materialia. 122 (2017) 448–511. https://doi.org/10.1016/j.actamat.2016.08.081.
[138] S.F. Liu, Y. Wu, H.T. Wang, W.T. Lin, Y.Y. Shang, J.B. Liu, K. An, X.J. Liu, H. Wang, Z.P. Lu, Transformation-reinforced high-entropy alloys with superior mechanical properties via tailoring stacking fault energy, Journal of Alloys and Compounds. 792 (2019) 444–455. https://doi.org/10.1016/j.jallcom.2019.04.035.
[139] M. Kang, W. Woo, Y.-K. Lee, B.-S. Seong, Neutron diffraction analysis of stacking fault energy in Fe–18Mn–2Al–0.6C twinning-induced plasticity steels, Materials Letters. 76 (2012) 93–95. https://doi.org/10.1016/j.matlet.2012.02.075.
[140] B. Cai, B. Liu, S. Kabra, Y. Wang, K. Yan, P.D. Lee, Y. Liu, Deformation mechanisms of Mo alloyed FeCoCrNi high entropy alloy: In situ neutron diffraction, Acta Materialia. 127 (2017) 471–480. https://doi.org/10.1016/j.actamat.2017.01.034.
[141] H.S. Lipson, X-ray diffraction by B. E. Warren, Acta Crystallographica Section A. 27 (1971) 192–192. https://doi.org/10.1107/S0567739471000445.
[142] C. Haase, F. Tang, M.B. Wilms, A. Weisheit, B. Hallstedt, C. Varvenne, A. Luque, W.A. Curtin, I. Toda-Caraballo, S. Oliver, L. Zhao, A.J. Gormley, R. Chapman, C. Boyer, Y. Li, K. Yang, S. Liu, B.B. Kappes, B. Amin-ahmadi, O. Benafan, X. Zhang, A.P. Stebner, S. Luo, T. Li, X. Wang, M. Faizan, L. Zhang, F.G. Coury, P. Wilson, K.D. Clarke, M.J. Kaufman, A.J. Clarke, S.Z. Han, E.A. Choi, S.H. Lim, S. Kim, J. Lee, S. Ranganathan, A general formulation for solid solution hardening effect in multicomponent alloys, Acta Materialia. 167 (2019) 100898. https://doi.org/10.1016/j.msea.2017.01.099.
[143] S. Bhowmik, J. Zhang, S.C. Vogel, S.S. Nene, R.S. Mishra, B.A. McWilliams, M. Knezevic, Effects of plasticity-induced martensitic transformation and grain refinement on the evolution of microstructure and mechanical properties of a metastable high entropy alloy, Journal of Alloys and Compounds. 891 (2022) 161871. https://doi.org/10.1016/j.jallcom.2021.161871.
[144] W.W. Jian, G.M. Cheng, W.Z. Xu, H. Yuan, M.H. Tsai, Q.D. Wang, C.C. Koch, Y.T. Zhu, S.N. Mathaudhu, Ultrastrong Mg Alloy via Nano-spaced Stacking Faults, Materials Research Letters. 1 (2013) 61–66. https://doi.org/10.1080/21663831.2013.765927.
[145] Y. Bu, Z. Li, J. Liu, H. Wang, D. Raabe, W. Yang, Nonbasal Slip Systems Enable a Strong and Ductile Hexagonal-Close-Packed High-Entropy Phase, Physical Review Letters. 122 (2019)

075502. https://doi.org/10.1103/PhysRevLett.122.075502.
[146] M. Frank, Y. Chen, S.S. Nene, S. Sinha, K. Liu, K. An, R.S. Mishra, Investigating the deformation mechanisms of a highly metastable high entropy alloy using in-situ neutron diffraction, Materials Today Communications. 23 (2020) 100858. https://doi.org/10.1016/j.mtcomm.2019.100858.
[147] F. Galbusera, A.G. Demir, J. Platl, C. Turk, R. Schnitzer, B. Previtali, Processability and cracking behaviour of novel high-alloyed tool steels processed by Laser Powder Bed Fusion, Journal of Materials Processing Technology. 302 (2022) 117435. https://doi.org/10.1016/j.jmatprotec.2021.117435.
[148] B. Cantor, I.T.H. Chang, P. Knight, A.J.B. Vincent, Microstructural development in equiatomic multicomponent alloys, Materials Science and Engineering: A. 375–377 (2004) 213–218. https://doi.org/10.1016/j.msea.2003.10.257.
[149] B. Cantor, Multicomponent high-entropy Cantor alloys, Progress in Materials Science. 120 (2021) 100754. https://doi.org/10.1016/j.pmatsci.2020.100754.
[150] H. Jiang, H. Zhang, T. Huang, Y. Lu, T. Wang, T. Li, Microstructures and mechanical properties of Co2MoxNi2VWx eutectic high entropy alloys, Materials & Design. 109 (2016) 539–546. https://doi.org/10.1016/j.matdes.2016.07.113.
[151] O.N. Senkov, G.B. Wilks, J.M. Scott, D.B. Miracle, Mechanical properties of Nb25Mo25Ta25W25 and V20Nb20Mo20Ta20W20 refractory high entropy alloys, Intermetallics. 19 (2011) 698–706. https://doi.org/10.1016/j.intermet.2011.01.004.
[152] Y. Shi, B. Yang, P. Liaw, Corrosion-Resistant High-Entropy Alloys: A Review, Metals. 7 (2017) 43. https://doi.org/10.3390/met7020043.
[153] C.L. Wu, S. Zhang, C.H. Zhang, H. Zhang, S.Y. Dong, Phase evolution and cavitation erosion-corrosion behavior of FeCoCrAlNiTi x high entropy alloy coatings on 304 stainless steel by laser surface alloying, Journal of Alloys and Compounds. 698 (2017) 761–770. https://doi.org/10.1016/j.jallcom.2016.12.196.
[154] I. Basu, V. Ocelík, J.T.M. De Hosson, Size effects on plasticity in high-entropy alloys, Journal of Materials Research. 33 (2018) 3055–3076. https://doi.org/10.1557/jmr.2018.282.
[155] J. Gu, M. Song, Annealing-induced abnormal hardening in a cold rolled CrMnFeCoNi high entropy alloy, Scripta Materialia. 162 (2019) 345–349. https://doi.org/10.1016/j.scriptamat.2018.11.042.
[156] M. Laurent-Brocq, A. Akhatova, L. Perrière, S. Chebini, X. Sauvage, E. Leroy, Y. Champion, Insights into the phase diagram of the CrMnFeCoNi high entropy alloy, Acta Materialia. 88 (2015) 355–365. https://doi.org/10.1016/j.actamat.2015.01.068.
[157] G. Laplanche, A. Kostka, O.M. Horst, G. Eggeler, E.P. George, Microstructure evolution and critical stress for twinning in the CrMnFeCoNi high-entropy alloy, Acta Materialia. 118 (2016) 152–163. https://doi.org/10.1016/j.actamat.2016.07.038.
[158] H. Nam, B. Moon, S. Park, N. Kim, S. Song, N. Park, Y. Na, N. Kang, Gas tungsten arc weldability of stainless steel 304 using CoCrFeMnNi filler metals for cryogenic applications, Science and Technology of Welding and Joining. 27 (2022) 33–42. https://doi.org/10.1080/13621718.2021.1996851.
[159] J.P. Oliveira, A. Shamsolhodaei, J. Shen, J.G. Lopes, R.M. Gonçalves, M. de Brito Ferraz, L. Piçarra, Z. Zeng, N. Schell, N. Zhou, H. Seop Kim, Improving the ductility in laser welded joints of CoCrFeMnNi high entropy alloy to 316 stainless steel, Materials & Design. 219 (2022) 110717. https://doi.org/10.1016/j.matdes.2022.110717.
[160] M. Ma, R. Lai, J. Qin, B. Wang, H. Liu, D. Yi, Effect of weld reinforcement on tensile and fatigue properties of 5083 aluminum metal inert gas (MIG) welded joint: Experiments and numerical simulations, International Journal of Fatigue. 144 (2021) 106046. https://doi.org/10.1016/j.ijfatigue.2020.106046.
[161] J.P. Oliveira, J. Shen, Z. Zeng, J.M. Park, Y.T. Choi, N. Schell, E. Maawad, N. Zhou, H.S. Kim, Dissimilar laser welding of a CoCrFeMnNi high entropy alloy to 316 stainless steel, Scripta Materialia. 206 (2022) 114219. https://doi.org/10.1016/j.scriptamat.2021.114219.
[162] A. Singh, D.A. Basha, Y. Matsushita, K. Tsuchiya, Z. Lu, T.-G. Nieh, T. Mukai, Domain structure and lattice effects in a severely plastically deformed CoCrFeMnNi high entropy alloy, Journal of Alloys and Compounds. 812 (2020) 152028. https://doi.org/10.1016/j.jallcom.2019.152028.
[163] X. Ma, J. Chen, X. Wang, Y. Xu, Y. Xue, Microstructure and mechanical properties of cold drawing CoCrFeMnNi high entropy alloy, Journal of Alloys and Compounds. 795 (2019) 45–53. https://doi.org/10.1016/j.jallcom.2019.04.296.
[164] Z. Zhu, X. Ma, C. Wang, G. Mi, S. Zheng, The metallurgical behaviors and crystallographic

characteristic on macro deformation mechanism of 316 L laser-MIG hybrid welded joint, Materials & Design. 194 (2020) 108893. https://doi.org/10.1016/j.matdes.2020.108893.
[165] X.-M. Chen, Y.C. Lin, F. Wu, EBSD study of grain growth behavior and annealing twin evolution after full recrystallization in a nickel-based superalloy, Journal of Alloys and Compounds. 724 (2017) 198–207. https://doi.org/10.1016/j.jallcom.2017.07.027.
[166] W.L. Grube, S.R. Rouze, The Origin, Growth and Annihilation of Annealing Twins in Austenite, Canadian Metallurgical Quarterly. 2 (1963) 31–52. https://doi.org/10.1179/cmq.1963.2.1.31.
[167] C. Wang, J. Yu, Y. Zhang, Y. Yu, Phase evolution and solidification cracking sensibility in laser remelting treatment of the plasma-sprayed CrMnFeCoNi high entropy alloy coating, Materials & Design. 182 (2019) 108040. https://doi.org/10.1016/j.matdes.2019.108040.
[168] C. Zhang, J. Zhu, C. Ji, Y. Guo, R. Fang, S. Mei, S. Liu, Laser powder bed fusion of high-entropy alloy particle-reinforced stainless steel with enhanced strength, ductility, and corrosion resistance, Materials and Design. 209 (2021) 109950. https://doi.org/10.1016/j.matdes.2021.109950.
[169] R. Sokkalingam, P. Mastanaiah, V. Muthupandi, K. Sivaprasad, K.G. Prashanth, Electron-beam welding of high-entropy alloy and stainless steel: microstructure and mechanical properties, Materials and Manufacturing Processes. 35 (2020) 1885–1894. https://doi.org/10.1080/10426914.2020.1802045.
[170] B. Gludovatz, A. Hohenwarter, D. Catoor, E.H. Chang, E.P. George, R.O. Ritchie, A fracture-resistant high-entropy alloy for cryogenic applications, Science. 345 (2014) 1153–1158. https://doi.org/10.1126/science.1254581.
[171] N.K. Adomako, G. Shin, N. Park, K. Park, J.H. Kim, Laser dissimilar welding of CoCrFeMnNi-high entropy alloy and duplex stainless steel, Journal of Materials Science & Technology. 85 (2021) 95–105. https://doi.org/10.1016/j.jmst.2021.02.003.
[172] Y.-K. Kim, Y.-A. Joo, H.S. Kim, K.-A. Lee, High temperature oxidation behavior of Cr-Mn-Fe-Co-Ni high entropy alloy, Intermetallics. 98 (2018) 45–53. https://doi.org/10.1016/j.intermet.2018.04.006.
[173] J.P. Oliveira, D. Barbosa, F.M.B. Fernandes, R.M. Miranda, Tungsten inert gas (TIG) welding of Ni-rich NiTi plates: functional behavior, Smart Materials and Structures. 25 (2016) 03LT01. https://doi.org/10.1088/0964-1726/25/3/03LT01.
[174] H. Nam, S. Park, E.-J. Chun, H. Kim, Y. Na, N. Kang, Laser dissimilar weldability of cast and rolled CoCrFeMnNi high-entropy alloys for cryogenic applications, Science and Technology of Welding and Joining. 25 (2020) 127–134. https://doi.org/10.1080/13621718.2019.1644471.
[175] G. Qin, R. Chen, H. Zheng, H. Fang, L. Wang, Y. Su, J. Guo, H. Fu, Strengthening FCC-CoCrFeMnNi high entropy alloys by Mo addition, Journal of Materials Science & Technology. 35 (2019) 578–583. https://doi.org/10.1016/j.jmst.2018.10.009.
[176] A.J. Zaddach, C. Niu, C.C. Koch, D.L. Irving, Mechanical Properties and Stacking Fault Energies of NiFeCrCoMn High-Entropy Alloy, JOM. 65 (2013) 1780–1789. https://doi.org/10.1007/s11837-013-0771-4.
[177] A.J. Zaddach, R.O. Scattergood, C.C. Koch, Tensile properties of low-stacking fault energy high-entropy alloys, Materials Science and Engineering: A. 636 (2015) 373–378. https://doi.org/10.1016/j.msea.2015.03.109.
[178] B. Li, Z. Qin, H. Xue, Z. Sun, T. Gao, Optimization of shot peening parameters for AA7B50-T7751 using response surface methodology, Simulation Modelling Practice and Theory. 115 (2022) 102426. https://doi.org/10.1016/j.simpat.2021.102426.
[179] B. Nagarajan, D. Kumar, Z. Fan, S. Castagne, Effect of deep cold rolling on mechanical properties and microstructure of nickel-based superalloys, Materials Science and Engineering: A. 728 (2018) 196–207. https://doi.org/10.1016/j.msea.2018.05.005.
[180] Z. Cui, Y. Mi, D. Qiu, P. Dong, Z. Qin, D. Gong, W. Li, Microstructure and mechanical properties of additively manufactured CrMnFeCoNi high-entropy alloys after ultrasonic surface rolling process, Journal of Alloys and Compounds. 887 (2021) 161393. https://doi.org/10.1016/j.jallcom.2021.161393.
[181] H.-Y. Huang, I.-C. Kuo, C.-W. Zhang, Friction-stir welding of aluminum alloy with an iron-based metal as reinforcing material, Science and Engineering of Composite Materials. 25 (2018) 123–131. https://doi.org/10.1515/secm-2016-0065.
[182] A. Hasnaoui, H. Van Swygenhoven, P.M. Derlet, Dimples on Nanocrystalline Fracture Surfaces As Evidence for Shear Plane Formation, Science. 300 (2003) 1550–1552. https://doi.org/10.1126/science.1084284.

[183] Y. Zhao, X. Zhang, H. Quan, Y. Chen, S. Wang, S. Zhang, Effect of Mo addition on structures and properties of FeCoNiCrMn high entropy alloy film by direct current magnetron sputtering, Journal of Alloys and Compounds. 895 (2022) 162709. https://doi.org/10.1016/j.jallcom.2021.162709.
[184] K. Cho, Y. Fujioka, T. Nagase, H.Y. Yasuda, Grain refinement of non-equiatomic Cr-rich CoCrFeMnNi high-entropy alloys through combination of cold rolling and precipitation of σ phase, Materials Science and Engineering: A. 735 (2018) 191–200. https://doi.org/10.1016/j.msea.2018.08.038.
[185] L. Jiang, Y. Lu, W. Wu, Z. Cao, T. Li, Microstructure and Mechanical Properties of a CoFeNi2V0.5Nb0.75 Eutectic High Entropy Alloy in As-cast and Heat-treated Conditions, Journal of Materials Science & Technology. 32 (2016) 245–250. https://doi.org/10.1016/j.jmst.2015.08.006.
[186] O.N. Senkov, G.B. Wilks, J.M. Scott, D.B. Miracle, Intermetallics Mechanical properties of Nb 25 Mo 25 Ta 25 W 25 and V 20 Nb 20 Mo 20 Ta 20 W 20 refractory high entropy alloys, Intermetallics. 19 (2011) 698–706. https://doi.org/10.1016/j.intermet.2011.01.004.
[187] M. Zhang, X. Zhou, X. Yu, J. Li, Surface & Coatings Technology Synthesis and characterization of refractory TiZrNbWMo high-entropy alloy coating by laser cladding, Surface & Coatings Technology. 311 (2017) 321–329. https://doi.org/10.1016/j.surfcoat.2017.01.012.
[188] B. Schuh, F. Mendez-martin, B. Völker, E.P. George, H. Clemens, R. Pippan, A. Hohenwarter, Acta Materialia Mechanical properties , microstructure and thermal stability of a nanocrystalline CoCrFeMnNi high-entropy alloy after severe plastic deformation, Acta Materialia. 96 (2015) 258–268. https://doi.org/10.1016/j.actamat.2015.06.025.
[189] K.G. Pradeep, Y. Deng, Z. Li, D. Raabe, C.C. Tasan, overcome the strength – ductility trade-off, Nature. 534 (2016) 227–230. https://doi.org/10.1038/nature17981.
[190] Y. Lu, X. Gao, L. Jiang, Z. Chen, T. Wang, J. Jie, H. Kang, Y. Zhang, S. Guo, H. Ruan, Y. Zhao, Z. Cao, T. Li, Directly cast bulk eutectic and near-eutectic high entropy alloys with balanced strength and ductility in a wide temperature range, Acta Materialia. 124 (2017) 143–150. https://doi.org/10.1016/j.actamat.2016.11.016.
[191] B. Gwalani, V. Soni, M. Lee, S. Mantri, Y. Ren, R. Banerjee, Optimizing the coupled effects of Hall-Petch and precipitation strengthening in a Al 0.3 CoCrFeNi high entropy alloy, Materials & Design. 121 (2017) 254–260. https://doi.org/10.1016/j.matdes.2017.02.072.
[192] C. Shang, E. Axinte, J. Sun, X. Li, P. Li, J. Du, P. Qiao, Y. Wang, CoCrFeNi (W 1 − x Mo x) high-entropy alloy coatings with excellent mechanical properties and corrosion resistance prepared by mechanical alloying and hot pressing sintering, Materials & Design. 117 (2017) 193–202. https://doi.org/10.1016/j.matdes.2016.12.076.
[193] J. Ding, A. Inoue, Y. Han, F.L. Kong, S.L. Zhu, Z. Wang, E. Shalaan, F. Al-Marzouki, High entropy effect on structure and properties of (Fe,Co,Ni,Cr)-B amorphous alloys, Journal of Alloys and Compounds. 696 (2017) 345–352. https://doi.org/10.1016/j.jallcom.2016.11.223.
[194] B. Gludovatz, A. Hohenwarter, D. Catoor, E.H. Chang, E.P. George, R.O. Ritchie, A fracture-resistant high-entropy alloy for cryogenic applications, Science. 345 (2014) 1153–1158. https://doi.org/10.1126/science.1254581.
[195] M.J. Yao, K.G. Pradeep, C.C. Tasan, D. Raabe, A novel, single phase, non-equiatomic FeMnNiCoCr high-entropy alloy with exceptional phase stability and tensile ductility, Scripta Materialia. 72–73 (2014) 5–8. https://doi.org/10.1016/j.scriptamat.2013.09.030.
[196] Y. Deng, C.C. Tasan, K.G. Pradeep, H. Springer, A. Kostka, D. Raabe, Design of a twinning-induced plasticity high entropy alloy, Acta Materialia. 94 (2015) 124–133. https://doi.org/10.1016/j.actamat.2015.04.014.
[197] M.A. Hemphill, T. Yuan, G.Y. Wang, J.W. Yeh, C.W. Tsai, A. Chuang, P.K. Liaw, Fatigue behavior of Al0.5CoCrCuFeNi high entropy alloys, Acta Materialia. 60 (2012) 5723–5734. https://doi.org/10.1016/j.actamat.2012.06.046.
[198] C. Tong, Y. Chen, S. Chen, J. Yeh, T. Shun, C. Tsau, S. Lin, S. Chang, Microstructure Characterization of Al x CoCrCuFeNi High-Entropy Alloy System with Multiprincipal Elements, 36 (2005).
[199] W. Li, D. Xie, D. Li, Y. Zhang, Y. Gao, P.K. Liaw, Mechanical behavior of high-entropy alloys, Progress in Materials Science. 118 (2021) 100777. https://doi.org/10.1016/j.pmatsci.2021.100777.
[200] H. Alloys, Y. Lu, Y. Dong, S. Guo, L. Jiang, H. Kang, T. Wang, B. Wen, Z. Wang, J. Jie, Z. Cao, H. Ruan, T. Li, A Promising New Class of, (n.d.) 1–5. https://doi.org/10.1038/srep06200.

[201] X. Jin, Y. Zhou, L. Zhang, X. Du, B. Li, A novel Fe 20 Co 20 Ni 41 Al 19 eutectic high entropy alloy with excellent tensile properties, Materials Letters. 216 (2018) 144–146. https://doi.org/10.1016/j.matlet.2018.01.017.
[202] Y. Guo, L. Liu, Y. Zhang, J. Qi, B. Wang, Z. Zhao, J. Shang, J. Xiang, A superfine eutectic microstructure and the mechanical properties of CoCrFeNiMo x high-entropy alloys, Journal of Materials Research. 33 (2018) 3258–3265. https://doi.org/10.1557/jmr.2018.177.
[203] Ł. Rogal, J. Morgiel, Z. Ś, F. Czerwi, Materials Science & Engineering A Microstructure and mechanical properties of the new Nb25Sc25Ti25Zr25 eutectic high entropy alloy, 651 (2016) 590–597. https://doi.org/10.1016/j.msea.2015.10.071.
[204] P. Shi, W. Ren, T. Zheng, Z. Ren, X. Hou, J. Peng, P. Hu, Y. Gao, Y. Zhong, P.K. Liaw, Enhanced strength–ductility synergy in ultrafine-grained eutectic high-entropy alloys by inheriting microstructural lamellae, Nature Communications. 10 (2019) 489. https://doi.org/10.1038/s41467-019-08460-2.
[205] I.S. Wani, T. Bhattacharjee, S. Sheikh, Y. Lu, S. Chatterjee, S. Guo, P.P. Bhattacharjee, N. Tsuji, Effect of severe cold-rolling and annealing on microstructure and mechanical properties of AlCoCrFeNi 2.1 eutectic high entropy alloy, IOP Conference Series: Materials Science and Engineering. 194 (2017) 012018. https://doi.org/10.1088/1757-899X/194/1/012018.
[206] S.R. Reddy, S. Yoshida, T. Bhattacharjee, N. Sake, A. Lozinko, S. Guo, P.P. Bhattacharjee, N. Tsuji, Nanostructuring with Structural-Compositional Dual Heterogeneities Enhances Strength-Ductility Synergy in Eutectic High Entropy Alloy, Scientific Reports. 9 (2019) 1–9. https://doi.org/10.1038/s41598-019-47983-y.
[207] T. Bhattacharjee, I.S. Wani, S. Sheikh, I.T. Clark, T. Okawa, S. Guo, P.P. Bhattacharjee, N. Tsuji, Simultaneous Strength-Ductility Enhancement of a Nano-Lamellar AlCoCrFeNi2.1 Eutectic High Entropy Alloy by Cryo-Rolling and Annealing, Scientific Reports. 8 (2018) 3276. https://doi.org/10.1038/s41598-018-21385-y.
[208] M.H. Asoushe, A.Z. Hanzaki, H.R. Abedi, B. Mirshekari, T. Wegener, S.V. Sajadifar, T. Niendorf, Thermal stability, microstructure and texture evolution of thermomechanical processed AlCoCrFeNi2.1 eutectic high entropy alloy, Materials Science and Engineering: A. 799 (2021) 140012. https://doi.org/10.1016/j.msea.2020.140012.
[209] A. Patel, I. Wani, S.R. Reddy, S. Narayanaswamy, A. Lozinko, R. Saha, S. Guo, P.P. Bhattacharjee, Strain-path controlled microstructure, texture and hardness evolution in cryo-deformed AlCoCrFeNi 2.1 eutectic high entropy alloy, Intermetallics. 97 (2018) 12–21. https://doi.org/10.1016/j.intermet.2018.03.007.
[210] I.S. Wani, T. Bhattacharjee, S. Sheikh, P.P. Bhattacharjee, S. Guo, N. Tsuji, Materials Science & Engineering A eutectic high entropy alloy using thermo-mechanical processing, Materials Science & Engineering A. 675 (2016) 99–109. https://doi.org/10.1016/j.msea.2016.08.048.
[211] I.S. Wani, T. Bhattacharjee, S. Sheikh, Y.P. Lu, S. Chatterjee, S. Guo, N. Tsuji, T. Bhattacharjee, S. Sheikh, Y.P. Lu, S. Chatterjee, Entropy Alloy, 3831 (2016). https://doi.org/10.1080/21663831.2016.1160451.
[212] T. Xiong, S. Zheng, J. Pang, X. Ma, Scripta Materialia alloy achieved via precipitation strengthening in a heterogeneous structure, Scripta Materialia. 186 (2020) 336–340. https://doi.org/10.1016/j.scriptamat.2020.04.035.
[213] P. Shi, Y. Zhong, Y. Li, W. Ren, T. Zheng, Z. Shen, B. Yang, J. Peng, P. Hu, Y. Zhang, P.K. Liaw, Y. Zhu, Multistage work hardening assisted by multi-type twinning in ultrafine-grained heterostructural eutectic high-entropy alloys, Materials Today. 41 (2020) 62–71. https://doi.org/10.1016/j.mattod.2020.09.029.
[214] T. Bhattacharjee, R. Zheng, Y. Chong, S. Sheikh, S. Guo, I.T. Clark, T. Okawa, I.S. Wani, P.P. Bhattacharjee, A. Shibata, N. Tsuji, Effect of low temperature on tensile properties of AlCoCrFeNi2.1 eutectic high entropy alloy, Materials Chemistry and Physics. 210 (2018) 207–212. https://doi.org/10.1016/j.matchemphys.2017.06.023.
[215] Y. Zhang, X. Wang, J. Li, Y. Huang, Y. Lu, X. Sun, Materials Science & Engineering A Deformation mechanism during high-temperature tensile test in an eutectic, Materials Science & Engineering A. 724 (2018) 148–155. https://doi.org/10.1016/j.msea.2018.03.078.
[216] S. Shukla, T. Wang, S. Cotton, R.S. Mishra, Hierarchical microstructure for improved fatigue properties in a eutectic high entropy alloy, Scripta Materialia. 156 (2018) 105–109. https://doi.org/10.1016/j.scriptamat.2018.07.022.
[217] N.R. Jaladurgam, A. Lozinko, S. Guo, T.L. Lee, M. Hörnqvist Colliander, Temperature dependent load partitioning and slip mode transition in a eutectic AlCoCrFeNi2.1 high entropy alloy,

Materialia. 17 (2021) 101118. https://doi.org/10.1016/j.mtla.2021.101118.
[218] L. Wang, C. Yao, J. Shen, Y. Zhang, T. Wang, Y. Ge, L. Gao, G. Zhang, Microstructures and room temperature tensile properties of as-cast and directionally solidified AlCoCrFeNi2.1 eutectic high-entropy alloy, Intermetallics. 118 (2020) 106681. https://doi.org/10.1016/j.intermet.2019.106681.
[219] Y. Zhang, X. Wang, J. Li, Y. Huang, Y. Lu, X. Sun, Deformation mechanism during high-temperature tensile test in an eutectic high-entropy alloy AlCoCrFeNi2.1, Materials Science and Engineering: A. 724 (2018) 148–155. https://doi.org/10.1016/j.msea.2018.03.078.
[220] I.S. Wani, T. Bhattacharjee, S. Sheikh, P.P. Bhattacharjee, S. Guo, N. Tsuji, Tailoring nanostructures and mechanical properties of AlCoCrFeNi2.1 eutectic high entropy alloy using thermo-mechanical processing, Materials Science and Engineering: A. 675 (2016) 99–109. https://doi.org/10.1016/j.msea.2016.08.048.
[221] Y. Lu, X. Gao, L. Jiang, Z. Chen, T. Wang, Acta Materialia Directly cast bulk eutectic and near-eutectic high entropy alloys with balanced strength and ductility in a wide temperature range, Acta Materialia. 124 (2017) 143–150. https://doi.org/10.1016/j.actamat.2016.11.016.
[222] P. Li, H. Sun, S. Wang, X. Hao, H. Dong, Rotary friction welding of AlCoCrFeNi2.1 eutectic high entropy alloy, Journal of Alloys and Compounds. 814 (2020) 152322. https://doi.org/10.1016/j.jallcom.2019.152322.
[223] P. Li, S. Wang, Y. Xia, X. Hao, H. Dong, Diffusion bonding of AlCoCrFeNi2.1 eutectic high entropy alloy to TiAl alloy, Journal of Materials Science & Technology. 45 (2020) 59–69. https://doi.org/10.1016/j.jmst.2019.10.041.
[224] L. Zhang, Y. Zhang, Tensile Properties and Impact Toughness of AlCoxCrFeNi3.1–x (x = 0.4, 1) High-Entropy Alloys, Frontiers in Materials. 7 (2020). https://doi.org/10.3389/fmats.2020.00092.
[225] D. Choudhuri, S.G. Srinivasan, R.S. Mishra, Deformation of lamellar FCC-B2 nanostructures containing Kurdjumov-Sachs interfaces: Relation between interfacial structure and plasticity, International Journal of Plasticity. 125 (2020) 191–209. https://doi.org/10.1016/j.ijplas.2019.09.014.
[226] T. Xiong, W. Yang, S. Zheng, Z. Liu, Y. Lu, R. Zhang, Y. Zhou, X. Shao, B. Zhang, J. Wang, F. Yin, P.K. Liaw, X. Ma, Faceted Kurdjumov-Sachs interface-induced slip continuity in the eutectic high-entropy alloy, AlCoCrFeNi2.1, Journal of Materials Science & Technology. 65 (2021) 216–227. https://doi.org/10.1016/j.jmst.2020.04.073.
[227] Y. Zhang, J. Li, X. Wang, Y. Lu, Y. Zhou, X. Sun, The interaction and migration of deformation twin in an eutectic high-entropy alloy AlCoCrFeNi2.1, Journal of Materials Science & Technology. 35 (2019) 902–906. https://doi.org/10.1016/j.jmst.2018.09.067.
[228] J. Miao, H. Liang, A. Zhang, J. He, J. Meng, Y. Lu, Tribological behavior of an AlCoCrFeNi2.1 eutectic high entropy alloy sliding against different counterfaces, Tribology International. 153 (2021) 106599. https://doi.org/10.1016/j.triboint.2020.106599.
[229] S.R. Reddy, U. Sunkari, A. Lozinko, R. Saha, S. Guo, P.P. Bhattacharjee, Microstructural design by severe warm-rolling for tuning mechanical properties of AlCoCrFeNi2.1 eutectic high entropy alloy, Intermetallics. 114 (2019). https://doi.org/10.1016/j.intermet.2019.106601.
[230] T. Wang, M. Komarasamy, S. Shukla, R.S. Mishra, Simultaneous enhancement of strength and ductility in an AlCoCrFeNi2.1 eutectic high-entropy alloy via friction stir processing, Journal of Alloys and Compounds. 766 (2018) 312–317. https://doi.org/10.1016/j.jallcom.2018.06.337.
[231] W. Zhang, L. Liu, S. Peng, J. Ren, F. Wu, J. Shang, M. Chen, Y. Zhang, Z. Zhao, J. Qi, B. Wang, W. Chen, The tensile property and notch sensitivity of AlCoCrFeNi2.1 high entropy alloy with a novel “steel-frame” eutectic microstructure, Journal of Alloys and Compounds. 863 (2021) 158747. https://doi.org/10.1016/j.jallcom.2021.158747.
[232] S.R. Reddy, U. Sunkari, A. Lozinko, S. Guo, P.P. Bhattacharjee, Development and homogeneity of microstructure and texture in a lamellar AlCoCrFeNi 2.1 eutectic high-entropy alloy severely strained in the warm-deformation regime, Journal of Materials Research. 34 (2019) 687–699. https://doi.org/10.1557/jmr.2018.409.
[233] D. Choudhuri, S. Shukla, P.A. Jannotti, S. Muskeri, S. Mukherjee, J.T. Lloyd, R.S. Mishra, Characterization of as-cast microstructural heterogeneities and damage mechanisms in eutectic AlCoCrFeNi2.1 high entropy alloy, Materials Characterization. 158 (2019) 109955. https://doi.org/10.1016/j.matchar.2019.109955.
[234] Y. Lu, Y. Dong, S. Guo, L. Jiang, H. Kang, T. Wang, B. Wen, Z. Wang, J. Jie, Z. Cao, H. Ruan, T. Li, A Promising New Class of High-Temperature Alloys: Eutectic High-Entropy Alloys, Scientific Reports. 4 (2015) 6200. https://doi.org/10.1038/srep06200.

[235] W. Chen, Y. Wang, L. Wang, J. Zhou, Effect of lamellar microstructure on fatigue crack initiation and propagation in AlCoCrFeNi2.1 eutectic high-entropy alloy, Engineering Fracture Mechanics. 246 (2021) 107615. https://doi.org/10.1016/j.engfracmech.2021.107615.
[236] T. Xiong, W. Yang, S. Zheng, Z. Liu, Y. Lu, R. Zhang, Y. Zhou, X. Shao, B. Zhang, J. Wang, F. Yin, P.K. Liaw, X. Ma, Journal of Materials Science & Technology Faceted Kurdjumov-Sachs interface-induced slip continuity in the, Journal of Materials Science & Technology. 65 (2021) 216–227. https://doi.org/10.1016/j.jmst.2020.04.073.
[237] R.J. Vikram, B.S. Murty, D. Fabijanic, S. Suwas, Insights into micro-mechanical response and texture of the additively manufactured eutectic high entropy alloy AlCoCrFeNi2.1, Journal of Alloys and Compounds. 827 (2020) 154034. https://doi.org/10.1016/j.jallcom.2020.154034.
[238] X. Gao, Y. Lu, B. Zhang, N. Liang, G. Wu, G. Sha, J. Liu, Y. Zhao, Microstructural origins of high strength and high ductility in an AlCoCrFeNi2.1 eutectic high-entropy alloy, Acta Materialia. 141 (2017) 59–66. https://doi.org/10.1016/j.actamat.2017.07.041.
[239] S. Muskeri, V. Hasannaeimi, R. Salloom, M. Sadeghilaridjani, S. Mukherjee, Small-scale mechanical behavior of a eutectic high entropy alloy, Scientific Reports. 10 (2020). https://doi.org/10.1038/s41598-020-59513-2.
[240] T.S. Reddy, I.S. Wani, T. Bhattacharjee, S.R. Reddy, R. Saha, P.P. Bhattacharjee, Severe plastic deformation driven nanostructure and phase evolution in a Al0.5CoCrFeMnNi dual phase high entropy alloy, Intermetallics. 91 (2017) 150–157. https://doi.org/10.1016/j.intermet.2017.09.002.
[241] N. Park, B.-J. Lee, N. Tsuji, The phase stability of equiatomic CoCrFeMnNi high-entropy alloy: Comparison between experiment and calculation results, Journal of Alloys and Compounds. 719 (2017) 189–193. https://doi.org/10.1016/j.jallcom.2017.05.175.
[242] Y.C. Liang, J.T. Guo, Y. Xie, L.Y. Sheng, L.Z. Zhou, Z.Q. Hu, Effect of growth rate on the tensile properties of DS NiAl/Cr(Mo) eutectic alloy produced by liquid metal cooling technique, Intermetallics. 18 (2010) 319–323. https://doi.org/10.1016/j.intermet.2009.08.002.
[243] K. Yamanaka, M. Mori, K. Kuramoto, A. Chiba, Development of new Co–Cr–W-based biomedical alloys: Effects of microalloying and thermomechanical processing on microstructures and mechanical properties, Materials & Design. 55 (2014) 987–998. https://doi.org/10.1016/j.matdes.2013.10.052.
[244] B. Wang, H. He, M. Naeem, S. Lan, S. Harjo, T. Kawasaki, Y. Nie, H.W. Kui, T. Ungár, D. Ma, A.D. Stoica, Q. Li, Y. Ke, C.T. Liu, X.-L. Wang, Deformation of CoCrFeNi high entropy alloy at large strain, Scripta Materialia. 155 (2018) 54–57. https://doi.org/10.1016/j.scriptamat.2018.06.013.
[245] N. Stepanov, M. Tikhonovsky, N. Yurchenko, D. Zyabkin, M. Klimova, S. Zherebtsov, A. Efimov, G. Salishchev, Effect of cryo-deformation on structure and properties of CoCrFeNiMn high-entropy alloy, Intermetallics. 59 (2015) 8–17. https://doi.org/10.1016/j.intermet.2014.12.004.
[246] S. Morooka, Y. Tomota, T. Kamiyama, Heterogeneous deformation behavior studied by in situ neutron diffraction during tensile deformation for ferrite, martensite and pearlite steels, ISIJ International. 48 (2008) 525–530. https://doi.org/10.2355/isijinternational.48.525.
[247] Y. Tomota, P. Lukáš, D. Neov, S. Harjo, Y.R. Abe, In situ neutron diffraction during tensile deformation of a ferrite-cementite steel, Acta Materialia. 51 (2003) 805–817. https://doi.org/10.1016/S1359-6454(02)00472-X.
[248] Y. Tomota, P. Lukas, S. Harjo, J.H. Park, N. Tsuchida, D. Neov, In situ neutron diffraction study of IF and ultra low carbon steels upon tensile deformation, Acta Materialia. 51 (2003) 819–830. https://doi.org/10.1016/S1359-6454(02)00473-1.
[249] K. Ma, H. Wen, T. Hu, T.D. Topping, D. Isheim, D.N. Seidman, E.J. Lavernia, J.M. Schoenung, Mechanical behavior and strengthening mechanisms in ultrafine grain precipitation-strengthened aluminum alloy, Acta Materialia. 62 (2014) 141–155. https://doi.org/10.1016/j.actamat.2013.09.042.
[250] D. Choudhuri, P.A. Jannotti, S. Muskeri, S. Shukla, S. Gangireddy, S. Mukherjee, B.E. Schuster, J.T. Lloyd, R.S. Mishra, Ballistic Response of a FCC-B2 Eutectic AlCoCrFeNi2.1 High Entropy Alloy, Journal of Dynamic Behavior of Materials. 5 (2019) 495–503. https://doi.org/10.1007/s40870-019-00220-z.
[251] G.J. Davies, J.G. Garland, Solidification Structures and Properties of Fusion Welds, International Metallurgical Reviews. 20 (1975) 83–108. https://doi.org/10.1179/imtlr.1975.20.1.83.
[252] S.A. David, S.S. Babu, J.M. Vitek, Welding: Solidification and microstructure, JOM. 55 (2003) 14–20. https://doi.org/10.1007/s11837-003-0134-7.

[253] S.A. David, J.M. Vitek, Correlation between solidification parameters and weld microstructures, International Materials Reviews. 34 (1989) 213–245. https://doi.org/10.1179/imr.1989.34.1.213.
[254] B. Gludovatz, A. Hohenwarter, D. Catoor, E.H. Chang, E.P. George, R.O. Ritchie, A fracture-resistant high-entropy alloy for cryogenic applications, Science. 345 (2014) 1153–1158. https://doi.org/10.1126/science.1254581.
[255] Y. Zhu, S. Zhou, Z. Xiong, Y. Liang, Y. Xue, L. Wang, Enabling stronger eutectic high-entropy alloys with larger ductility by 3D printed directional lamellae, Additive Manufacturing. 39 (2021) 101901. https://doi.org/10.1016/j.addma.2021.101901.
[256] H. Zheng, R. Chen, G. Qin, X. Li, Y. Su, H. Ding, J. Guo, H. Fu, Phase separation of AlCoCrFeNi2.1 eutectic high-entropy alloy during directional solidification and their effect on tensile properties, Intermetallics. 113 (2019) 106569. https://doi.org/10.1016/j.intermet.2019.106569.
[257] T. Nagase, M. Takemura, M. Matsumuro, T. Maruyama, Solidification Microstructure of $AlCoCrFeNi_{2.1}$ Eutectic High Entropy Alloy Ingots, MATERIALS TRANSACTIONS. 59 (2018) 255–264. https://doi.org/10.2320/matertrans.F-M2017851.
[258] Q. Fan, C. Chen, C. Fan, Z. Liu, X. Cai, S. Lin, C. Yang, Effect of high Fe content on the microstructure, mechanical and corrosion properties of AlCoCrFeNi high-entropy alloy coatings prepared by gas tungsten arc cladding, Surface and Coatings Technology. 418 (2021) 127242. https://doi.org/10.1016/j.surfcoat.2021.127242.
[259] Y.J. Liang, L. Wang, Y. Wen, B. Cheng, Q. Wu, T. Cao, Q. Xiao, Y. Xue, G. Sha, Y. Wang, Y. Ren, X. Li, L. Wang, F. Wang, H. Cai, High-content ductile coherent nanoprecipitates achieve ultrastrong high-entropy alloys, Nature Communications. 9 (2018) 1–8. https://doi.org/10.1038/s41467-018-06600-8.
[260] J. Miao, H. Yao, J. Wang, Y. Lu, T. Wang, T. Li, Surface modification for AlCoCrFeNi2.1 eutectic high-entropy alloy via laser remelting technology and subsequent aging heat treatment, Journal of Alloys and Compounds. 894 (2022) 162380. https://doi.org/10.1016/j.jallcom.2021.162380.
[261] R. Trivedi, P. Magnin, W. Kurz, Theory of eutectic growth under rapid solidification conditions, Acta Metallurgica. 35 (1987) 971–980. https://doi.org/10.1016/0001-6160(87)90176-3.
[262] D. Parkes, W. Xu, D. Westerbaan, S.S. Nayak, Y. Zhou, F. Goodwin, S. Bhole, D.L. Chen, Microstructure and fatigue properties of fiber laser welded dissimilar joints between high strength low alloy and dual-phase steels, Materials & Design. 51 (2013) 665–675. https://doi.org/10.1016/j.matdes.2013.04.076.
[263] C.-C. Tung, J.-W. Yeh, T. Shun, S.-K. Chen, Y.-S. Huang, H.-C. Chen, On the elemental effect of AlCoCrCuFeNi high-entropy alloy system, Materials Letters. 61 (2007) 1–5. https://doi.org/10.1016/j.matlet.2006.03.140.
[264] A. Lozinko, O. V. Mishin, T. Yu, U. Klement, S. Guo, Y. Zhang, Quantification of microstructure in a eutectic high entropy alloy AlCoCrFeNi 2.1, IOP Conference Series: Materials Science and Engineering. 580 (2019) 012039. https://doi.org/10.1088/1757-899X/580/1/012039.
[265] I.S. Wani, T. Bhattacharjee, S. Sheikh, I.T. Clark, M.H. Park, T. Okawa, S. Guo, P.P. Bhattacharjee, N. Tsuji, Cold-rolling and recrystallization textures of a nano-lamellar AlCoCrFeNi2.1 eutectic high entropy alloy, Intermetallics. 84 (2017) 42–51. https://doi.org/10.1016/j.intermet.2016.12.018.
[266] D. Durinck, P.T. Jones, B. Blanpain, P. Wollants, G. Mertens, J. Elsen, Slag Solidification Modeling Using the Scheil?Gulliver Assumptions, Journal of the American Ceramic Society. 90 (2007) 1177–1185. https://doi.org/10.1111/j.1551-2916.2007.01597.x.
[267] D. Piorunek, J. Frenzel, N. Jöns, C. Somsen, G. Eggeler, Chemical complexity, microstructure and martensitic transformation in high entropy shape memory alloys, Intermetallics. 122 (2020) 106792. https://doi.org/10.1016/j.intermet.2020.106792.
[268] Y. Huang, M. Long, P. Liu, D. Chen, H. Chen, L. Gui, T. Liu, S. Yu, Effects of Partition Coefficients, Diffusion Coefficients, and Solidification Paths on Microsegregation in Fe-Based Multinary Alloy, Metallurgical and Materials Transactions B. 48 (2017) 2504–2515. https://doi.org/10.1007/s11663-017-1045-2.
[269] S. Güler, E.D. Alkan, M. Alkan, Vacuum arc melted and heat treated AlCoCrFeNiTiX based high-entropy alloys: Thermodynamic and microstructural investigations, Journal of Alloys and Compounds. 903 (2022) 163901. https://doi.org/10.1016/j.jallcom.2022.163901.
[270] T. Xiong, S. Zheng, J. Pang, X. Ma, High-strength and high-ductility AlCoCrFeNi2.1 eutectic high-entropy alloy achieved via precipitation strengthening in a heterogeneous structure, Scripta Materialia. 186 (2020) 336–340. https://doi.org/10.1016/j.scriptamat.2020.04.035.

[271] Y. Wang, W. Chen, J. Zhang, J. Zhou, A quantitative understanding on the mechanical behavior of AlCoCrFeNi2.1 eutectic high-entropy alloy, Journal of Alloys and Compounds. 850 (2021) 156610. https://doi.org/10.1016/j.jallcom.2020.156610.
[272] S.R. Reddy, S. Yoshida, U. Sunkari, A. Lozinko, J. Joseph, R. Saha, D. Fabijanic, S. Guo, P.P. Bhattacharjee, N. Tsuji, Engineering heterogeneous microstructure by severe warm-rolling for enhancing strength-ductility synergy in eutectic high entropy alloys, Materials Science and Engineering: A. 764 (2019) 138226. https://doi.org/10.1016/j.msea.2019.138226.
[273] O.N. Senkov, G.B. Wilks, J.M. Scott, D.B. Miracle, Mechanical properties of Nb25Mo25Ta25W25 and V20Nb20Mo20Ta20W20 refractory high entropy alloys, Intermetallics. 19 (2011) 698–706. https://doi.org/10.1016/j.intermet.2011.01.004.
[274] D. Wei, X. Li, J. Jiang, W. Heng, Y. Koizumi, W. Choi, B. Lee, H.S. Kim, H. Kato, A. Chiba, Novel Co-rich high performance twinning-induced plasticity (TWIP) and transformation-induced plasticity (TRIP) high-entropy alloys, Scripta Materialia. 165 (2019) 39–43. https://doi.org/10.1016/j.scriptamat.2019.02.018.
[275] S.S. Nene, M. Frank, P. Agrawal, S. Sinha, K. Liu, S. Shukla, R.S. Mishra, B.A. McWilliams, K.C. Cho, Microstructurally flexible high entropy alloys: Linkages between alloy design and deformation behavior, Materials & Design. 194 (2020) 108968. https://doi.org/10.1016/j.matdes.2020.108968.
[276] X. Gao, Y. Lu, J. Liu, J. Wang, T. Wang, Y. Zhao, Extraordinary ductility and strain hardening of Cr26Mn20Fe20Co20Ni14 TWIP high-entropy alloy by cooperative planar slipping and twinning, Materialia. 8 (2019) 100485. https://doi.org/10.1016/j.mtla.2019.100485.
[277] J. Su, D. Raabe, Z. Li, Hierarchical microstructure design to tune the mechanical behavior of an interstitial TRIP-TWIP high-entropy alloy, Acta Materialia. 163 (2019) 40–54. https://doi.org/10.1016/j.actamat.2018.10.017.
[278] Z. Fei, Z. Pan, D. Cuiuri, H. Li, S. Van Duin, Z. Yu, Microstructural characterization and mechanical properties of K-TIG welded SAF2205/AISI316L dissimilar joint, Journal of Manufacturing Processes. 45 (2019) 340–355. https://doi.org/10.1016/j.jmapro.2019.07.017.
[279] Z. Li, C.C. Tasan, H. Springer, B. Gault, D. Raabe, Interstitial atoms enable joint twinning and transformation induced plasticity in strong and ductile high-entropy alloys, Scientific Reports. 7 (2017) 40704. https://doi.org/10.1038/srep40704.
[280] S.M. Vakili, A. Zarei-Hanzaki, A.S. Anoushe, H.R. Abedi, M.H. Mohammad-Ebrahimi, M. Jaskari, S.S. Sohn, D. Ponge, L.P. Karjalainen, Reversible dislocation movement, martensitic transformation and nano-twinning during elastic cyclic loading of a metastable high entropy alloy, Acta Materialia. 185 (2020) 474–492. https://doi.org/10.1016/j.actamat.2019.12.040.
[281] P. Agrawal, R.S. Haridas, S. Thapliyal, S. Yadav, R.S. Mishra, B.A. McWilliams, K.C. Cho, Metastable high entropy alloys: An excellent defect tolerant material for additive manufacturing, Materials Science and Engineering: A. 826 (2021) 142005. https://doi.org/10.1016/j.msea.2021.142005.
[282] H. Beladi, I.B. Timokhina, Y. Estrin, J. Kim, B.C. De Cooman, S.K. Kim, Orientation dependence of twinning and strain hardening behaviour of a high manganese twinning induced plasticity steel with polycrystalline structure, Acta Materialia. 59 (2011) 7787–7799. https://doi.org/10.1016/j.actamat.2011.08.031.
[283] A.A. Saleh, D.W. Brown, E. V. Pereloma, B. Clausen, C.H.J. Davies, C.N. Tomé, A.A. Gazder, An in-situ neutron diffraction study of a multi-phase transformation and twinning-induced plasticity steel during cyclic loading, Applied Physics Letters. 106 (2015) 171911. https://doi.org/10.1063/1.4919455.
[284] J. Ahmed, M. Daly, Yield strength insensitivity in a dual-phase high entropy alloy after prolonged high temperature annealing, Materials Science and Engineering: A. 820 (2021) 141586. https://doi.org/10.1016/j.msea.2021.141586.
[285] S.S. Nene, P. Agrawal, M. Frank, A. Watts, S. Shukla, C. Morphew, A. Chesetti, J.S. Park, R.S. Mishra, Transformative high entropy alloy conquers the strength-ductility paradigm by massive interface strengthening, Scripta Materialia. 203 (2021) 114070. https://doi.org/10.1016/j.scriptamat.2021.114070.
[286] Y.H. Jo, J. Yang, W. Choi, K. Doh, D. Lee, H.S. Kim, B.-J. Lee, S.S. Sohn, S. Lee, Body-centered-cubic martensite and the role on room-temperature tensile properties in Si-added SiVCrMnFeCo high-entropy alloys, Journal of Materials Science & Technology. 76 (2021) 222–230. https://doi.org/10.1016/j.jmst.2020.10.038.
[287] M. Frank, S.S. Nene, Y. Chen, S. Thapliyal, S. Shukla, K. Liu, S. Sinha, T. Wang, M.J. Frost, K.

An, R.S. Mishra, Direct evidence of the stacking fault-mediated strain hardening phenomenon, Applied Physics Letters. 119 (2021) 081906. https://doi.org/10.1063/5.0062153.
[288] S. Fu, H. Bei, Y. Chen, T.K. Liu, D. Yu, K. An, Deformation mechanisms and work-hardening behavior of transformation-induced plasticity high entropy alloys by in -situ neutron diffraction, Materials Research Letters. 6 (2018) 620–626. https://doi.org/10.1080/21663831.2018.1523239.
[289] A. Sittiho, M. Bhattacharyya, J. Graves, S.S. Nene, R.S. Mishra, I. Charit, Friction stir processing of a high entropy alloy Fe42Co10Cr15Mn28Si5 with transformative characteristics: Microstructure and mechanical properties, Materials Today Communications. 28 (2021) 102635. https://doi.org/10.1016/j.mtcomm.2021.102635.
[290] Phase- and Size-Dependent Optical and Magnetic Properties of CoO Nanoparticles.pdf, (n.d.). https://doi.org/10.1021/jp512790.
[291] S. Bhowmik, J. Zhang, S.C. Vogel, S.S. Nene, R.S. Mishra, B.A. McWilliams, M. Knezevic, Effects of plasticity-induced martensitic transformation and grain refinement on the evolution of microstructure and mechanical properties of a metastable high entropy alloy, Journal of Alloys and Compounds. 891 (2022) 161871. https://doi.org/10.1016/j.jallcom.2021.161871.
[292] T. Gebhardt, D. Music, M. Ekholm, I.A. Abrikosov, L. Vitos, A. Dick, T. Hickel, J. Neugebauer, J.M. Schneider, The influence of additions of Al and Si on the lattice stability of fcc and hcp Fe-Mn random alloys, Journal of Physics Condensed Matter. 23 (2011) 1–8. https://doi.org/10.1088/0953-8984/23/24/246003.
[293] P. Agrawal, S. Thapliyal, S.S. Nene, R.S. Mishra, B.A. McWilliams, K.C. Cho, Excellent strength-ductility synergy in metastable high entropy alloy by laser powder bed additive manufacturing, Additive Manufacturing. 32 (2020) 101098. https://doi.org/10.1016/j.addma.2020.101098.
[294] R. Xiong, H. Peng, H. Si, W. Zhang, Y. Wen, Thermodynamic calculation of stacking fault energy of the Fe–Mn–Si–C high manganese steels, Materials Science and Engineering: A. 598 (2014) 376–386. https://doi.org/10.1016/j.msea.2014.01.046.
[295] Z. Li, C.C. Tasan, K.G. Pradeep, D. Raabe, A TRIP-assisted dual-phase high-entropy alloy: Grain size and phase fraction effects on deformation behavior, Acta Materialia. 131 (2017) 323–335. https://doi.org/10.1016/j.actamat.2017.03.069.
[296] S. Wei, J. Kim, C.C. Tasan, Boundary micro-cracking in metastable Fe45Mn35Co10Cr10 high-entropy alloys, Acta Materialia. 168 (2019) 76–86. https://doi.org/10.1016/j.actamat.2019.01.036.
[297] H. Huang, Y. Wu, J. He, H. Wang, X. Liu, K. An, W. Wu, Z. Lu, Phase-Transformation Ductilization of Brittle High-Entropy Alloys via Metastability Engineering, Advanced Materials. 29 (2017) 1701678. https://doi.org/10.1002/adma.201701678.
[298] K.Y. Xie, Z. Alam, A. Caffee, K.J. Hemker, Pyramidal I slip in c-axis Compressed Mg Single Crystals, (2015).
[299] S. Papula, S. Anttila, J. Talonen, T. Sarikka, I. Virkkunen, H. Hänninen, Strain hardening of cold-rolled lean-alloyed metastable ferritic-austenitic stainless steels, Materials Science and Engineering: A. 677 (2016) 11–19. https://doi.org/10.1016/j.msea.2016.09.038.
[300] D.T. Pierce, J.A. Jiménez, J. Bentley, D. Raabe, J.E. Wittig, The influence of stacking fault energy on the microstructural and strain-hardening evolution of Fe–Mn–Al–Si steels during tensile deformation, Acta Materialia. 100 (2015) 178–190. https://doi.org/10.1016/j.actamat.2015.08.030.
[301] Z. Li, D. Raabe, Strong and Ductile Non-equiatomic High-Entropy Alloys: Design, Processing, Microstructure, and Mechanical Properties, JOM. 69 (2017) 2099–2106. https://doi.org/10.1007/s11837-017-2540-2.
[302] D.T. Pierce, J.A. Jiménez, J. Bentley, D. Raabe, C. Oskay, J.E. Wittig, The influence of manganese content on the stacking fault and austenite/ε-martensite interfacial energies in Fe–Mn–(Al–Si) steels investigated by experiment and theory, Acta Materialia. 68 (2014) 238–253. https://doi.org/10.1016/j.actamat.2014.01.001.
[303] S. Gangireddy, B. Gwalani, R. Banerjee, R.S. Mishra, High Strain Rate Response of Al0.7CoCrFeNi High Entropy Alloy: Dynamic Strength Over 2 GPa from Thermomechanical Processing and Hierarchical Microstructure, Journal of Dynamic Behavior of Materials. 5 (2019) 1–7. https://doi.org/10.1007/s40870-018-00178-4.
[304] S. Gangireddy, B. Gwalani, K. Liu, R. Banerjee, R.S. Mishra, Microstructures with extraordinary dynamic work hardening and strain rate sensitivity in Al0.3CoCrFeNi high entropy alloy, Materials Science and Engineering A. 734 (2018) 42–50. https://doi.org/10.1016/j.msea.2018.07.088.
[305] S. Gangireddy, B. Gwalani, R.S. Mishra, Grain size dependence of strain rate sensitivity in a single phase FCC high entropy alloy Al0.3CoCrFeNi, Materials Science and Engineering A. 736

(2018) 344–348. https://doi.org/10.1016/j.msea.2018.09.009.
[306] N. Kumar, M. Komarasamy, P. Nelaturu, Z. Tang, P.K. Liaw, R.S. Mishra, Friction Stir Processing of a High Entropy Alloy Al0.1CoCrFeNi, JOM. 67 (2015) 1007–1013. https://doi.org/10.1007/s11837-015-1385-9.
[307] Z. Li, F. Körmann, B. Grabowski, J. Neugebauer, D. Raabe, Ab initio assisted design of quinary dual-phase high-entropy alloys with transformation-induced plasticity, Acta Materialia. 136 (2017) 262–270. https://doi.org/10.1016/j.actamat.2017.07.023.
[308] M. Calcagnotto, D. Ponge, E. Demir, D. Raabe, Orientation gradients and geometrically necessary dislocations in ultrafine grained dual-phase steels studied by 2D and 3D EBSD, Materials Science and Engineering: A. 527 (2010) 2738–2746. https://doi.org/10.1016/j.msea.2010.01.004.
[309] C.L. Yang, Z.J. Zhang, T. Cai, P. Zhang, Z.F. Zhang, Recovery of strain-hardening rate in Ni-Si alloys, Scientific Reports. 5 (2015) 15532. https://doi.org/10.1038/srep15532.
[310] U.F. Kocks, H. Mecking, Physics and phenomenology of strain hardening: The FCC case, Progress in Materials Science. 48 (2003) 171–273. https://doi.org/10.1016/S0079-6425(02)00003-8.
[311] G. Taylor, J.W. Christian, Experiments on the deformation of niobium single crystals. I. Stress versus strain curves and slip systems in compression and tension, Philosophical Magazine. 15 (1967) 873–892. https://doi.org/10.1080/14786436708221635.
[312] S. Kuang, Y. Kang, H. Yu, R. Liu, Stress-strain partitioning analysis of constituent phases in dual phase steel based on the modified law of mixture, International Journal of Minerals, Metallurgy and Materials. 16 (2009) 393–398. https://doi.org/10.1016/S1674-4799(09)60070-4.
[313] S.S. Nene, S. Sinha, M. Frank, K. Liu, R.S. Mishra, B.A. McWilliams, K.C. Cho, Unexpected strength–ductility response in an annealed, metastable, high-entropy alloy, Applied Materials Today. 13 (2018) 198–206. https://doi.org/10.1016/j.apmt.2018.09.002.
[314] S.S. Nene, M. Frank, K. Liu, S. Sinha, R.S. Mishra, B. McWilliams, K.C. Cho, Reversed strength-ductility relationship in microstructurally flexible high entropy alloy, Scripta Materialia. 154 (2018) 163–167. https://doi.org/10.1016/j.scriptamat.2018.05.043.
[315] M.A. Gharghouri, G.C. Weatherly, J.D. Embury, The interaction of twins and precipitates in a Mg-7.7 at.% Al alloy, Philosophical Magazine A. 78 (1998) 1137–1149. https://doi.org/10.1080/01418619808239980.
[316] S. Sinha, A. Pukenas, A. Ghosh, A. Singh, W. Skrotzki, N.P. Gurao, Effect of initial orientation on twinning in commercially pure titanium, Philosophical Magazine. 97 (2017) 775–797. https://doi.org/10.1080/14786435.2017.1279364.
[317] Y.T. Zhu, Deformation twinning in a nanocrystalline hcp Mg alloy, 64 (2011) 213–216. https://doi.org/10.1016/j.scriptamat.2010.10.024.
[318] S. Sinha, S.S. Nene, M. Frank, K. Liu, R.A. Lebensohn, R.S. Mishra, Deformation mechanisms and ductile fracture characteristics of a friction stir processed transformative high entropy alloy, Acta Materialia. 184 (2020) 164–178. https://doi.org/10.1016/j.actamat.2019.11.056.
[319] S.S. Nene, K. Liu, S. Sinha, M. Frank, S. Williams, R.S. Mishra, Superplasticity in fine grained dual phase high entropy alloy, Materialia. 9 (2020) 100521. https://doi.org/10.1016/j.mtla.2019.100521.
[320] O. Muránsky, P. Šittner, J. Zrník, E.C. Oliver, In situ neutron diffraction investigation of the collaborative deformation–transformation mechanism in TRIP-assisted steels at room and elevated temperatures, Acta Materialia. 56 (2008) 3367–3379. https://doi.org/10.1016/j.actamat.2008.03.026.
[321] , Longfei Li, (n.d.) 1–42.
[322] O. Gra, L. Kru, G. Frommeyer, L.W. Meyer, High strength Fe ± Mn ± (Al , Si) TRIP / TWIP steels development Ð properties Ð application, 16 (2000) 1391–1409.
[323] K. Yan, K. Liss, I.B. Timokhina, E. V Pereloma, In situ synchrotron X-ray diffraction studies of the effect of microstructure on tensile behavior and retained austenite stability of thermo-mechanically processed transformation induced plasticity steel, Materials Science and Engineering: A. 662 (2016) 185–197. https://doi.org/10.1016/j.msea.2016.03.048.
[324] J. Liu, C. Chen, Q. Feng, X. Fang, H. Wang, F. Liu, J. Lu, D. Raabe, Dislocation activities at the martensite phase transformation interface in metastable austenitic stainless steel: An in-situ TEM study, Materials Science and Engineering: A. 703 (2017) 236–243. https://doi.org/10.1016/j.msea.2017.06.107.
[325] G. Niu, Q. Tang, H.S. Zurob, H. Wu, L. Xu, N. Gong, Strong and ductile steel via high dislocation

density and heterogeneous nano/ultrafine grains, Materials Science and Engineering: A. 759 (2019) 1–10. https://doi.org/10.1016/j.msea.2019.04.112.
[326] B.C. De Cooman, Y. Estrin, S.K. Kim, Twinning-induced plasticity (TWIP) steels, Acta Materialia. 142 (2018) 283–362. https://doi.org/10.1016/j.actamat.2017.06.046.
[327] Y. Han, H. Li, H. Feng, K. Li, Y. Tian, Z. Jiang, Simultaneous enhancement in strength and ductility of Fe50Mn30Co10Cr10 high-entropy alloy via nitrogen alloying, Journal of Materials Science & Technology. 65 (2021) 210–215. https://doi.org/10.1016/j.jmst.2020.04.072.
[328] A.V. Druker, A. Perotti, I. Esquivel, J. Malarría, Design of Devices and Manufacturing of Fe-Mn-Si Shape Memory Alloy Couplings, Procedia Materials Science. 8 (2015) 878–885. https://doi.org/10.1016/j.mspro.2015.04.148.
[329] C. Garcia-Mateo, H.K.D.. Bhadeshia, Nucleation theory for high-carbon bainite, Materials Science and Engineering: A. 378 (2004) 289–292. https://doi.org/10.1016/j.msea.2003.10.355.
[330] R.S. Mishra, R.S. Haridas, P. Agrawal, High entropy alloys – Tunability of deformation mechanisms through integration of compositional and microstructural domains, Materials Science and Engineering: A. 812 (2021) 141085. https://doi.org/10.1016/j.msea.2021.141085.
[331] O. Bouaziz, N. Guelton, Modelling of TWIP effect on work-hardening, Materials Science and Engineering: A. 319–321 (2001) 246–249. https://doi.org/10.1016/S0921-5093(00)02019-0.
[332] W. Woo, J.S. Jeong, D.-K. Kim, C.M. Lee, S.-H. Choi, J.-Y. Suh, S.Y. Lee, S. Harjo, T. Kawasaki, Stacking Fault Energy Analyses of Additively Manufactured Stainless Steel 316L and CrCoNi Medium Entropy Alloy Using In Situ Neutron Diffraction, Scientific Reports. 10 (2020) 1350. https://doi.org/10.1038/s41598-020-58273-3.
[333] S. Martin, C. Ullrich, D. Rafaja, Deformation of Austenitic CrMnNi TRIP/TWIP Steels: Nature and Role of the ε−martensite, Materials Today: Proceedings. 2 (2015) S643–S646. https://doi.org/10.1016/j.matpr.2015.07.366.
[334] Y.Y. Shang, Y. Wu, J.Y. He, X.Y. Zhu, S.F. Liu, H.L. Huang, K. An, Y. Chen, S.H. Jiang, H. Wang, X.J. Liu, Z.P. Lu, Solving the strength-ductility tradeoff in the medium-entropy NiCoCr alloy via interstitial strengthening of carbon, Intermetallics. 106 (2019) 77–87. https://doi.org/10.1016/j.intermet.2018.12.009.
[335] Y. Wang, B. Liu, K. Yan, M. Wang, S. Kabra, Y.-L. Chiu, D. Dye, P.D. Lee, Y. Liu, B. Cai, Probing deformation mechanisms of a FeCoCrNi high-entropy alloy at 293 and 77 K using in situ neutron diffraction, Acta Materialia. 154 (2018) 79–89. https://doi.org/10.1016/j.actamat.2018.05.013.
[336] M. Kang, W. Woo, Y.-K. Lee, B.-S. Seong, Neutron diffraction analysis of stacking fault energy in Fe–18Mn–2Al–0.6C twinning-induced plasticity steels, Materials Letters. 76 (2012) 93–95. https://doi.org/10.1016/j.matlet.2012.02.075.
[337] M. Frank, S.S. Nene, Y. Chen, B. Gwalani, E.J. Kautz, A. Devaraj, K. An, R.S. Mishra, Correlating work hardening with co-activation of stacking fault strengthening and transformation in a high entropy alloy using in-situ neutron diffraction, Scientific Reports. 10 (2020) 22263. https://doi.org/10.1038/s41598-020-79492-8.
[338] A. Reviews, Quick links to online content, n.d.
[339] Q. Fang, Y. Chen, J. Li, C. Jiang, B. Liu, Y. Liu, P.K. Liaw, Probing the phase transformation and dislocation evolution in dual-phase high-entropy alloys, International Journal of Plasticity. 114 (2019) 161–173. https://doi.org/10.1016/j.ijplas.2018.10.014.
[340] I.A. Yakubtsov, A. Ariapour, D.D. Perovic, Effect of nitrogen on stacking fault energy of f.c.c. iron-based alloys, Acta Materialia. 47 (1999) 1271–1279. https://doi.org/10.1016/S1359-6454(98)00419-4.
[341] J.W. Brooks, M.H. Loretto, R.E. Smallman, Direct observations of martensite nuclei in stainless steel, Acta Metallurgica. 27 (1979) 1839–1847. https://doi.org/10.1016/0001-6160(79)90074-9.
[342] S. Mahajan, M.L. Green, D. Brasen, A model for the FCC→HCP transformation, its applications, and experimental evidence, Metallurgical Transactions A. 8 (1977) 283–293. https://doi.org/10.1007/BF02661642.
[343] S.S. Nene, S. Sinha, M. Frank, K. Liu, R.S. Mishra, B.A. McWilliams, K.C. Cho, Unexpected strength–ductility response in an annealed, metastable, high-entropy alloy, Applied Materials Today. 13 (2018) 198–206. https://doi.org/10.1016/j.apmt.2018.09.002.
[344] S. Hyuk Park, S. Hong, C.S. Lee, In-plane anisotropic deformation behavior of rolled Mg–3Al–1Zn alloy by initial {10–12} twins, Materials Science and Engineering: A. 570 (2013) 149–163. https://doi.org/10.1016/j.msea.2013.01.071.
[345] O. Muránsky, M.R. Barnett, D.G. Carr, S.C. Vogel, E.C. Oliver, Investigation of deformation twinning in a fine-grained and coarse-grained ZM20 Mg alloy: Combined in situ neutron

diffraction and acoustic emission, Acta Materialia. 58 (2010) 1503–1517. https://doi.org/10.1016/j.actamat.2009.10.057.
[346] D. Sarker, D.L. Chen, Texture transformation in an extruded magnesium alloy under pressure, Materials Science and Engineering: A. 582 (2013) 63–67. https://doi.org/10.1016/j.msea.2013.06.048.
[347] L. Song, B. Wu, L. Zhang, X. Du, Y. Wang, C. Esling, Twinning characterization of fiber-textured AZ31B magnesium alloy during tensile deformation, Materials Science and Engineering: A. 710 (2018) 57–65. https://doi.org/10.1016/j.msea.2017.10.055.
[348] K. Hantzsche, J. Bohlen, J. Wendt, K.U. Kainer, S.B. Yi, D. Letzig, Effect of rare earth additions on microstructure and texture development of magnesium alloy sheets, Scripta Materialia. 63 (2010) 725–730. https://doi.org/10.1016/j.scriptamat.2009.12.033.
[349] B.C. Wonsiewicz, Plasticity of Magnesium Crystals, S.B. Massachusetts Institute of Technology, 1966.
[350] J. Koike, Enhanced deformation mechanisms by anisotropic plasticity in polycrystalline Mg alloys at room temperature, Metallurgical and Materials Transactions A. 36 (2005) 1689–1696. https://doi.org/10.1007/s11661-005-0032-4.
[351] B.L. Wu, Y.D. Zhang, G. Wan, M. Humbert, F. Wagner, C. Esling, Primary twinning selection with respect to orientation of deformed grains in ultra-rapidly compressed AZ31 alloy, Materials Science and Engineering: A. 541 (2012) 120–127. https://doi.org/10.1016/j.msea.2012.02.012.
[352] J.R. Bingert, T.A. Mason, G.C. Kaschner, G.T. Gray, P.J. Maudlin, Deformation twinning in polycrystalline Zr: Insights from electron backscattered diffraction characterization, Metallurgical and Materials Transactions A. 33 (2002) 955–963. https://doi.org/10.1007/s11661-002-0165-7.
[353] S. Lee, S.-J. Lee, B.C. De Cooman, Austenite stability of ultrafine-grained transformation-induced plasticity steel with Mn partitioning, Scripta Materialia. 65 (2011) 225–228. https://doi.org/10.1016/j.scriptamat.2011.04.010.
[354] S. Chatterjee, H.-S. Wang, J.R. Yang, H.K.D.H. Bhadeshia, Mechanical stabilisation of austenite, Materials Science and Technology. 22 (2006) 641–644. https://doi.org/10.1179/174328406X86128.
[355] P.J. Jacques, F. Delannay, J. Ladrière, On the influence of interactions between phases on the mechanical stability of retained austenite in transformation-induced plasticity multiphase steels, Metallurgical and Materials Transactions A. 32 (2001) 2759–2768. https://doi.org/10.1007/s11661-001-1027-4.
[356] T. Edition, Phase Transformations in Metals and Alloys, Talor & Francis Group, 21352.
[357] L. Song, B. Wu, L. Zhang, X. Du, Y. Wang, C. Esling, J. Liu, C. Chen, Q. Feng, X. Fang, H. Wang, F. Liu, J. Lu, D. Raabe, Author ' s Accepted Manuscript, Materials Science & Engineering A. (2017). https://doi.org/10.1016/j.msea.2017.06.107.
[358] I. Tamura, Deformation-induced martensitic transformation and transformation-induced plasticity in steels, Metal Science. 16 (1982) 245–253. https://doi.org/10.1179/030634582790427316.
[359] Y. Liu, H. Yang, G. Tan, S. Miyazaki, B. Jiang, Y. Liu, Stress-induced FCC ↔ HCP martensitic transformation in CoNi, Journal of Alloys and Compounds. 368 (2004) 157–163. https://doi.org/10.1016/j.jallcom.2003.07.015.
[360] M. Javanbakht, V.I. Levitas, Interaction between phase transformations and dislocations at the nanoscale. Part 2: Phase field simulation examples, Journal of the Mechanics and Physics of Solids. 82 (2015) 164–185. https://doi.org/10.1016/j.jmps.2015.05.006.
[361] V.I. Levitas, M. Javanbakht, Thermodynamically consistent phase field approach to dislocation evolution at small and large strains, Journal of the Mechanics and Physics of Solids. 82 (2015) 345–366. https://doi.org/10.1016/j.jmps.2015.05.009.
[362] P.J. Jacques, Q. Furnémont, F. Lani, T. Pardoen, F. Delannay, Multiscale mechanics of TRIP-assisted multiphase steels: I. Characterization and mechanical testing, Acta Materialia. 55 (2007) 3681–3693. https://doi.org/10.1016/j.actamat.2007.02.029.
[363] X. Wu, P. Jiang, L. Chen, F. Yuan, Y.T. Zhu, Extraordinary strain hardening by gradient structure, Proceedings of the National Academy of Sciences. 111 (2014) 7197–7201. https://doi.org/10.1073/pnas.1324069111.
[364] M. Naeem, H. He, F. Zhang, H. Huang, S. Harjo, T. Kawasaki, B. Wang, S. Lan, Z. Wu, F. Wang, Y. Wu, Z. Lu, Z. Zhang, C.T. Liu, X.L. Wang, Cooperative deformation in high-entropy alloys at ultralow temperatures, Science Advances. 6 (2020). https://doi.org/10.1126/sciadv.aax4002.
[365] W. Woo, E.-W. Huang, J.-W. Yeh, H. Choo, C. Lee, S.-Y. Tu, In-situ neutron diffraction studies on high-temperature deformation behavior in a CoCrFeMnNi high entropy alloy, Intermetallics.

62 (2015) 1–6. https://doi.org/10.1016/j.intermet.2015.02.020.
[366] H. He, M. Naeem, F. Zhang, Y. Zhao, S. Harjo, T. Kawasaki, B. Wang, X. Wu, S. Lan, Z. Wu, W. Yin, Y. Wu, Z. Lu, J.-J. Kai, C.-T. Liu, X.-L. Wang, Stacking Fault Driven Phase Transformation in CrCoNi Medium Entropy Alloy, Nano Letters. 21 (2021) 1419–1426. https://doi.org/10.1021/acs.nanolett.0c04244.
[367] M. Meyers, A. Engineering, S. Diego, E. Conferences, H. Senior, S. Award, T.M.S.D. Scientist, E. Awards, L.H. Award, K. Chawla, M. Science, Mechanical behavior of materials, Choice Reviews Online. 46 (2009) 46-6830-46–6830. https://doi.org/10.5860/CHOICE.46-6830.
[368] J. Wang, L. Wang, G. Zhu, B. Zhou, T. Ying, X. Zhang, Q. Huang, Y. Shen, X. Zeng, H. Jiang, Understanding the High Strength and Good Ductility in LPSO-Containing Mg Alloy Using Synchrotron X-ray Diffraction, Metallurgical and Materials Transactions A. 49 (2018) 5382–5392. https://doi.org/10.1007/s11661-018-4881-z.
[369] M. Frank, S.S. Nene, Y. Chen, B. Gwalani, E.J. Kautz, A. Devaraj, K. An, Correlating work hardening with co‐activation of stacking fault strengthening and transformation in a high entropy alloy using in‐situ neutron diffraction, (2020) 1–11. https://doi.org/10.1038/s41598-020-79492-8.
[370] S.J. Sun, Y.Z. Tian, H.R. Lin, H.J. Yang, X.G. Dong, Y.H. Wang, Z.F. Zhang, Achieving high ductility in the 1.7 GPa grade CoCrFeMnNi high-entropy alloy at 77 K, Materials Science and Engineering: A. 740–741 (2019) 336–341. https://doi.org/10.1016/j.msea.2018.10.094.
[371] F. Otto, A. Dlouhý, C. Somsen, H. Bei, G. Eggeler, E.P. George, The influences of temperature and microstructure on the tensile properties of a CoCrFeMnNi high-entropy alloy, Acta Materialia. 61 (2013) 5743–5755. https://doi.org/10.1016/j.actamat.2013.06.018.
[372] R.S. Haridas, P. Agrawal, S. Yadav, P. Agrawal, A. Gumaste, R.S. Mishra, Work hardening in metastable high entropy alloys: a modified five-parameter model, Journal of Materials Research and Technology. 18 (2022) 3358–3372. https://doi.org/10.1016/j.jmrt.2022.04.016.
[373] P. Agrawal, S. Gupta, S. Shukla, S.S. Nene, S. Thapliyal, M.P. Toll, R.S. Mishra, Role of Cu addition in enhancing strength-ductility synergy in transforming high entropy alloy, Materials & Design. 215 (2022) 110487. https://doi.org/10.1016/j.matdes.2022.110487.
[374] S.S. Nene, S. Gupta, C. Morphew, R.S. Mishra, Friction stir butt welding of a high strength Al-7050 alloy with a metastable transformative high entropy alloy, Materialia. 11 (2020) 100740. https://doi.org/10.1016/j.mtla.2020.100740.
[375] S. Gupta, P. Agrawal, S.S. Nene, R.S. Mishra, Friction stir welding of γ-fcc dominated metastable high entropy alloy: Microstructural evolution and strength, Scripta Materialia. 204 (2021) 114161. https://doi.org/10.1016/j.scriptamat.2021.114161.
[376] A. Sittiho, M. Bhattacharyya, J. Graves, S.S. Nene, R.S. Mishra, I. Charit, Friction stir processing of a high entropy alloy Fe42Co10Cr15Mn28Si5 with transformative characteristics: Microstructure and mechanical properties, Materials Today Communications. 28 (2021) 102635. https://doi.org/10.1016/j.mtcomm.2021.102635.
[377] W. Kurz, C. Bezençon, M. Gäumann, Columnar to equiaxed transition in solidification processing, Science and Technology of Advanced Materials. 2 (2001) 185–191. https://doi.org/10.1016/S1468-6996(01)00047-X.
[378] W. Zhang, J. Shen, J.P. Oliveira, B.J. Kooi, Y. Pei, Crystallographic orientation-dependent deformation characteristics of additive manufactured interstitial-strengthened high entropy alloys, Scripta Materialia. 222 (2023) 115049. https://doi.org/10.1016/j.scriptamat.2022.115049.
[379] O. Dmitrieva, D. Ponge, G. Inden, J. Millán, P. Choi, J. Sietsma, D. Raabe, Chemical gradients across phase boundaries between martensite and austenite in steel studied by atom probe tomography and simulation, Acta Materialia. 59 (2011) 364–374. https://doi.org/10.1016/j.actamat.2010.09.042.
[380] D. Raabe, S. Sandlöbes, J. Millán, D. Ponge, H. Assadi, M. Herbig, P.-P. Choi, Segregation engineering enables nanoscale martensite to austenite phase transformation at grain boundaries: A pathway to ductile martensite, Acta Materialia. 61 (2013) 6132–6152. https://doi.org/10.1016/j.actamat.2013.06.055.
[381] Q. Guo, M. Qu, C.A. Chuang, L. Xiong, A. Nabaa, Z.A. Young, Y. Ren, P. Kenesei, F. Zhang, L. Chen, Phase transformation dynamics guided alloy development for additive manufacturing, Additive Manufacturing. 59 (2022) 103068. https://doi.org/10.1016/j.addma.2022.103068.
[382] Z.G. Zhu, X.H. An, W.J. Lu, Z.M. Li, F.L. Ng, X.Z. Liao, U. Ramamurty, S.M.L. Nai, J. Wei, Selective laser melting enabling the hierarchically heterogeneous microstructure and excellent mechanical properties in an interstitial solute strengthened high entropy alloy, Materials

Research Letters. 7 (2019) 453–459. https://doi.org/10.1080/21663831.2019.1650131.
[383] R.S. Mishra, S.S. Nene, Some Unique Aspects of Mechanical Behavior of Metastable Transformative High Entropy Alloys, Metallurgical and Materials Transactions A. 52 (2021) 889–896. https://doi.org/10.1007/s11661-021-06138-3.
[384] P. Sahu, A.S. Hamada, R.N. Ghosh, L.P. Karjalainen, X-ray Diffraction Study on Cooling-Rate-Induced γ fcc→ε hcp Martensitic Transformation in Cast-Homogenized Fe-26Mn-0.14C Austenitic Steel, Metallurgical and Materials Transactions A. 38 (2007) 1991–2000. https://doi.org/10.1007/s11661-007-9240-4.
[385] M. Hou, K. Li, X. Li, X. Zhang, S. Rui, Y. Wu, Z. Cai, Effects of Pulsed Magnetic Fields of Different Intensities on Dislocation Density, Residual Stress, and Hardness of Cr4Mo4V Steel, Crystals. 10 (2020) 115. https://doi.org/10.3390/cryst10020115.
[386] S. Mitra, K.S. Arora, B. Bhattacharya, S.B. Singh, Effect of Welding Speed on the Prediction Accuracy of Residual Stress in Laser Welded 1.2 mm Thick Dual Phase Steel, Lasers in Manufacturing and Materials Processing. 7 (2020) 74–87. https://doi.org/10.1007/s40516-019-00107-w.
[387] Y. Liu, B. Wang, R. Liu, J. Guo, W. Shi, Effect of Allotropic Transformation on Plasticity of Fe-15Mn-10Al-0.3C Dual Phase Steel during Annealing, Cailiao Yanjiu Xuebao/Chinese Journal of Materials Research. 33 (2019) 837–847. https://doi.org/10.11901/1005.3093.2019.136.
[388] P. Agrawal, R.S. Haridas, P. Agrawal, R.S. Mishra, Deformation based additive manufacturing of a metastable high entropy alloy via Additive friction stir deposition, Additive Manufacturing. 60 (2022) 103282. https://doi.org/10.1016/j.addma.2022.103282.
[389] P. Niu, R. Li, Z. Fan, T. Yuan, Z. Zhang, Additive manufacturing of TRIP-assisted dual-phases Fe50Mn30Co10Cr10 high-entropy alloy: Microstructure evolution, mechanical properties and deformation mechanisms, Materials Science and Engineering: A. 814 (2021) 141264. https://doi.org/10.1016/j.msea.2021.141264.
[390] I. Calliari, M. Pellizzari, M. Zanellato, E. Ramous, The phase stability in Cr–Ni and Cr–Mn duplex stainless steels, Journal of Materials Science. 46 (2011) 6916–6924. https://doi.org/10.1007/s10853-011-5657-7.
[391] A. Kundu, S. Ghosh, R. Banerjee, S. Ghosh, B. Sanyal, New quaternary half-metallic ferromagnets with large Curie temperatures, Scientific Reports. 7 (2017) 1803. https://doi.org/10.1038/s41598-017-01782-5.
[392] Y. Hou, T. Liu, D. He, Z. Li, L. Chen, H. Su, P. Fu, P. Dai, W. Huang, Sustaining strength-ductility synergy of SLM Fe50Mn30Co10Cr10 metastable high-entropy alloy by Si addition, Intermetallics. 145 (2022) 107565. https://doi.org/10.1016/j.intermet.2022.107565.
[393] D.G. Shaysultanov, K.S. Raimov, N.D. Stepanov, Effect of carbon content, deformation and annealing on the structure and properties of interstitial TRIP high-entropy alloys, IOP Conference Series: Materials Science and Engineering. 1014 (2021) 012052. https://doi.org/10.1088/1757-899X/1014/1/012052.
[394] M. Koyama, H. Springer, S. V. Merzlikin, K. Tsuzaki, E. Akiyama, D. Raabe, Hydrogen embrittlement associated with strain localization in a precipitation-hardened Fe–Mn–Al–C light weight austenitic steel, International Journal of Hydrogen Energy. 39 (2014) 4634–4646. https://doi.org/10.1016/j.ijhydene.2013.12.171.
[395] K. Ichii, M. Koyama, C.C. Tasan, K. Tsuzaki, Localized Plasticity and Associated Cracking in Stable and Metastable High-Entropy Alloys Pre-Charged with Hydrogen, Procedia Structural Integrity. 13 (2018) 716–721. https://doi.org/10.1016/j.prostr.2018.12.119.